Acoustical response of shear layers

Please check the document version of this publication:

• A submitted manuscript is the version of the article upon submission and before peer-review. There can be important differences between the submitted version and the official published version of record. People interested in the research are advised to contact the author for the final version of the publication, or visit the DOI to the publisher's website.
• The final author version and the galley proof are versions of the publication after peer review.
• The final published version features the final layout of the paper including the volume, issue and page numbers.

Link to publication

Acoustical Response of Shear Layers

by

Gerben Kooijman

Acoustical Response of Shear Layers

PROEFSCHRIFT

ter verkrijging van de graad van doctor aan de
Technische Universiteit Eindhoven op gezag van
de Rector Magnificus, prof.dr.ir. C.J. van Duijn,
voor een commissie aangewezen door het College
voor Promoties in het openbaar te verdedigen op
woensdag 31 januari 2007 om 16.00 uur

door

Gerben Kooijman

geboren te 's-Hertogenbosch

Dit proefschrift is goedgekeurd door de promotoren:

prof.dr.ir. M.E.H. van Dongen
en
prof.dr.ir. A. Hirschberg

Copromotor:
dr. Y. Aurégan

De ultieme droom is promoveren

Gert Kruys, trainer FC Den Bosch
Stadsblad 's-Hertogenbosch, 20 augustus 2003

aan mijn ouders,

aan Lisa

Contents

Chapter 1

Introduction

1.1 Aeroacoustics

Originally, acoustics was the study of small pressure perturbation waves in air, which can be detected by the human ear: sound. An extended definition can be found in Pierce [89]: *Acoustics is the science of sound, including its production, transmission, and effects.* Here, sound is related to a mechanical wave, or oscillating perturbations of a steady state of a solid, liquid or gaseous medium propagating from a sound source through the medium. Not only frequencies f of the perturbations audible for a normal person, 20 Hz $\leq f \leq$ 20 kHz, but also lower (infrasound) and higher (ultrasound) frequencies are included.

In this study propagation of audible sound in a gaseous medium, like air, is considered. The pressure fluctuations p' associated with (audible) sound are small compared to the atmospheric pressure p_{atm}: $p'/p_{atm} = O(10^{-10}) - O(10^{-3})$. This justifies linearization of the equations of fluid dynamics, that describe sound propagation.

Aeroacoustics deals with the study of the interaction between sound and flow. Due to this interaction either absorption or generation of sound by the flow can occur. A first important contribution to this topic was made by Lighthill [63, 64]. From the mass and momentum conservation equations of fluid dynamics he derived a non-homogeneous wave equation for the linear perturbations. The nonhomogeneous term is considered as the deviation from a reference acoustical field, which is an extrapolation of the field at the position of the listener, and which satisfies the homogeneous wave equation. This deviation acts as a source of sound. This so-called aeroacoustic analogy is a very general definition and does not provide new information compared to the conservation equations of fluid dynamics. However, the analogy is useful in the sense that it allows for approximations in the source term.

For low Mach number flows in free space, with a source region small compared to

the wavelength of the sound, Powell [90] showed that the source term in Lighthill's analogy is related to the Coriolis force associated with the vorticity of the flow. A generalization of this vortex sound theory to high Mach numbers and to confined flows was provided by Howe [43]. Instead of using the aeroacoustic analogy, in some cases the interaction between flow and acoustic field is described by analytical, e.g. [22, 94], or numerical, e.g. [14], solutions of the linearized Euler equations. This approach is considered in this thesis.

1.2 Technological applications

Besides the application to musical instruments, in particular wind instruments, especially the production of unwanted sound by machinery is an important incentive for research in the field of aeroacoustics. Examples are noise from jet engine inlets and outlets and combustion engine exhausts as well as flow induced pulsations in ventilation ducts and gas transport systems. In the latter cases the generation of sound is often associated with flow separation from an edge, for instance at a discontinuity in cross-section of a duct. Vorticity is shed from the edge and is concentrated in the shear layer, which is formed downstream and separates the region of flow from a stagnant fluid region. In the presence of a resonator, a feedback-loop can occur between the acoustical field and the vortex shedding at the edge, leading to self-sustained oscillations, called whistling.

In order to suppress noise from jet engines and internal combustion engines, acoustic lining is used in the walls of jet engine inlets and outlets and exhaust pipes. These acoustic liners consist of one or more layers of perforated plates backed with honeycomb structure, forming arrays of acoustic Helmholtz resonators [72]. For sound attenuation in industrial duct systems and exhaust pipes also mufflers comprising expansions and constrictions in cross section or diaphragms can be used. Due to the presence of mean flow, shear layers are formed in the wall perforations of liners and downstream of the expansion or diaphragm in a muffler. The interaction between shear layers and the imposed acoustic field , i.e. the acoustical response of the shear layers, is of particular interest. It can namely result in absorption of the sound, as intended in these applications, but also in amplification of the sound. In this work the aeroacoustical response of shear layers to an imposed acoustical oscillation, rather than the above mentioned phenomenon of whistling, is studied.

1.3 Thesis outline

This thesis deals with the acoustical response of shear layers in two different configurations. The first configuration is a sudden area expansion in a two-dimensional rectangular or cylindrical duct, where a shear layer is formed downstream of the ex-

pansion. The second one is a rectangular slot in which a shear layer is formed due to grazing mean flow. The study is restricted to the regime of linear perturbations, and comprises both experimental work and theoretical modelling.

The present theoretical modelling can be considered as a continuation of the theoretical work of Boij and Nilsson [16, 17] on the area expansion in a rectangular duct and Howe [45, 47] on the aperture with grazing flow respectively. Here, mainly an extension to the influence of the mean flow profile and of the upstream edge condition is made. Also, for the area expansion, an extension from rectangular to cylindrical geometry is made. The experimental work presented is a continuation of the work of Golliard [36]. In the present study the influence of boundary layer and shear layer characteristics is addressed in more detail. Also, the influence of the orifice edge geometry and the issue of linearity are investigated. Furthermore, the accuracy of the measurements is increased. More related work found in literature will be discussed in each chapter separately.

The present theoretical modelling of the shear layer response for these configurations is carried out by means of a modal analysis method developed by Aurégan [9] *et al.*, see e.g. reference [9]. An extension to a wider range of mean flow profiles and the related imposition of a Kutta condition is made. In the method, the relevant geometries are divided into several ducts. In each duct the acoustic field is solved as an expansion of eigenmodes, assuming a harmonic wave. By applying continuity of momentum and mass flux for the acoustic field at the interfaces between the ducts the aeroacoustic behaviour is solved.

First, in chapter 2, the method of solving the acoustic field as an expansion of eigenmodes in a duct carrying mean flow is treated. From the linearized Euler equations for conservation of mass and momentum a generalized eigenvalue problem for the modes and their wavenumbers is derived for different mean flow configurations. Here, discretization in the transverse direction of the duct is employed. Classification of the modes, found when solving the generalized eigenvalue problem, will be treated. Furthermore, comparison of results with analytical solutions will be presented for some specific mean flow configurations.

In chapter 3 the modal analysis method is applied to the area expansion in a duct. The influence of the profile of the shear layer flow and the imposed condition at the edge of the area discontinuity will be studied. Furthermore, results are compared to an alternative theoretical model by Boij and Nilsson [16, 17] for infinitely thin shear layers in a rectangular duct and to experimental data for a cylindrical pipe obtained by Ronneberger [100]. In this context also attention will be given to the influence of the area expansion ratio and to the comparison between rectangular and cylindrical geometry.

In chapter 4 an experimental study on the aeroacoustical response of a shear layer formed in a rectangular orifice due to grazing mean flow is presented. Following Golliard [36], the effect of mean flow is given as a change in the acoustical impedance

of the orifice relative to the impedance in quiescent fluid. This is measured by means of a multi-microphone impedance tube method. In particular the influence of grazing flow boundary layer characteristics and the orifice edge geometry is investigated.

Chapter 5 deals with the application of the modal analysis to predict the aeroacoustical response of a shear layer in a rectangular orifice due to grazing mean flow. Results for an infinitely thin shear layer are compared to the prediction by Howe's [47] analytical model. Furthermore, model results are compared with experiment results.

The work presented in this thesis is performed in parallel with the work of Leroux [62] and Testud [109] at the Laboratoire d'Acoustique de l'Université du Maine, and that of Özdemir [83] at the Engineering Fluid Dynamics group of the University of Twente. Leroux [62] and Testud [109] studied the acoustical wave propagation in lined ducts with mean flow, respectively the aeroacoustical response of diaphragms experimentally as well as theoretically with the modal analysis method. Özdemir [83] applied a finite element numerical solution of the linearized Euler equations to a rectangular slot in a channel.

Chapter 2

Modal analysis

2.1 Introduction

In the present study of the aeroacoustical response of shear layers, geometrical configurations comprised of several linked ducts will be considered in theoretical modelling. In focussing on the effect of boundary layer and shear layer profile, especially acoustics of ducts containing non-uniform mean flow is of interest. The literature on the topic of sound propagation in ducts with sheared mean flow is quite extensive. Various mean flow profiles for circular, annular and rectangular ducts are treated. A review is given by Möhring *et al.* [71] and Nayfeh *et al.* [81].

Pridmore-Brown [91] first derived an equation, which now bears his name, for the transverse modes in a two dimensional duct with parallel shear flow, assuming complete separability in all space and time variables. Subsequently, papers concerning this problem by e.g. Mungur and Gladwell [75], Mungur and Plumblee [76], Eversman [31], Hersh [39], Savkar [101], Shankar [103, 104, 105], Ko [54, 55], Mikhail and Abdelhamid [70], and Nayfeh *et al.* [80] followed. Often these studies dealt with attenuation in lined ducts related to jet engine noise. The associated extension to circular and annular ducts was first made by Mungur and Plumblee [76]. Generally, the Pridmore-Brown equation was solved numerically. Alternative approaches to the numerical solution were proposed by Ko [56] and Nagel and Brand [79]. The issue of completeness of the modes was dealt with by Swinbanks [107], Nilsson and Brander [82] and Mani [66]. An analysis of many properties of modes and wavenumbers was made by Agarwal and Bull [2]. Gogate and Munjal [33] proposed an analytical solution for wave propagation in lined ducts with laminar mean flow, while numerically tackling the boundary condition. Bihhadi and Gervais [13] extended this approach to take into account transverse temperature gradients. Comparison of theory with experimental results was done by Tack and Lambert [108] and more recently by Pagneux

and Froelich [84]. Vilenski and Rienstra [111, 112] presented an asymptotic analytical solution as well as a numerical solution for high frequencies.

In this chapter a finite difference method to obtain a generalized eigenvalue problem for modes and wavenumbers in a two dimensional duct with hard walls and shear flow will be presented. After treating the general non-uniform parallel flow case, more particular (shear layer profile) configurations are considered.

2.2 Duct modes for non uniform mean flow

Consider a two-dimensional rectangular duct infinite in x-direction and with height h in y-direction, cf. figure 2.1. A non-uniform mean flow $U(y)$ in the x-direction, only dependent on the y-coordinate, is assumed. In the following the linear pressure and velocity disturbance in the duct are solved in terms of eigenmodes.

The equations describing the motion of a perfect and isentropic fluid are the Euler equations for conservation of momentum and mass:

$$\rho \frac{\mathrm{D} \overrightarrow{v}}{\mathrm{D}t} = -\overrightarrow{\nabla} p, \tag{2.1}$$

$$\frac{1}{\rho} \frac{\mathrm{D}\rho}{\mathrm{D}t} = -\overrightarrow{\nabla} \cdot \overrightarrow{v}, \tag{2.2}$$

and:

$$c^2 \frac{\mathrm{D}\rho}{\mathrm{D}t} = \frac{\mathrm{D}p}{\mathrm{D}t}, \tag{2.3}$$

with:

$$\frac{\mathrm{D}}{\mathrm{D}t} = \frac{\partial}{\partial t} + \overrightarrow{v} \cdot \overrightarrow{\nabla}.$$

Here ρ is the mass density, p the pressure, $\overrightarrow{v}$ the velocity vector and c the speed of sound. Linearization with $c = c_0 + c'$, $\rho = \rho_0 + \rho'$, $p = p_0 + p'$, where $\rho' << \rho_0$, and
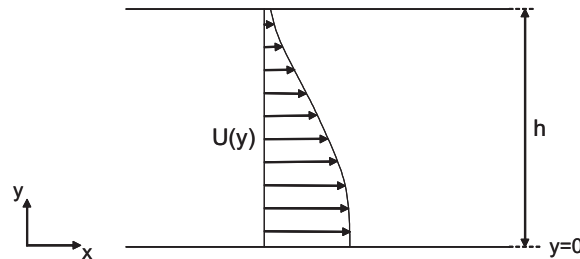
Figure 2.1: Two-dimensional rectangular duct with non-uniform mean flow

$\vec{v} = U(y)\vec{e}_x + u'\vec{e}_x + v'\vec{e}_y$, with $\vec{e}_x, \vec{e}_y$ unit vectors in the x- and y-direction, gives from equation (2.1):

$$\rho_0\Big(\frac{\partial}{\partial t} + U\frac{\partial}{\partial x}\Big)u' + \rho_0\frac{\mathrm{d}U}{\mathrm{d}y}v' = -\frac{\partial p'}{\partial x}, \tag{2.4}$$

and

$$\rho_0\Big(\frac{\partial}{\partial t} + U\frac{\partial}{\partial x}\Big)v' = -\frac{\partial p'}{\partial y}. \tag{2.5}$$

From equation (2.2) we obtain:

$$\frac{1}{\rho_0 c_0^2}\Big(\frac{\partial}{\partial t} + U\frac{\partial}{\partial x}\Big)p' = -\Big(\frac{\partial u'}{\partial x} + \frac{\partial v'}{\partial y}\Big), \tag{2.6}$$

with use of equation (2.3). Taking $\rho_0(\frac{\partial}{\partial t} + U\frac{\partial}{\partial x})$ (2.6) and subtracting $\frac{\partial}{\partial x}$ (2.4) and $\frac{\partial}{\partial y}$ (2.5) gives:

$$\frac{1}{c_0^2}\Big(\frac{\partial}{\partial t} + U\frac{\partial}{\partial x}\Big)^2 p' - \Big(\frac{\partial^2 p'}{\partial x^2} + \frac{\partial^2 p'}{\partial y^2}\Big) = 2\rho_0\frac{\mathrm{d}U}{\mathrm{d}y}\frac{\partial v'}{\partial x}. \tag{2.7}$$

This corresponds to a convective wave equation for the pressure disturbance with a source term incorporating the shear of the mean flow. Subsequently, we employ the following non-dimensionalization of the relevant quantities:

$$p_* = \frac{1}{\rho_0 c_0^2}p', \qquad (x_*, y_*, h_*) = (\frac{x}{h}, \frac{y}{h}, 1),$$

$$(u_*, v_*) = \frac{1}{c_0}(u', v'), \qquad \omega_* = \frac{\omega h}{c_0}, \tag{2.8}$$

$$M(y) = M_0 f(y) = \frac{1}{c_0}U(y), \qquad t_* = \frac{c_0 t}{h},$$

with M the Mach number and ω the angular frequency of sound. The function $f(y)$ prescribes the profile of the mean flow. M_0 is a fixed number, which is generally chosen to give the y-averaged Mach number. Using the above, the dimensionless form of the linearized momentum equation in the y-direction, equation (2.5), and the wave equation for the pressure disturbance, equation (2.7), becomes:

$$\Big(\frac{\partial}{\partial t_*} + M_0 f\frac{\partial}{\partial x_*}\Big)v_* = -\frac{\partial p_*}{\partial y_*}, \tag{2.9}$$

respectively:

$$\Big(\frac{\partial}{\partial t_*} + M_0 f\frac{\partial}{\partial x_*}\Big)^2 p_* - \Big(\frac{\partial^2}{\partial x_*^2} + \frac{\partial^2}{\partial y_*^2}\Big)p_* = 2M_0\frac{\mathrm{d}f}{\mathrm{d}y_*}\frac{\partial v_*}{\partial x_*}, \tag{2.10}$$

Assuming harmonic waves in the x-direction, the following complex form is taken:

$$p_* = P(y_*)\exp(-\mathrm{i}k_*x_*)\exp(\mathrm{i}\omega_*t_*),$$
$$v_* = V(y_*)\exp(-\mathrm{i}k_*x_*)\exp(\mathrm{i}\omega_*t_*), \tag{2.11}$$
$$q_* = Q(y_*)\exp(-\mathrm{i}k_*x_*)\exp(\mathrm{i}\omega_*t_*),$$

with $\mathrm{i}^2 = -1$. Here, we have introduced the quantity q_* for later use:

$$q_* = \mathrm{i}\frac{\partial p_*}{\partial x_*}. \tag{2.12}$$

The actual physical pressure and velocity disturbance are given by the real part of their complex form given in equation (2.11). The quantity k_* is the dimensionless wavenumber according to: $k_* = kh$, where k is the wavenumber with dimension. Since $\frac{\partial}{\partial t_*} \equiv \mathrm{i}\omega_*$ and $\frac{\partial}{\partial x_*} \equiv -\mathrm{i}k_*$, we can write equations (2.9) and (2.10) as:

$$\mathrm{i}(\omega_* - M_0 f k_*)V = -\frac{\mathrm{d}P}{\mathrm{d}y_*}, \tag{2.13}$$

$$(1 - M_0^2 f^2)k_*^2 P + 2\omega_* M_0 f k_* P - \omega_*^2 P - \frac{\mathrm{d}^2 P}{\mathrm{d}y_*^2} = -2\mathrm{i}M_0\frac{\mathrm{d}f}{\mathrm{d}y_*}k_*V, \tag{2.14}$$

using the forms in equation (2.11). These equations are discretized by taking N equally spaced points in the y_*-coordinate. The spacing between interior points is $\Delta h_* = h_*/N = 1/N$, whereas the first and last point is taken half a spacing, i.e. $h_*/2N = 1/2N$, from the duct wall. The discrete form of equations (2.13,2.14) can then be written as:

$$\mathrm{i}\omega_*\mathbf{V} - \mathrm{i}M_0\mathbf{f}k_*\mathbf{V} = -\mathbf{D_1}\mathbf{P}, \tag{2.15}$$

$$(\mathbf{I} - M_0^2\mathbf{f^2})k_*^2\mathbf{P} + 2\omega_* M_0\mathbf{f}k_*\mathbf{P} - (\omega_*^2\mathbf{I} + \mathbf{D_2})\mathbf{P} = -2\mathrm{i}M_0\mathbf{f_a}k_*\mathbf{V}. \tag{2.16}$$

Here $\mathbf{I}$ is the $(N \times N)$ identity matrix. $\mathbf{P}$ and $\mathbf{V}$ are $(N \times 1)$ column vectors giving the value of $P(y)$ and $V(y)$ at the discrete points. $\mathbf{f}$, $\mathbf{f^2}$ and $\mathbf{f_a}$ are $(N \times N)$ matrices with on their diagonal the values of $f(y_*)$, $f^2(y_*)$ and $\frac{\mathrm{d}f(y_*)}{\mathrm{d}y_*}$ respectively at the discrete points. $\mathbf{D_1}$ and $\mathbf{D_2}$ are $(N \times N)$ matrices giving the first respectively second order differential operator with respect to y_*. These matrices also account for the boundary condition $\frac{\partial p_*}{\partial y_*} = 0$ at the duct walls. Differential matrices with orders of accuracy Δh_*^2, Δh_*^4 and Δh_*^6 are given in appendix C. From the definition of q_*, see equation (2.12), and equation (2.11) it follows that: $Q(y) = k_*P(y)$, or in discrete form: $\mathbf{Q} = k_*\mathbf{P}$. Using this, equations (2.15,2.16) can be written in a single matrix equation:

$$
k_* \begin{pmatrix} \mathbf{I} - M_0^2 \mathbf{f^2} & 2\mathrm{i}M_0 \mathbf{f_a} & \mathbf{0} \\ \mathbf{0} & \mathrm{i}M_0\mathbf{f} & \mathbf{0} \\ \mathbf{0} & \mathbf{0} & \mathbf{I} \end{pmatrix} \begin{pmatrix} \mathbf{Q} \\ \mathbf{V} \\ \mathbf{P} \end{pmatrix} =
$$

$$
\begin{pmatrix} -2\omega_* M_0 \mathbf{f} & \mathbf{0} & \omega_*^2 \mathbf{I} + \mathbf{D_2} \\ \mathbf{0} & \mathrm{i}\omega_* \mathbf{I} & \mathbf{D_1} \\ \mathbf{I} & \mathbf{0} & \mathbf{0} \end{pmatrix} \begin{pmatrix} \mathbf{Q} \\ \mathbf{V} \\ \mathbf{P} \end{pmatrix}. \tag{2.17}
$$

This equation is a generalized eigenvalue problem. Solving it gives all eigenvectors, i.e. modes, $\mathbf{Q}_e$ and $\mathbf{P}_e$ and $\mathbf{V}_e$, as well as the corresponding eigenvalues, i.e. dimensionless wavenumbers, k_{e*}. In total $3N$ modes are found, which can generally be divided in N acoustic modes propagating (or decaying) in the $+x$-direction, N acoustic modes propagating (or decaying) in the $-x$-direction, and N hydrodynamic modes propagating in the direction of the mean flow ($+x$-direction). The total solution for q_*, and the non-dimensional pressure and velocity disturbance p_* respectively v_* at the discrete points is a linear combination of these modes:

$$
\mathbf{q}_*(x_*, t_*) = \sum_{n=1}^{3N} C_n \mathbf{Q}_{e,n} \exp(-\mathrm{i}k_{e,n*}x_*) \exp(\mathrm{i}\omega_* t_*),
$$

$$
\mathbf{v}_*(x_*, t_*) = \sum_{n=1}^{3N} C_n \mathbf{V}_{e,n} \exp(-\mathrm{i}k_{e,n*}x_*) \exp(\mathrm{i}\omega_* t_*), \tag{2.18}
$$

$$
\mathbf{p}_*(x_*, t_*) = \sum_{n=1}^{3N} C_n \mathbf{P}_{e,n} \exp(-\mathrm{i}k_{e,n*}x_*) \exp(\mathrm{i}\omega_* t_*),
$$

with n an index for the modes and C_n the coefficient of mode n.

An important observation here is that if the eigenvalue problem has a certain solution k_*, $\mathbf{Q}$, $\mathbf{V}$, $\mathbf{P}$, also k_*^*, $\mathbf{Q}^*$, $-\mathbf{V}^*$, $\mathbf{P}^*$ is a solution, where superscript $*$ denotes the complex conjugate. This result can readily be verified on basis of the non-discrete equations (2.13,2.14) and the relation $Q = k_* P$. Solutions are thus found in complex conjugate pairs.

Furthermore, starting from equation (2.7) a differential equation for the pressure disturbance p' only, known as the Pridmore-Brown equation [91], could immediately have been derived when using equation (2.5) to eliminate the velocity disturbance v'. Subsequently, with use of equations (2.8) and (2.11) for the non-dimensionalization and the form of the pressure and velocity disturbance respectively, this would be:

$$
(\omega_* - M_0 f k_*)\big((\omega_* - M_0 f k_*)^2 - k_*^2\big)P + 2M_0 \frac{\mathrm{d}f}{\mathrm{d}y_*} k_* \frac{\mathrm{d}P}{\mathrm{d}y_*}
$$

$$
+ (\omega_* - M_0 f k_*)\frac{\mathrm{d}^2 P}{\mathrm{d}y_*^2} = 0. \tag{2.19}
$$

Alternatively, this dimensionless equation could also be derived directly by combining equations (2.13) and (2.14). Clearly, the Pridmore-Brown in the form given by equation (2.19) contains the wavenumber k_* up to the third order. Besides the parameter $Q = k_* P$ a parameter equal to $k_* Q$ would have to be used instead of V, in order to solve the eigenmodes and accompanying wavenumbers by a generalized eigenvalue problem method as above. In this respect using the quantity V can be regarded as just a matter of choice. However, it is preferable, because V has a direct physical interpretation and, moreover, it can directly be used in applying continuity between different duct regions, as will be seen in the application of the modal analysis to specific problems further on.

The method to solve modes of the acoustic pressure and velocity disturbance has now been discussed for the general case of non-uniform mean flow across the entire duct. The same method can be applied in the case of a uniform flow across the duct, provided that some modifications are made. Furthermore, in studying shear layers, configurations, in which a uniform or non-uniform flow is present in only a part of a duct, whereas the fluid is quiescent in the rest of the duct, are of interest. Also for these cases the method is applicable in a modified form. The concerning modifications to the generalized eigenvalue problem involved with these specific flow configurations will be treated below.

2.3   Duct modes for partly non-uniform flow

In studying the aeroacoustical behaviour of shear layers, the case where non-uniform mean flow is present in only a part of a duct, whereas the fluid is quiescent in the rest of the duct will be considered. This configuration is illustrated in figure 2.2. For
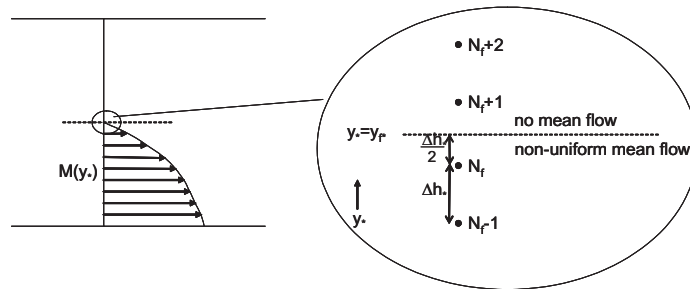

Figure 2.2: Schematic representation of a duct, in which only partly non-uniform mean flow is present for $y_* < y_{f*}$. The mean flow velocity tends to zero for $y_* \uparrow y_{f*}$, and is thus continuous. The interface at $y_* = y_{f*}$ is exactly between two interior points.

$y_* < y_{f*}$, at the first N_f discrete points, there is a certain mean flow with Mach number $M(y_*)$. This mean flow tends to zero as y_* approaches y_{f*}. For $y_* > y_{f*}$, at the last $N - N_f$ points, the mean flow is zero. The mean flow is thus continuous in y_*, whereas in general its derivative with respect to y_* is not. The interface between mean flow and still fluid at $y_* = y_{f*}$ is chosen exactly between two interior points, see figure 2.2.

The fact that the mean flow velocity and its derivative are zero for the $N - N_f$ discrete points at $y_* > y_{f*}$ has the consequence that an equal number of rows and columns in the matrix in the left hand side of the generalized eigenvalue problem, equation (2.17), become zero. The concerning rows correspond to the equations for the elements of vector $\mathbf{V}$ at these discrete points where mean flow is absent. The 'zero-columns' correspond to the same elements of $\mathbf{V}$ as they are used as input for the other equations on the rows of equation (2.17). Clearly, for the generalized eigenvalue problem to remain solvable, these 'zero-rows and -columns', as well as the corresponding ones in the matrix in the right hand side of equation (2.17), have to be omitted. This means that in the generalized eigenvalue problem $\mathbf{V}$ is only defined for the (first) N_f points, at which mean flow is present. Note that in principle the values of V at the discrete points where mean flow is absent can be found by equation (2.15), which reduces to: $\mathrm{i}\omega_*\mathbf{V} = -\mathbf{D_1P}$, once the eigenmodes of P are obtained. Since the number of equations and the number of unknowns ($\mathbf{Q}$, $\mathbf{V}$ and $\mathbf{P}$) is reduced to $2N + N_f$, compared to $3N$ for the case where non-uniform mean flow is present everywhere in the duct, also less modes are found. Generally, for this configuration N acoustic modes propagating (or decaying) in the $+x$-direction and N acoustic modes propagating (or decaying) in the $-x$-direction are obtained. Since hydrodynamic modes are associated with shear of the mean flow, a number N_f of them, equal to the number of discrete point with flow, are found.

2.4   Duct modes for (partly) uniform mean flow

In case a uniform mean flow is present everywhere in the duct, the vector $\mathbf{V}$ is not needed in the generalized eigenvalue problem, equation (2.17). The reason for this case is not as obvious as the reason why a part of $\mathbf{V}$ must be omitted in case of partly non-uniform flow. For uniform flow across the duct there are namely no rows or columns in the matrices of the eigenvalue problem which become zero. However, for uniform flow the wavenumber k_* only appears up to the second power, instead of up to the third power the Pridmore-Brown equation (2.19). Consequently, in formulating an eigenvalue problem, in which wavenumber k_* appears as the eigenvalue, the use of vectors $\mathbf{Q}$ and $\mathbf{P}$ is sufficient, and the vector $\mathbf{V}$ can be omitted:

$$k_* \begin{pmatrix} (1 - M_0^2)\mathbf{I} & \mathbf{0} \\ \mathbf{0} & \mathbf{I} \end{pmatrix} \begin{pmatrix} \mathbf{Q} \\ \mathbf{P} \end{pmatrix} = \begin{pmatrix} -2\omega_* M_0 \mathbf{I} & \omega_*^2 \mathbf{I} + \mathbf{D_2} \\ \mathbf{I} & \mathbf{0} \end{pmatrix} \begin{pmatrix} \mathbf{Q} \\ \mathbf{P} \end{pmatrix}. \qquad (2.20)$$

Here, M_0 is the uniform mean flow Mach number. Note that when mean flow is completely absent in the duct, the same formulation of the eigenvalue problem as above can be used with $M_0 = 0$ substituted. Solving equation (2.20) with N discrete points in the duct generally gives N acoustic modes propagating/decaying in the $+x$-direction, and N acoustic modes propagating/decaying in the $-x$-direction. No hydrodynamic modes are found, since the mean flow has no shear.

A more special case is that of an infinitely thin shear layer separating a region where uniform mean flow is present and a region where no mean flow is present. Here the mean flow is not continuous in y_*, and special care has to be taken to ensure that the pressure disturbance and the fluid displacement are continuous over the shear layer. The configuration of an infinitely thin shear layer in a duct is illustrated in figure 2.3. Uniform mean flow is present at the first N_f points for $y_* < y_{f*}$. At the last $N - N_f$ points for $y_* > y_{f*}$ there is no mean flow. Halfway between point N_f and N_{f+1}, at the transition between uniform mean flow and no mean flow, an additional point is introduced. At this point we considerer the amplitude P_{flow} respectively V_{flow} of the acoustic pressure and velocity in y-direction as 'seen' from the region with flow, as well as the acoustic pressure and velocity amplitude, P_{noflow} respectively V_{noflow}, seen from the no flow region . Employing a second order polynomial expansion in y_*
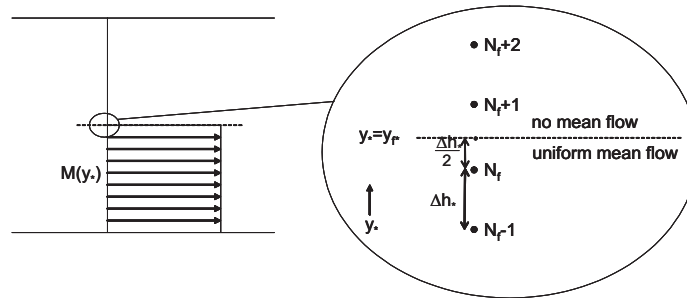
Figure 2.3: Schematic representation of a duct, in which only partly uniform mean flow is present. The interface between the part with uniform flow and the part with quiescent fluid is at $y_* = y_{f*}$, and is exactly between two interior points. An intermediate point is added here, at which the velocity disturbance in the y_*-direction taken at the flow side ($y_* \uparrow y_{f*}$) as well as the no flow side ($y_* \downarrow y_{f*}$) are introduced as extra variables.

for $P(y_*)$ around $y_* = y_{f*}$, and using equation (2.13), it can be deduced that:

$$P_{flow} = \frac{-\mathbf{P}(N_f - 1) + 9\mathbf{P}(N_f)}{8} - \frac{3i\Delta h_*(\omega_* - M_0 k_*)V_{flow}}{8},$$

$$P_{noflow} = \frac{9\mathbf{P}(N_f + 1) - \mathbf{P}(N_f + 2)}{8} + \frac{3i\Delta h_*\omega_* V_{noflow}}{8}. \qquad (2.21)$$

Furthermore, the second derivative accurate to order $(\Delta h_*)^2$ of the acoustic pressure amplitude at points N_f and $N_f + 1$ changes into:

$$\frac{\mathrm{d}^2 P}{\mathrm{d}y_*^2}\big|_{N_f} = \frac{\mathbf{P}(N_f - 1) - \mathbf{P}(N_f)}{(\Delta h_*)^2} - \frac{i(\omega_* - M_0 k_*)V_{flow}}{\Delta h_*},$$

$$\frac{\mathrm{d}^2 P}{\mathrm{d}y_*^2}\big|_{N_f+1} = \frac{-\mathbf{P}(N_f + 1) + \mathbf{P}(N_f + 2)}{(\Delta h_*)^2} + \frac{i\omega_* V_{noflow}}{\Delta h_*}, \qquad (2.22)$$

given that these points are interior points, i.e. the boundary condition for the pressure at the duct walls is not 'felt' at these points. Demanding continuity of pressure at the interface between mean flow and no mean flow yields: $P_{flow} = P_{noflow}$, and hence from equation (2.21):

$$3i\Delta h_* M_0 k_* V_{flow} = \mathbf{P}(N_f - 1) - 9\mathbf{P}(N_f) + 9\mathbf{P}(N_f + 1) - \mathbf{P}(N_f + 2)$$
$$+3i\Delta h_*\omega_* V_{flow} + 3i\Delta h_*\omega_* V_{noflow}. \qquad (2.23)$$

Furthermore, the acoustic fluid displacement in complex non dimensional form:

$$\delta_* = D(y_*)\exp(-ik_* x_*)\exp(i\omega_* t_*), \qquad (2.24)$$

is given by the convective derivative of the velocity:

$$i(\omega_* - M_0 f k_*)D = V. \qquad (2.25)$$

The additional continuity of displacement required at the interface thus gives:

$$M_0 k_* V_{noflow} = \omega_* V_{noflow} - \omega_* V_{flow}. \qquad (2.26)$$

Equations (2.23) and (2.26) can now be incorporated in order to get the eigenvalue problem for the case of partly uniform flow:

$$k_* \begin{pmatrix} \mathbf{I} - M_0^2\mathbf{f^2} & \mathbf{0} & \mathbf{0} & \mathbf{0} \\ \mathbf{0} & \mathbf{I} & 0 & 0 \\ \mathbf{0} & \mathbf{0} & 3i\Delta h_* M_0 & 0 \\ \mathbf{0} & \mathbf{0} & 0 & M_0 \end{pmatrix} \begin{pmatrix} \mathbf{Q} \\ \mathbf{P} \\ V_{flow} \\ V_{noflow} \end{pmatrix} =$$

$$\begin{pmatrix} -2\omega_* M_0\mathbf{f} & \omega_*^2\mathbf{I} + \mathbf{D_2} & \mathbf{0} & \mathbf{0} \\ \mathbf{I} & \mathbf{0} & 0 & 0 \\ \mathbf{0} & \dots 1, -9, 9, 1 \dots & 3i\Delta h_*\omega_* & 3i\Delta h_*\omega_* \\ \mathbf{0} & \mathbf{0} & -\omega_* & \omega_* \end{pmatrix} \begin{pmatrix} \mathbf{Q} \\ \mathbf{P} \\ V_{flow} \\ V_{noflow} \end{pmatrix}, \qquad (2.27)$$

where rows N_f and $N_f + 1$ of the second derivative matrix $\mathbf{D_2}$, have to be modified according to equation (2.22). Since this equation is derived for accuracy of order $(\Delta h_*)^2$, only $\mathbf{D_2}$ accurate to order $(\Delta h_*)^2$ can be used. Furthermore, the profile function f here obviously equals 1 for $y_* < y_{f*}$ (first N_f points), and 0 for $y_* > y_{f*}$.

Solving the eigenvalue problem not only returns the eigen modes for vectors Q and P but also corresponding modes for the parameters V_{flow} and V_{noflow}. In addition, since two more equations are added compared to the case of uniform flow (or no flow) everywhere in the duct, two more modes are found. These two modes are related to the hydrodynamic instability of the infinitely thin shear layer, known as the Kelvin-Helmholtz instability waves. The fact that two extra modes are found enables us to apply a Kutta condition at the intermediate point, in case the uniform flow passes an edge. This will be discussed in the next chapter.

2.5 Duct modes for partly non-uniform flow with velocity jump

For configurations in which mean flow passes an edge, it can be interesting to consider (the effect of) a non-uniform flow profile, while still being able to straightforwardly apply a Kutta condition at the edge. For this purpose, a partly non-uniform flow profile with a velocity jump at the flow/no flow interface is considered, see figure 2.4. To solve eigenmodes for this flow configuration a combination of what is formulated in sections 2.3 and 2.4 applies. Firstly, because flow is only present at the first N_f
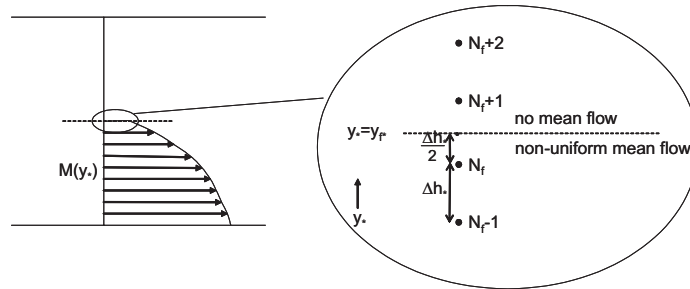
Figure 2.4: Schematic representation of a duct, in which non-uniform mean flow is present for $y_* < y_{f*}$, and where at the interface at $y_* = y_{f*}$, exactly between two subsequent points, a jump in velocity occurs. As with the infinetely thin shear layer, section 2.4, an intermediate point is added here, at which the velocity disturbance in the y_*-direction taken at the flow side ($y_* \uparrow y_{f*}$) as well as the no flow side ($y_* \downarrow y_{f*}$) are introduced as extra variables.

discrete points, only the equations with/for V at these points are kept. Secondly, as with partly uniform flow, section 2.4, an extra point is introduced at the flow/no flow interface, where the y-dependent part of pressure and velocity disturbance as seen from the flow side -P_{flow}, V_{flow}- as well as the no flow side -P_{noflow}, V_{noflow}- are considered. Analogous to equation (2.22) the second order derivative of the acoustic pressure, accurate to order $(\Delta h_*)^2$, amplitude at points N_f and $N_f + 1$ changes into:

$$
\frac{\mathrm{d}^2 P}{\mathrm{d}y_*^2}\Big|_{N_f} = \frac{\mathbf{P}(N_f - 1) - \mathbf{P}(N_f)}{(\Delta h_*)^2} - \frac{\mathrm{i}(\omega_* - M_{int}k_*)V_{flow}}{\Delta h_*},
$$
$$
\frac{\mathrm{d}^2 P}{\mathrm{d}y_*^2}\Big|_{N_f+1} = \frac{-\mathbf{P}(N_f + 1) + \mathbf{P}(N_f + 2)}{(\Delta h_*)^2} + \frac{\mathrm{i}\omega_* V_{noflow}}{\Delta h_*}, \qquad (2.28)
$$

where M_{int} is the (jump in) Mach number at the interface. Unlike with the configuration of partly uniform flow, the first derivative also occurs in the eigenvalue problem for the first N_f points here, since flow is non-uniform. The first order derivative of the acoustic pressure amplitude, accurate to order $(\Delta h_*)^2$, at point N_f becomes:

$$
\frac{\mathrm{d}P}{\mathrm{d}y_*}\Big|_{N_f} = \frac{\mathbf{P}(N_f) - \mathbf{P}(N_f - 1)}{2\Delta h_*} - \frac{\mathrm{i}(\omega_* - M_{int}k_*)V_{flow}}{2}. \qquad (2.29)
$$

Furthermore, adding continuity in pressure and displacement over the flow/no flow interface in the eigenvalue problem yields the extra equations:

$$
3\mathrm{i}\Delta h_* M_{int}k_* V_{flow} = \mathbf{P}(N_f - 1) - 9\mathbf{P}(N_f) + 9\mathbf{P}(N_f + 1) - \mathbf{P}(N_f + 2)
$$
$$
+3\mathrm{i}\Delta h_* \omega_* V_{flow} + 3i\Delta h_* \omega_* V_{noflow}, \qquad (2.30)
$$

and

$$
M_{int}k_* V_{noflow} = \omega_* V_{noflow} - \omega_* V_{flow}, \qquad (2.31)
$$

analoguous to (2.23) and (2.26). Generally, for this flow configuration N acoustic modes propagating/decaying in the $+x$-direction, N acoustic modes propagating/or decaying in the $-x$-direction, N_f neutral hydrodynamic modes and 2 hydrodynamic instability modes are found.

2.6   Classification of the modes

In the preceding part of this chapter the method to determine the modes for the acoustic pressure and velocity disturbance in a duct has been discussed for different mean flow configurations. The existence of different types of modes, namely acoustic modes and hydrodynamic modes, is already mentioned there. Here, this distinction will be treated in more detail.

Generally, acoustic modes propagate or decay along the fluid in both directions. The lowest order acoustic modes are the plane waves, which always have real wavenumber and therefore propagate. Higher order acoustic modes have a wavenumber with an imaginary part when they are 'cut-off', such that they decay exponentially. As already mentioned in section 2.2 these will be found in complex conjugate pairs, of which one decays in the $+x$ direction and the other one decays in the $-x$ direction. With increasing frequency ever more higher order modes are cut-on, such that their wavenumbers become real and they will propagate. For a still fluid the wavenumbers of evanescent acoustic modes are purely imaginary, when mean flow is present the wavenumbers can have an additional real part. Hydrodynamic modes are associated with vorticity disturbances arising from shear in the mean flow. They are stationary with respect to the fluid, i.e. they propagate with the (local) mean flow velocity. Hydrodynamic modes can be either neutral, which means their wavenumber is purely real, or unstable, which means the wavenumber has an additional positive imaginary part such that the mode grows exponentially in the direction of propagation (i.e. in the current $\exp(i(\omega t - kx))$ convention). An unstable hydrodynamic mode is also accompanied with its complex conjugated counterpart, which decays exponentially.

Formally, when modes and their wavenumbers are calculated, the direction of propagation is not known. This especially becomes a relevant issue when an unstable hydrodynamic mode may be present, since it can be confused with an acoustic mode decaying in the $-x$ direction, as both (can) have a wavenumber with positive real and imaginary part. In order to determine the direction of propagation of modes, two causality criteria are available, viz. the Briggs-Bers formalism [12, 18] and the Crighton-Leppington formalism [21, 49]. In both cases the wavenumbers of the modes are traced while letting the angular frequency ω go from a complex value to its eventual real value. In the Briggs-Bers formalism $\Re(\omega)$ is kept constant while $\Im(\omega)$ runs from $-\infty$ to 0, whereas in the Crighton-Leppington formalism $|\omega|$ is fixed and $\arg(\omega)$ runs from $-\frac{1}{2}\pi$ to 0, see figure 2.5. For the current $\exp(i(\omega t - kx))$ convention, if a wavenumber originates in the lower complex plane, the mode is right running, if it originates in the upper complex plane the mode propagates to the left. This implies that if the wavenumber crosses the real axis the mode is unstable.

As an illustration wavenumber tracing is performed for a duct with partly uniform mean flow and a duct with partly non-uniform mean flow. For the first case uniform mean flow is present in the lower half of the duct and the fluid is quiescent in the upper half of the duct, such that the Mach number equals $M(y_*) = M_0 f(y_*)$ with:

$$
f(y_*) = \begin{cases} 1 & y_* < 0.5, \\ 0 & y_* > 0.5. \end{cases}
$$

For the non-uniform flow case Poiseuille flow is present in the lower half of the duct
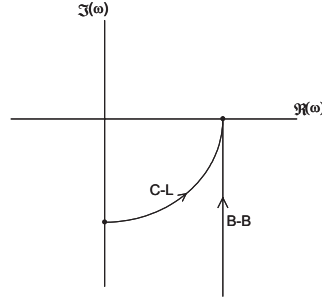
Figure 2.5: Variation of the angular frequency ω in the complex plane to its final real value for causality analysis according to Briggs-Bers formalism (B-B) and Crighton-Leppington formalism (C-L).

whereas the fluid is still in the upper half, such that $M(y_*) = M_0 f(y_*)$ with:

$$
f(y_*) = \begin{cases} \frac{3}{2}\left(1 - (2y_*)^2\right) & y_* < 0.5, \\ \\ 0 & y_* > 0.5, \end{cases}
$$

and M_0 is here the Mach number averaged over the part with flow. For both cases the dimensionless angular frequency is set at $\omega_* = 0.2$, $M_0 = 0.1$ and a number of $N = 10$ discrete points is taken. Figure 2.6 shows a plot of the two sample flow profiles together with the location of the discrete points. The traces of the wavenumbers, divided by $k_0 = \omega/c_0$, in the complex plane according to both the Briggs-Bers and the Crighton-Leppington formalism are shown in figures 2.7 and 2.8 for the uniform and the non-uniform flow case respectively. Here, the two different causality criteria give the same results regarding the direction of propagation of the modes. However, it has to be noted that Rienstra and Peake [96] have shown that for some cases they actually disagree, and the Briggs-Bers formalism can not be used.

Generally, in this study the global aeroacoustic behaviour of two geometrical configurations will be studied at low frequency. This means that higher order modes will be cut-off, and the aeroacoustical behaviour will be derived from the propagating plane waves. Technically, for this purpose only a distinction between left running and right-running waves and the identification of the plane waves is needed. The plane waves could be discerned in a straightforward way by the form of the mode itself: the y-dependent part of the pressure disturbance, $P(y)$, will be almost constant and the y-dependent part of the velocity disturbance in the y direction, $V(y)$, will be nearly zero. An identification of these modes on basis of their wavenumber can be made
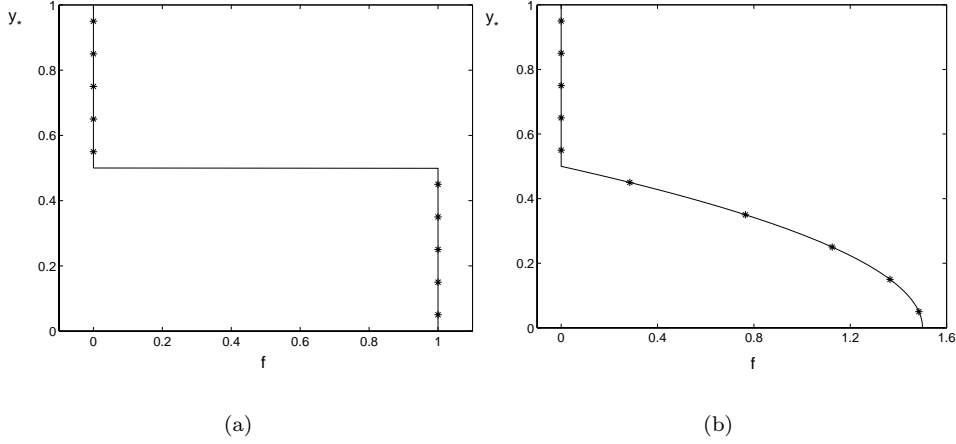
Figure 2.6: Sample flow profiles taken for the tracing of wavenumbers in the complex plane. a) partly uniform flow, b) partly non-uniform Poiseuille flow. The markers show the locations of the $N = 10$ discrete points.

using the propagation velocity. The phase velocity of a mode is given by:

$$v_p = \frac{\omega}{\Re(k)}, \tag{2.32}$$

which implies that:

$$\Re\left(\frac{k}{k_0}\right) = \frac{c_0}{v_p}. \tag{2.33}$$

The (quasi) plane waves propagate with the speed of sound c_0 corrected with a Doppler shift due to the mean flow. The plane wave propagating to the left against mean flow will thus have a velocity of about $-c_0(1- <M>)$, and the plane wave propagating to the right with mean flow will have a velocity of about $c_0(1+ <M>)$, where $<M>$ is the mean flow Mach number averaged over the entire duct. For the sample flow cases above, with a average Mach number of M_0 in the lower half of the duct and zero mean flow in the upper half, the wavenumbers of the plane modes are expected to have a values of $\frac{k}{k_0} = \pm\frac{1}{1\pm0.5M_0}$, or $\frac{k}{k_0} = -1.0526$ and $\frac{k}{k_0} = 0.9524$ respectively. Indeed, in figures 2.7 and 2.8 values of $\frac{k}{k_0} = -1.0485$ and $\frac{k}{k_0} = 0.9490$ for the partly uniform flow configuration, and $\frac{k}{k_0} = -1.0476$ and $\frac{k}{k_0} = 0.9473$ for the partly non-uniform flow configuration are found.

As the hydrodynamic modes propagate with the local flow velocity, it is expected for the partly non-uniform flow configuration, that for these modes $\Re(k/k_0) >$
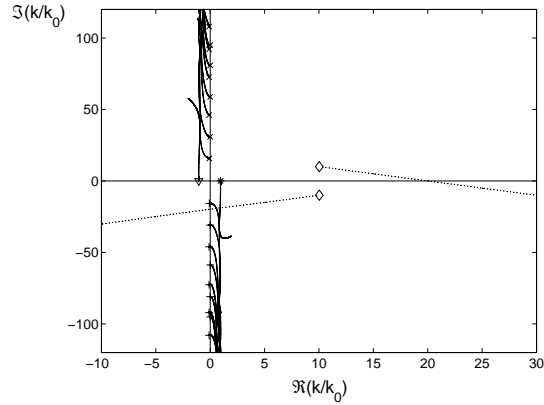
(a) Briggs-Bers formalism
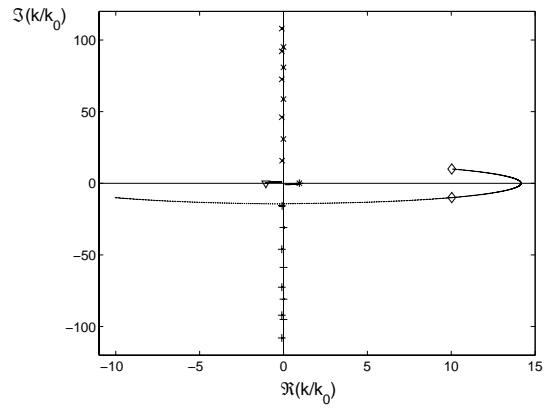
(b) Crighton-Leppington formalism

Figure 2.7: Tracing of the wavenumbers for partly uniform flow (infinitely thin shear layer) in a duct with $w_* = 0.2$, $M_0 = 0.1$, and $N = 10$ according to the Briggs-Bers formalism and the Crighton-Leppington formalism. The markers indicate the eventual values of the wavenumbers for real angular frequency. A classification is given: $*$ marker: $+x$ acoustic propagating, ∇ marker: $-x$ acoustic propagating, $+$ markers: $+x$ acoustic evanescent, $\times$ markers: $-x$ acoustic evanescent, $\diamond$ markers: hydrodynamic unstable/evanescent. Notice that in the C-L formalism the trace of the hydrodynamic evanescent mode coincides with part of the trace of the hydrodynamic unstable mode.
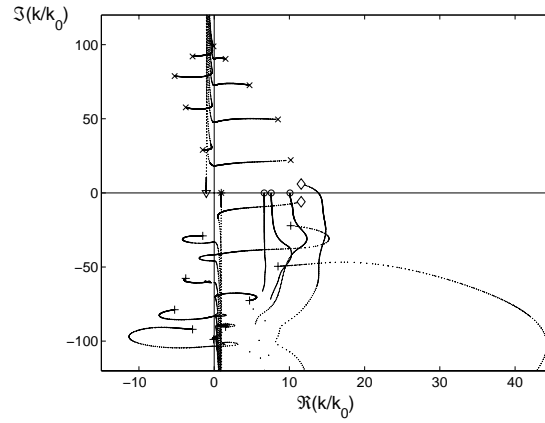
(a) Briggs-Bers formalism
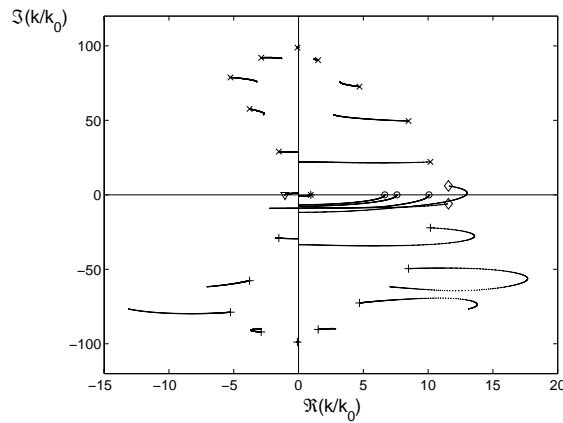
(b) Crighton-Leppington formalism

Figure 2.8: Tracing of the wavenumbers for partly non-uniform Poiseuille flow in a duct with $w_* = 0.2$, $M_0 = 0.1$, and $N = 10$ according to the Briggs-Bers formalism and the Crighton-Leppington formalism. The markers indicate the eventual values of the wavenumbers for real angular frequency. A classification is given: $*$ marker: $+x$ acoustic propagating, ∇ marker: $-x$ acoustic propagating, $+$ markers: $+x$ acoustic evanescent, $\times$ markers: $-x$ acoustic evanescent, $\circ$ markers: hydrodynamic neutral, $\diamond$ markers: hydrodynamic unstable/evanescent.

$1/1.5M_0 = 6.6667$. Also, since they propagate in the direction of the mean flow, they must originate in the lower complex wavenumber plane. Three of these modes, which have zero imaginary part, are found in figure 2.8. These are the neutral hydrodynamic modes. The neutral hydrodynamic mode with the smallest wavenumber has $\Re(k/k_0) = 6.6673$. Furthermore, one such mode is found, of which the wavenumber trace has crossed the real axis to settle at a positive imaginary value. This is the hydrodynamic unstable mode, which is accompanied by its decaying complex conjugate counterpart. As expected, the total number of hydrodynamic modes found is thus five: equal to the number of discrete points at which sheared mean flow is present. The rest of the modes are cut-off acoustic modes, all decaying in their direction of propagation. Notice that, according to the above, neutral hydrodynamic modes are always expected at a higher wavenumber than the plane acoustic mode propagating in $+x$-direction. A distinction can thus easily be made. This also extends to cut-on propagating higher order acoustic modes, since these will have smaller wavenumbers than the plane wave.

For the partly uniform flow configuration, besides the acoustic modes, two hydrodynamic modes, an unstable one and its complex conjugate, are found. The value of $\Re(k/k_0)$ equals 10.0317 for these modes, so that their phase velocity is close to the mean flow velocity which has $M_0 = 0.1$. These modes correspond to the well known Kelvin-Helmholtz instability waves, which will be discussed in more detail further on.

2.7 Comparison with analytical solutions

In order to investigate the accuracy of the modes and wavenumbers, obtained by the method described above, results of calculations, carried out using a Matlab script, will be compared to analytical solutions. Acoustic modes, hydrodynamic unstable modes and hydrodynamic neutral modes will be treated separately, as analytical solutions for these can only be obtained for different specific flow configurations.

2.7.1 Acoustic modes

In case of uniform mean flow in a duct, equation (2.14) reduces to:

$$(1 - M_0^2)k_*^2 P + 2\omega_* M_0 k_* P - \omega_*^2 P - \frac{\mathrm{d}^2 P}{\mathrm{d}y_*^2} = 0, \qquad (2.34)$$

which has the solution:

$$\begin{aligned}
P_{e,n}(y_*) &= \cos((n-1)\pi y_*), \\
k_{e,n*} &= \frac{-\omega_* M_0 \pm \sqrt{\omega_*^2 - ((n-1)\pi)^2}}{1 - M_0^2}, \qquad n \geq 1,
\end{aligned} \qquad (2.35)$$

satisfying the boundary condition $\frac{\mathrm{d}P}{\mathrm{d}y_*} = 0$ at $y_* = 0$ and $y_* = h_* = 1$. Results for the pressure disturbance modes obtained from the generalized eigenvalue problem, equation (2.35), with $M_0 = 0$, $\omega = 0.1$ and $N = 16$, are shown in figure 2.9. Second order differential matrix $\mathbf{D_2}$ accurate to order $(\Delta h_*)^2$ is used. Only the modes identified as propagating/decaying to the right are displayed, since the same solutions are obtained for the left running modes. Also, the analytical solution given by equation (2.35) is indicated for each mode. All modes are perfectly resolved at the discrete points. The relative error with respect to the analytical solution is observed to be $\sim 10^{-9}$ at maximum, which is for the highest order modes.

The relative error of calculated wavenumbers with respect to the analytical solution, equation (2.35), is shown in figure 2.10 in case mean flow is absent: $M_0 = 0$. The number of discrete points is set at $N = 200$, three dimensionless angular frequencies are taken: $\omega_* = 0.01$ (low frequency), $\omega_* = \pi - 0.001$, which is just below the cut-on of the first higher order mode at $\omega_* = \pi$, and an intermediate value $\omega_* = 0.1$. Only the right running modes are considered, since the left running modes only differ in the sign of the wavenumber. Results are depicted for cases where the second order differential matrix $\mathbf{D_2}$ accurate to order $(\Delta h_*)^2$, $(\Delta h_*)^4$ or $(\Delta h_*)^6$ is utilized in equation (2.20). Except for the first two or three modes the error seems to be independent of frequency for a given order of accuracy. The relative error is then proportional to n^2, n^4, respectively n^6 for order of accuracy $(\Delta h_*)^2$, $(\Delta h_*)^4$, and $(\Delta h_*)^6$ in the used differential matrix . The relative error in the wavenumber of the plane wave mode is fairly the same for different orders of accuracy used, and it increases with smaller frequency, i.e. smaller wavenumber. For the first higher order mode the relative error becomes comparatively large just below its cut-on frequency, where the (absolute) value of its wavenumber is small.

Figure 2.11 shows the relative error in the calculated wavenumber with respect to the analytical solution in absence of mean flow for fixed angular frequency $\omega_* = 0.1$, but for different numbers of discrete points. Also here results are obtained using the second order differential matrix $\mathbf{D_2}$ accurate to order $(\Delta h_*)^2$, $(\Delta h_*)^4$ or $(\Delta h_*)^6$. Figure 2.12 shows the same plot, but with the index of the mode n on the abscissa instead of the index of the mode divided by the total number of right running modes: n/N. In figure 2.11 it can be seen that, in a relative manner, for a given order of accuracy, the relative error is about the same for all N for about the last 80% of the modes (higher N gives a slightly higher error). Figure 2.12 shows that, in an absolute manner, the error of a given mode decreases with increasing N (except for the first couple of modes which have very low error). After the first couple of modes the relative error is proportional to $1/N^2$, $1/N^4$, and $1/N^6$ for order of accuracy $(\Delta h_*)^2$, $(\Delta h_*)^4$, and $(\Delta h_*)^6$ respectively. This results in the fact that in figure 2.12 for each order of accuracy the graphs of the relative error for different number of points, say N_1 and N_2 with $N_2 > N_1$, are parallel, with spacing equal to the factor $(N_1/N_2)^2$, $(N_1/N_2)^4$, and $(N_1/N_2)^6$ for order of accuracy $(\Delta h_*)^2$, $(\Delta h_*)^4$ and $(\Delta h_*)^6$ respectively.
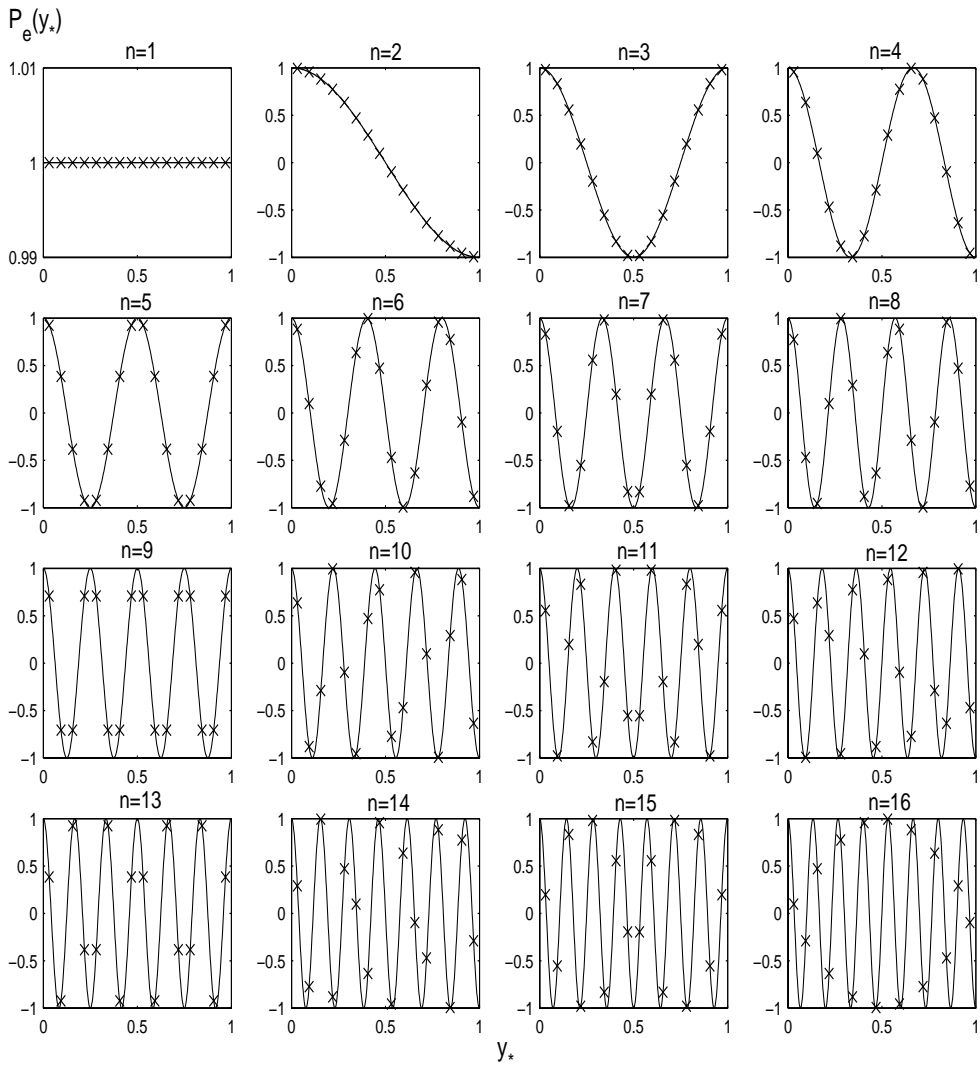
Figure 2.9: Pressure disturbance modes in a duct without mean flow with $\omega_* = 0.1$ and $N = 16$. The markers indicate the results obtained by solving the discrete generalized eigenvalue problem (2.20), in case of differential matrix accurate to order $(\Delta h_*)^2$. The solid lines indicate the analytical solution, equation (2.35).
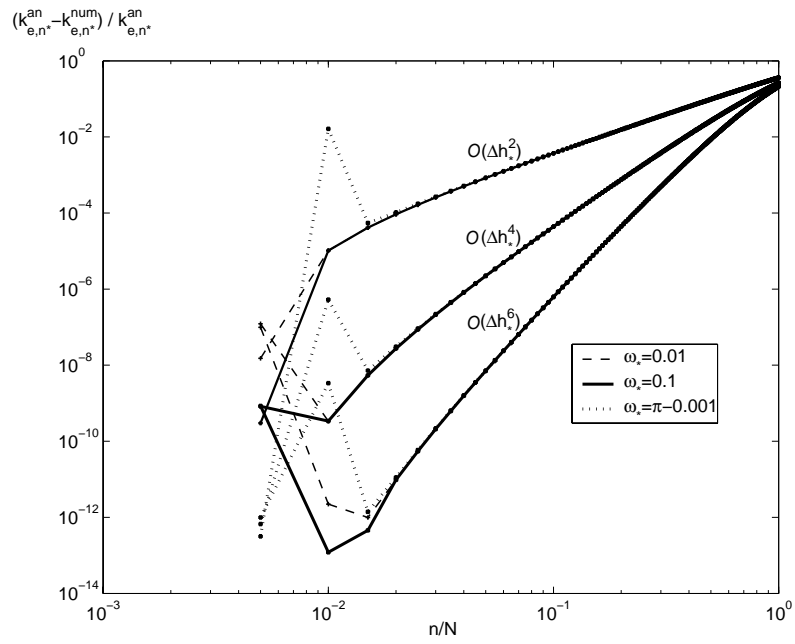
Figure 2.10: Relative error of calculated wavenumbers $k_{e,n*}^{num}$ of right running modes with respect to the analytical solution $k_{e,n*}^{an}$ versus index of modes n over total number of right running modes N in case mean flow is absent. Number of discrete points and right running modes is $N = 200$. Results are shown for three dimensionless frequencies ω_*, and for the second order differential matrix accurate to order $(\Delta h_*)^2$, $(\Delta h_*)^4$ or $(\Delta h_*)^6$.
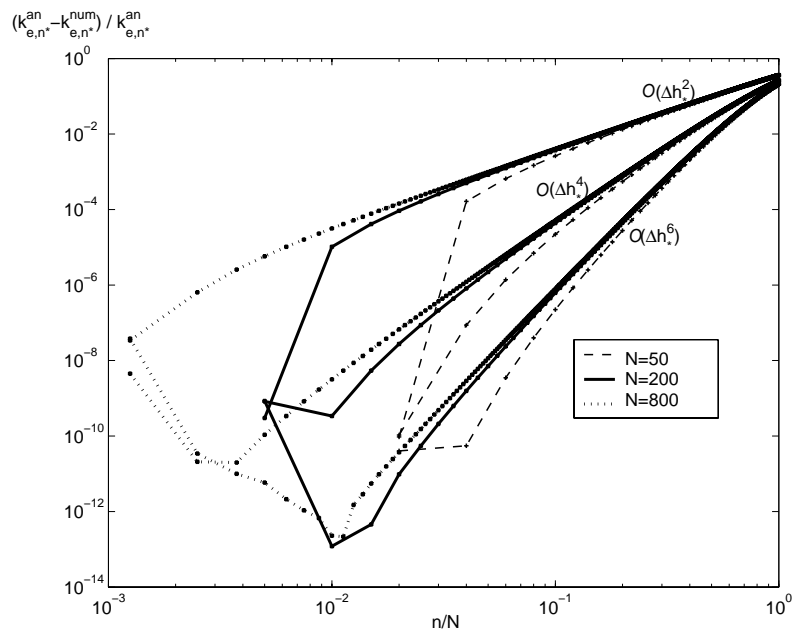
Figure 2.11: Relative error of calculated wavenumbers $k_{e,n*}^{num}$ of right running modes with respect to the analytical solution $k_{e,n*}^{an}$ versus index of modes n over total number of right running modes N in case mean flow is absent. Dimensionless frequency is $\omega_* = 0.1$. Results are shown for three numbers of discrete points N, and for the second order differential matrix accurate to order $(\Delta h_*)^2$, $(\Delta h_*)^4$ or $(\Delta h_*)^6$.
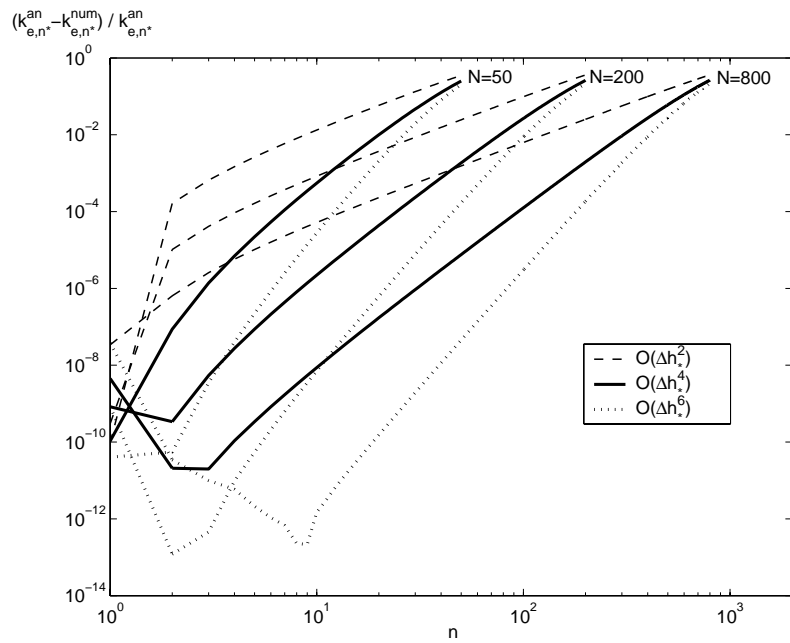
Figure 2.12: Relative error of calculated wavenumbers $k_{e,n*}^{num}$ of right running modes with respect to the analytical solution $k_{e,n*}^{an}$ in case mean flow is absent. Dimensionless frequency is $\omega_* = 0.1$. Plot is identical to figure 2.11, but with index n of the modes on abscissa instead of n/N.

2.7.2 Unstable hydrodynamic modes

Hydrodynamic modes are associated with shear in the mean flow rather than with compressibility of the medium, as applies for acoustic modes. As mentioned, these modes can be stable as well as unstable.

The configuration of two parallel infinite streams of incompressible inviscid fluids with different velocities and densities was recognized by Helmholtz [38], whereas the accompanying problem of instability was first posed and solved by Kelvin [51]. It is now commonly known as the Kelvin-Helmholtz instability for an infinitely thin shear layer, see also e.g. ref. [11, 29]. The hydrodynamic modes and wavenumbers for an infinitely thin shear layer in an incompressible fluid with homogeneous density can be readily solved analytically. Results will be compared to those obtained by the present modal analysis method.

For continuous parallel flows Rayleigh [92] first proved that the presence of an inflexion point in the flow profile is a necessary condition for instability. Subsequently stronger criteria have been derived by others, see for instance Drazin and Reid [29]. For a generalized hyperbolic-tangent flow profile hydrodynamic modes and wavenumbers are obtained by Michalke [67, 68, 69] by numerically solving the Rayleigh equation, see appendix B. Also comparison of these results with those obtained by the present modal analysis method will be made.

Infinitely thin shear layer

When fluid is considered to be incompressible, the Euler equation for conservation of mass (2.2) changes into:

$$\overrightarrow{\nabla} \cdot \overrightarrow{v} = 0. \tag{2.36}$$

The incompressible variant of equation (2.14) can subsequently be deduced in the same way as in section 2.2:

$$\left(k_*^2 - \frac{\mathrm{d}^2}{\mathrm{d}y_*^2}\right)P = -2\mathrm{i}M_0\frac{\mathrm{d}f}{\mathrm{d}y_*}k_*V, \tag{2.37}$$

while equation (2.13) remains unchanged. In case of a duct with partly uniform mean flow, i.e. an infinitely thin shear layer, for which the flow profile f is given in figure 2.6a, the right hand side of (2.37) equals 0 except at the shear layer itself. The solution for the pressure mode, beneath- respectively above the shear layer, is then given by:

$$P_{hu}(y_*) = \begin{cases} \cosh(k_{hu*}y_*) & y_* < 0.5, \\[2mm] \cosh(k_{hu*}(y_* - 1)) & y_* > 0.5. \end{cases} \tag{2.38}$$

Here the boundary condition $\frac{\mathrm{d}P}{\mathrm{d}y_*} = 0$ at the duct walls at $y_* = 0$ and $y_* = h_* = 1$, as well as continuity of pressure at $y_* = 0.5$ is satisfied. Furthermore, in the same

way as in section 2.4, continuity of displacement δ_* is imposed over the shear layer. Equations (2.25) and (2.13) give for the y-dependant part of the displacement:

$$D(y_*) = \frac{1}{(\omega_* - M_0 f k_*)^2} \frac{\mathrm{d}P}{\mathrm{d}y_*}. \tag{2.39}$$

After substitution of equation (2.38) in (2.39), continuity of D at $y_* = 0.5$ implies for the wavenumber:

$$k_{hu*} = \frac{w_*}{M_0}(1 \pm \mathrm{i}). \tag{2.40}$$

The solution given by equations (2.38) and (2.40) is well known as the Kelvin-Helmholtz instability waves for a infinitely thin vortex sheet. The solution by modal analysis is obtained from the generalized eigenvalue problem in the form given by equation (2.27), which is accurate to order $(\Delta h_*)^2$. In order to approximate the incompressible limit both the square of the dimensionless angular frequency and the Mach number should be small: $w_*^2 \ll 1$ and $M_0^2 \ll 1$. Figures 2.13, 2.14 and 2.15 show the unstable hydrodynamic pressure mode obtained from modal analysis compared to the incompressible analytical solution, equations (2.38,2.40), for $\omega_* = 0.1$ and $M_0 = 0.1$, for $\omega_* = 0.01$ and $M_0 = 0.01$, and for $\omega_* = 0.1$ and $M_0 = 0.01$ respectively. In all cases the number of discrete points is $N = 50$. The maximum of the absolute value of the pressure mode, $|P_{hu}|$, is scaled to unity. Note that the decaying hydrodynamic pressure mode only differs from the unstable one by an opposite phase. For

Figure 2.13: Magnitude and phase of the unstable hydrodynamic pressure wave P_{hu} for an infinitely thin shear layer obtained from modal analysis ($\times$ markers) compared to the incompressible analytical solution (solid line) for $\omega_* = 0.1$, $M_0 = 0.1$, $N = 50$. The maximum of $|P_{hu}|$ is scaled to unity.

Figure 2.14: Magnitude and phase of the unstable hydrodynamic pressure wave P_{hu} for an infinitely thin shear layer obtained from modal analysis ($\times$ markers) compared to the incompressible analytical solution (solid line) for $\omega_* = 0.01$, $M_0 = 0.01$, $N = 50$. The maximum of $|P_{hu}|$ is scaled to unity.
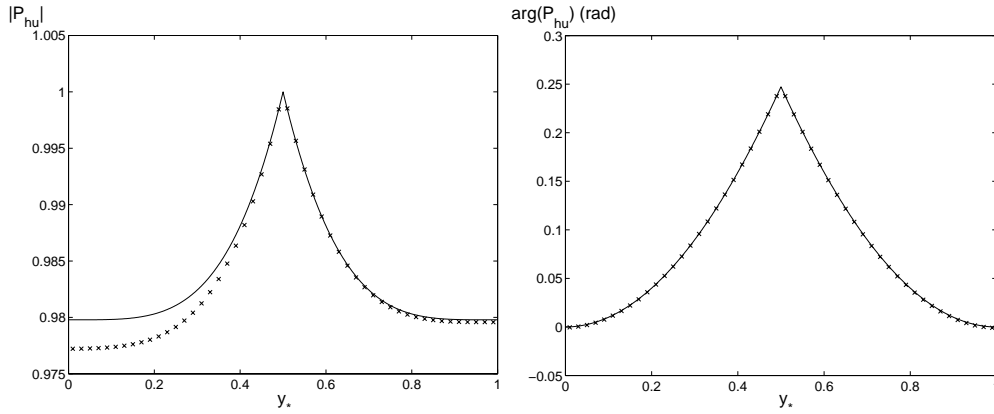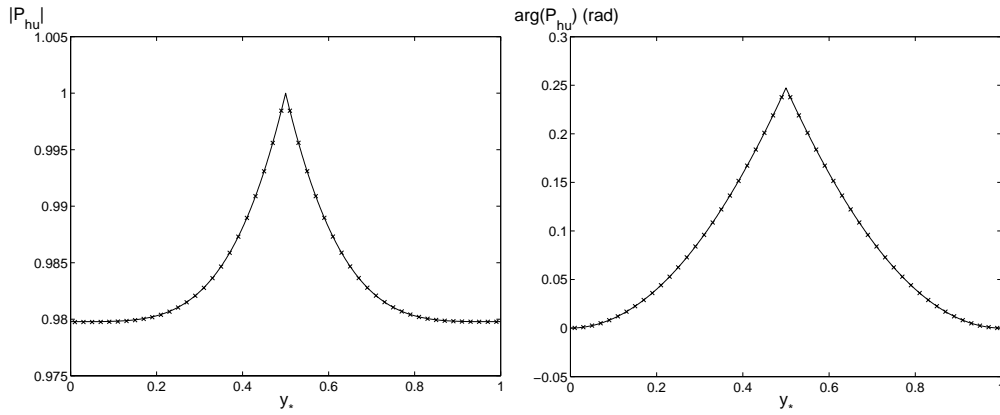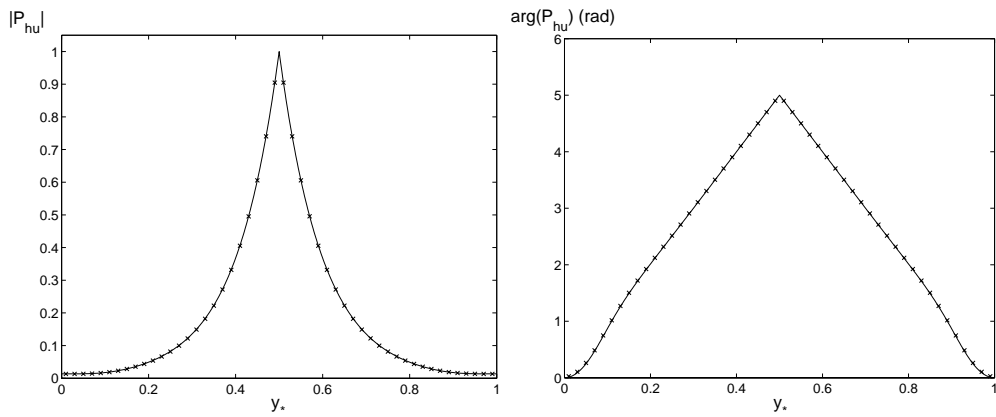

Figure 2.15: Magnitude and phase of the unstable hydrodynamic pressure wave P_{hu} for an infinitely thin shear layer obtained from modal analysis ($\times$ markers) compared to the incompressible analytical solution (solid line) for $\omega_* = 0.1$, $M_0 = 0.01$, $N = 50$. The maximum of $|P_{hu}|$ is scaled to unity.

$\omega_* = 0.1$ and $M_0 = 0.1$ clearly a deviation from the incompressible analytical solution can be seen, especially for the magnitude of the mode. For $\omega_* = 0.01$ and $M_0 = 0.01$ very good agreement between the result from modal analysis and the analytical solution is observed: the relative error is at maximum $\sim 10^{-5}$ for both magnitude and phase. When only the Mach number is small: $M_0 = 0.01$, while $\omega_* = 0.1$, cf. figure 2.15, agreement between modal analysis and the incompressible solution is also quite good with a maximum relative error of $\sim 10^{-5}$ for magnitude and phase. When taking ω_* smaller than 0.1 while keeping M_0 at 0.1 more significant deviation was seen. Apparently, the approximation of the incompressible limit by the modal analysis result is more sensitive to the Mach number than the dimensionless frequency (Helmholtz number). This is also seen in figure 2.16, where the deviation in the wavenumber of the hydrodynamic instability, when comparing the modal analysis result and the incompressible analytical solution, is plotted against both Mach number M_0 and dimensionless angular frequency ω_* for $N = 50$. For the real part of the wavenumber the deviation is almost independent of the dimensionless frequency. The deviation of the imaginary part however does depend on both Mach number and dimensionless frequency. Along the path where ω_* is kept equal to M_0 the deviation in both real and imaginary part is found to increase with the square of $\omega_* = M_0$. For a higher number of points N no significantly different result as in figure 2.16 was found, indicating that the calculation has converged.

Generalized hyperbolic-tangent shear layer profile

The spatial instability of a free shear layer with a more realistic flow profile was investigated by Michalke [67, 68, 69], see also appendix B. He numerically solved the (incompressible) Rayleigh equation for a generalized hyperbolic-tangent velocity profile, equation (B.8), to obtain the wavenumber k_{hu} of the hydrodynamic instability wave. In the current non-dimensionalization this flow profile is given by:

$$f(y_*) = 1 - (1 + me^{m\phi(m)\frac{y_*-0.5}{\theta_*}})^{-1/m},$$
$$\phi(m) = \int_0^1 \frac{1-z}{1-z^m}\mathrm{d}z, \tag{2.41}$$

with m a profile parameter and $\theta_* = \theta/h$ the non-dimensional momentum thickness of the shear layer. Here, the inflexion point of the profile is set at $y_* = 0.5$. Note that in Michalke's formulation the y-coordinate extends from $-\infty$ to $+\infty$, as opposed to the restriction of y to the duct region in modal analysis.

Calculations are performed for profile parameter $m = 1$ and $m = 6$, using differential matrices accurate to order $O(\Delta h_*^2)$. For the momentum thickness three different values are taken: $\theta_* = 0.025$, $\theta_* = 0.05$, and $\theta_* = 0.1$. The profiles for these parameter values are displayed in figure 2.17. The hydrodynamic instability wavenumbers, non-dimensionalized by the momentum thickness, obtained from modal analysis are shown

$|(\Re(k_{hu}^{num}) - \Re(k_{hu}^{an})) / \Re(k_{hu}^{an})|$

$|(\Im(k_{hu}^{num}) - \Im(k_{hu}^{an})) / \Im(k_{hu}^{an})|$
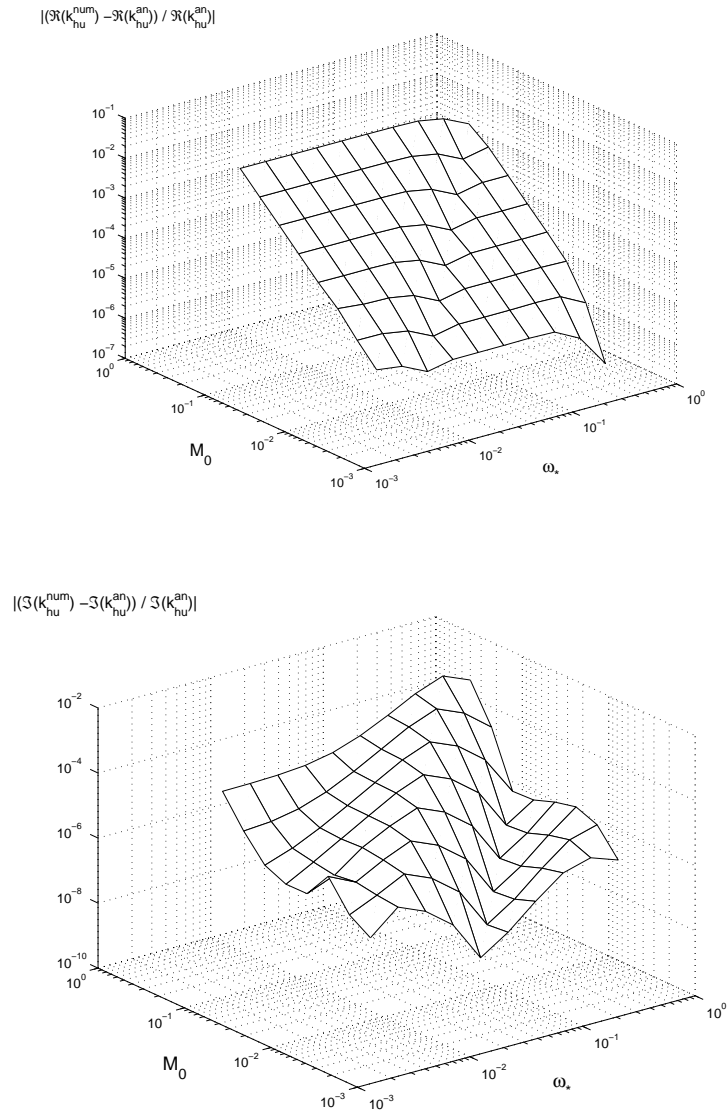
Figure 2.16: Relative deviation in the real and imaginary part of the wavenumber k_{hu*} of the unstable hydrodynamic wave for an infinitely thin shear layer when comparing the modal analysis result (superscript num) and the incompressible analytical solution superscript (an). Here $N = 50$, but virtually the same result was found for higher N.

(a) m=1 (b) m=6
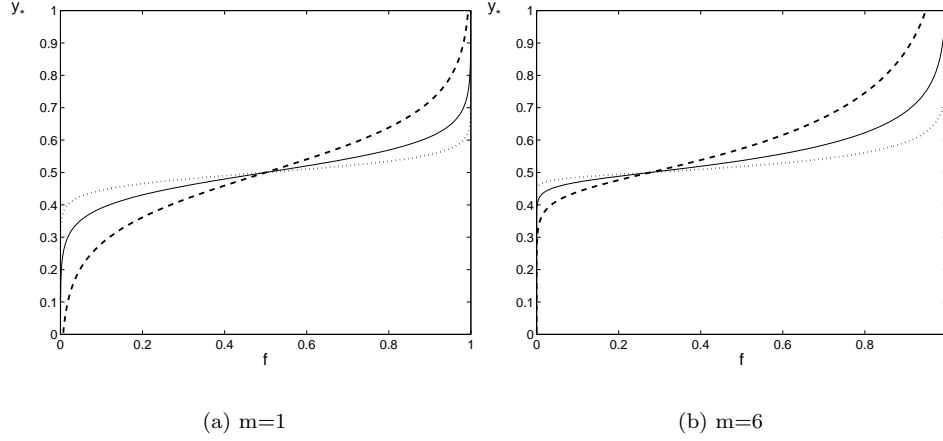
Figure 2.17: Generalized hyperbolic-tangent velocity profile, eq (2.41), in a duct for profile parameters $m = 1$ and $m = 6$, and for non-dimensional momentum thickness $\theta_* = 0.1$ (dashed line), $\theta_* = 0.05$ (solid line), and $\theta_* = 0.025$ (dotted line).

in figures 2.18 and 2.19 for $m = 1$ and $m = 6$ respectively. On the horizontal axes is the Strouhal number based on the momentum thickness $\omega\theta/U_0$, with $U_0 = M_0 c_0$. The results of Michalke [67] are indicated by the solid lines. The dimensionless angular frequency is set at $\omega_* = 0.01$ in the calculations. Results of calculations with smaller ω_* and hence smaller M_0 gave no significant difference, assuring sufficient approximation of the incompressible limit. Furthermore, the spacing between discrete points is kept constant with respect to θ_* at $\Delta h_*/\theta_* = 0.1$. This implies $N = 100$, $N = 200$, and $N = 400$ for $\theta_* = 0.025$, $\theta_* = 0.05$, and $\theta_* = 0.1$ respectively. Results were found to be converged 'visually' for these numbers of discrete points in all cases. For both flow profile parameters good agreement between modal analysis results and Michalke's results are observed for the smallest momentum thickness to duct height ratio: $\theta_* = 0.025$. For larger θ_* significant deviation is seen, especially for profile parameter $m = 1$ case and at low Strouhal numbers. The results thus confirm that in the incompressible limit the modal analysis result for the wavenumber of the hydrodynamic instability approaches Michalke's result for a generalized hyperbolic-tangent shear layer unbounded in the y-direction, if the duct hight compared to momentum thickness is sufficiently large.
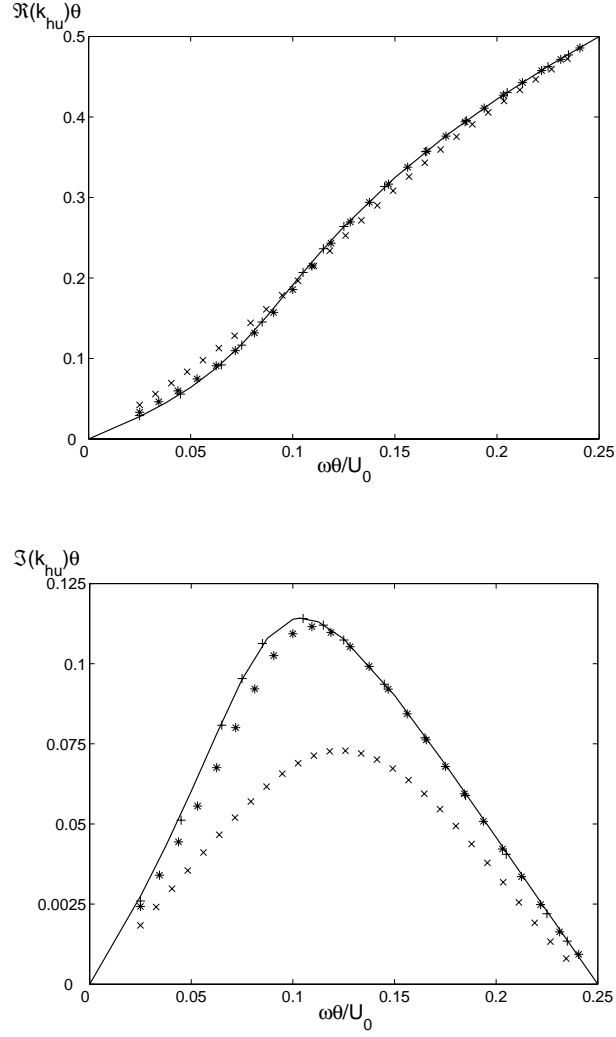
Figure 2.18: Real and imaginary part of the wavenumber k_{hu} of the unstable hydro-dynamic mode versus Strouhal number for the hyperbolic- tangent profile, eq. (2.41), with $m = 1$. Modal analysis calculation are with $\omega_* = 0.01$ and dimensionless momentum thickness $\theta_* = 0.025$ (+), $\theta_* = 0.05$ (∗) and $\theta_* = 0.1$ (×). The solid line represents a fit of the incompressible result found by Michalke [67]. The spacing between discrete points is kept constant with respect to θ_* at $\Delta h_*/\theta_* = 0.1$, implying $N = 400$, $N = 200$ and $N = 100$ respectively.
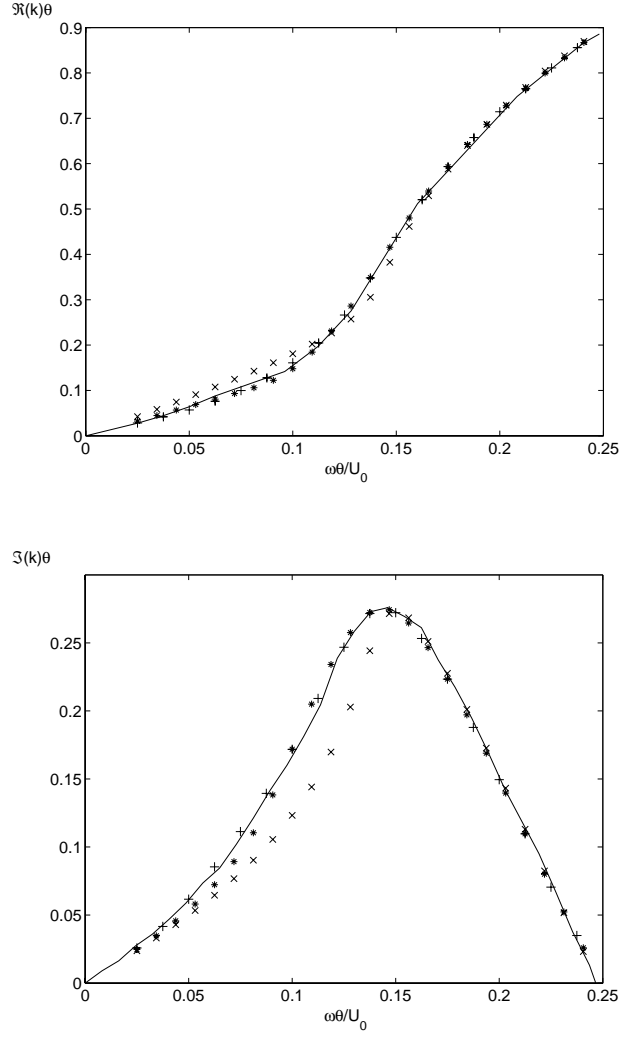
Figure 2.19: Real and imaginary part of the wavenumber k_{hu} of the unstable hydro-dynamic mode versus Strouhal number for the hyperbolic- tangent profile, eq. (2.41), with $m = 6$. Modal analysis calculation are with $\omega_* = 0.01$ and dimensionless momentum thickness $\theta_* = 0.025$ (+), $\theta_* = 0.05$ (∗) and $\theta_* = 0.1$ (×). The solid line represents a fit of the incompressible result found by Michalke [67]. The spacing between discrete points is kept constant with respect to θ_* at $\Delta h_*/\theta_* = 0.1$, implying $N = 400$, $N = 200$ and $N = 100$ respectively.

2.7.3 Neutral hydrodynamic modes

In the preceding sections, in which acoustic and hydrodynamic unstable modes were considered, the quantity $\omega_* - M_0 f k_*$ did not vanish. However, when $\omega_* - M_0 f k_* = 0$ at a certain point y_{s*}, such that $k_* = \omega_*/M_0 f(y_{s*})$, the Pridmore-Brown equation (2.19) is singular at $y_* = y_{s*}$. Generally, the solution for P in the vicinity of the singular point is found as a series development by substituting a Taylor expansion of $\omega_* - M_0 f k_*$ around $y_* = y_{s*}$ in the Pridmore-Brown equation, see e.g. Lees and Lin [61]. Clearly, since $0 \le y_{s*} \le 1$, a continuous hydrodynamic spectrum with purely real wavenumbers $\omega_*/M_0 f_{\max} \le k_{hs*} \le \omega_*/M_0 f_{\min}$ is obtained for non-uniform flow. This continuous set of modes is analyzed by e.g. Swinbanks [107]. In the present discretized modal analysis hydrodynamic neutral modes are expected to have wavenumbers with value $k_{hs*} = \omega_*/M_0 f(y_*)$ at the discrete points.

For a duct with a Poiseuille mean flow profile the calculated wavenumbers, using differential matrices accurate to order Δh_*^2, are compared with the expected values at the discrete points. Figure 2.20 shows the calculated values of $k_0/M_0 k_{hs}$, which is equal to the phase velocity of the modes divided by the average main flow velocity U_0. The values should coincide with the profile function f, also plotted in the figure, at the discrete points. Indeed excellent agreement is seen, the relative deviation is in the order of machine precision ($O(10^{-16})$). Note that, as no hydrodynamic instability occurs for such profile, all of the hydrodynamic modes found are neutral. The same comparison is made for a duct with Poiseuille mean flow only in the lower half (see also figure 2.6b). Figure 2.21 shows the results for a Mach number at which no hydrodynamic instability occurs and for a higher Mach number where also hydrodynamic unstable modes are present. When no hydrodynamic instability is found, the wavenumbers of the neutral modes again perfectly agree with the expected values at all discrete points. In case hydrodynamic instability occurs two of the calculated hydrodynamic modes are unstable, leaving two less solved neutral modes. The wavenumber values for these neutral modes are in agreement with the expected value, but the neutral modes with phase velocity corresponding with the flow velocity at the two discrete points just before the mean flow to no mean flow transition are not found.

Also hydrodynamic neutral modes for the hyperbolic-tangent shear layer profile, equation (2.41), with profile parameter $m = 1$ are considered. For this case the deviation in wavenumber turns out to be more significant. Figure 2.22 shows the relative error of the calculated wavenumbers of the hydrodynamic neutral modes k_{hs}^{num} with respect to the expected analytical value k_{hs}^{an} versus the discrete points in y_*. The dimensionless frequency is $\omega_* = 0.01$ and the momentum thickness to duct height ratio is $\theta_* = 0.025$. This flow profile is also considered in the previous section and is shown in figure 2.17a. The Strouhal number is chosen $\omega\theta/U_0 = 0.3$, such that no hydrodynamic instability occurs, see figure 2.18. Calculations are performed using differential matrices accurate to order Δh_*^2 (fig.2.22a), Δh_*^4 (fig.2.22b) and Δh_*^6 (fig.2.22c) at different number of discrete points N. For the $O(\Delta h_*^4)$ and $O(\Delta h_*^6)$ calculations con-
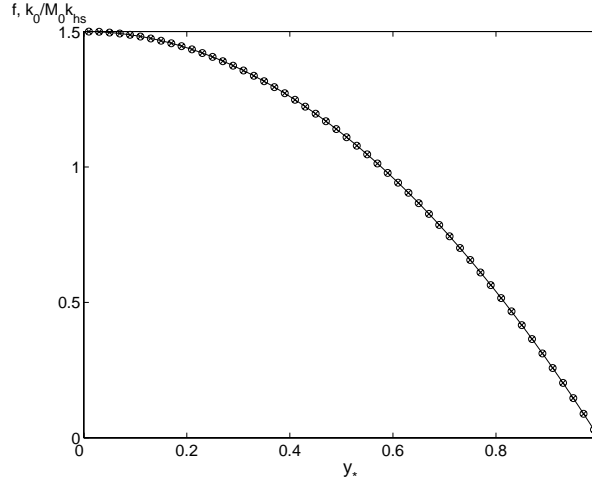
Figure 2.20: Calculated values of the hydrodynamic neutral wavenumbers k_{hs} for a duct with Poiseuille mean flow plotted as $k_0/M_0 k_{hs}$ ($\times$ markers) coincide with the value of the profile function f at the discrete points ($\circ$ markers). Parameter values are $\omega_* = 0.1$, $N = 50$, $M_0 = 0.1$

vergence in the wavenumber deviation is -at least visually- established at $N = 200$. For the $O(\Delta h_*^2)$ calculations are done up to $N = 500$, where convergence in the wavenumber deviation was no yet completely observed. The wavenumber deviation against position y_* for the different orders of accuracy, each at the highest number of points N used, are shown together in figure 2.22d. The largest deviation in the wavenumbers is seen in the region of the actual shear layer, where mean flow velocity changes most rapidly. However, halfway the duct at the inflexion point, where shear is maximum, a local minimum in the wavenumber deviation is seen. The error in the wavenumber versus position is quite similar for the $O(\Delta h_*^4)$ and $O(\Delta h_*^6)$ calculations, whereas the $O(\Delta h_*^2)$ calculation additionally shows relatively large error in the lower half of the shear layer. Remarkably, the error in the wavenumbers for the $O(\Delta h_*^4)$ calculation is in general smaller than for the $O(\Delta h_*^6)$ calculation.
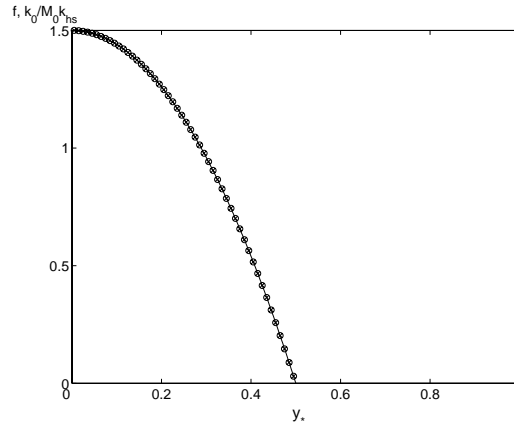
(a) no hydrodynamic instability
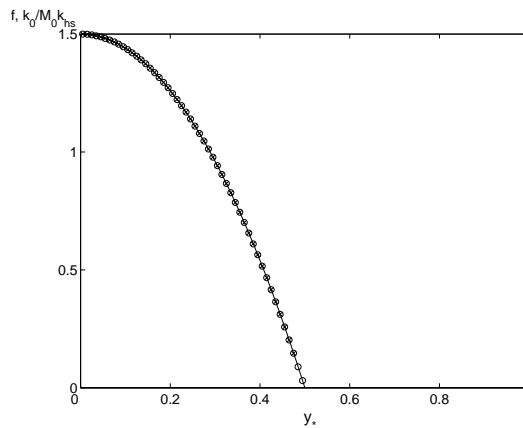
(b) hydrodynamic instability

Figure 2.21: Calculated values of the hydrodynamic neutral wavenumbers k_{hs} for a duct with Poiseuille mean flow only in the lower half plotted as $k_0/M_0 k_{hs}$ ($\times$ marker) coincide with the value of the profile function f at the discrete points ($\circ$ markers). (a) Average Mach number is $M_0 = 0.02$: no hydrodynamic instability occurs, neutral hydrodynamic modes are solved at all discrete points. (b) $M_0 = 0.1$: hydrodynamic instability occurs and consequently two less neutral hydrodynamic modes, at the two discrete points before the flow/no flow transition, are solved. Other parameters are $\omega_* = 0.2$ and $N = 100$

(a)

(b)

(c)

(d)
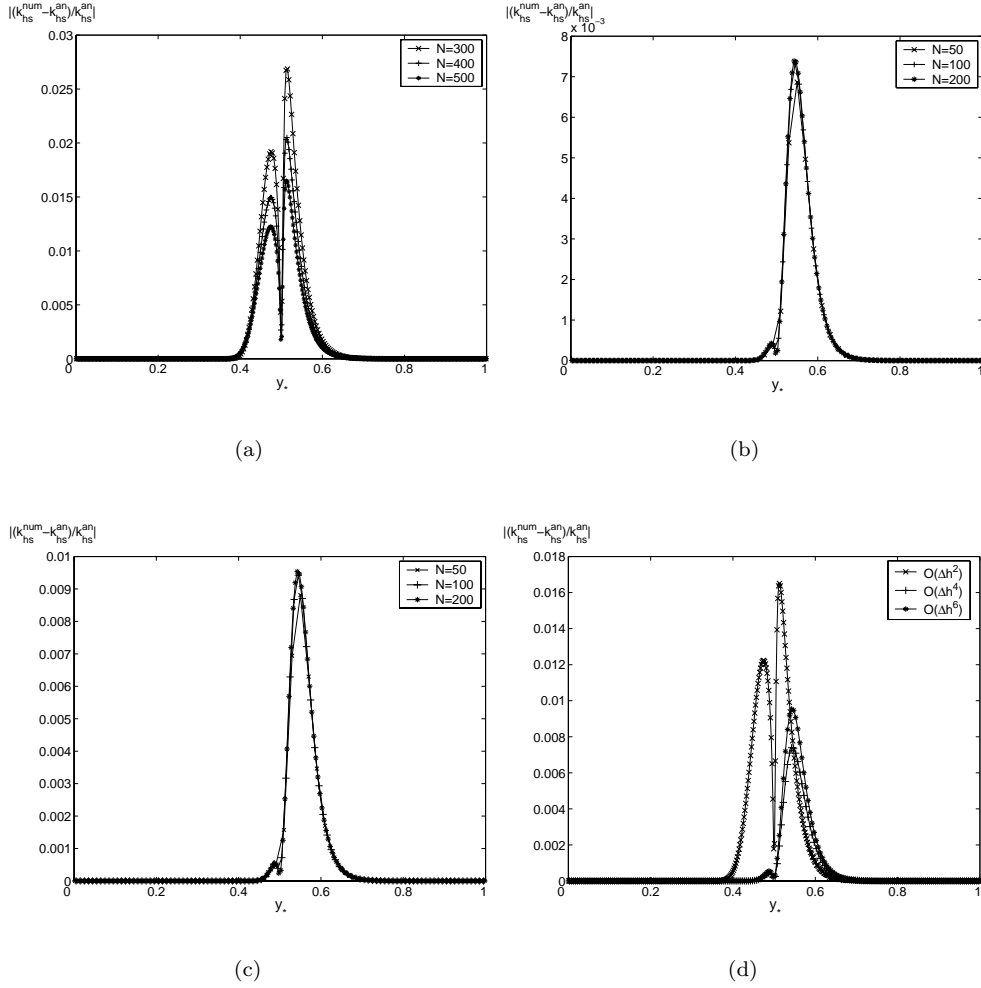
Figure 2.22: Relative error of the calculated wavenumbers of the hydrodynamic neutral modes k_{hs}^{num} with respect to the expected analytical value k_{hs}^{an} versus the discrete points in y_* for a hyperbolic-tangent shear layer profile, eq. (2.41), with $m = 1$. Furthermore $\omega_* = 0.01$ and $\theta_* = 0.025$. This flow profile is also given in figure 2.17a. Calculations are done at different number of discrete points N for differential matrices accurate to order $O(\Delta h_*^2)$ (a), $O(\Delta h_*^4)$ (b) and $O(\Delta h_*^6)$ (c). (d) shows results for different orders of accuracy together, each for the highest number N.

2.8   Conclusion

A finite difference method to obtain a discrete generalized eigenvalue problem for the transverse modes and their accompanying wavenumbers for the linear pressure and velocity disturbance in a two dimensional rectangular duct with parallel shear flow has been presented. Application of the method to some particular shear layer profiles, which will be considered in flow configurations further on, is treated in more detail. Causality criteria to discern the direction of propagation of the modes as well as a classification in acoustic (propagating or evanescent) and hydrodynamic (unstable or neutral) modes are discussed. In absence of mean flow the analytically well known modes are resolved perfectly at the discrete points and good convergence of the calculated wavenumber to the analytical values is observed. For an infinitely thin shear layer the calculated modes and wavenumbers of the hydrodynamic instability approach the incompressible analytical solution well for low Helmholtz and Mach number. Also, in the incompressible limit, the wavenumbers of the unstable hydrodynamic modes for a generalized hyperbolic-tangent shear layer profile are found to be in good agreement with the solution obtained by Michalke [67, 68, 69], where the shear layer is not bounded perpendicular to the flow direction, provided that shear layer momentum thickness to duct height ratio is sufficiently small (about 0.025). The continuum of neutral hydrodynamic modes with phase velocities corresponding to the mean flow velocity is solved at the discrete points. For a duct with (partly) non uniform Poiseuille flow the calculated wavenumbers perfectly agree with the expected values. However, when hydrodynamic instability occurs, the two neutral hydrodynamic modes with phase velocity corresponding to the mean flow velocity at the discrete points closest to the flow to no flow transition are not resolved anymore 'in favour' of the two unstable modes. For the hyperbolic-tangent profile more significant deviation is seen for the calculated wavenumbers of neutral hydrodynamic modes which correspond to the region where shear is largest.

Chapter 3

Area expansion in a duct: modal analysis

3.1 Introduction

Perhaps the most simple duct configuration, in which a shear layer is formed, is that of a sudden area expansion in a two-dimensional duct with mean flow. Technical applications are internal combustion engine exhaust silencers and silencers in industrial duct systems.

Probably the most extensive experimental work on this topic is that of Ronneberger [100]. He presented results for both magnitude and phase of the reflection- as well as transmission coefficients of the acoustic plane pressure waves at an area expansion in a cylindrical duct with anechoic termination.

Early models to describe the acoustical properties of an area expansion in a duct with flow are that of Ronneberger [97] and Alfredson and Davies [3]. Here, in a low-frequency plane wave approximation, one-dimensional linearized equations for the conservation of mass, momentum and energy are applied to a control volume around the area expansion. Dissipation is accounted for by entropy fluctuations, associated with the formation of vortices in the mixing region downstream of the expansion, which is thus included in the control volume. Alfredson and Davies [3] compared theoretical prediction and experimental data for the reflection coefficient up to a Mach number of 0.15, reasonable agreement was found. Ronneberger [97] compared predicted and measured results for the reflection coefficient up to Mach numbers of 0.6, but also here only good agreement was obtained for Mach numbers below ∼0.15. Cummings [23] proposed a similar model, in which scattering is assumed to occur in the control volume, where the flow has not yet expanded, while energy losses due to the vorticity are now accounted for by entropy waves downstream of the control volume.

Comparison with Ronneberger's experimental results yielded better agreement for the higher Mach numbers. Furthermore, in a later correspondence [24] he concluded that entropy fluctuations need not to be taken into account as they are of secondary importance and probably are negligible compared to higher order modes and shear flow effects. All of the above mentioned models lack the effects of higher order modes as they are low-frequency (plane wave) approximations.

Lambert and Steinbrueck [59] proposed a low frequency, low Mach number model on the basis of the statement that the magnitude of the reflection coefficient at an area expansion is only Mach number dependent, whereas its phase is only frequency dependent. The magnitude is calculated from applying conservation equations to a control volume around the area expansion, in which the mean flow has expanded. The phase is calculated from an equivalent end correction for no mean flow [50]. Davies [26] proposed a similar model where the phase is calculated from either an equivalent end correction or by including higher order modes in the matching of the ducts upstream and downstream of the area expansion. The use of an equivalent end correction for the phase of the reflection coefficient was extended to higher frequencies by Peat [85], who also compared results of the analytical model with a finite element method. It has to be noted here, that the, in these models, assumed dependency of magnitude and phase of the reflection coefficient on only Mach number respectively only frequency is actually in contradiction with (for example) experimental results of Ronneberger [100] and theoretical results of Boij and Nilsson [16] (see also below). Also, in the closely related problems of reflection at an open pipe with mean flow and scattering at a diaphragm in a pipe with mean flow the magnitude and phase is found to be dependent on both Mach number and frequency. This was shown experimentally by Peters [87] and Allam and Åbom [4] and theoretically by Munt [77, 78], Rienstra [95] and Cargill [19] for the open pipe, and by e.g. Hofmans [42] and Testud [109] for the diaphragm.

Aurégan [5, 7] presented a simplified multi-modal model for the aero-acoustic behaviour of a sudden area expansion at low frequency in a cylindrical duct. The uniform mean flow was considered to remain unexpanded after the area discontinuity. The effect of entropy fluctuations due to mixing downstream of the expansion is not accounted for. The acoustic pressure and radial velocity field downstream of the expansion was expanded into six modes assuming a prescribed form [106]: a plane wave mode and a mode accounting for higher-order effects in either direction of propagation, and two hydrodynamic modes. Subsequently, applying continuity of mean acoustic pressure and volume flux and a Kutta condition at the area discontinuity gave the acoustic behaviour. A favourable comparison of the predicted magnitude of the reflection coefficient with the experimental results of Ronneberger [100] was shown.

An alternative method was given by Dupère and Dowling [30]. They described the interaction of the shear layer with the sound field by means of an acoustic analogy,

in which the shear layer acts as a source/sink term in the wave equation in the downstream duct. Note that this is similar to the method of Howe for the acoustical response of a shear layer in a wall aperture, extensively described in appendix A. In the model of Dupère and Dowling the Mach number is very low and the shear layer is assumed to be thick, such that hydrodynamic instability does not occur.

Recently, Boij and Nilsson [16] presented a model for the scattering at an area discontinuity in a rectangular two-dimensional duct carrying uniform mean flow. Also in this model the flow is considered to remain unexpanded after the area discontinuity. Higher order acoustic modes and hydrodynamic modes are taken into account, and the problem is solved with the Wiener-Hopf technique with application of a Kutta condition at the edge of the area discontinuity. A favourable comparison for the scattering coefficients with experimental results of Ronneberger [97, 100] is made. For this purpose a normalization of the Helmholtz number for both rectangular and cylindrical ducts is proposed. In a later paper [17] they addressed the issue of (in)stability of the vortex sheet. As the mean flow is assumed to be uniform and continues unaltered after the expansion, an infinitely thin shear layer forms. As discussed in e.g. section 2.4 of this thesis such a vortex sheet is always unstable. However, a real shear layer with finite thickness becomes stable for sufficiently large Strouhal numbers. This is seen for instance for the hyperbolic-tangent profile discussed in appendix B.2. Boij and Nilsson accounted for this physical effect by suppressing the hydrodynamic instability mode for higher Strouhal numbers. This was done by introducing a gradually relaxed Kutta condition at the edge, with empirical coefficients as to give a better fit with experimental results for the downstream reflection coefficient. They reported that the effect of the relaxed Kutta condition on the downstream transmission coefficient is negligible. In the same paper they also calculate the absorption of energy at the area expansion, either accounting for the expansion of the flow downstream of the area discontinuity or not accounting for it.

In this chapter modal analysis, as described in the preceding chapter, is applied to solve the aeroacoustical behaviour of a sudden area expansion in a duct. As in the model of Aurégan [5, 7] and Boij and Nilsson [16] the contribution of entropy waves due to the expansion of the flow downstream of the area discontinuity is neglected here. Besides the possibility of comparison with other models and experiments from literature, especially the established convergence of this method for this particular geometry was motivating. First, the related mode matching will be treated for different flow configurations. Subsequently, the effect of the mean flow profile and application of a Kutta condition is investigated. Furthermore, results are compared with those obtained by Boij and Nilsson [16, 17] and with experiments by Ronneberger [100]. Specifically, in the light of the Helmholtz number scaling proposed by Boij and Nilsson [16] as mentioned above, a comparison between results for a two-dimensional rectangular and a two-dimensional cylindrical geometry is made.

3.2   Matching modes

In this section application of modal analysis, as described in the previous chapter, in order to solve the aeroacoustic behaviour of a sudden area expansion will be treated. The pressure and velocity disturbance both upstream and downstream of the area discontinuity are expanded in eigenmodes. Matching modes by demanding continuity of momentum and volume flux at the discontinuity subsequently gives a relation between modes propagating towards the area discontinuity and modes propagating away from the discontinuity. If the mean flow profile is chosen such that the velocity at the edge of the expansion is nonzero, additionally a Kutta condition has to be imposed. These two cases -Kutta condition and no Kutta condition- will be dealt with separately.

3.2.1   Without Kutta condition

Consider a sudden area expansion in a two dimensional rectangular duct, figure 3.1. The geometrical configuration can be split into a duct at $x < 0$ with height h_1 and a duct at $x > 0$ with height h_2. The two are indicated in the figure with boxed numbers 1 and 2 respectively. In duct 1 parallel non-uniform mean flow is present. The mean flow is assumed to continue with unaltered profile in duct 2, where thus only partially non-uniform flow is present. In duct 1 N_1 discrete points are taken in the y-direction, with spacing $\Delta h = h_1/N_1$, while the first and last point are at a distance $\Delta h/2$ from the wall. Similarly, in duct 2 N_2 discrete points are taken with the same spacing $\Delta h = h_2/N_2$, such that $N_2/N_1 = h_2/h_1$. The discrete points in duct 1 and the first N_1 discrete points in duct 2 are thus at the same y values.

According to section 2.2, solving the generalized eigenvalue problem, eq. (2.17), for duct 1 gives $3N_1$ modes and wavenumbers for the pressure and velocity disturbances.
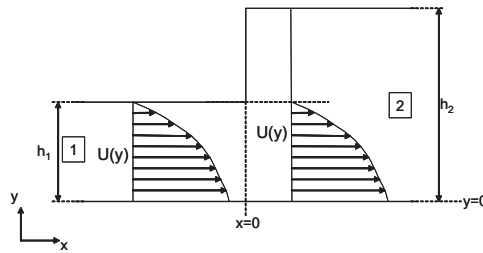

Figure 3.1: Area expansion in a two-dimensional duct. Configuration is split in duct 1 with height h_1 and duct 2 with height h_2. Non-uniform mean flow is present in duct 1 and is assumed to continue in duct 2 with unaltered profile.

Both N_1 acoustic and N_1 hydrodynamic modes propagating in the $+x$-direction and N_1 acoustic modes propagating in the $-x$-direction are found. The generalized eigenvalue problem for the modes in duct 2 has to be solved according to section 2.3. A number of N_2 acoustic modes propagating in either direction and N_1 hydrodynamic modes are found here. The modes for the velocity disturbance are only defined at the first N_1 points, where mean flow is present.

At the interface between the two ducts at $x = 0$ continuity of mass flux and momentum applies. As derived in appendix D this yields continuity of the dimensionless pressure and velocity disturbances p_* and v_* as well as continuity of the parameter q_*, where $q_* = i\partial p_*/\partial x_*$, cf. equation (2.12). In duct 2 the hard wall at $x = 0$ for $y > h_1$ yields the condition that the velocity disturbance in the x-direction, normal to the wall, is zero. This implies that $q_* = 0$ for $y > h_1$. With the modal expansion form for the discretized parameters $\mathbf{q}_*$ $\mathbf{v}_*$ and $\mathbf{p}_*$, given by equation (2.18), the above stated conditions at $x = 0$ applied at the discrete points yield the following set of $2N_1 + N_2$ equations:

$$\begin{aligned} \mathbf{Q_1^+ C_1^+} + \mathbf{Q_1^- C_1^-} \\ \mathbf{0} \end{aligned} = \mathbf{Q_2^+ C_2^+} + \mathbf{Q_2^- C_2^-} \quad \begin{matrix} \} N_1 \\ \} N_2 - N_1 \end{matrix}$$

$$\mathbf{V_1^+ C_1^+} + \mathbf{V_1^- C_1^-} = \mathbf{V_2^+ C_2^+} + \mathbf{V_2^{\;-} C_2^-} \quad \} N_1 \qquad\qquad (3.1)$$

$$\begin{aligned} \mathbf{P_1^+ C_1^+} + \mathbf{P_1^- C_1^-} \\ \times \end{aligned} = \mathbf{P_2^+ C_2^+} + \mathbf{P_2^- C_2^-} \quad \begin{matrix} \} N_1 \\ \} N_2 - N_1 \end{matrix}$$

Here, the eigenmodes $\mathbf{Q}_e$, $\mathbf{V}_e$ and $\mathbf{P}_e$ are in the columns of matrices $\mathbf{Q}$, $\mathbf{V}$ and $\mathbf{P}$. The additional subscripts 1 and 2 refer to duct 1 and 2 respectively. The use of superscripts $+$ and $-$ reflects a distinction between modes propagating to the $+x$-direction (acoustic and hydrodynamic) and the $-x$-direction (only acoustic). Vectors $\mathbf{C}$ contain the coefficients of the modes. The pressure disturbance in duct 2 for $y > h_1$, thus at the last $N_2 - N_1$ points, is not governed by any equation, this is indicated by the cross in the set of equations above. Equations (3.1) are written in a matrix equation as follows:

$$\underbrace{\begin{pmatrix} -\mathbf{Q_1^-} & \mathbf{Q_2^+} \\ \mathbf{0} & \mathbf{Q_2^+} \\ -\mathbf{V_1^-} & \mathbf{V_2^+} \\ -\mathbf{P_1^-} & \mathbf{P_2^+}(1:N_1,:) \end{pmatrix}}_{\mathbf{s_1}} \begin{pmatrix} \mathbf{C_1^-} \\ \mathbf{C_2^+} \end{pmatrix} = \underbrace{\begin{pmatrix} \mathbf{Q_1^+} & -\mathbf{Q_2^-} \\ \mathbf{0} & -\mathbf{Q_2^-} \\ \mathbf{V_1^+} & -\mathbf{V_2^{\;-}} \\ \mathbf{P_1^+} & -\mathbf{P_2^-}(1:N_1,:) \end{pmatrix}}_{\mathbf{s_2}} \begin{pmatrix} \mathbf{C_1^+} \\ \mathbf{C_2^-} \end{pmatrix}. \qquad (3.2)$$

As mentioned the pressure disturbance in duct 2 only comes into the equations at the first N_1 points. Therefore, only the first N_1 rows of $\mathbf{P_2^+}$ and $\mathbf{P_2^-}$, containing the

pressure disturbance modes, are considered in the equation above as indicated. Both matrices $\mathbf{S_1}$ and $\mathbf{S_2}$ in (3.2) are square with size $(2N_1 + N_2) \times (2N_1 + N_2)$. $\mathbf{S_1}$ can be inverted to obtain the scattering matrix: $\mathbf{S} = \mathbf{S_1}^{-1}\mathbf{S_2}$. This matrix relates the coefficients of all modes propagating away from the area expansion in the duct to the coefficients of the modes propagating towards the area expansion:

$$\begin{pmatrix} \mathbf{C_1^-} \\ \mathbf{C_2^+} \end{pmatrix} = \mathbf{S} \begin{pmatrix} \mathbf{C_1^+} \\ \mathbf{C_2^-} \end{pmatrix}. \tag{3.3}$$

The scattering matrix contains the complete aeroacoustical behaviour of the area expansion geometry.

Generally, only the reflection and transmission of the (quasi-)plane acoustic waves is of interest, since these modes always propagate irrespective of frequency. Reflection and transmission coefficients of the plane wave pressure disturbance at the duct expansion can be defined in either direction. When sorting the above given eigenmode matrices such that the plane wave modes, both for $+x$ and $-x$ propagating, are in the first column, they are given by:

$$R^+ = \frac{\mathbf{C_1^-}(1)}{\mathbf{C_1^+}(1)} = \mathbf{S}(1,1), \qquad T^- = \frac{\mathbf{C_1^-}(1)}{\mathbf{C_2^-}(1)} = \mathbf{S}(1, 2N_1 + 1),$$

$$T^+ = \frac{\mathbf{C_2^+}(1)}{\mathbf{C_1^+}(1)} = \mathbf{S}(N_1 + 1, 1), \qquad R^- = \frac{\mathbf{C_2^+}(1)}{\mathbf{C_2^-}(1)} = \mathbf{S}(N_1 + 1, 2N_1 + 1). \tag{3.4}$$

It has to be noted here that all calculated plane wave modes have to be equally normalized first for these relations to be useful. Therefore, in calculations the y-averaged amplitude of the pressure disturbance plane wave modes are set to unity.

3.2.2 With Kutta condition

Consider the same configuration of an area expansion in a two-dimensional duct as in figure 3.1. Only now either uniform flow or non-uniform flow with slip velocity at the upper wall is present in duct 1, see figure 3.2. The flow profile is again assumed to continue unaltered into duct 2. For the uniform flow case modes in duct 1 and 2 are solved according to section 2.4, equations (2.20) and (2.27) respectively. In duct 1 N_1 acoustic modes propagating in either direction are found. In duct 2 N_2 acoustic modes propagating in either direction and 2 hydrodynamic unstable Kelvin-Helmholtz modes are found. For non-uniform flow with slip modes in duct 1 are solved according to section 2.2 equation (2.17). The modes in duct 2 are solved according to section 2.5. In duct 1 N_1 acoustic and hydrodynamic modes propagating to the right and N_1 acoustic modes propagating to the left are found. In duct 2 N_2 acoustic modes propagating in either direction and $N_1 + 2$ hydrodynamic modes are found.

In both cases the velocity disturbance in the y-direction at the side with mean flow and the side without mean flow is available as an extra parameter at the flow / no flow

(a)   (b)
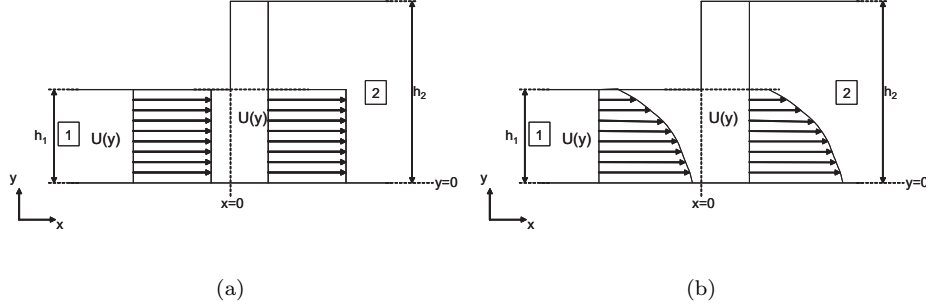
Figure 3.2: Area expansion in a two dimensional rectangular duct as in figure 3.1. a) Uniform mean flow is present in duct 1 and is assumed to continue in duct 2 with unaltered profile. b) Non-uniform mean flow with a slip velocity at the upper wall is present in duct 1, profile is unaltered in duct 2. Procedure of finding modes in duct 2 is as discussed in sections 2.4 and 2.5 respectively. The extra variables defined at the flow / no flow interface are utilized to apply a Kutta condition.

interface in duct 2. The amplitude of these variables were denoted V_{flow} and V_{noflow} respectively. The latter will now be used to apply a Kutta condition at the edge at $x = 0, y = h_1$. The Kutta condition states that the flow leaves the edge tangentially, such that the fluid displacement δ as well as the derivative of the displacement with respect to x equals zero at the edge:

$$\delta = 0, \qquad \frac{\partial \delta}{\partial x} = 0 \qquad \text{at} \qquad x = 0, \quad y = h_1. \qquad (3.5)$$

The velocity disturbance equals the convective derivative of the displacement, equation (2.25), such that from (3.5) the condition: $V_{noflow} = 0$, $k_* V_{noflow} = 0$ is obtained at $x = 0$. Note that for simplicity this is in a 'single mode' notation. In effect these conditions apply for the sum over all the modes. Incorporating the Kutta condition in the matching of pressure and mass flux between duct 1 and 2 gives for uniform flow, analogous to equation (3.2):

$$\underbrace{\begin{pmatrix} -\mathbf{Q_1^-} & \mathbf{Q_2^+} \\ \mathbf{0} & \\ -\mathbf{P_1^-} & \mathbf{P_2^+}(1:N_1,:) \\ \mathbf{0} & \mathbf{V_{nf}^+} \\ \mathbf{0} & \mathbf{V_{nf}^+ k_2^+} \end{pmatrix}}_{\mathbf{S_1}} \begin{pmatrix} \mathbf{C_1^-} \\ \mathbf{C_2^+} \end{pmatrix} = \underbrace{\begin{pmatrix} \mathbf{Q_1^+} & -\mathbf{Q_2^-} \\ \mathbf{0} & \\ \mathbf{P_1^+} & -\mathbf{P_2^-}(1:N_1,:) \\ \mathbf{0} & -\mathbf{V_{nf}^-} \\ \mathbf{0} & -\mathbf{V_{nf}^- k_2^-} \end{pmatrix}}_{\mathbf{S_2}} \begin{pmatrix} \mathbf{C_1^+} \\ \mathbf{C_2^-} \end{pmatrix}. \qquad (3.6)$$

Here, the modes of V_{noflow} are in the columns of matrix $\mathbf{V_{nf}}$. Since V_{noflow} is defined at a single point, these modes are just a single value. As for the other matrices containing modes for pressure disturbance etc. a distinction between $+x$-propagating and $-x$-propagating modes is made denoted by the additional superscripts. Matrices $\mathbf{k_2}$ contain the values of the wavenumbers in duct 2 on the diagonal, such that $\mathbf{V_{nf}k_2}$ gives the modes multiplied by their corresponding wavenumber. The indication $(1 : N_1, :)$ behind matrices P_2 denotes the rows and columns respectively, which are taken into account. Thus here, only the first N_1 rows (of the total of N_2 rows) and all of the $N_2 + 2$ columns are considered. $\mathbf{S_1}$ measures $(N_1 + N_2 + 2) \times (N_1 + N_2 + 2)$ and $\mathbf{S_2}$ measures $(N_1 + N_2 + 2) \times (N_1 + N_2)$ in the equation above. Since $\mathbf{S_1}$ is square it can (in general) be inverted. Subsequent multiplication with $\mathbf{S_2}$ gives the $(N_1 + N_2 + 2) \times (N_1 + N_2)$ scattering matrix $\mathbf{S}$ analoguous to eq.(3.3). The reflection and transmission coefficients of the plane waves are given by:

$$R^+ = \mathbf{S}(1,1), \qquad\qquad T^- = \mathbf{S}(1, N_1 + 1),$$
$$T^+ = \mathbf{S}(N_1 + 1, 1), \qquad\qquad R^- = \mathbf{S}(N_1 + 1, N_1 + 1). \qquad (3.7)$$

In the same way, for non-uniform flow with slip the following equation is derived:

$$\underbrace{\begin{pmatrix} -\mathbf{Q_1^-} & \mathbf{Q_2^+} \\ \mathbf{0} & \mathbf{Q_2^+} \\ -\mathbf{V_1^-} & \mathbf{V_2^+} \\ -\mathbf{P_1^-} & \mathbf{P_2^+}(1:N_1,:) \\ \mathbf{0} & \mathbf{V_{nf}^+} \\ \mathbf{0} & \mathbf{V_{nf}^+k_2^+} \end{pmatrix}}_{\mathbf{S_1}} \begin{pmatrix} \mathbf{C_1^-} \\ \mathbf{C_2^+} \end{pmatrix} = \underbrace{\begin{pmatrix} \mathbf{Q_1^+} & -\mathbf{Q_2^-} \\ \mathbf{0} & -\mathbf{Q_2^-} \\ \mathbf{V_1^+} & -\mathbf{V_2^-} \\ \mathbf{P_1^+} & -\mathbf{P_2^-}(1:N_1,:) \\ \mathbf{0} & -\mathbf{V_{nf}^-} \\ \mathbf{0} & -\mathbf{V_{nf}^-k_2^-} \end{pmatrix}}_{\mathbf{S_2}} \begin{pmatrix} \mathbf{C_1^+} \\ \mathbf{C_2^-} \end{pmatrix}, \qquad (3.8)$$

Here $\mathbf{S_1}$ measures $(2N_1 + N_2 + 2) \times (2N_1 + N_2 + 2)$ and $\mathbf{S_2}$ measures $(2N_1 + N_2 + 2) \times (2N_1 + N_2)$. Also here a $(2N_1 + N_2 + 2) \times (2N_1 + N_2)$ scattering matrix can be obtained by: $\mathbf{S} = \mathbf{S_1}^{-1}\mathbf{S_2}$. And the reflection and transmission coefficients of the plane waves are given by:

$$R^+ = \mathbf{S}(1,1), \qquad\qquad T^- = \mathbf{S}(1, 2N_1 + 1),$$
$$T^+ = \mathbf{S}(N_1 + 1, 1), \qquad\qquad R^- = \mathbf{S}(N_1 + 1, 2N_1 + 1). \qquad (3.9)$$

3.2.3 Further thoughts about the Kutta condition

The mode matching at an area expansion in a duct has been discussed for three mean flow configurations: non-uniform flow, where mean flow velocity is zero at the edge of the area discontinuity, non-uniform flow with a slip velocity at the edge, and uniform mean flow. In the present analysis viscosity of the fluid is neglected. However, as a consequence, when the mean flow velocity at the upper wall of duct 1, and thus at

the edge of the area expansion, is nonzero, the flow will 'follow' the contour of the area expansion, and flow velocity becomes infinite at the edge (potential flow). To overcome this unphysical behaviour, the effect of viscosity near the edge is included by demanding flow separation: the flow leaves the edge tangentially. This is known as the Kutta condition. In the preceding, the Kutta condition was thus imposed for the mean flow, by assuming that the mean flow profile in the duct upstream of the area expansion continues unaltered downstream of the expansion.

For the acoustic field the effect of viscosity at the edge can be included in the same way by applying a Kutta condition, demanding that the acoustic displacement and its derivative with respect to the mean flow direction is zero at the edge. As shown above, this condition can however only be imposed explicitly for non-uniform mean flow with a slip velocity at the edge and for uniform mean flow.

This means that for the non-uniform flow configuration the effect of viscosity is included in the way it affects the boundary layer profile of the mean flow. Here, the mean flow also satisfies the no slip condition at the wall due to viscosity. For the acoustic field however, the effect of viscosity is not accounted for. For the uniform mean flow configuration the effect of viscosity is included for the mean flow and the acoustic field only near the edge, where the Kutta condition is applied for both. For the configuration of non-uniform mean flow with slip velocity at the wall the effect of viscosity is included in the way it affects the mean flow boundary layer profile. However a mean flow slip velocity at the wall is allowed. This slip velocity enables us to include the effect of viscosity for the acoustic field near the edge by applying a Kutta condition. Also, for the mean flow the Kutta condition at the edge is fulfilled.

When modelling the acoustic behaviour of, in this case, an area expansion in a duct, or any geometry containing an edge, the validity of a Kutta condition actually depends on the exact physical configuration, which is modelled. The Kutta condition namely cancels the unphysical singularity in the (acoustic) flow field at the edge. However, this singular behaviour is an outcome of the fact that in the model the edge is sharp. In reality the edge will not be sharp, but is rounded with a certain radius of curvature r_e. The question whether or not to apply the Kutta condition in the model depends on the ratio of certain variables in the physical situation. In absence of mean flow, the acoustic Kutta condition holds when the acoustic boundary layer thickness, given by:

$$\delta_{ac} = \sqrt{\frac{2\nu}{\omega}}, \tag{3.10}$$

with ν the kinematic viscosity, and the amplitude of the acoustic fluid displacement, see e.g. equations (2.24,2.25), are both large compared to the edge's radius of curvature r_e, see e.g. Disselhorst [28].

When mean flow is present, it is expected that also the ratio of the acoustic boundary layer thickness and the thickness δ^+ of the viscous sublayer of the mean

flow, given by:

$$\delta^+ = \frac{\nu}{u_{fric}}, \tag{3.11}$$

is important. Here, ν is the kinematic viscosity (for air: $\nu = 1.51 \ 10^{-5} \ \mathrm{m^2 s^{-1}}$), and u_{fric} is the friction velocity given by:

$$u_{fric} = \sqrt{\frac{\tau_w}{\rho_0}}, \tag{3.12}$$

with τ_w the shear stress at the wall, and ρ_0 the mass density. Peters [87] showed that for $\delta_{ac}/\delta^+ \geq 10$ there is a strong coupling between mean flow and acoustic field. When a Kutta condition applies for the mean flow, also a Kutta condition for the acoustic field could be expected in this regime.

For the configuration of non-uniform flow with slip velocity, there is an additional aspect. It can be regarded as an intermediate case between the non-uniform flow configuration and the uniform flow configuration, where a slip velocity at the wall is introduced in order to apply the Kutta condition for the acoustic field, while the effect of viscosity on the mean flow boundary layer profile is still accounted for. The question arises here which mean flow slip velocity has to be taken, and a physical argument is needed. The effect of the wall on the acoustic field is confined to a region within a distance of the acoustical boundary layer thickness δ_{ac} from the wall. A reasonable approach may therefore be to take the actual mean flow velocity at a distance δ_{ac} from the wall as the mean flow slip velocity at the wall in the model.

In the following, the influence of the mean flow profile configuration - non-uniform, non-uniform with slip, or uniform - and the associated application of a Kutta condition (or not) for the acoustic field, on the scattering at an area expansion will be investigated. This will provide some insight in the effect of applying a Kutta condition for the acoustic field in the first place, without discussing the issue of which configuration is physically most relevant.

3.3 Influence of flow configuration

3.3.1 Flow profile and Kutta condition

Consider a non-uniform velocity profile with slip velocity at the upper wall of duct 1, as was shown in figure 3.2b. The mean flow continues unaltered into duct 2, resulting in a partly non-uniform flow with velocity jump at the mean flow to no mean flow interface. Here, we take the following profile function:

$$f(y) = \begin{cases} \frac{m+1}{m}(1 - f_{int})(1 - (\frac{y}{h_1})^m) + f_{int} & 0 \leq y \leq h_1, \\ \\ 0 & h_1 < y \leq h_2, \end{cases} \tag{3.13}$$

where m is a profile parameter setting the steepness of the profile. The parameter f_{int} sets the slip velocity or velocity jump, and will be denoted as the slip coefficient. If $f_{int} = 0$ the slip velocity is zero, if $f_{int} = 1$ the mean flow profile is uniform, and the shear layer in duct 2 becomes infinitely thin. The average of $f(y)$ in duct 1 equals unity, such that M_0 is the mean Mach number according to the definition $M(y) = M_0 f(y)$. Figure 3.3 shows the flow profile, eq. (3.13), in duct 2 for $m = 10$ and $f_{int} = 0$, $f_{int} = 0.5$, and $f_{int} = 1$. The ratio of duct heights is taken $h_1/h_2 = 0.35$. Calculations for the scattering matrix of an area expansion with $h_1/h_2 = 0.35$ and the above flow profile function with $m = 10$ are performed for different values of the slip coefficient f_{int}, namely $f_{int} = 0$, $f_{int} = 0.1$, $f_{int} = 0.5$, $f_{int} = 0.9$, and $f_{int} = 1$. The Helmholtz number on duct height h_1 is fixed at $\omega h_1/c_0 = 0.11$, while the mean Mach number M_0 is varied. The number of points is $N_1 = 70$ in duct 1 and $N_2 = 200$ in duct 2. For $f_{int} = 0$, where the mean flow is (partly) non-uniform, the modes in duct 1 and duct 2 are calculated with the method of section 2.2 respectively section 2.3. The matching between the two ducts to obtain the scattering matrix is as described in section 3.2.1. No Kutta condition is thus explicitly applied in this case. For $f_{int} = 1$ the mean flow is (partly) uniform. In this case modes in duct 1 and 2 are calculated according to section 2.4, and the matching procedure is as described in section 3.2.2. The Kutta condition is explicitly imposed. For intermediate values, $0 < f_{int} < 1$, the mean flow in duct 2 is partly non-uniform with a slip velocity at the flow/no flow interface, hence the modes are calculated according to section 2.5.
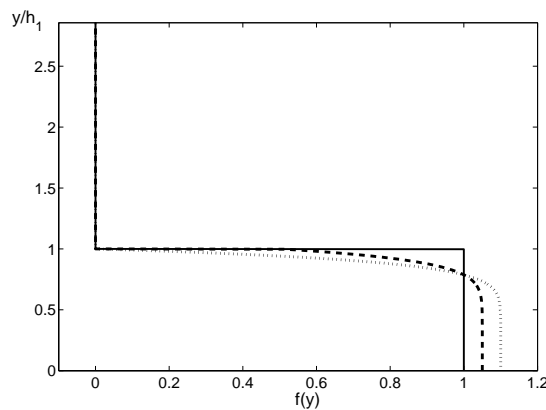

Figure 3.3: Flow profile $f(y)$ in duct 2 as given by equation (3.13) with flow profile parameter $m = 10$ and with different values of slip coefficient f_{int}. Dotted line: $f_{int} = 0$, dashed line: $f_{int} = 0.5$, solid line $f_{int} = 1$. For $f_{int} = 0$ the flow is partly non-uniform without velocity jump, for $f_{int} = 1$ the flow becomes partly uniform.

Modes in duct 1 can be calculated as in section 2.2. Also for this case the Kutta condition is applied in the matching between the two ducts, cf. section 3.2.2. Results for the plane wave pressure reflection and transmission coefficients as function of Strouhal number $\omega h_1/U_0$, with $U_0 = M_0 c_0$, are shown in figures 3.4 through 3.7.

The effect of going from a uniform flow profile to a non-uniform profile is here to increase the magnitude of the reflection and transmission coefficients except for R^-, of which the magnitude is decreased. Especially the magnitudes of the reflection and transmission coefficients change smoothly as the flow profile is gradually changed. Results for $f_{int} = 0.1$, giving a non-uniform flow with a small slip velocity in the shear layer, are nearly the same as those for $f_{int} = 0$, where the slip velocity vanishes. This indicates that application of the Kutta condition in the first case does not have a significant effect on the results compared to the latter case where the Kutta condition is not imposed. Also for $f_{int} = 0.9$ results are almost the same as for $f_{int} = 1$. For $f_{int} = 0.9$ neutral hydrodynamic modes are obtained, whereas in the $f_{int} = 1$ case, for which mean flow is uniform, they are absent. Therefore, it can be concluded that any effect of the neutral hydrodynamic modes vanishes as the flow profile is gradually changed from non-uniform to uniform. Furthermore, the imaginary part of the wavenumber of the unstable hydrodynamic mode in duct 2 (i.e. the amplification of the hydrodynamic instability) is shown in figure 3.8. For non-uniform flow without velocity jump in the shear layer, $f_{int} = 0$, the hydrodynamic instability vanishes above a certain Strouhal number. This behaviour is typically found for physical shear layers as discussed in appendix B.2 for the hyperbolic-tangent shear layer. For other values of f_{int} hydrodynamic instability always occurs due to the velocity jump in the shear layer. Consequently, for Strouhal number larger than about 3 the growth rate of the hydrodynamic instability found for $f_{int} = 0.1$ begins to differ significantly from that found for $f_{int} = 0$. Nevertheless, the corresponding results for the reflection and transmission coefficients, figures 3.4 through 3.7, are also practically the same for these higher Strouhal numbers. The effect of the hydrodynamic instability, and in particular the non-vanishing of it, is thus negligible for high Strouhal numbers. This conclusion was also drawn by Boij and Nilsson [17] and Howe [44]. Moreover, for low and high Strouhal number especially the magnitudes of the reflection and transmission coefficients converge to the same value for all values of f_{int}, indicating insignificance of the mean flow profile in these limits.

3.3.2   Area expansion ratio

A striking feature is the hump in reflection and transmission found around Strouhal number equal to 1, cf. figures 3.4 through 3.7. For the values of f_{int} equal to 0.5 or less, the phase plots even suggest a sudden jump. This feature may be connected to the behaviour of the hydrodynamic instability, since in the plot of hydrodynamic instability growth rate, figure 3.8, also a hump is seen for all values of f_{int} around the same Strouhal number. It turns out that this is caused by the asymmetry in the

Figure 3.4: Magnitude and phase of the downstream plane wave pressure reflection coefficient R^+ at an area expansion versus Strouhal number $\omega h_1/U_0$ with $\omega h_1/c_0 = 0.11$, $h_1/h_2 = 0.35$, $N_1 = 70$ and $N_2 = 200$. Mean flow profile is given by eq.(3.13), where $m = 10$ and $f_{int} = 0$ ($\times$), $f_{int} = 0.1$ ($*$), $f_{int} = 0.5$ (∇), $f_{int} = 0.9$ ($+$) and $f_{int} = 1$ ($\cdot$) respectively. For $f_{int} = 0$ no Kutta condition is applied in the mode matching procedure, for other values of f_{int} a Kutta condition is applied. Quasi-stationary solution without mean flow is: $R^+ = -0.4815$.
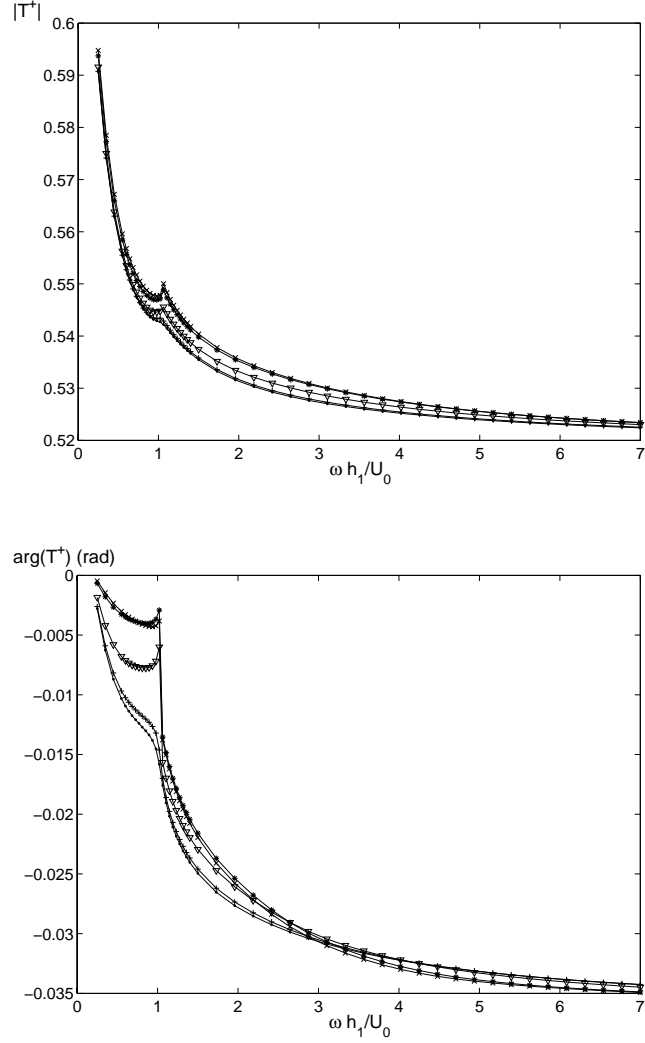
Figure 3.5: Magnitude and phase of the downstream plane wave pressure transmission coefficient T^+ at an area expansion versus Strouhal number $\omega h_1/U_0$ with $\omega h_1/c_0 = 0.11$, $h_1/h_2 = 0.35$, $N_1 = 70$ and $N_2 = 200$. Mean flow profile is given by eq.(3.13), where $m = 10$ and $f_{int} = 0$ ($\times$), $f_{int} = 0.1$ ($*$), $f_{int} = 0.5$ (∇), $f_{int} = 0.9$ ($+$) and $f_{int} = 1$ ($\cdot$) respectively. For $f_{int} = 0$ no Kutta condition is applied in the mode matching procedure, for other values of f_{int} a Kutta condition is applied. Quasi-stationary solution without mean flow is: $T^+ = 0.5185$.
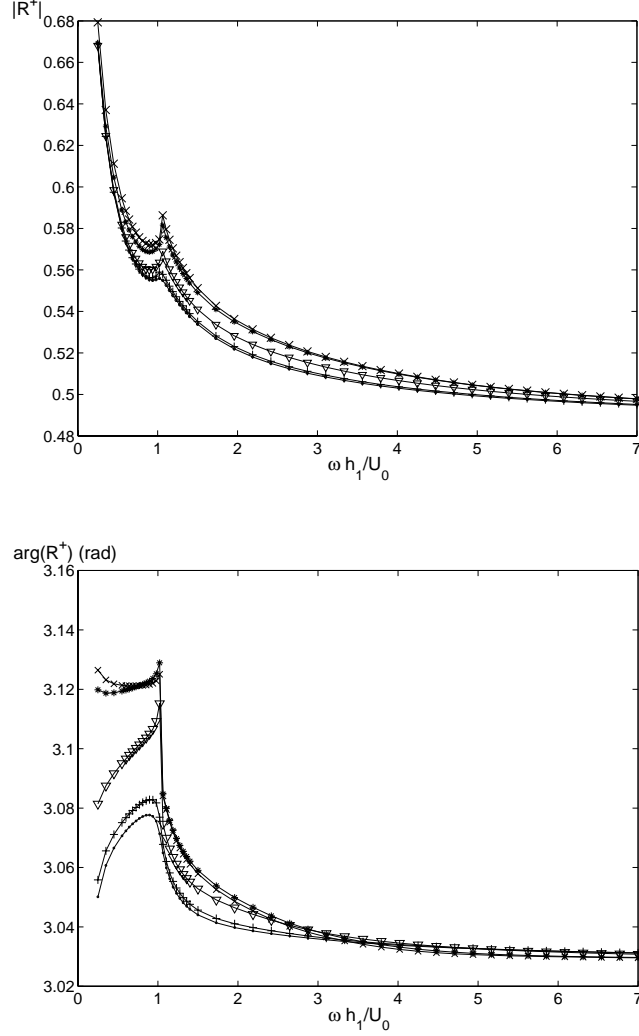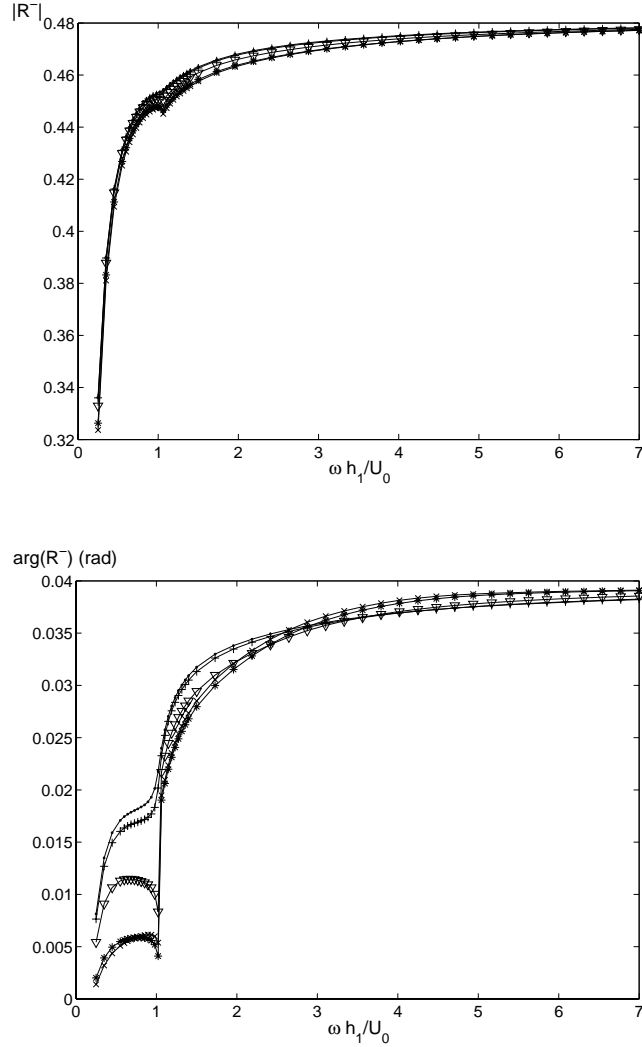
Figure 3.6: Magnitude and phase of the upstream plane wave pressure reflection coefficient R^- at an area expansion versus Strouhal number $\omega h_1/U_0$ with $\omega h_1/c_0 = 0.11$, $h_1/h_2 = 0.35$, $N_1 = 70$ and $N_2 = 200$. Mean flow profile is given by eq.(3.13), where $m = 10$ and $f_{int} = 0$ ($\times$), $f_{int} = 0.1$ ($*$), $f_{int} = 0.5$ (∇), $f_{int} = 0.9$ ($+$) and $f_{int} = 1$ ($\cdot$) respectively. For $f_{int} = 0$ no Kutta condition is applied in the mode matching procedure, for other values of f_{int} a Kutta condition is applied. Quasi-stationary solution without mean flow is: $R^- = 0.4815$.
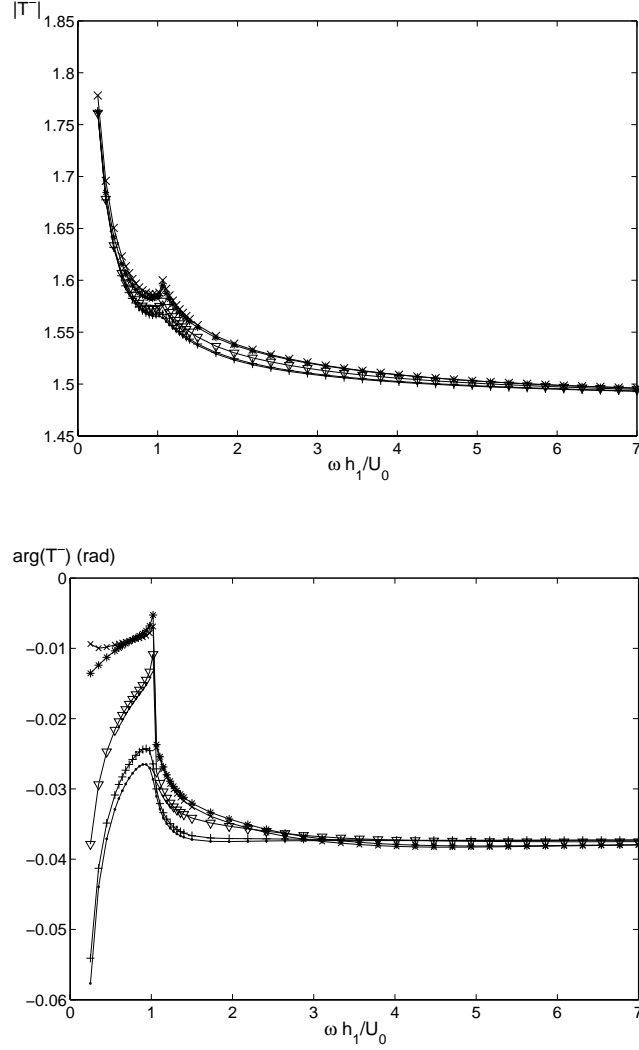
Figure 3.7: Magnitude and phase of the upstream plane wave pressure transmission coefficient T^- at an area expansion versus Strouhal number $\omega h_1/U_0$ with $\omega h_1/c_0 = 0.11$, $h_1/h_2 = 0.35$, $N_1 = 70$ and $N_2 = 200$. Mean flow profile is given by eq.(3.13), where $m = 10$ and $f_{int} = 0$ (x), $f_{int} = 0.1$ (*), $f_{int} = 0.5$ (∇), $f_{int} = 0.9$ (+) and $f_{int} = 1$ (.) respectively. For $f_{int} = 0$ no Kutta condition is applied in the mode matching procedure, for other values of f_{int} a Kutta condition is applied. Quasi-stationary solution without mean flow is: $T^- = 1.4815$.

Figure 3.8: Imaginary part of the wavenumber k_{hu} of the hydrodynamic instability (i.e growth rate) in duct 2 of the area expansion geometry scaled to $k_0 = \omega/c_0$ versus Strouhal number $\omega h_1/U_0$ for $\omega h_1/c_0 = 0.11$. Mean flow profile is given by eq. (3.13), where $m = 10$ and $f_{int} = 0$ ($\times$), $f_{int} = 0.1$ ($*$), $f_{int} = 0.5$ (∇), $f_{int} = 0.9$ ($+$) and $f_{int} = 1$ ($\cdot$) respectively.

flow profile, i.e. the fact that in duct 2 of the expansion geometry the mean flow to no mean flow transition is not halfway the duct. This will be illustrated below for both partly uniform flow and partly non-uniform flow.

uniform flow

Figure 3.9 shows the imaginary part of the wavenumber of the unstable hydrodynamic mode as function of Strouhal number $\omega h_1/U_0$ for different ratios of h_1 and h_2, obtained by modal analysis calculations in case of partly uniform mean flow. As above, also here $\omega_* = \omega h_1/c_0 = 0.11$. The number of points in the part with mean flow is fixed at $N_1 = 70$, the total number of points N_2 is thus determined by the ratio h_1/h_2. Indeed, the dependence of the (imaginary part of the) hydrodynamic wavenumber on the Strouhal number strongly varies with h_1/h_2 ratio. For Strouhal numbers larger than about 2 all results for $h_1/h_2 \leq 0.5$ coincide. The results for $h_1/h_2 = 0.7$ only coincide with those for other h_1/h_2 ratios above a Strouhal number of approximately 5.5.

The hydrodynamic instability is also calculated for the incompressible case. For
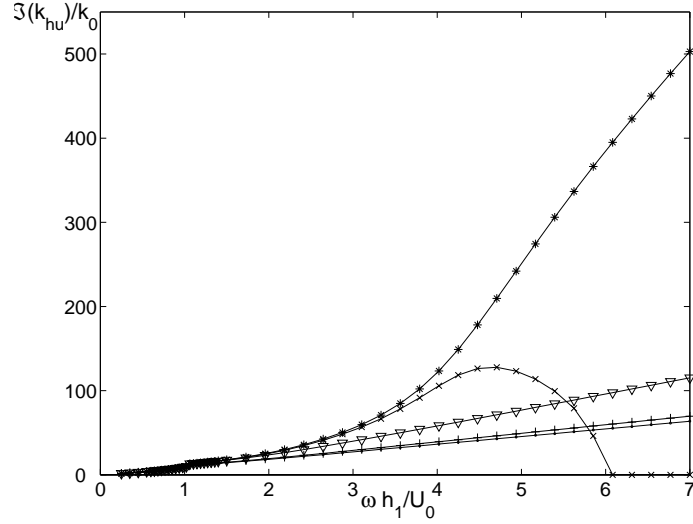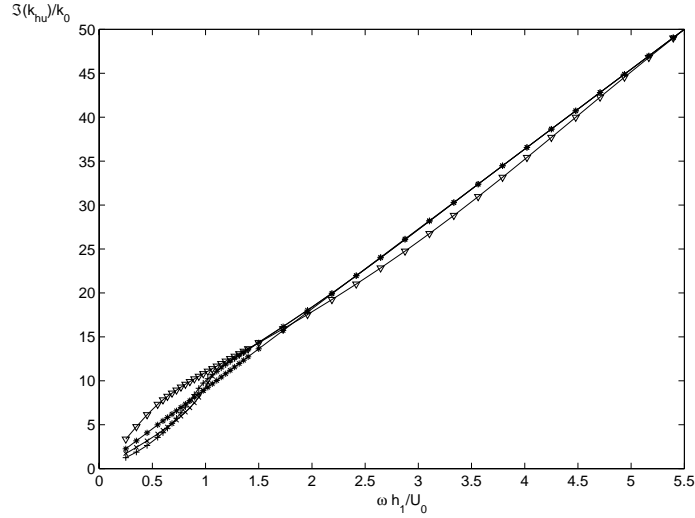
Figure 3.9: Imaginary part of the wavenumber k_{hu} of the hydrodynamic instability (i.e growth rate) in duct 2 of the area expansion geometry scaled to $k_0 = \omega/c_0$ for partly uniform mean flow as function of Strouhal number $\omega h_1/U_0$. Modal analysis calculations with $\omega h_1/c_0 = 0.11$ and $N_1 = 70$. h_1/h_2 ratios are $h_1/h_2 = 0.175$ $(+)$, $h_1/h_2 = 0.35$ $(\times)$, $h_1/h_2 = 0.5$ $(*)$, and $h_1/h_2 = 0.7$ (∇).

partly uniform flow in a duct, giving an infinitely thin shear layer, the incompressible solution for the hydrodynamic instability modes was already given in section 2.7.2, in particular equations (2.38) and (2.40), in case the shear layer is halfway the duct. More generally, if the shear layer is at $y = h_1$, as is considered in this chapter for duct 2 downstream of the area expansion with $0 \leq y \leq h_2$ (figure 3.1), the incompressible solution is found in the same way:

$$P_{hu}(y_*) = \begin{cases} A\cosh(k_{hu*}y_*) & 0 \leq y_* \leq 1, \\ \\ B\cosh(k_{hu*}(y_* - h_{2*})) & 1 \leq y_* \leq h_{2*}. \end{cases} \tag{3.14}$$

In this case h_1 is used for non-dimensionalisation, thus $h_{2*} = h_2/h_1$. A and B are coefficients determined by the wavenumber k_{hu*}. The wavenumber is found by demanding continuity of pressure and displacement at $y = h_1$, giving:

$$\frac{\tanh(k_{hu*})}{(\omega_* - M_0 k_{hu*})^2} = \frac{\tanh(k_{hu*}(1 - h_{2*}))}{w_*^2}. \tag{3.15}$$

This equation has to be solved numerically. The results obtained by modal analy-
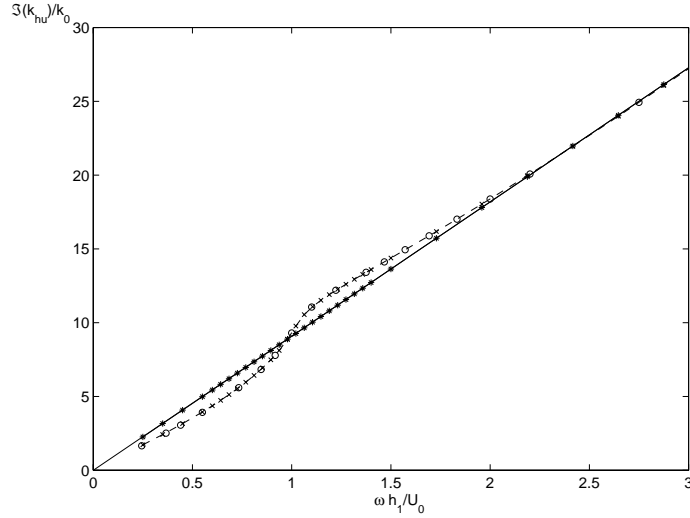
Figure 3.10: Imaginary part of the wavenumber of the hydrodynamic instability (i.e growth rate) in duct 2 of the area expansion geometry scaled to $k_0 = \omega/c_0$ for partly uniform mean flow as function of Strouhal number $\omega h_1/U_0$. Modal analysis calculations with $\omega h_1/c_0 = 0.11$ and $N_1 = 70$. h_1/h_2 ratios are $h_1/h_2 = 0.35$ ($\times$) and $h_1/h_2 = 0.5$ ($*$). Comparison with the incompressible solution is made: $\circ$ markers: $h_1/h_2 = 0.35$, solid line: $h_1/h_2 = 0.5$.

sis for ratios $h_1/h_2 = 0.35$ and $h_1/h_2 = 0.5$, cf. figure 3.9, are compared to the incompressible solution, equations (3.15) and (2.40) respectively, in figure 3.10. The incompressible solutions for the hydrodynamic wavenumber are close to the results of the compressible modal analysis. This suggests that the observed behaviour of the hydrodynamic instability really is an effect related to the area expansion ratio h_1/h_2, regardless the presence of acoustic modes.

The magnitude and phase of the downstream plane wave pressure reflection coefficient R^+ at the area expansion with uniform flow are shown in figure 3.11 for the different h_1/h_2 ratios. The observed hump (i.e. local maximum) in the magnitude and phase of the reflection coefficient for $h_1/h_2 = 0.175$ and $h_1/h_2 = 0.35$ seems to coincide with the inflexion point in the plot of hydrodynamic instability growth rate versus Strouhal number, cf. figure 3.9. For the other h_1/h_2 ratios the dependence of hydrodynamic instability growth rate as well as reflection coefficient on Strouhal number is more smooth.

A more elaborate picture of the influence of the area expansion ratio on the eigenmodes is given in figure 3.12. Here, the wavenumbers of the plane wave acoustic
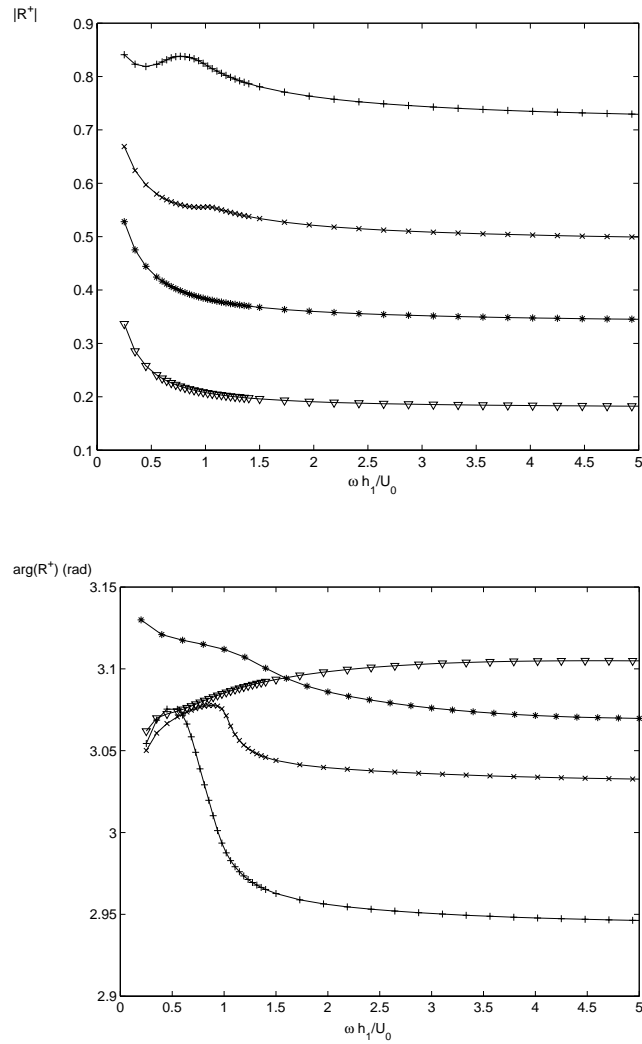
Figure 3.11: Magnitude and phase of the downstream plane wave pressure reflection coefficient R^+ at an area expansion versus Strouhal number $\omega h_1/U_0$ for (partly) uniform flow. Modal analysis calculation with $\omega h_1/c_0 = 0.11$ and $N_1 = 70$. Area expansion ratios are $h_1/h_2 = 0.175$ (+), $h_1/h_2 = 0.35$ ($\times$), $h_1/h_2 = 0.5$ ($*$), and $h_1/h_2 = 0.7$ (∇).

(a) $h_1/h_2 = 0.35$

(b) $h_1/h_2 = 0.5$

Figure 3.12: Wavenumbers of the plane wave acoustic modes, the first six higher order evanescent acoustic modes and the hydrodynamic instability modes for different Strouhal numbers $\omega h_1/U_0$ in case of an infinitely thin shear layer. Dimensionless angular frequency and number of points in duct part with flow are fixed at $\omega h_1/c_0 = 0.11$ respectively $N_1 = 70$. (a) ratio $h_1/h_2 = 0.35$, (b) ratio $h_1/h_2 = 0.5$. Strouhal numbers are between 0.25 ($\times$ markers) and 2 (+ markers), wavenumbers for Strouhal number equal to 1 are indicated by the $*$ markers for all other values by the $\bullet$ markers. Note that for $h_1/h_2 = 0.35$ more points are taken in the vicinity of Strouhal= 1.

modes, the first six higher order evanescent acoustic modes in both directions and the hydrodynamic modes are shown for different Strouhal numbers for $h_1/h_2 = 0.35$ and $h_1/h_2 = 0.5$. Besides the influence of the expansion ratio on the hydrodynamic modes, discussed above, also the acoustic modes are strongly affected by the expansion ratio. Moving from $h_1/h_2 = 0.5$ to $h_1/h_2 = 0.35$ the imaginary part of the wavenumber of the evanescent acoustic modes decreases, which means they are less damped. Also for some evanescent acoustic modes the real part of the wavenumber (related to the the phase velocity) becomes significant. A clear maximum in the real part of the wavenumber of the first evanescent acoustic mode is seen around a Strouhal number of 1.

non-uniform flow

Similarly, the jump seen in the reflection and transmission coefficients for non-uniform flow, cf. figures 3.4 through 3.7, is connected to the behaviour of the modes' wavenumbers as function of the area expansion ratio. For the flow profile, given by equation (3.13), with $f_{int} = 0$ (no velocity jump in the shear layer) and $m = 10$, the wavenumbers of the modes in downstream duct 2 for several Strouhal numbers $\omega h_1/U_0$ are shown in figure 3.13 for expansion ratios $h_1/h_2 = 0.35$ and $h_1/h_2 = 0.5$. For Strouhal number around 1 the wavenumbers of the first higher order evanescent acoustic modes and the hydrodynamic instability modes are very close for the $h_1/h_2 = 0.35$ case compared to the $h_1/h_2 = 0.5$ case. At first sight the traces of the wavenumbers as function of Strouhal number for these modes seem to be well distinguishable for $h_1/h_2 = 0.35$. However, for low Strouhal number the wavenumber of the hydrodynamic instability mode is expected to tend to zero, while for higher Strouhal number at least the real part of the wavenumber is expected to be large compared to the wavenumber of the first higher order evanescent acoustic mode. This would be in contradiction with the two supposed traces of the wavenumbers of these modes. Causality analysis for the modes, cf. section 2.6, indicates that indeed a 'jump' occurs between the first higher order evanescent acoustic mode and the hydrodynamic unstable mode at a certain Strouhal number. Remarkably, according to the Briggs-Bers formalism the jump accors between Strouhal number $\omega h_1/U_0 = 1.047$ and $\omega h_1/U_0 = 1.048$, whereas the Crighton-Leppington formalism indicates the jump between Strouhal number $\omega h_1/U_0 = 1.048$ and $\omega h_1/U_0 = 1.049$, see figures 3.14 and 3.15 respectively. The traces entering the pictures from the right originate in the lower complex plane, while the traces entering from the left originate in the upper complex plane. This leads to the given classification of the modes. The pressure disturbance $P(y)$ of the two modes is shown in figure 3.16 for Strouhal number 1.047. For Strouhal numbers 1.048 and 1.049, where the jump from hydrodynamic unstable to acoustic evanescent and vice versa has occured (depending on causality criterium formalism), the modes stay virtually the same. Clearly, the two modes are very similar, and a distinction on basis of their shape could not readily be made.
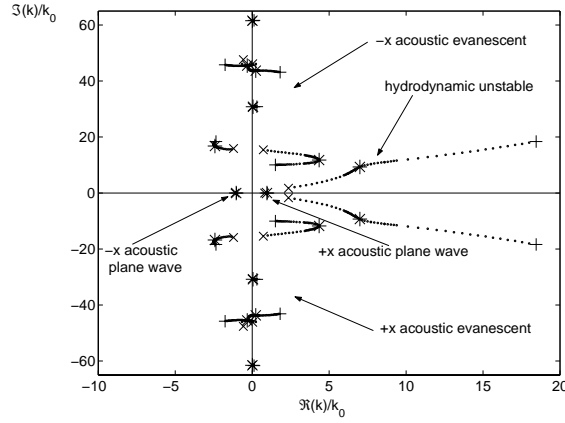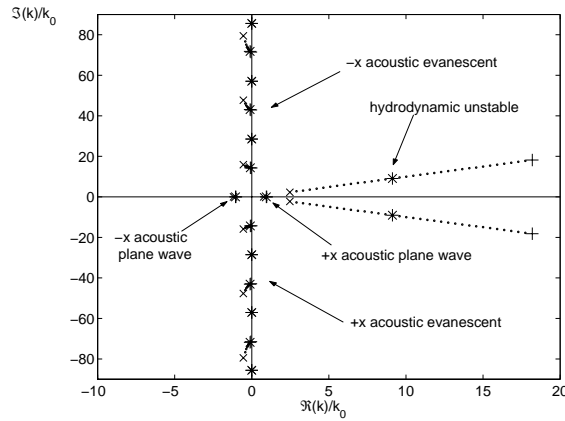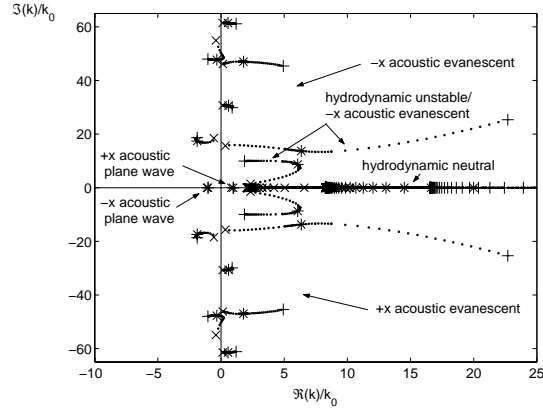
(a) $h_1/h_2 = 0.35$
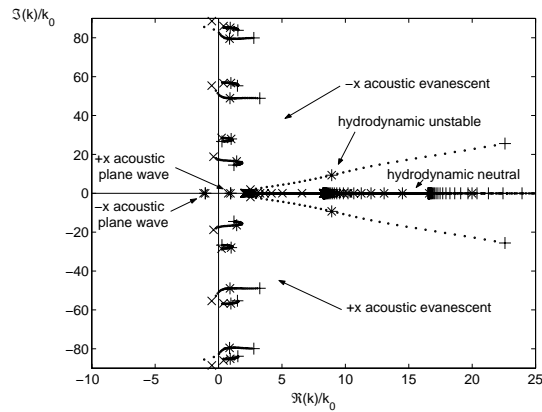
(b) $h_1/h_2 = 0.5$

Figure 3.13: Wavenumbers of the plane wave acoustic modes, the first six higher order evanescent acoustic modes, hydrodynamic instability modes and neutral hydrodynamic modes for different Strouhal numbers $\omega h_1/U_0$ in case of partly non-uniform flow. Flow profile is as given by equation (3.13) with $f_{int} = 0$ and $m = 10$. Dimensionless angular frequency and number of points in duct part with flow are fixed at $\omega h_1/c_0 = 0.11$ respectively $N_1 = 70$. (a) ratio $h_1/h_2 = 0.35$, (b) ratio $h_1/h_2 = 0.5$. Strouhal numbers are between 0.25 ($\times$ markers) and 2 ($+$ markers), wavenumbers for Strouhal number equal to 1 are indicated by the $*$ markers, and for all other values by the $\cdot$ markers. Note that for $h_1/h_2 = 0.35$ more points are taken in the vicinity of Strouhal= 1.
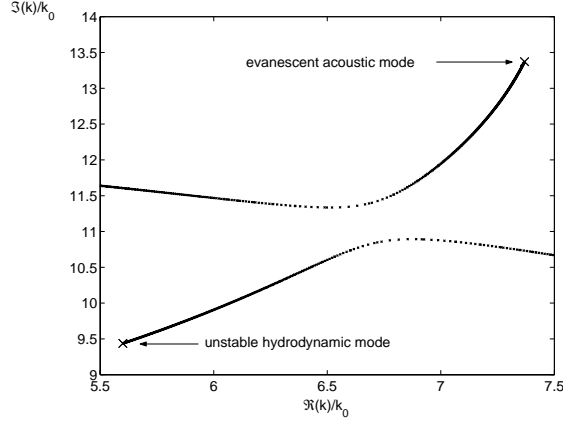
(a) $\omega h_1/U_0 = 1.047$
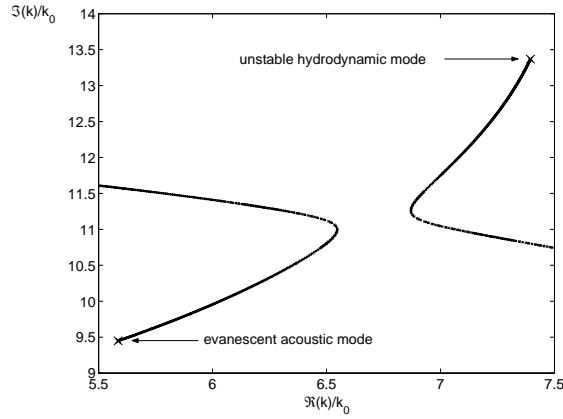
(b) $\omega h_1/U_0 = 1.048$

Figure 3.14: Briggs-Bers causality analysis (see section 2.6) for the first evanescent acoustic mode and the hydrodynamic instability mode for Strouhal numbers $\omega h_1/U_0 = 1.047$ (a) and $\omega h_1/U_0 = 1.048$ (b) for partly non-unform flow with $h_1/h_2 = 0.35$. Flow profile is as given by equation (3.13) with $f_{int} = 0$ and $m = 10$. Number of points in duct are $N_1 = 70$ and $N_2 = 200$. Values for final real dimensionless angular frequency $\omega h_1/c_0 = 0.11$ are indicated by the large $\times$ markers. A 'jump' between the two modes occurs.
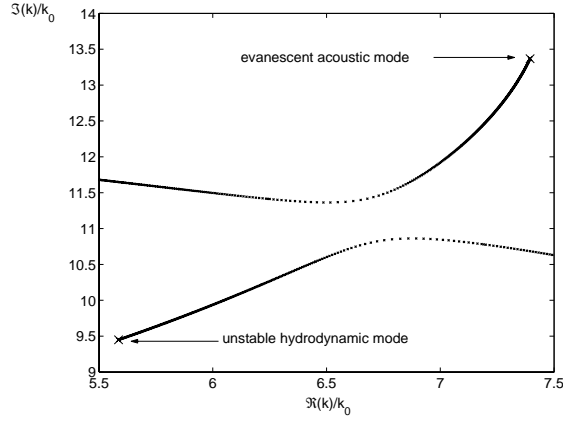
(a) $\omega h_1/U_0 = 1.048$
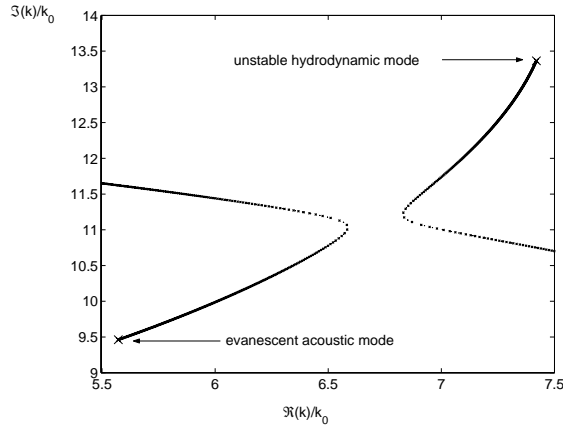
(b) $\omega h_1/U_0 = 1.049$

Figure 3.15: Crighton-Leppington causality analysis (see section 2.6) for the first evanescent acoustic mode and the hydrodynamic instability mode for Strouhal numbers $\omega h_1/U_0 = 1.048$ (a) and $\omega h_1/U_0 = 1.049$ (b) for partly non-unform flow with $h_1/h_2 = 0.35$. Flow profile is as given by equation (3.13) with $f_{int} = 0$ and $m = 10$. Number of points in duct are $N_1 = 70$ and $N_2 = 200$. Values for final real dimensionless angular frequency $\omega h_1/c_0 = 0.11$ are indicated by the large $\times$ markers. A 'jump' between the two modes occurs.
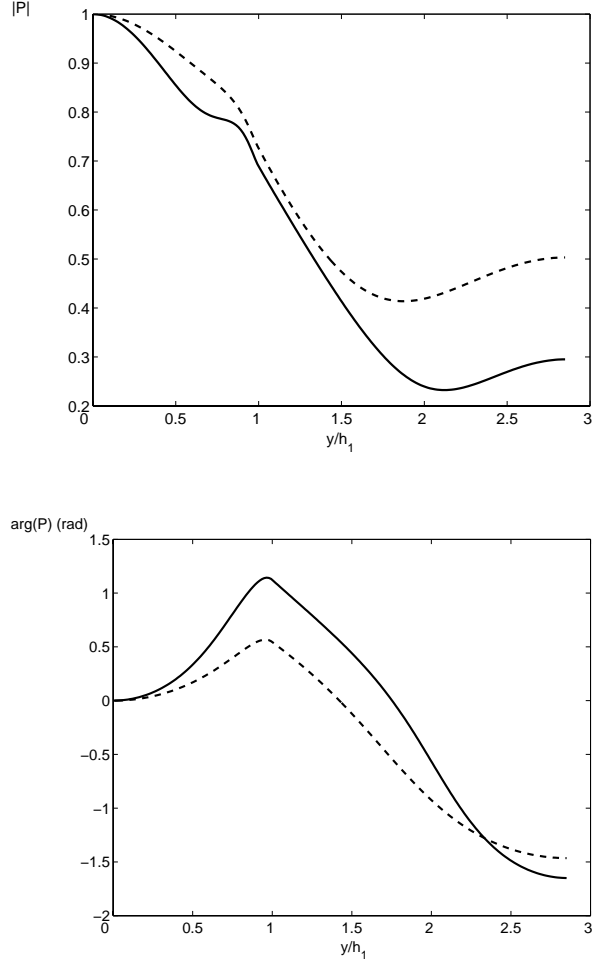
Figure 3.16: Absolute value and phase for the pressure disturbance $P(y)$ of the two modes with wavenumber $k/k_0 \approx 5.60 + 9.44i$ (dashed line) and $k/k_0 = 7.37 + 13.37i$ (solid line), which jump from hydrodynamic unstable to acoustic evenescent and vice versa. Absolute value and phase at the first discrete point are scaled to unity respectively set at zero. Strouhal number is $\omega h_1/U_0 = 1.047$, dimensionless angular frequency $\omega h_1/c_0 = 0.11$. For Strouhal numbers 1.048 and 1.049 the modes are virtually the same. Flow profile is as given by equation (3.13) with $f_{int} = 0$ and $m = 10$. Number of points in duct are $N_1 = 70$ and $N_2 = 200$.

The jump between acoustic evanescent and hydrodynamic unstable mode coincides with the jump in reflection and transmission coefficients, which occurs at the same Strouhal number, already seen in figures 3.4 through 3.7. The result for the downstream reflection coefficient R^+ for expansion ratio $h_1/h_2 = 0.35$ is again shown in figure 3.17 together with the result for $h_1/h_2 = 0.5$. The Crighton-Leppington causality analysis is utilized, giving a jump in both magnitude and phase of the reflection coefficient between Strouhal number $\omega h_1/U_0 = 1.048$ and $\omega h_1/U_0 = 1.049$. Using the Briggs-Bers causality analysis gives the same results, only the jump occurs between $\omega h_1/U_0 = 1.047$ and $\omega h_1/U_0 = 1.048$. For expansion ratio $h_1/h_2 = 0.5$ no jump occurs between the first acoustic evanescent and hydrodynamic unstable mode, and consequently no jump in reflection coefficient is observed, although a hump can be seen in the phase of the reflection coefficient around Strouhal number 1. This was also seen for an infinitely thin shear layer at the same expansion ratio, cf. figure 3.11.

3.4 Cartesian and cylindrical geometry

Boij and Nilsson [16, 17] presented a model for scattering at an area expansion in a two-dimensional rectangular duct. They proposed a scaling between two-dimensional rectangular and two-dimensional cylindrical geometry, such that comparison with experimental data of Ronneberger [97, 100], obtained for an expansion in a cylindrical duct, could be made. In this section modal analysis calculations for an area expansion in both two-dimensional rectangular and two-dimensional cylindrical geometry will be compared, in order to test the proposed scaling.

3.4.1 Scaling of the Helmholtz number

In order to compare their theoretical predictions for an expansion in a two-dimensional rectangular duct with the experimental data of Ronneberger [97, 100] for an expansion in a cylindrical duct, Boij and Nilsson [16, 17] proposed a scaling of the Helmholtz number. For low frequencies well below the cut-on of the first higher order acoustic mode, only a plane wave is incident on the area expansion. For cylindrical geometry the incident sound pressure field is thus independent of the angular coordinate, and consequently higher order modes which are only dependent on the radial coordinate (radial modes) will be excited at the expansion. From this they reasoned that the area expansion in a cylindrical duct can be considered to be a two-dimensional problem, and hence can be related to their theory for a two-dimensional rectangular duct. Furthermore, they argued that the predominant feature is the onset of higher order modes in the large duct downstream of the expansion. For low frequency the wavelength is much larger than the transverse dimension of the duct, such that geometrical details will not be resolved by the sound field. The plane wave scattering at the area expansion would therefore be reasonably similar for a rectangular and a cylindrical

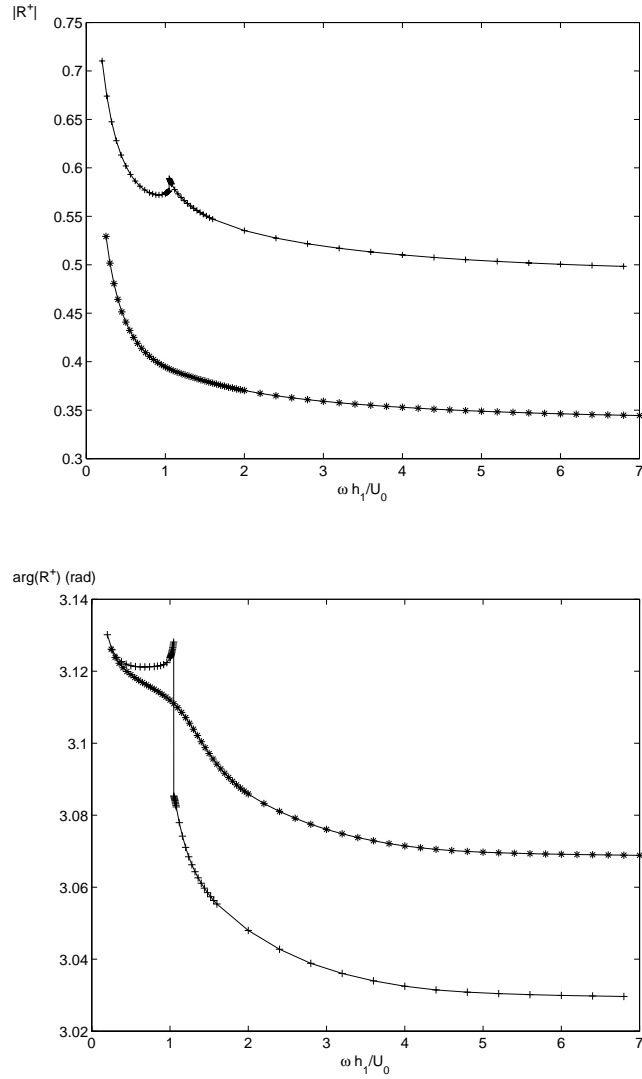Figure 3.17: Magnitude and phase of the downstream plane wave pressure reflection coefficient R^+ at an area expansion against Strouhal number $\omega h_1/U_0$ for partly non-uniform flow. Flow profile is as given by equation (3.13) with $f_{int} = 0$ and $m = 10$. Modal analysis calculation with $\omega h_1/c_0 = 0.11$ and $N_1 = 70$. Area expansion ratios are $h_1/h_2 = 0.35$ ($\times$) and $h_1/h_2 = 0.5$ ($*$).

duct if the expansion ratio is the same, and provided that the frequency is normalised by the cut-on frequency of the first higher order mode in the downstream duct. This leads to their definition of the normalized Helmholtz number:

$$He^* = \frac{(k_0 h_2)_{rec}}{(k_0 h_2)_0} = \frac{(k_0 r_2)_{cyl}}{(k_0 r_2)_0}. \tag{3.16}$$

Here $(k_0 h_2)_{rec}$ and $(k_0 r_2)_{cyl}$ are the Helmholtz numbers based on the downstream duct height h_2 and the downstream duct radius r_2 in rectangular and cylindrical geometry respectively. $(k_0 h_2)_0$ and $(k_0 r_2)_0$ are the cut-on Helmholtz numbers for the first higher order mode (without mean flow) for the downstream rectangular and cylindrical duct respectively. They are given by $(k_0 h_2)_0 = \pi$ and $(k_0 r_2)_0 = \kappa_0 \approx 3.832$. The area expansion ratio η is given by:

$$\eta = \frac{h_1}{h_2} = \frac{r_1^2}{r_2^2}, \tag{3.17}$$

with h_1 and r_1 the height respectively radius of the smaller upstream duct. Combining the two equations (3.16,3.17) above gives:

$$He^* = \frac{1}{\eta} \frac{(k_0 h_1)_{rec}}{\pi} = \frac{1}{\sqrt{\eta}} \frac{(k_0 r_1)_{cyl}}{\kappa_0}, \tag{3.18}$$

with $(k_0 h_1)_{rec}$ and $(k_0 r_1)_{cyl}$ the Helmholtz numbers based on the upstream duct height respectively the upstream duct radius in rectangular and cylindrical geometry.

3.4.2 Comparison rectangular and cylindrical calculations

The method to determine the eigenmodes in a two-dimensional rectangular duct, as discussed in the previous chapter, and the related mode matching employed to calculate the scattering at a sudden area expansion in a duct, described above, can easily be extended to a two-dimensional cylindrical geometry with only minor changes. Details are given in appendix E. Mode matching is the same as for rectangular geometry, see section 3.2.

Calculations for an area expansion in both a two-dimensional rectangular duct and a two-dimensional cylindrical duct with uniform mean flow (infinitely thin shear layer) have been carried out for expansion ratios $\eta = 0.33$ and $\eta = 0.5$. For $\eta = 0.33$ the Helmholtz numbers on the duct heights in the rectangular geometry are $k_0 h_1 = 0.1$ and $k_0 h_2 = 0.3$, and the number of points is $N_1 = 70$ respectively $N_2 = 210$. For the cylindrical geometry the Helmholtz numbers on the duct radii are $k_0 r_1 = 0.2113$ and $k_0 r_2 = 0.3652$, and number of points is $N_1 = 70$ and $N_2 = 121$ respectively. The normalized Helmholtz number, eq.(3.18), for both geometries is $He^* = 0.095$. For the expansion ratio $\eta = 0.5$ we have $k_0 h_1 = 0.1$, $k_0 h_2 = 0.2$, $N_1 = 70$, $N_2 = 140$

for rectangular geometry and $k_0 r_1 = 0.1725$, $k_0 r_2 = 0.2440$, $N_1 = 70$ and $N_2 = 99$ for cylindrical geometry. Normalized Helmholtz number is $He^* = 0.064$. Figure 3.18 shows the absolute values of the reflection and transmission coefficients versus Mach number M for the two area expansion ratios for both rectangular and cylindrical geometry. The relative deviation in absolute value of the reflection and transmission coefficients between the rectangular and cylindrical calculations is given in figure 3.19 for both expansion ratios. The relative deviation is defined as:

$$\left| \frac{|R^+|_{rec} - |R^+|_{cyl}}{|R^+|_{rec}} \right|,$$

etcetera. Generally, for both expansion ratios the results of the rectangular and cylindrical calculations are reasonably close, cf. figure 3.18. Around Mach number $M = 0.1$, corresponding to a Strouhal number $\omega h_1 / U_0 = 1$, a hump in reflection and transmission coefficients is seen, especially for $|R^+|$ and $|T^-|$, for the rectangular calculations with expansion ratio $\eta = 0.33$. This feature is an effect of the area expansion ratio h_1/h_2, as discussed above section 3.3.2. However, in the cylindrical calculations it is not observed (as strongly). This results in a relatively large deviation, especially for $|R^+|$ and $|T^-|$, around Mach number $M = 0.1$, cf. figure 3.19. Also, for expansion ratio $\eta = 0.5$ an increased relative deviation is found around Mach number $M = 0.1$, although it is about 5 times smaller than for $\eta = 0.33$. The relative deviation in the magnitude of the upstream reflection and transmission coefficients, R^- and T^-, increases with mean flow velocity for higher Mach numbers, whereas for the downstream reflection and transmission coefficients, R^+ and T^+ the deviation in magnitude remains relatively small.

3.4.3 Influence of ratio of duct radii

For equal area expansion ratio, $\eta = h_1/h_2 = r_1^2/r_2^2$, results for reflection and transmission coefficients display a deviation when calculated for rectangular or cylindrical geometry, cf. figure 3.18 and 3.19. Specifically a hump in R^+ and T^- is seen around a Strouhal number of 1 for the rectangular geometry. Figure 3.11 indicates that this feature only occurs for ratios h_1/h_2 less than 0.5. In comparing the rectangular and cylindrical geometry calculations, figure 3.18 and 3.19, the lowest value for the expansion ratio is $\eta = 0.33$. This yields a ratio of duct heights in rectangular geometry of $h_1/h_2 = 0.33$ and a much larger ratio of duct radii in cylindrical geometry of $r_1/r_2 = 0.57$. The behaviour of reflection and transmission coefficients for some other different ratios of r_1/r_2 is shown in figure 3.20 in case of uniform mean flow. As for rectangular geometry with ratio of duct heights h_1/h_2 less than 0.5, cf.figure 3.18, a hump in the magnitude of downstream reflection coefficient R^+ and upstream transmission coefficient T^- is seen around Mach number $M = 0.05$ for ratio of radii r_1/r_2 less than 0.5. This feature, which is connected to the behaviour of the modes in section
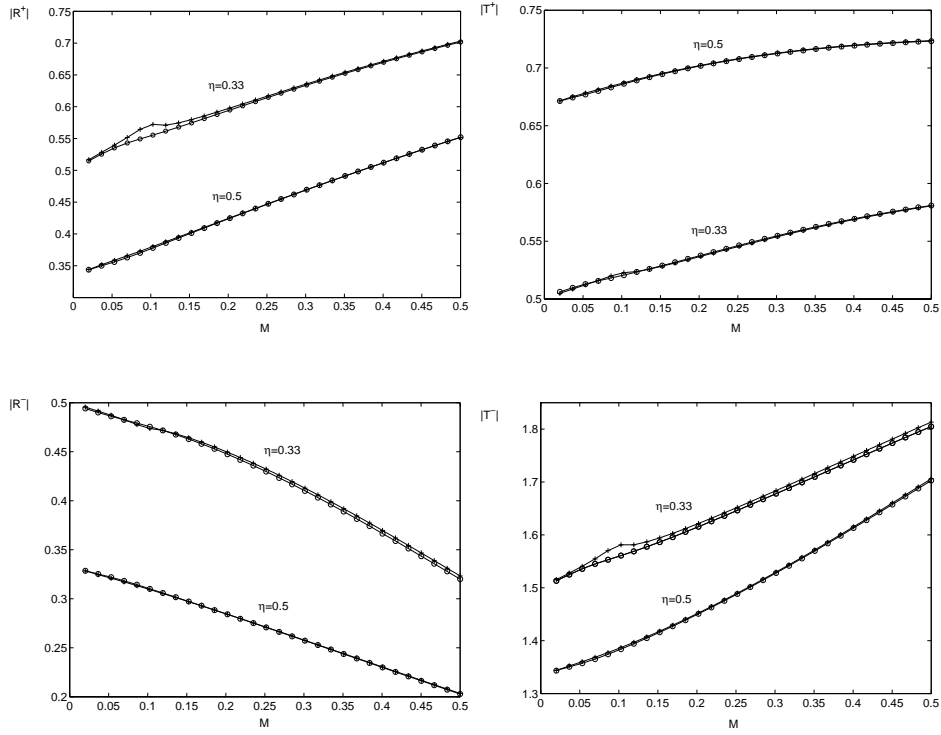
Figure 3.18: Absolute values of the reflection and transmission coefficients versus Mach number M for rectangular geometry ($+$ markers) and cylindrical geometry ($\circ$ markers) for two area expansion ratios η in case of an infinitely thin shear layer. For $\eta = 0.33$: $He^* = 0.095$, $k_0 h_1 = 0.1$, $k_0 h_2 = 0.3$, $k_0 r_1 = 0.2113$, $k_0 r_2 = 0.3652$, $N_1 = 70$, and $N_2 = 210$ respectively $N_2 = 121$ for rectangular and cylindrical geometry. For $\eta = 0.5$: $He^* = 0.064$, $k_0 h_1 = 0.1$, $k_0 h_2 = 0.2$, $k_0 r_1 = 0.1725$, $k_0 r_2 = 0.2440$, $N_1 = 70$, and $N_2 = 140$ respectively $N_2 = 99$ for rectangular and cylindrical geometry.

(a) $\eta = 0.33$ (b) $\eta = 0.5$
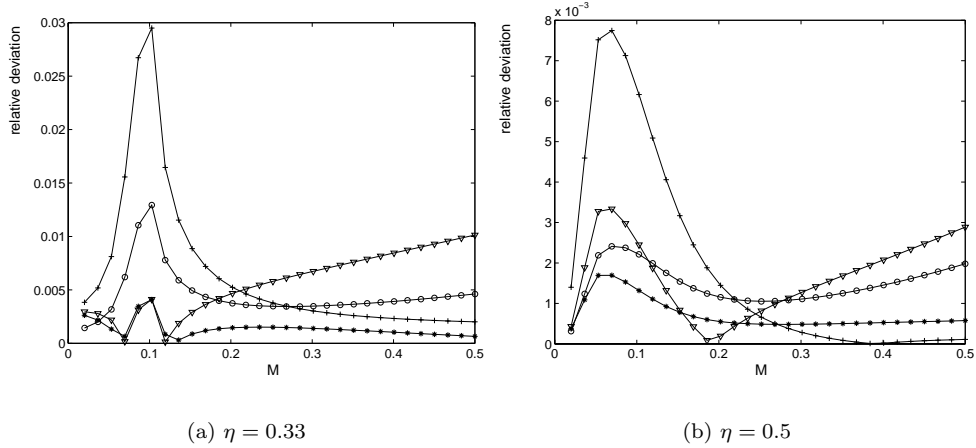
Figure 3.19: Relative deviation in $|R^+|$ (+ markers), $|T^+|$ (∗ markers), $|R^-|$ (∇ markers) and $|T^-|$ (∘ markers) when comparing calculations for rectangular and cylindrical geometry, cf. figure 3.18, for expansion ratio $\eta = 0.33$ (a) and $\eta = 0.5$ (b).

3.3.2, thus depends in the same manner on the ratio of duct heights for rectangular geometry respectively duct radii for cylindrical geometry.

3.5 Comparison with an alternative model and experimental data

Boij and Nilsson [16, 17] presented a model for scattering at an area expansion in a two-dimensional rectangular duct with uniform mean flow based on the Wiener-Hopf technique. Results were compared to experimental data of Ronneberger [97, 100] for a cylindrical pipe using the Helmholtz scaling discussed above in section 3.4.1. In the experiments of Ronneberger the pipe radius upstream of the expansion is $r_1 = 25$ mm, the pipe radius downstream of the expansion is $r_2 = 42.5$ mm. This yields an area expansion ratio of $\eta = 0.35$. Measurements are done at various frequencies and Mach numbers. Here, we will compare with the experiments, and corresponding model calculations of Boij and Nilsson, for which the frequency is $f = 500$ Hz. This gives a Helmholtz number on the upstream duct radius of $k_0 r_1 = 0.227$ and a normalized Helmholtz number $He^* = 0.10$. For the rectangular geometry this yields a Helmholtz number on the upstream duct height of $k_0 h_1 = 0.11$.

Figure 3.21 shows the absolute value and phase of the downstream reflection coefficient, R^+, for the above configuration in a rectangular duct calculated by the modal analysis method with number of points $N_1 = 70$ and $N_2 = 200$, as well as obtained by Boij and Nilsson [17]. The absolute value of the downstream transmission coefficient, T^+, calculated by the two models is given in figure 3.22. The results of the two models are very similar. In particular, both show the hump in reflection and transmission around Strouhal number 1. For the phase of R^+ no significant difference is
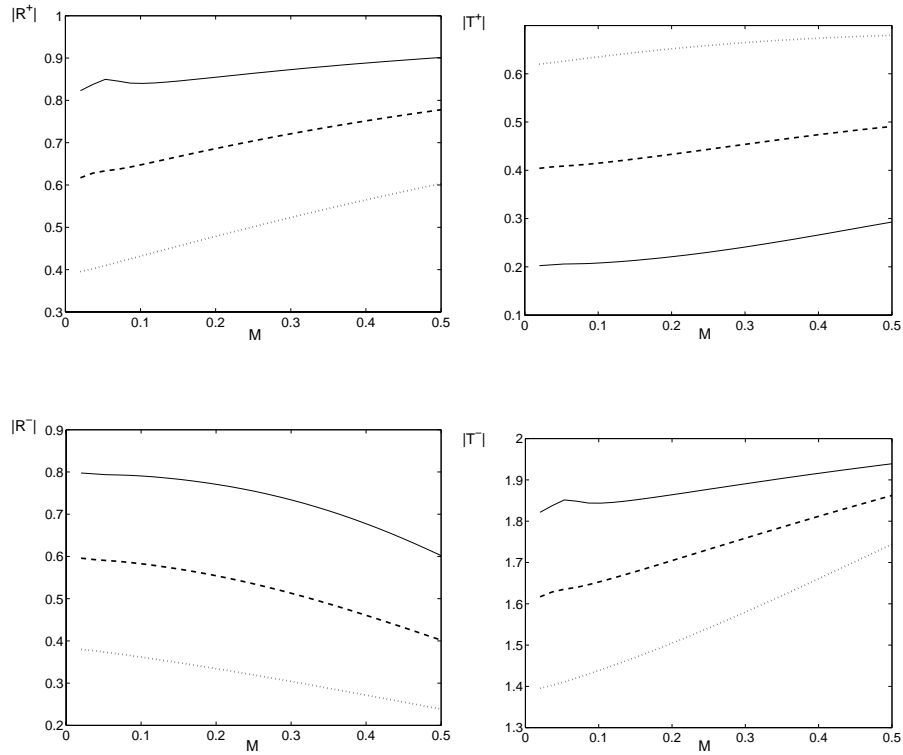
Figure 3.20: Absolute value of reflection and transmission coefficients at an area expansion in a two-dimensional cylindrical geometry for uniform mean flow versus Mach number M for different ratios r_1/r_2 of duct radii upstream and downstream of the expansion. Helmholtz number on upstream duct radius is $k_0 r_1 = 0.1$, number of points in upstream duct is $N_1 = 70$. Dotted lines: $r_1/r_2 = 0.67$ ($N_2 = 105$), dashed lines: $r_1/r_2 = 0.5$ ($N_2 = 140$), solid lines: $r_1/r_2 = 0.35$ ($N_2 = 200$).
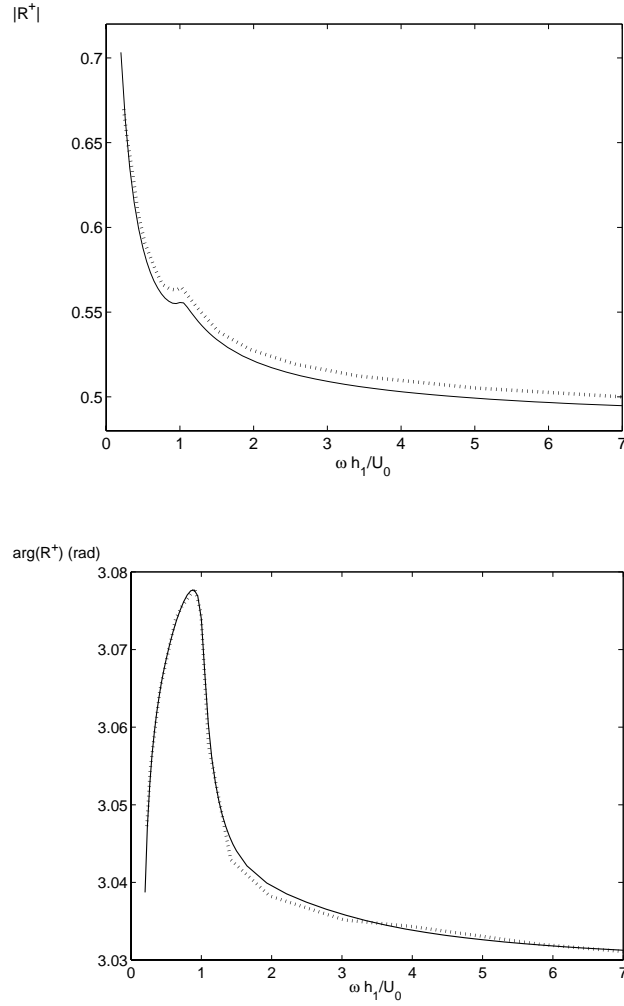
Figure 3.21: Magnitude and phase of the downstream reflection coefficient R^+ at an area expansion in a two-dimensional rectangular duct with uniform flow versus Strouhal number. Helmholtz number on upstream duct height: $k_0 h_1 = 0.11$, area expansion ratio: $\eta = h_1/h_2 = 0.35$, normalized Helmholtz number: $He^* = 0.10$. Solid lines: results of modal analysis method ($N_1 = 70$, $N_2 = 200$). Dotted lines: fit of Boij and Nilsson's result [16, 17]. Quasi-stationary limit without mean flow is: $R^+ = -0.4815$.
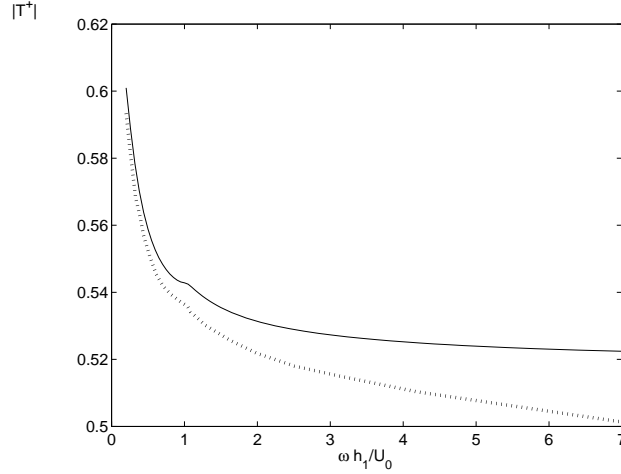
Figure 3.22: Absolute value of the downstream transmission coefficient T^+ at an area expansion in a two-dimensional rectangular duct with uniform flow versus Strouhal number. Helmholtz number on upstream duct height: $k_0 h_1 = 0.11$, area expansion ratio: $\eta = h_1/h_2 = 0.35$, normalized Helmholtz number: $He^* = 0.10$. Solid lines: results of modal analysis method ($N_1 = 70$, $N_2 = 200$). Dotted lines: fit of Boij and Nilsson's result [17]. Quasi-stationary limit without mean flow is: $T^+ = 0.5185$.

seen between the two models (The difference seen in the graph is due to the error in extracting the data from reference [16]). Nevertheless, a deviation in the results for the absolute values is seen. Generally, the mode matching method gives a lower absolute value for the reflection coefficient and a higher one for the transmission coefficient than Boij and Nilsson's model. For the absolute value of the reflection coefficient the deviation between the two models is fairly constant at about 1%, at least above a Strouhal number of ~ 0.5. The absolute value of the transmission coefficient displays a larger deviation, it increases from about 1% for low Strouhal number to about 4% for high Strouhal number.

In comparing model results with experimental data, particularly the effect of introducing a non-uniform mean flow will be investigated. The flow profile in the upstream tube in Ronneberger's experiments can be assumed to obey the empirical power law for turbulent pipe flow as given by Schlichting [102], such that we have:

$$f(r) = \begin{cases} \frac{(2m+1)(m+1)}{2m^2}\left(1 - \frac{r}{r_1}\right)^{\frac{1}{m}} & 0 \le y \le r_1, \\ \\ 0 & r_1 < y \le r_2 \end{cases} . \tag{3.19}$$

The value of the profile function $f(r)$ averaged over the upstream pipe area πr_1^2 equals unity. the Mach number as function of radius is given by: $M(r) = M_0 f(r)$, such that M_0 is the area averaged Mach number in the upstream pipe. The profile parameter m varies with Reynolds number Re on the pipe diameter and the average mean flow velocity:

$$Re = \frac{2r_1 U_0}{\nu},\qquad(3.20)$$

with $U_0 = M_0 c_0$ and ν the kinematic viscosity. For air at room temperature and atmospheric pressure $\nu = 1.5 \cdot 10^{-5}$ m^{2}s^{-1}. Values for m at different Reynolds numbers are given in table 3.1. For the measurements with mean flow the Mach numbers are in the range of $M_0 \approx 0.018$ to $M_0 \approx 0.45$. The upstream pipe radius is $r_1 = 2.5 \cdot 10^{-2}$ m. This gives values for the Reynolds number in the range $Re \approx 2.1 \cdot 10^4$ to $Re \approx 5.1 \cdot 10^5$. Consequently, the profile parameter will be between $m \approx 6.5$ for low Mach number and $m \approx 7.7$ for high Mach number. Besides this turbulent profile we consider the profile given by equation (3.13) for rectangular geometry. For cylindrical geometry it is given by:

$$f(r) = \begin{cases} \frac{m+2}{m}\left(1 - \left(\frac{r}{r_1}\right)^m\right) & 0 \leq y \leq r_1 \\ \\ 0 & r_1 < y \leq r_2 \end{cases}\qquad(3.21)$$

Also here the average of the profile function over the upstream pipe area equals unity. This profile is close to laminar. Figures 3.23 through 3.26 show the experimental data of Ronneberger [100] for the downstream and upstream reflection and transmission coefficients at the area expansion with the above given configuration. The results are plotted versus the Strouhal number based on the equivalent upstream duct height h_1 in rectangular geometry. On basis of the representation of the data in reference [100], the error in the magnitudes and phases is estimated at ± 0.01 and ± 0.04 ($\approx \pm 0.01\pi$) respectively. The figures also show results of mode matching calculations for cylindrical geometry with uniform mean flow as well as with the turbulent flow profile, eq.(3.19), with $m = 7$, and the flow profile of eq.(3.21) with $m = 15$. These latter two non-uniform profiles are plotted in figure 3.27. The number of points in the mode matching calculations is $N_1 = 118$ and $N_2 = 200$. If applicable, also the results of Boij and Nilsson are given. The effect of a non-uniform mean flow compared to uniform mean flow on the magnitude of the reflection and transmission coefficients in the mode matching method is opposite for the turbulent pipe flow and the alternative

Table 3.1: Values of profile parameter m for the turbulent pipe flow profile, equation (3.19), as function of Reynolds number Re, given by Schlichting [102].

Re	$4 \cdot 10^3$	$2.3 \cdot 10^4$	$1.1 \cdot 10^5$	$1.1 \cdot 10^6$	$2.0 \cdot 10^6$	$3.2 \cdot 10^6$
m	6.0	6.6	7.0	8.8	10	10

Figure 3.23: Magnitude and phase of downstream reflection coefficient R^+ at an area expansion. Helmholtz number on upstream duct radius: $k_0 r_1 = 0.227$, expansion ratio: $\eta = 0.35$, normalized Helmholtz number: $He^* = 0.10$. On the horizontal axis is the Strouhal number based on the equivalent upstream duct height h_1 in rectangular geometry. $*$ markers: experimental data Ronneberger [100]. Mode matching calculations in cylindrical geometry ($N_1 = 118$, $N_2 = 200$) for: uniform mean flow (solid line), turbulent pipe flow, eq. (3.19), with $m = 7$ (dashed line), and flow profile eq.(3.21) with $m = 15$ (dotted line). Solid line with $\bullet$ markers: fit of Boij and Nilsson's result [16, 17]. Quasi-stationary limit without mean flow is: $R^+ = -0.4815$.

Figure 3.24: Magnitude and phase of downstream transmission coefficient T^+ at an area expansion. Helmholtz number on upstream duct radius: $k_0 r_1 = 0.227$, expansion ration: $\eta = 0.35$, normalized Helmholtz number: $He^* = 0.10$. On the horizontal axis is the Strouhal number based on the equivalent upstream duct height h_1 in rectangular geometry. $*$ markers: experimental data Ronneberger [100]. Mode matching calculations in cylindrical geometry ($N_1 = 118$, $N_2 = 200$) for: uniform mean flow (solid line), turbulent pipe flow, eq. (3.19), with $m = 7$ (dashed line), and flow profile eq.(3.21) with $m = 15$ (dotted line). Solid line with $\bullet$ markers: fit of Boij and Nilsson's result [17]. Quasi-stationary limit without mean flow is: $T^+ = 0.5185$.

Figure 3.25: Magnitude and phase of upstream reflection coefficient R^- at an area expansion. Helmholtz number on upstream duct radius: $k_0 r_1 = 0.227$, expansion ration: $\eta = 0.35$, normalized Helmholtz number: $He^* = 0.10$. On the horizontal axis is the Strouhal number based on the equivalent upstream duct height h_1 in rectangular geometry. $*$ markers: experimental data Ronneberger [100]. Mode matching calculations in cylindrical geometry ($N_1 = 118$, $N_2 = 200$) for: uniform mean flow (solid line), turbulent pipe flow, eq.(3.19), with $m = 7$ (dashed line), and flow profile eq.(3.21) with $m = 15$ (dotted line). Quasi-stationary limit without mean flow is: $R^- = 0.4815$.
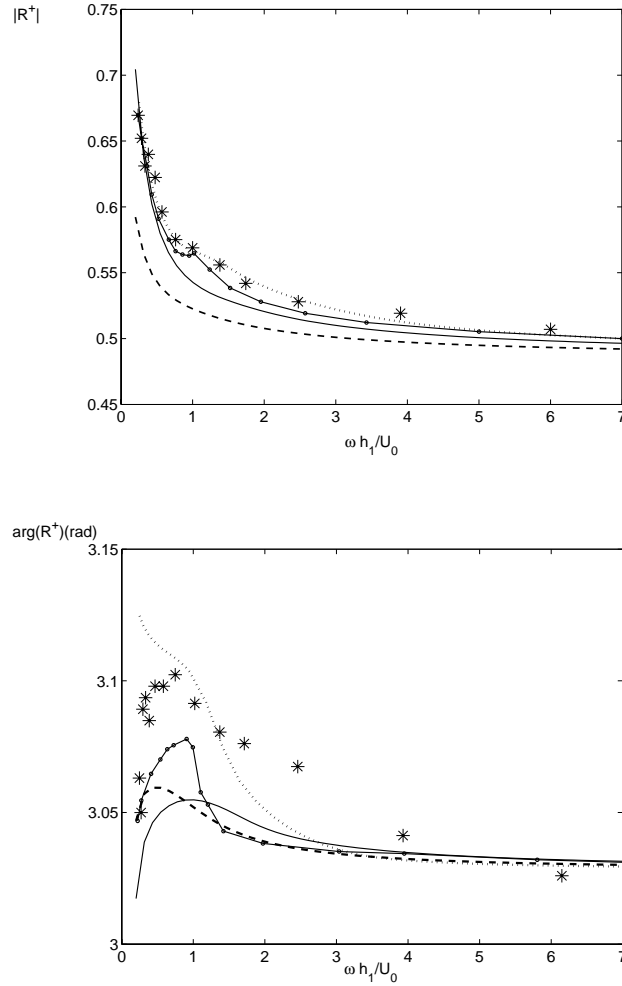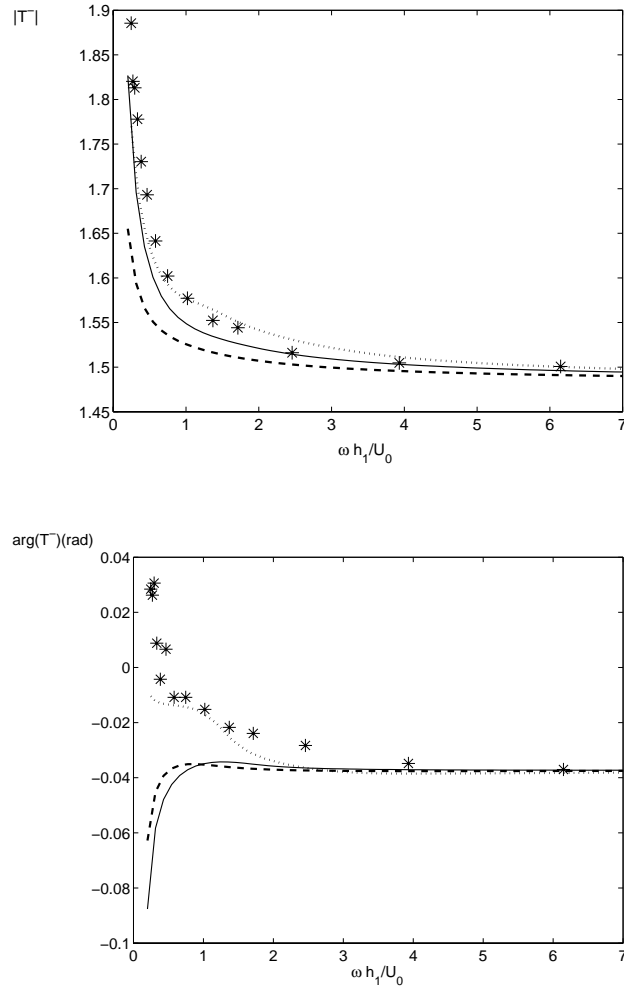
Figure 3.26: Magnitude and phase of upstream transmission coefficient T^- at an area expansion. Helmholtz number on upstream duct radius: $k_0 r_1 = 0.227$, expansion ratio: $\eta = 0.35$, normalized Helmholtz number: $He^* = 0.10$. On the horizontal axis is the Strouhal number based on the equivalent upstream duct height h_1 in rectangular geometry. $*$ markers: experimental data Ronneberger [100]. Mode matching calculations in cylindrical geometry ($N_1 = 118$, $N_2 = 200$) for: uniform mean flow (solid line), turbulent pipe flow, eq.(3.19), with $m = 7$ (dashed line), and flow profile eq.(3.21) with $m = 15$ (dotted line). Quasi-stationary limit without mean flow is: $T^- = 1.4815$.
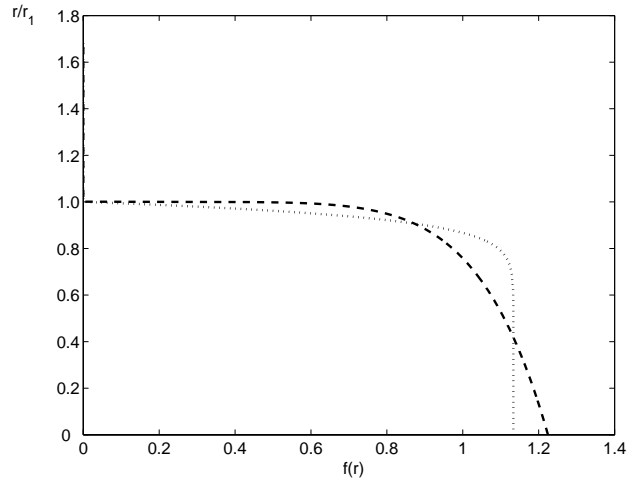
Figure 3.27: Non-uniform flow profiles as used in the mode matching calculations, figures 3.23 through 3.26. Dashed line: turbulent pipe flow, equation (3.19), with parameter $m = 7$. Dotted line: flow profile function, equation (3.21), with $m = 15$.

profile. The magnitudes of R^+, T^+ and T^- decrease when taking the turbulent profile compared to the uniform flow profile, whereas the magnitude of R^- increases. For the alternative non-uniform profile this is exactly opposite. Concerning the phase of the reflection and transmission coefficients the turbulent profile and the alternative non-uniform profile qualitatively have the same effect compared to uniform flow for R^+ and T^-. For the phase of T^+ and R^- the effect is opposite. The flow profile which gives the best fit between mode matching calculations and experimental data varies for the different reflection and transmission coefficients. For the magnitude of R^+ the alternative non-uniform profile clearly gives a better resemblance with experimental data compared to the uniform profile, whereas the turbulent profile gives a worse prediction. For the phase of R^+ the alternative profile seems to give better results for some Strouhal numbers, however the turbulent profile gives the best results for very low Strouhal. The experimental data for the magnitude of the downstream transmission coefficient T^+ is between the mode matching results for uniform flow and turbulent pipe flow. The alternative profile gives worse resemblance compared to uniform flow. The same as for T^+ is more or less seen for the upstream reflection coefficient R^-. Although here, clearly, the turbulent profile gives better resemblance with experiments for the magnitude of R^- at Strouhal numbers larger than 1. The alternative profile gives a worse prediction for both magnitude and phase of R^-. For the upstream transmission coefficient T^- the results for the alternative non-uniform

flow profile are most consistent with experimental data, both for magnitude and phase. The turbulent profile gives a worse prediction at least for the magnitude of T^- compared to the other profiles.

In short, for the magnitudes of R^+ and T^- the calculations with the alternative non-uniform flow profile give a better prediction than those with uniform flow. The calculations with the turbulent flow give a worse prediction. For the magnitudes of T^+ and R^- the calculations with the turbulent flow profile give a slightly better resemblance with experiments than those with uniform flow. The alternative non-uniform profile clearly gives a worse prediction in these cases. For the phase of the reflection and transmission coefficients the result of the calculations are most consistent with experiments for large Strouhal number. Here, the results for the different flow profiles coincide. At low Strouhal numbers the deviation in phase between experiments and calculations is larger. The alternative non-uniform profile seems to give a better prediction in this range than the uniform flow profile, except for R^-.

3.6   Conclusion

In this chapter scattering at a sudden area expansion in a duct carrying mean (sheared) flow has been modelled with a modal analysis method. Here, the pressure and velocity disturbance field are solved as an expansion of eigenmodes both upstream and downstream of the area expansion. Mode matching at the area discontinuity, i.e. demanding continuity of the proper acoustic variables, subsequently gives the scattering matrix, which relates all modes.

The influence of the mean flow profile is examined. Uniform flow, giving an infinitely thin shear layer downstream of the area expansion, non-uniform flow and non-uniform flow with a slip velocity / velocity jump in the shear layer is considered. In the former and latter case a Kutta condition is explicitly applied at the edge of the area discontinuity. It is found that the plane wave scattering coefficients gradually change when the flow profile is gradually changed from uniform to non-uniform through a non-uniform profile with slip. The non-uniform flow case, where no Kutta condition is applied, is thus the limiting case of non-uniform flow with slip velocity, where a Kutta condition is applied, for slip velocity going to zero. The uniform flow case, where neutral hydrodynamic modes vanish, is the maximum slip velocity limit for the case of non-uniform flow with slip velocity. For high Strouhal numbers no difference is seen in the results for the scattering coefficients obtained for different flow profiles.

The comparison of scattering results for two-dimensional rectangular and two-dimensional cylindrical duct geometry with the same area expansion ratio by means of a scaling of the Helmholtz number, as proposed in literature [16], is investigated. Generally, the suggested scaling is found to be useful. However, around a Strouhal number of about unity, specific behaviour of the scattering coefficients is observed

depending on the ratio of duct heights respectively the ratio of duct radii. Since for given area expansion ratio the ratios of duct heights and ratio of duct radii is not the same, a deviation between calculations for the two geometries can be seen. Furthermore, the mentioned effect is found to be connected to the behaviour of the wavenumbers of the first evanescent acoustic mode and the hydrodynamic instability mode. For the incompressible solution, when only hydrodynamic modes are present, this behaviour is also observed. For non-uniform flow the behaviour is, for sufficient low area expansion ratio, related to an exchange between the first evanescent acoustic mode and the hydrodynamic unstable mode around a Strouhal number of 1. Here, the Briggs-Bers and the Crighton-Leppington causality criteria do not exactly agree at which Strouhal number the exchange occurs.

Results for the plane wave scattering coefficients as calculated by modal analysis are fairly consistent with experimental data from literature [100] for an area expansion in a cylindrical pipe. Taking a turbulent pipe flow profile in the calculations yields a better agreement compared to a uniform flow profile for the downstream transmission and the upstream reflection coefficient. However, worse agreement is seen for the upstream transmission and downstream reflection coefficient. On the contrary, compared to uniform flow an alternative non-uniform profile, which is close to laminar, gives worse agreement for the downstream transmission and the upstream reflection coefficient, whereas prediction for the other coefficients improves.

Chapter 4

Effect of grazing flow on orifice impedance: experiments

4.1 Introduction

In this chapter an experimental study on the influence of grazing mean flow on the acoustical behaviour of an orifice in a wall will be presented. First, quantities to define the acoustical behaviour, and especially the effect of mean grazing flow on it, are treated. Subsequently, earlier experimental studies found in literature are discussed. A description of the utilized multi-microphone impedance tube set-up, as well as the geometries of the different orifices used are given. Furthermore, a thorough characterization of the grazing mean flow properties is presented. Subsequently, experimental results are given. Linearity of the acoustical behaviour, as well as the influence of mean grazing flow properties and orifice geometry is treated.

4.2 Quantities for the acoustical behaviour of an orifice

The acoustical behaviour of an orifice in a wall can be quantitatively expressed in several ways. The different definitions will be treated below. Furthermore, quantities to describe the effect of grazing flow on the acoustical behaviour of an orifice are given.

Consider an aperture with (Fourier transformed) acoustic pressure disturbances p_+
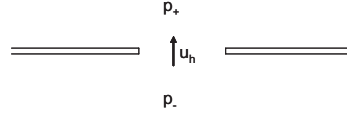
Figure 4.1: Orifice with acoustic pressures p_+ and p_- above respectively beneath. Area averaged acoustic velocity through the orifice is u_h.

and p_- above respectively beneath, see figure 4.1. Local incompressibility is assumed, the acoustic pressure disturbances are thus spatially uniform over the aperture. The area averaged velocity disturbance through the orifice, perpendicular to the wall, is denoted u_h.

Employing an $e^{+i\omega t}$ convention for harmonic disturbances, the Rayleigh conductivity of the aperture can be written as:

$$K_R = i\omega\rho_0 \frac{u_h S_0}{p_- - p_+},\tag{4.1}$$

where S_0 is the aperture area. The equation above is the same as the equation given for the Rayleigh conductivity in appendix A, equation (A.12), except for a different sign. This stems from the fact that, following the treatment of Howe [47], an $e^{-i\omega t}$ harmonic time dependence is used there. Note that the Rayleigh conductivity calculated in an $e^{-i\omega t}$ convention is the complex conjugate of the Rayleigh conductivity calculated in an $e^{+i\omega t}$ convention.

Another quantity to express the acoustic properties of an orifice is the effective length l_{eff}. The approach here is that the complex flow in the orifice region is represented by an equivalent length of the mass of fluid, with volume $S_0 l_{eff}$, which effectively participates in the acoustic motion. The effective length is found by integration of the linearized Euler equation for momentum in the direction perpendicular to the wall, in which the orifice is placed (see e.g. equation (B.4)):

$$l_{eff} = \frac{1}{i\omega\rho_0} \frac{p_- - p_+}{u_h} \quad = \frac{S_0}{K_R}.\tag{4.2}$$

In case the motion is purely reactive, the effective length is real. If also dissipation is present, the effective length will have an imaginary part.

The last -and probably most commonly used- quantity to be discussed here, which represents the acoustical behaviour of an orifice, is the (acoustical) impedance. Non-dimensionalized to the characteristic impedance $\rho_0 c_0$ of the fluid, it is given by:

$$Z_h \equiv \frac{1}{\rho_0 c_0} \frac{p_- - p_+}{u_h} \quad = ik_0 l_{eff} \quad = ik_0 \frac{S_0}{K_R},\tag{4.3}$$

with $k_0 = \omega/c_0$. The impedance can be decomposed in a resistance r and a reactance δ:

$$r = \Re(Z_h),$$
$$\delta = \frac{1}{k_0}\Im(Z_h). \tag{4.4}$$

From equation (4.3) it follows that $\delta = \Re(l_{eff})$, so that indeed δ represents the inertia of the fluid in motion in the aperture. Often the wall thickness of the aperture is subtracted from δ to obtain a quantity referred to as the end correction. Writing the resistance and reactance as function of the Rayleigh conductivity, using equations (4.3) and (4.4), results in:

$$r = -k_0\Im(\frac{S_0}{K_R}),$$
$$\delta = \Re(\frac{S_0}{K_R}). \tag{4.5}$$

Substituting the Rayleigh conductivity for a rectangular slot with uniform grazing flow $U = U_+$ above and U_- beneath the orifice as calculated by Howe, cf. appendix A, more specifically equation (A.13), gives:

$$r = -\frac{k_0 L}{\pi}\Im(2F(Sr,\mu) + \Psi),$$
$$\delta = \frac{L}{\pi}\Re(2F(Sr,\mu) + \Psi),$$

where function $F(Sr,\mu)$ is given by equation (A.14). Furthermore, Sr is the Strouhal number $Sr = \omega L/U$, and μ is the ratio U_-/U_+. Note that also equation (A.10) is used. The quantity Ψ is related to the local approximations of the Green's function on either side of the aperture. It is determined by the geometry surrounding the aperture, and hence does not dependent on the mean flow. On basis of this result Golliard [36] proposed to subtract the resistance respectively reactance without flow, such that for fixed μ:

$$r_{flow} = r - r_{U=0} = -\frac{2k_0 L}{\pi}\Im(F(Sr) - F_{U=0}),$$
$$\delta_{flow} = \delta - \delta_{U=0} = \frac{2L}{\pi}\Re(F(Sr) - F_{U=0}).$$

Here, $F_{U=0}$ is the value of function F in case mean grazing flow velocity is zero. Note that $F_{U=0}$ differs from the value of $F(Sr,\mu)$ obtained for $Sr \to \infty$: $F_{U=0} = 0$, $F(Sr,\mu)|_{Sr\to\infty} = -2$. Subsequently, dividing r_{flow} and δ_{flow} by the Mach number

$M = U/c_0$ respectively the slit width L gives the non-dimensional scaled resistance and reactance due to the flow:

$$\tilde{r}_{flow} = \frac{r_{flow}}{M} = -\frac{2Sr}{\pi}\Im(F(Sr) - F_{U=0}),$$

$$\tilde{\delta}_{flow} = \frac{\delta_{flow}}{L} = \frac{2}{\pi}\Re(F(Sr) - F_{U=0}).$$

According to the theory of Howe, these quantities thus solely depend on the Strouhal number and are independent of the geometry surrounding the orifice.

Following the derivation above, in terms of the impedance the non-dimensional scaled resistance and reactance due to the flow are given by:

$$\tilde{r}_{flow} = \frac{1}{M}(\Re(Z_h) - \Re(Z_{h,U=0})),$$

$$\tilde{\delta}_{flow} = \frac{1}{k_0 L}(\Im(Z_h) - \Im(Z_{h,U=0})). \qquad (4.6)$$

The acoustic pressure p_+ above the orifice equals the radiation pressure p_{rad}. The effect of grazing flow on this radiation pressure was argued to be very small for Mach numbers below 0.2 [36]. Therefore in calculating the non-dimensional scaled resistance and reactance just as well a 'one-sided' orifice impedance Z_{h-} can be used:

$$Z_{h-} = \frac{1}{\rho_0 c_0}\frac{p_-}{u_h},$$

$$\tilde{r}_{flow} = \frac{1}{M}(\Re(Z_{h-}) - \Re(Z_{h-,U=0})), \qquad (4.7)$$

$$\tilde{\delta}_{flow} = \frac{1}{k_0 L}(\Im(Z_{h-}) - \Im(Z_{h-,U=0})).$$

In the following these quantities will sometimes simply be called resistance and reactance for convenience. From context it will be clear that actually the scaled versions $\tilde{r}_{flow}$ and $\tilde{\delta}_{flow}$ are meant.

4.3   Previous experimental studies

The effect of grazing flow on the acoustical impedance of orifices has been investigated experimentally by numerous authors, see e.g. ref. [25, 27, 34, 35, 36, 40, 52, 57, 58, 60, 65, 86, 98, 113].

Most of these studies are related to acoustic liners, which are used for sound absorption in exhaust systems of combustion engines and at jet engine inlets and outlets [72]. These liners consist of perforated plates backed with honeycomb structures, forming an array of Helmholtz resonators. Additionally, these arrays can be stacked

in two or three layers to obtain double Degree Of Freedom (DOF) respectively triple DOF liners.

Most of the investigations therefore concentrate on the working domain of these liners, i.e. at low Strouhal numbers and thick boundary layers. Results are often summarized in empirical laws. Generally, above a certain grazing flow velocity the resistance is found to increase, improving sound absorption, whereas the reactance decreases.

Goldman and Panton [34], Kooi and Sarin [57], Goldman and Chung [35], Cummings [25] and Kirby and Cummings [52] performed experiments with circular orifices (and louvres [52]) at low Strouhal numbers. The thickness of the turbulent boundary layers they had was several times the orifice diameter. On basis of the results empirical formulae or scaling variables were given for resistance and reactance. In all cases the influence of the boundary layer is translated into a dependence on the friction velocity. In reference [35] it is even stated that outer boundary layer parameters, such as the boundary layer thickness, have no influence on the acoustical properties. Cummings [25] also recognized the influence of the level of boundary layer turbulence.

More recently similar experiments were done by e.g. Dickey and Selamet [27], Malmary and Carbonne [65], and Seong-Hyun Lee and Jeong-Guon Ih [60]. In ref. [27] the use of a single set of empirical expressions for different (types of) perforates was strongly questioned. Malmary and Carbonne [65] compared their results with the empirical model given by Kirby and Cummings [52]. They found it to be valid up to a Mach number of 0.6, although it originally was derived for Mach numbers up to 0.2. They also showed the discrepancy between different empirical models from literature (among which those presented in ref. [25, 52, 57]). It was discussed that this discrepancy, besides the fact that some models do not consider boundary layer characteristics, are due to differences in experimental techniques and geometries used. Seong-Hyun Lee and Jeong-Guon Ih [60] presented an empirical model based on their experiments, which was argued to yield a better prediction of orifice impedance than other models from literature. However, strangely, they did not address the influence of boundary layer characteristics.

Ronneberger [98] measured the effect of grazing flow on the impedance of circular and oblong orifices. The boundary layer thickness, although not measured, was small (in the order of 1 percent of the aperture radius). He proposed an analytical model with 'considerable simplifications', which however qualitatively predicted his experimental results well. Furthermore, he reasoned that boundary layer characteristics must have influence, and he limited the validity of his model to the regime of small boundary layer thickness compared to orifice dimensions. In a later paper [99] Ronneberger questions his model more, especially in the higher Strouhal number range.

Golliard [36] performed experiments with rectangular slots in a 2 microphone impedance tube set-up. Measurements were done for different turbulent boundary
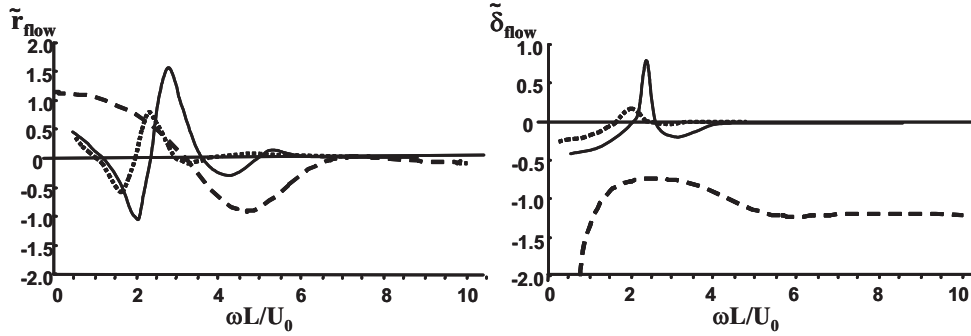
Figure 4.2: Sketch of experimental results obtained by Golliard [36] for the non-dimensional scaled resistance $\tilde{r}_{flow}$ and -reactance $\tilde{\delta}_{flow}$ versus Strouhal number $\omega L/U_0$ in case of a turbulent boundary layer with momentum thickness to slit width ratio $\theta/L = 0.079$ (solid line) respectively $\theta/L = 0.29$ (dotted line). Also the theoretical prediction of Howe [47], appendix A, for one-sided grazing flow, $U_+ = U_0$, $U_- = 0$, is shown (dashed line).

layers, with thickness in the order of the slot width L in flow direction, up to Strouhal numbers of order ten. He compared his results with the predictions of the analytical model for uniform grazing flow by Howe [47]. Figure 4.2 sketches the non-dimensional scaled resistance $\tilde{r}_{flow}$ and -reactance $\tilde{\delta}_{flow}$ versus Strouhal number $\omega L/U_0$ for two boundary layer cases as obtained by Golliard. Here U_0 is the grazing flow velocity outside the boundary layer. The boundary layer momentum thickness θ, cf. equation (4.15) below, was 1.1 mm and 4.0 mm respectively. The aperture width was L=1.4 cm in flow direction and 10 cm perpendicular to the flow. The results are compared with Howe's theoretical model, see appendix A, for single sided grazing flow: $U_+ = U_0$ and $U_- = 0$. Clearly, an effect of the boundary layer thickness is seen. When comparing experimental results with theory some qualitative agreement for the resistance is found, in the sense that both show oscillating behaviour (alternate regions of positive and negative resistance). However the scaling with Strouhal number is different, an effect which is also seen when comparing the two different boundary layer cases. Furthermore, the number of oscillations in the theoretical prediction is less than in the experiments. When comparing experiment and theory for the reactance no agreement is found. Especially, the fact that for large Strouhal number the predicted reactance $\tilde{\delta}_{flow}$ does not tend to zero is peculiar.

Considering the convection velocity of vorticity U_c as the relevant velocity for the influence of grazing flow on the impedance, subsequently a Strouhal number based on this convection velocity was employed by Golliard. The convection velocity was actually chosen for each configuration such that comparison between experiment and
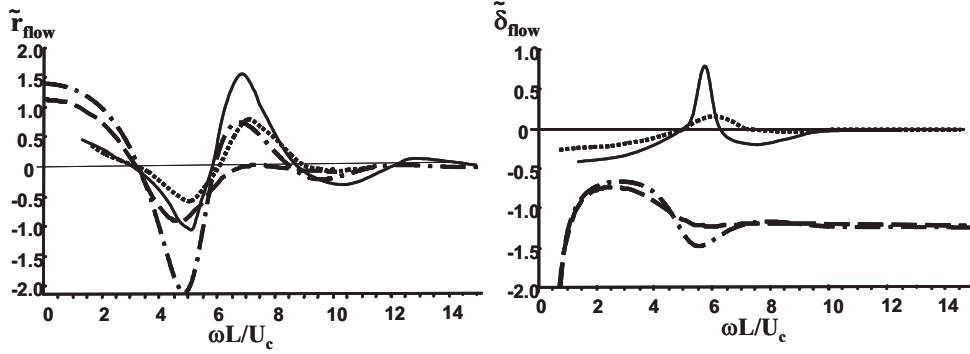
Figure 4.3: Sketch of experimental results obtained by Golliard [36] for the non-dimensional scaled resistance $\tilde{r}_{flow}$ and -reactance $\tilde{\delta}_{flow}$ in case of a turbulent boundary layer with momentum thickness to slit width ratio $\theta/L = 0.079$ (solid line) respectively $\theta/L = 0.29$ (dotted line). Here the Strouhal number $\omega L/U_c$ is based on the convection velocity of vorticity in the aperture. Also the theoretical prediction of Howe [47], appendix A, for one-sided grazing flow (dashed line) as well as for a two sided grazing flow with $U_- = 0.2U_+$ (dot-dash line) is shown.

theory was best. From this it appeared that the relation: $U_c/U_0 = 0.4(\delta_{tu}/L)^{-0.2}$ provided a reasonably good fit, where δ_{tu} is the turbulent boundary layer thickness, see section 4.6.1 below. The results for the same boundary layer cases as above, cf. figure 4.2, are shown in figure 4.3. The figure also shows the theoretical result for two-sided grazing flow, where $U_+ = U_0$ and $U_- = 0.2U_0$. Compared to one-sided grazing flow more oscillations are seen, giving a better (qualitative) agreement with experiments. Golliard therefore suggests that the velocity beneath the orifice, induced by entrainment, should be taken into account when analysing the behaviour of an orifice with one-sided imposed grazing flow. The experimental results of Golliard were first confirmed by the present author by measurements with a single microphone method [58]. Here, the change in orifice impedance due to grazing flow over a rectangular slot in a damped Helmholtz resonator was determined by measuring the transfer of sound from a loudspeaker outside the resonator to a microphone placed inside the resonator. These experiments will not be presented in this thesis.

Peat *et al.* [86] compared measurements on circular orifices both with Howe's theory in its original form and with a modified form as proposed by Jing *et al.* [48]. Regarding the original formulation of the theory basically the same conclusions were drawn as in Golliard's work [36]. The reactance predicted by the modified theory was argued to yield better (qualitative) agreement with experimental results, whereas resistance prediction became worse. Especially negative resistance, found in some

Strouhal ranges, was not predicted anymore. Furthermore, the vorticity convection velocity was not considered as the relevant velocity in comparing experiments with the modified theory, as opposed to comparison with the theory in the original formulation.

4.4   Impedance tube experiment

4.4.1   Setup

Acoustic measurements have been performed with an impedance tube in a semi-anechoic room. A multi-microphone layout is chosen in order to have better accuracy in a relatively wide frequency range compared to a 'standard' two microphone impedance tube set-up ([1, 10, 15, 20]). Figure 4.4 shows a picture of the setup, a schematic layout is given in figure 4.5. The set-up consists of a 70 cm long smooth steel tube with an inner radius of R=3.5 cm and an outer radius of 5.5 cm. A total of 7 microphones (PCB 116A) connected to charge amplifiers (Kistler 5011) are mounted in adapters in the wall of the tube. A signal generator (NI PXI-5411 arbitrary waveform generator) sends a harmonic signal with angular frequency ω via an amplifier (Toellner TOE 7608) to the loudspeaker. The loudspeaker couples the sound into the impedance tube at the back end through a piece of porous acoustical damping ma-
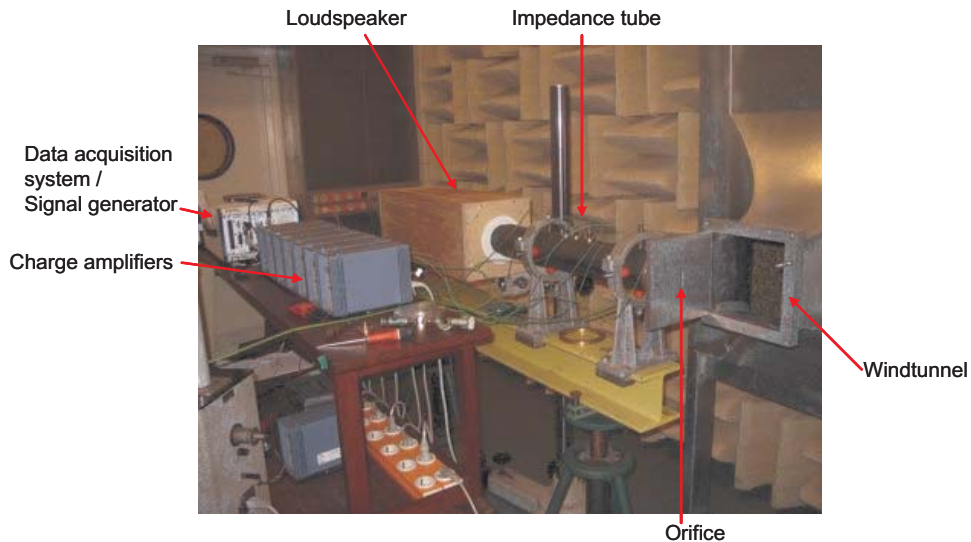
Figure 4.4: Picture of the impedance tube set-up
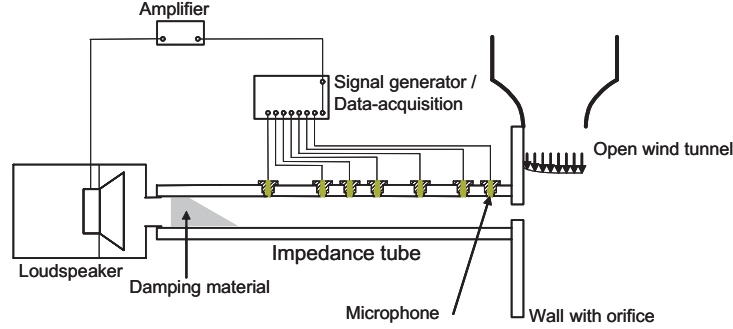
Figure 4.5: Schematic layout of the impedance tube set-up

terial. The damping material serves to prevent unwanted high acoustic amplitudes due to resonance. A plate with a rectangular slit is attached to the other end of the tube. The plate is positioned such that the orifice is centered above the tube. The geometries of the different slits used will be given further on. The plate is also fixed to the nozzle of an open windtunnel, which generates the grazing flow over the slit. In order to prevent acoustical leaks, o-rings are placed between the microphone adapters and the tube, as well as between the plate and the tube. The signals of the microphone's charge amplifiers as well as the function generator signal are digitally sampled by a dynamic signal acquisition (DSA) card (NI PXI-4472) at 10 kS/s. Both the DSA card and the signal generator module are driven by an embedded controller (NI PXI-8176). The three units are housed in a NI PXI-1042 8-slot chassis. For a single measurement microphone signals are recorded over a period of 100 s. Subsequently, as post-processing lock-in amplification is performed on an integer number of signal periods to determine the complex amplitudes of the microphone signals. From this the reflection coefficient at the end plate is calculated as described below.

4.4.2   Impedance measurement

Below the cut-on frequency of the first higher order acoustic mode in the tube (at f=2870 Hz), the acoustic pressure and velocity disturbance, p resp. u, in the tube are composed of a plane waves propagating to the right and a plane wave propagating to the left. The complex amplitudes are given by:

$$p(x) = p^+ \exp(-\mathrm{i}k^+ x) + p^- \exp(\mathrm{i}k^- x), \tag{4.8}$$

$$u(x) = \frac{1}{\rho_0 c_0}(p^+ \exp(-\mathrm{i}k^+ x) - p^- \exp(\mathrm{i}k^- x)). \tag{4.9}$$

Here $p^{\pm}$ is the complex amplitude at $x = 0$ of the pressure wave travelling in positive respectively negative x-direction, i.e. to the right and to the left in figure 4.5. In case of no mean flow through the tube the wave number $k^{\pm}$ is equal in both directions. Accounting for visco-thermal damping of the acoustical waves at the walls of the tube it is given by [53, 93, 110, 87]:

$$k^{\pm} = \frac{\omega}{c_0}\Big(1 + \frac{1-\mathrm{i}}{\sqrt{2}}\frac{1}{Sh}(1 + \frac{\gamma-1}{\sqrt{Pr}}) - \frac{\mathrm{i}}{Sh^2}(1 + \frac{\gamma-1}{\sqrt{Pr}} - \frac{1}{2}\gamma\frac{\gamma-1}{Pr})\Big), \qquad (4.10)$$

in the low frequency approximation, $kR \ll 1$, and for high shear numbers, $Sh = R\sqrt{\omega/\nu} \gg 1$. Here ν is the kinematic viscosity, γ the ratio of specific heats at constant pressure respectively constant volume, and Pr is the Prandtl number. For air at room temperature: $c_0 = 344$ ms^{-1}, $\nu = 1.51 \ 10^{-5}$ m^{2}s^{-1}, $\gamma = 1.4$, $Pr = 0.71$. In the current experiments $0.03 < kR < 0.6$, and the shear number ranges from $Sh \simeq 160$ for low frequency to $Sh \simeq 700$ for high frequency. The first correction to ω/c_0, which is proportional to Sh^{-1}, affects both phase velocity and damping of the acoustic plane waves. Here, it is a value of about $2 \ 10^{-3}$ for low frequency to $4 \ 10^{-4}$ for high frequency. The second term, proportional to Sh^{-2}, only affects the damping. In the present experiments it is in the order of 10^{-3} to $7 \ 10^{-3}$ of the value of the first correction for high and low frequency respectively, and therefore negligible. The effect on the damping coefficient of the plane waves due to visco-thermal losses in the bulk, see for instance Pierce [89] and Peters [87], appears to be at least two orders of magnitude smaller than that due to the losses at the wall given above. Therefore, it is neglected here.

Equation (4.8) can be written for all positions $x_1..x_7$ of the 7 microphones, giving an overdetermined problem for p^+ and p^-:

$$\underbrace{\begin{bmatrix} p(x_1) \\ \vdots \\ p(x_7) \end{bmatrix}}_{\mathbf{P_m}} = \underbrace{\begin{bmatrix} \exp(-\mathrm{i}k^+x_1) & \exp(\mathrm{i}k^-x_1) \\ \vdots & \vdots \\ \exp(-\mathrm{i}k^+x_7) & \exp(\mathrm{i}k^-x_7) \end{bmatrix}}_{\mathbf{M_{exp}}} \begin{bmatrix} p^+ \\ p^- \end{bmatrix}. \qquad (4.11)$$

Here we take $x = 0$ at the position of the end plate wall at the inside of the tube. The microphone positions are: $x_1 = -20$ mm, $x_2 = -70$ mm, $x_3 = -170$ mm, $x_4 = -310$ mm, $x_5 = -365$ mm, $x_6 = -410$ mm, $x_7 = -565$ mm. The least squares solution of (4.11) is found by:

$$\begin{bmatrix} p^+ \\ p^- \end{bmatrix} = (\mathbf{M_{exp}}^T\mathbf{M_{exp}})^{-1}\mathbf{M_{exp}}^T \cdot \mathbf{p_m}, \qquad (4.12)$$

where superscript T indicates the complex conjugate transpose. The impedance Z_{h-} of the orifice, as defined in equation (4.7), is now given by:

$$Z_{h-} = \frac{1}{\rho_0 c_0}\frac{p(0)}{u_h} = \frac{S_0}{S_{tube}}\frac{p^+ + p^-}{p^+ - p^-}, \qquad (4.13)$$

using equations (4.8) and (4.9). Here, from conservation of mass, the acoustic velocity through the orifice, u_h, equals S_{tube}/S_0 times the acoustic velocity $u(0)$ in the tube at $x = 0$. S_0 and S_{tube} are the (cross sectional) areas of the orifice and tube respectively. Note that in calculating the impedance by equation (4.13) the effect of visco-thermal damping on the wavenumber is not included, since it is only a small correction in the order of 10^{-3} at maximum. However, in calculating the complex pressure amplitudes $p^{\pm}$, cf. equations (4.11,4.12), it is included, since it has a cumulative effect in the wave propagation.

4.4.3 Accuracy

In order to increase accuracy the microphones are calibrated with respect to a reference microphone. This is done by placing the reference microphone and the microphone to be calibrated in a closed end wall at the end of the impedance tube. In this way the same sound pressure is imposed on the microphones. Any difference in the measured complex amplitudes of the microphones results in a calibration factor. The calibration is done at several frequencies. In the subsequent acoustical measurements the reference microphone is placed at the position closest to the end wall. After calibration, the reflection coefficient $R_0 = \frac{p_-}{p_+}$ at a closed end wall is measured in order to assess the accuracy of the set-up. Figure 4.6 shows the deviation of the absolute value $|R_0|$ from unity as well as the (deviation of the) phase ϕ of the reflection coefficient scaled to 2π radians. Both are $O(10^{-3})$ (for frequencies up to 800 Hz). Note that this is a systematic error. The reproducibility of the measurement (random error) is observed to be $O(10^{-4})$. From these results the error in the measured non-dimensional scaled resistance and reactance is estimated to be in the order of 10^{-2}.

4.5 Orifice geometries

Measurements are done with different rectangular orifices. Schematic cross sections are given in figure 4.7. All slits are symmetrically positioned in a 1.5 cm thick 20 cm × 20 cm aluminum plate. Four slits have width L=1 cm in flow direction and measure 5 cm perpendicular to the flow, cf. figure 4.7a through d. The first one has 27° sharp edges both upstream and downstream. The second one, figure 4.7b, has a single sharp 27° edge and a normal 90° edge. By rotating the plate half a turn the sharp or normal edge can be positioned upstream or downstream. The third orifice geometry, figure 4.7c, has a normal 90° edge on one side. At the other side a 0.1 mm thin phosphor bronze plate juts out 2 mm into the 12 mm wide slit in the plate, giving a sharp "0°" edge. Also here, both edges can be positioned either upstream or downstream. The last 1 cm wide slit, figure 4.7d, has two normal 90° edges. The distance of the windtunnel outlet to the upstream edge is L_w =9.5 cm for these four $L = 1$ cm orifices. By rotating the plate with the orifice given in figure 4.7d a quarter

turn a slit with normal 90° edges upstream and downstream is obtained measuring L=5 cm in flow direction and measuring 1 cm perpendicular to the flow, cf. figure 4.7e. Distance from windtunnel outlet to upstream edge is L_w=7.5 cm for this case.

4.6   Mean flow properties

4.6.1   Boundary layer characterization

In order to determine the grazing flow conditions at the upstream edge of the aperture boundary layer measurements have been performed. For this purpose a 5 μm hot-wire is used (Dantec 55P11 on a Dantec 55H20 support connected to Streamline cta module 90C10). The hot-wire measurements are done at a sample rate of 4000 S/s for 10 seconds. Different boundary layers have been realized by varying the main flow velocity U_0 outside the boundary layer and by tripping the flow at the windtunnel outlet. For this purpose a strip of sandpaper and a spoiler are used. Furthermore, measurements are done at distance $L_w = 7.5$ cm and $L_w = 9.5$ cm from the windtunnel outlet, corresponding to the different positions of the upstream edge of the aperture configurations used, cf. figure 4.7. The characteristics of the boundary layers based on the hot-wire measurements are listed in table 4.1. Here $Re_{L_w} = U_0 L_w / \nu$ is the Reynolds number based on the windtunnel outlet to orifice distance L_w, δ_{99} is the
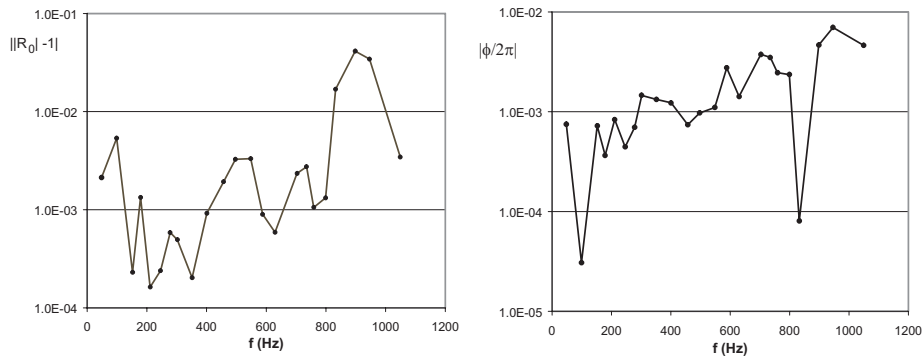
Figure 4.6: Impedance tube measurements of the reflection coefficient R_0 at a closed end wall. Absolute deviation of $|R_0|$ from unity and absolute value of the phase ϕ of R_0 scaled to 2π radians.
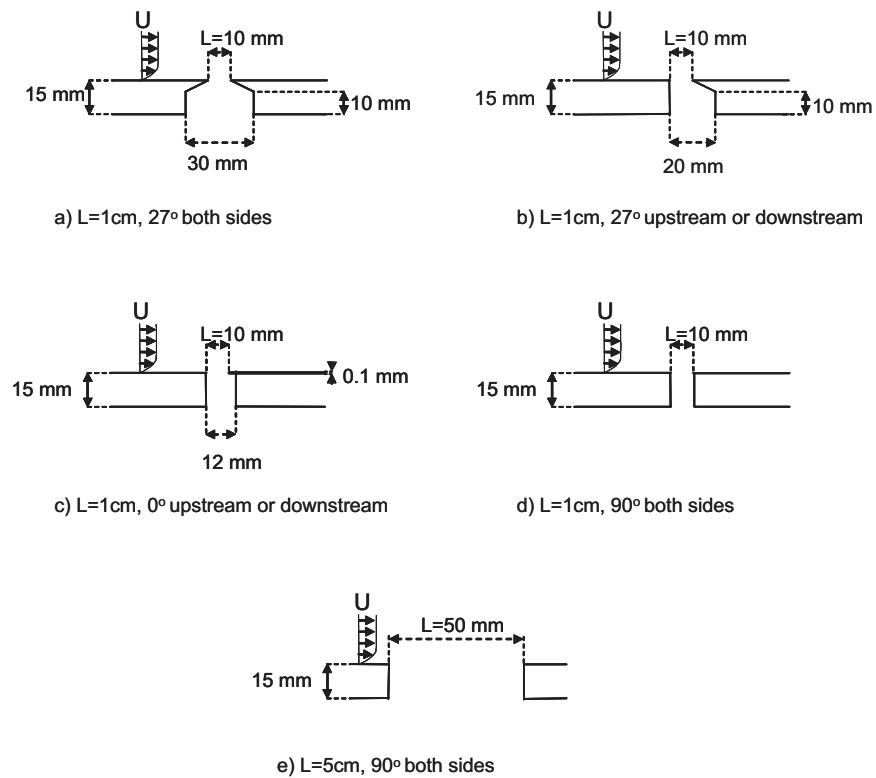
Figure 4.7: Schematical cross section of the different rectangular orifices used in experiments. Slits a through d measure $L = 1$ cm in grazing mean flow direction and have width of 5 cm perpendicular to the flow. They differ in edge geometry. Asymmetrical slits (b and c), can be placed with their sharp edge either downstream (as drawn) or upstream. Slit e has width $L = 5$ cm in flow direction and measures 1 cm perpendicular to the flow.

boundary layer thickness where $U(\delta_{99})/U_0 = 0.99$, δ_1 is the displacement thickness:

$$\delta_1 = \int_0^\infty \left(1 - \frac{U(y)}{U_0}\right) \mathrm{d}y, \tag{4.14}$$

and θ is the momentum thickness of the boundary layer:

$$\theta = \int_0^\infty \frac{U(y)}{U_0} \left(1 - \frac{U(y)}{U_0}\right) \mathrm{d}y. \tag{4.15}$$

The boundary layer profiles measured with the hot-wire are shown in figure 4.8. It can be seen that the profiles for $L_w = 7.5$ cm are almost similar to the equivalent profiles at $L_w = 9.5$ cm. The largest difference here is seen for the spoiler-tripped boundary layer. Also the sandpaper tripped boundary layers with $U_0 = 16.8$ m/s (V) and $U_0 = 34.1$ m/s (VII) are almost similar.

The measured data for boundary layers I to IV and VIII are fitted with a laminar Blasius profile [102]. A very good fit is obtained for profile I at $U_0 = 4$ m/s. For increasing velocities, boundary layers II to IV and VIII, the deviation from a Blasius profile becomes larger. The profiles V to VII and IX and X are fitted with a turbulent boundary layer velocity distribution given by the logarithmic law corrected with Coles' law of the wake [41]:

$$\begin{aligned}
\frac{U(y)}{u_{fric}} &= \frac{1}{\kappa} \ln(\frac{u_{fric}y}{\nu}) + B + \frac{\Pi}{\kappa}(1 - \cos(\pi \frac{y}{\delta_{tu}})), \qquad y \le \delta_{tu}, \\
\Pi &= \frac{\kappa}{2}\frac{U_0}{u_{fric}} - \frac{1}{2}\ln(\frac{u_{fric}\delta_{tu}}{\nu}) - \frac{B\kappa}{2}.
\end{aligned} \tag{4.16}$$

Table 4.1: Characteristics of the different boundary layers measured.

Boundary layer	L_w (cm)	U_0 (m/s)	Re_{L_w}	tripping	δ_{99} (mm)	δ_1 (mm)	θ (mm)	u_{fric}/U_0
I	9.5	4.0	2.53 10^4	-	5.0	1.38	0.55	
II	9.5	6.0	3.80 10^4	-	3.8	1.10	0.46	
III	9.5	8.8	5.57 10^4	-	3.1	0.90	0.38	
IV	9.5	16.8	1.06 10^5	-	2.5	0.67	0.29	
V	9.5	16.8	1.06 10^5	sandpaper	7.2	1.16	0.83	0.048
VI	9.5	16.8	1.06 10^5	spoiler	22.4	8.80	3.90	0.0175
VII	9.5	34.1	2.16 10^5	sandpaper	7.3	1.16	0.81	0.044
VIII	7.5	16.8	8.40 10^4	-	2.5	0.64	0.29	
IX	7.5	16.8	8.40 10^4	sandpaper	7.2	1.18	0.81	0.048
X	7.5	16.8	8.40 10^4	spoiler	22.3	9.13	3.63	0.0135

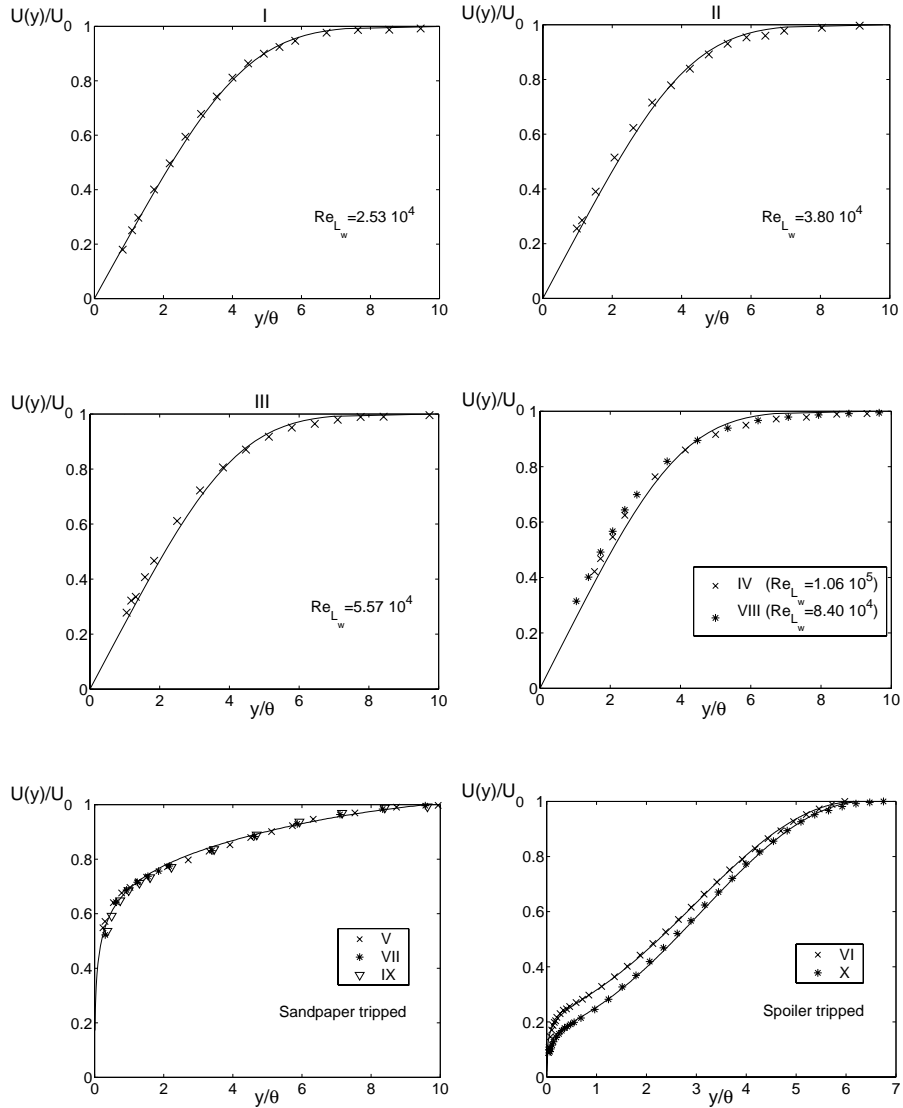Figure 4.8: Boundary layer profiles. Measured data are indicated with the markers, the solid lines give the corresponding fit. Profiles of boundary layers I, II, III, IV and VIII are fitted with a laminar Blasius profile [102]. Profiles of boundary layers V, VI, VII, IX and X are fitted with the logarithmic law for a turbulent boundary layer corrected with Coles' law of the wake [41], eq. (4.16).

Here u_{fric} is the friction velocity. Table I gives the friction velocity obtained from the fit for the concerning boundary layers. $B=5.1$ is a boundary layer constant, $\kappa=0.41$ is the von Kármán constant, and δ_{tu} is the turbulent boundary layer thickness, where $U(\delta_{tu}) = U_0$. Figure 4.8 shows reasonably good agreement between the measured profiles and the turbulent profile of equation (4.16).

In order to investigate the turbulence of the boundary layers more, the turbulent intensity Tu is considered. Following e.g. Schlichting [102], we define the turbulence intensity here as the ratio of the root mean square of the turbulent velocity fluctuations $U' = \sqrt{U_x'^2 + U_y'^2}$ perpendicular to the hot-wire and the velocity U_0 outside the boundary layer:

$$Tu = \frac{\sqrt{<U'^2>}}{U_0}. \tag{4.17}$$

Results are shown in figure 4.9. The turbulence intensity of the turbulent fitted boundary layers (i.e. numbers V, VI, VII, IX, and X), depicted in the lower two graphs of figure 4.9, is indeed larger than that of the laminar fitted boundary layers. However, especially for boundary layers IV and VIII the turbulence intensity is almost as large as for the turbulent fitted ones. Although it is still reasonably well fitted with a laminar Blasius profile, these boundary layers can be regarded as on the transition from laminar to turbulent. For boundary layer flows I to V the mean flow velocity at the point where the highest turbulence intensity is measured is shown in figure 4.10 as function of time for the first second of the measurement. It is seen that for the laminar fitted boundary layers, no. I to IV, the velocity fluctuations occur more rapidly with increasing main flow velocity. For the turbulent fitted boundary layer, no. V, very rapid fluctuations are observed compared to all other boundary layer flows.

Overlooking the results above, the boundary layers I to III will be regarded as laminar, whereas boundary layers IV and VIII are designated transitional. The sandpaper tripped boundary layers V, VII and IX are turbulent. Due to the pronounced form of a wake behind an object, see figure 4.8, the spoiler tripped boundary layers VI and X will be designated as turbulent wake.

4.6.2 Shear layer profiles

In studying its acoustical response the flow properties of the shear layer developing in the orifice are of interest. Therefore, hot-wire measurements of shear layer profiles are done for the 1 cm orifices with double sharp 27° edges and with double 90° edges, as well as for the 5 cm slit, cf. figure 4.7a, d and e respectively. Results for the 1 cm slot with sharp edges are shown in figure 4.11 for boundary layer flows I to V. Shear layer profiles at various distances from the upstream edge x_s are depicted, viz. $x_s = 2$ mm, $x_s = 4$ mm, $x_s = 6$ mm, and $x_s = 8$ mm. Also, the boundary layer profiles are shown ($x_s = 0$ mm). The y-coordinate on the horizontal axes is scaled to the momentum thickness θ_0 of the boundary layer. Shear layer profiles for the 1 cm slot with double
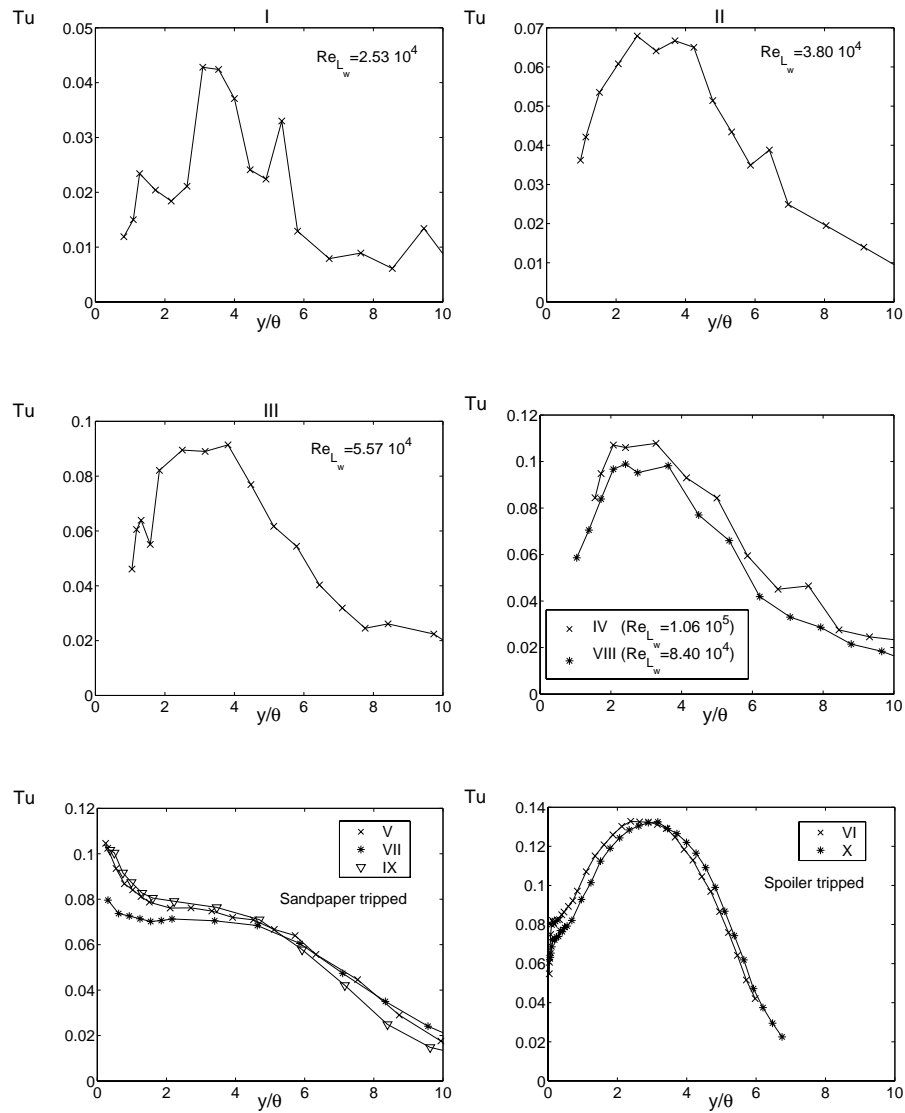
Figure 4.9: Turbulence intensity Tu of the different boundary layers.
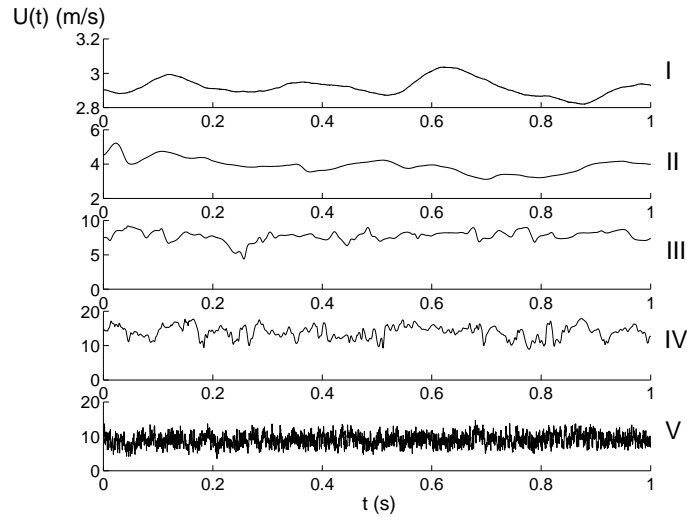
Figure 4.10: Mean flow velocity as function of time at the point in the boundary layer where turbulence intensity is maximum, cf. figure 4.9, for boundary layer flows I to V.

90° edges are shown in figure 4.12 at the same distances x_s for boundary layer flows IV and V. For the 5 cm slot shear layer profiles for boundary layer flow VIII and IX (to be compared with boundary layer IV and V for the 1 cm slots) are shown in figure 4.13 for various distances x_s from the upstream edge.

The shear layer profiles of boundary layer IV and V for the 1 cm slot with sharp edges and the 1 cm slot with normal edges are nearly identical. However, for turbulent boundary layer flow V the measured velocity does not seem to tend to zero at the lower side of the shear layer in case of the slot with normal edges. Here, the flow velocity remains more or less constant. Most probably this is caused by the fact that there is a significant entrainment velocity. Comparing the geometries of the two orifices it could be expected that the flow in the slot with normal edges will differ more from an 'ideal' parallel shear flow, especially near the upstream and downstream edge. In the case of normal edges the entrainment velocity will have a strong component normal to the main flow. This is illustrated in figure 4.14, giving a sketch of the entrained flow in the orifice for the two different geometries. The effect is also seen in shear layer measurements closest to the upstream edge for the 5 cm slot especially with turbulent boundary layer IX.

Analogous to the boundary layer momentum thickness, the shear layer momentum
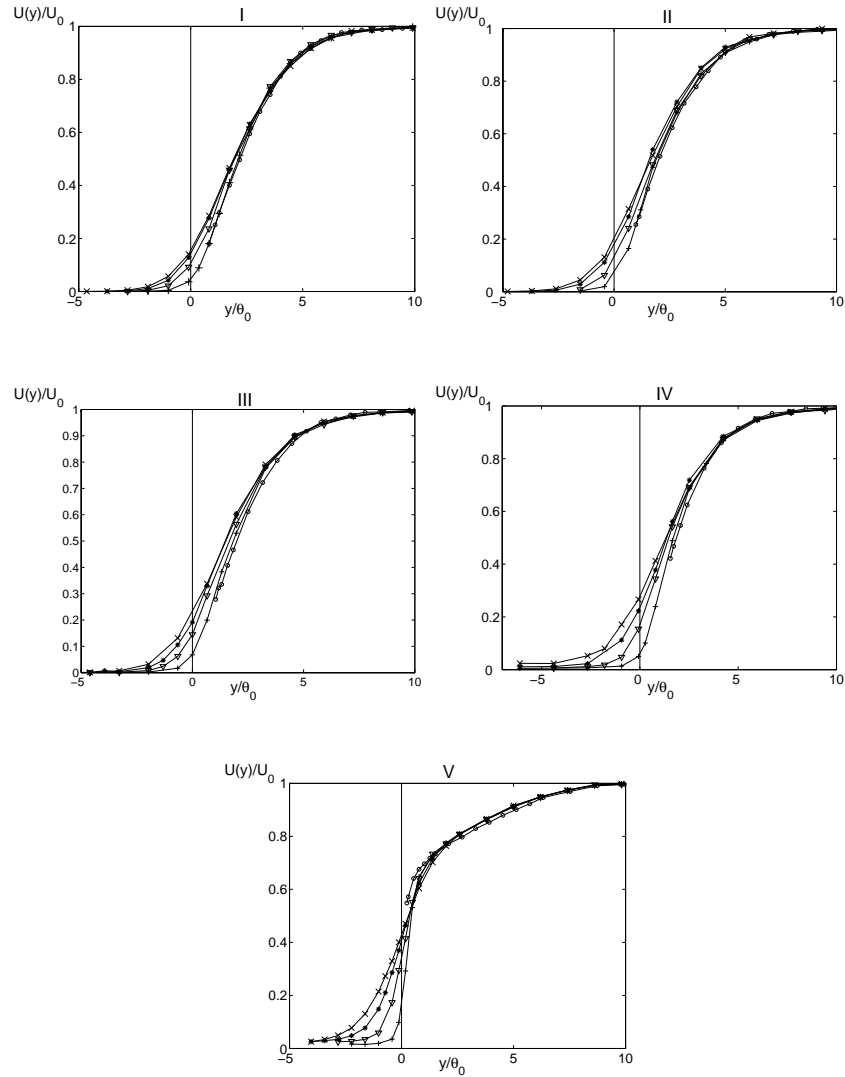
Figure 4.11: Shear layer profile measurements at various distances x_s from the up-stream edge for the 1 cm slot with double 27° edges, cf. figure 4.7a, and boundary layer flow I to V. ∘ markers: $x_s = 0$ mm (boundary layer profile), + markers: $x_s = 2$ mm, ∇ markers: $x_s = 4$ mm, $*$ markers: $x_s = 6$ mm, $\times$ markers: $x_s = 8$ mm. The y-coordinate is scaled to the boundary layer momentum thickness θ_0.
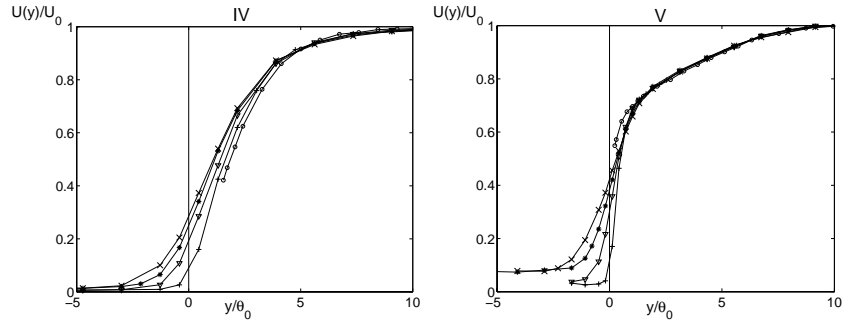
Figure 4.12: Shear layer profile measurements at various distances x_s from the up-stream edge for the 1 cm slot with double 90° edges, cf. figure 4.7d, and boundary layer flow IV and V. ∘ markers: $x_s = 0$ mm (boundary layer profile), + markers: $x_s = 2$ mm, ∇ markers: $x_s = 4$ mm, ∗ markers: $x_s = 6$ mm, × markers: $x_s = 8$ mm. The y-coordinate is scaled to the boundary layer momentum thickness θ_0.
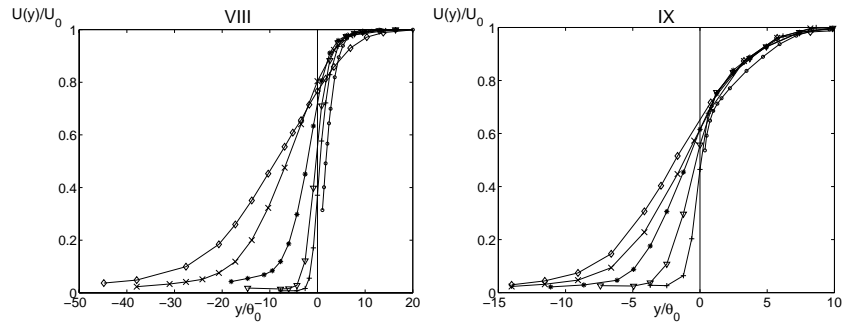
Figure 4.13: Shear layer profile measurements at various distances x_s from the up-stream edge for the 5 cm slot with double 90° edges, cf. figure 4.7e, and boundary layer flow VIII and IX. ∘ markers: $x_s = 0$ mm (boundary layer profile), + markers: $x_s = 5$ mm, ∇ markers: $x_s = 10$ mm, ∗ markers: $x_s = 20$ mm, × markers: $x_s = 30$ mm, ◇ markers: $x_s = 40$ mm for BL VIII or $x_s = 35$ mm for BL IX. The y-coordinate is scaled to the boundary layer momentum thickness θ_0.

(a)   (b)
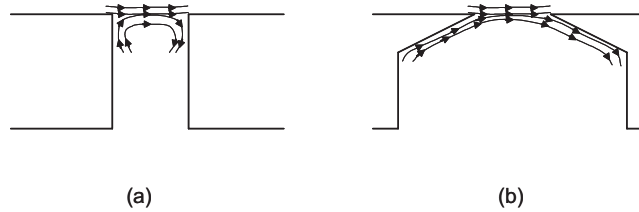
Figure 4.14: Sketch of the entrained flow in the orifice with normal 90° edges (a) and with 27° edges (b). In the former geometry the vertical velocity component near the upstream and downstream edge will be relatively large.

thickness is given by (see also equation B.9):

$$\theta = \int_{-\infty}^{\infty} \frac{U(y)}{U_0} \left(1 - \frac{U(y)}{U_0} \right) \mathrm{d}y. \tag{4.18}$$

The momentum thickness as function of the distance from the upstream edge calculated for the experimental data above is shown in figure 4.15 for the 1 cm slot with sharp edges for boundary layer flows I to V. For all boundary layer flows the data can be fitted well with a straight line, giving a linear increase of momentum thickness with distance. For the 5 cm slot momentum thickness as function of distance to upstream edge is depicted in figure 4.16. For the turbulent boundary layer IX a linear fit applies. As shown in the graph this fit agrees well with that applied to the data for the corresponding turbulent boundary layer V in case of the 1 cm slot with sharp edges (figure 4.15). For the transitional boundary layer VIII a linear increase in momentum thickness with distance is seen up to $x_s = 10$ mm. The linear fit applied to the data of the corresponding transitional boundary layer IV in case of the 1 cm slot with sharp edges, cf. figure 4.15, also applies reasonably well to these points. However, for larger distances from the upstream edge a stronger increase in momentum thickness is seen. Note that, in calculating the momentum thickness, for those cases in which a nonzero velocity is measured at the lower side of the shear layer due to the entrained normal velocity, an estimate of the (parallel) profile there is made. The error in the calculated values for θ/θ_0 is estimated at $\pm 5\%$. Furthermore, due to experimental constraints the shear layer profiles for the spoiler tripped turbulent wakes VI and X have not been measured.

Figure 4.15: Shear layer momentum thickness θ scaled by the corresponding boundary layer momentum thickness θ_0 against distance x_s from the upstream edge for the 1 cm slot with double 27° edges. + markers: BL I, ∗ markers: BL II, ∇ markers: BL III, ∘ markers: BL IV, ⋄ markers: BL V. A linear fit is applied to each data series.

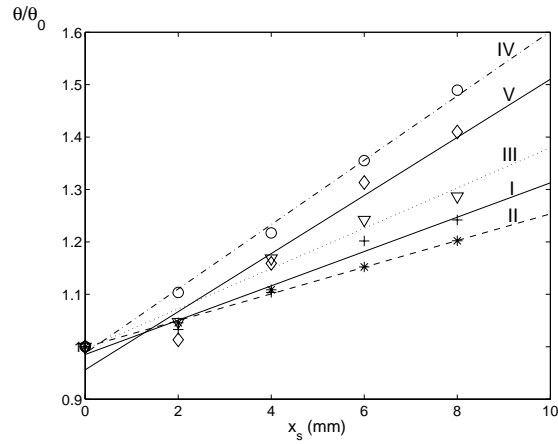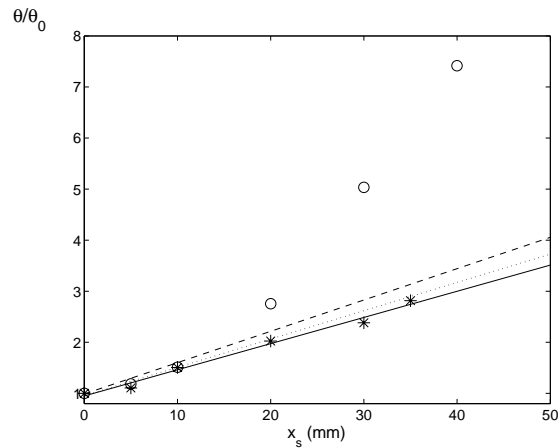Figure 4.16: Shear layer momentum thickness θ scaled by the corresponding boundary layer momentum thickness θ_0 versus distance x_s from the upstream edge for the 5 cm slot. ∘ markers: BL VIII, ∗ markers: BL IX. Solid line: linear fit of data for BL IX. Dashed and dotted line: linear fit of data for BL IV respectively BL V in case of 1 cm slot with sharp edges, cf. figure 4.15.

4.7 Results

4.7.1 Impedance without mean flow

The measured impedance in case mean flow is absent is shown in figure 4.17 for the various slots with different edge geometry, cf. figure 4.7. The real part of the impedance, i.e. the resistance r, increases with frequency. Results for the different orifice geometries are in general quite close. Between 500 Hz and 700 Hz some deviation is seen for the double 27° edge geometry compared to the others. At high frequency the resistance for the single sharp 0° edge geometry is higher than for the other geometries.

For monopole radiation the resistance is proportional to the square of the Helmholtz number based on the characteristic orifice dimension. As expected, the imaginary part of the impedance increases linearly with frequency, with different slope for the different edge geometries. The imaginary part of the impedance is namely proportional to the Helmholtz number with a constant related to the inertia of the fluid motion in the orifice, see also equation (4.4). Figure 4.18 shows the real part of the impedance scaled to the square of the Helmholtz number $k_0 R_e$ based on the hydraulic radius R_e of the aperture as well as the imaginary part of the impedance divided by the Helmholtz number $k_0 R_e$. Here, the hydraulic radius of the orifice is the equivalent radius of a circular orifice with the same area: $R_e = \sqrt{\frac{S_0}{\pi}}$. For the scaled resistance very large values are seen below $k_0 R_e = 0.05$ (which corresponds to a frequency of about
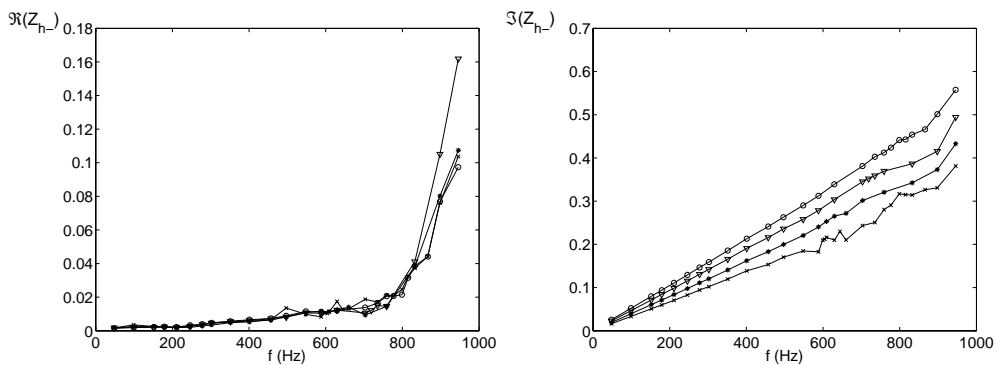
Figure 4.17: Real part and imaginary part of the aperture impedance Z_{h-} of the slots with different edge geometries, cf. figure 4.7. $\times$ markers: double sharp 27° edges, $*$ markers: single sharp 27° edge, $\circ$ markers: normal 90° edges, ∇ markers: single sharp 0° edge.
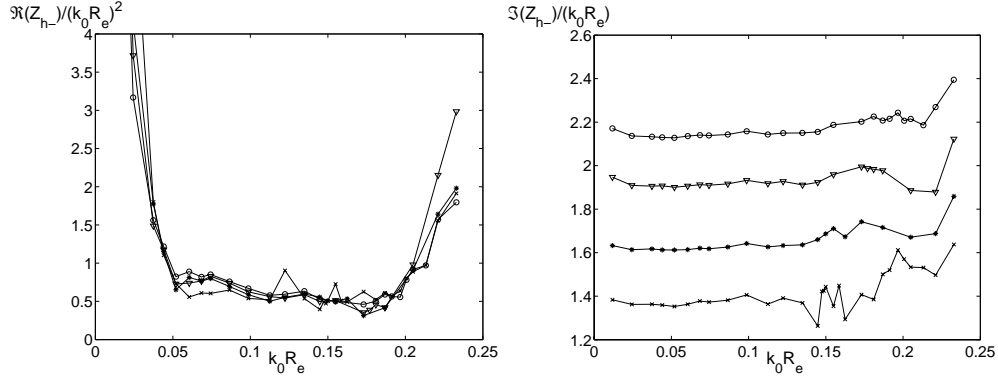
Figure 4.18: Real and imaginary part of the aperture impedance Z_{h-}, scaled to the Helmholtz number squared resp. the Helmholtz number, for the slots with different edge geometries, cf. figure 4.7. $\times$ markers: double sharp $27°$ edges, $*$ markers: single sharp $27°$ edge, $\circ$ markers: normal $90°$ edges, ∇ markers: single sharp $0°$ edge.

$f = 200$ Hz). This is most probably due to the limited accuracy of the measurement, as for low frequency the resistance is very small. Between a frequency of $f = 200$ Hz and $f = 800$ Hz, corresponding to $k_0 R_e$ between 0.05 and 0.2, the value for the scaled resistance is reasonably constant between 0.5 and 1. For higher frequency again large values are seen. Possible explanations for this are the decreased measurement accuracy for especially the absolute value of the reflection coefficient above $f = 800$ Hz, see also figure 4.6, and the effect of higher order radiation.

According to equation (4.4), the imaginary part of the impedance divided by Helmholtz number $k_0 R_e$ equals the ratio of reactance δ to hydraulic radius R_e. For all orifice geometries the observed values in figure 4.18 are fairly constant with frequency. Only at higher frequencies some deviation is found. As expected the value of the reactance for the different orifice geometries increases in the following order: double sharp $27°$ edges, single sharp $27°$ edge, single sharp $0°$ edge, and normal $90°$ edges. For the orifice with normal $90°$ edges the plate thickness (equal to 1.5 cm, or $1.19 R_e$) can simply be subtracted from the reactance δ to obtain an end correction. This end correction is then about equal to the hydraulic radius R_e.

The accuracy of reflection coefficient measurements, addressed in section 4.4.3 above, in relation to the orifice impedance without flow is studied more in figure 4.19. Here, the expected reflection coefficient R in case the orifice impedance is $Z_{h-} = 0.5(k_0 R_2)^2 + i1.8 k_0 R_e$, representative for the experimental results above, is compared to the error in the reflection coefficient at a closed wall. The figure shows the value of $|1 - |R||$ and $|\phi/2\pi|$, with ϕ the phase of the reflection coefficient, for both the orifice
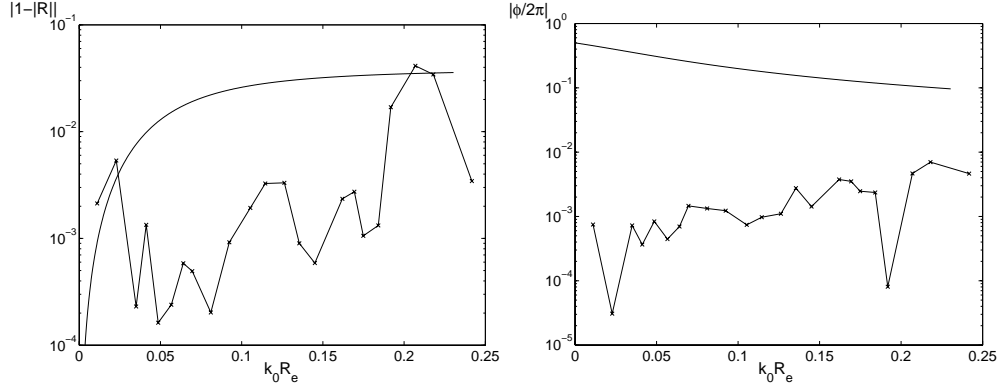
Figure 4.19: Magnitude and phase of the reflection coefficient R for an impedance $Z_{h-} = 0.5(k_0 R_e)^2 + i1.8 k_0 R_e$ (solid lines) compared to the error in R in case of a closed end wall (solid lines with $\times$ markers), cf. figure 4.6.

impedance mentioned above and for the measurements at a closed wall, cf. figure 4.6, as function of Helmholtz number $k_0 R_e$. It is observed that for low and high frequency the deviation of the absolute value of the reflection coefficient from unity, expected for the mentioned impedance, is of the same order as the error. In between, the error is about an order in magnitude smaller than the 'measured' value. The error in the phase of the reflection coefficient is at least an order of magnitude smaller than the 'measured' value. Thus indeed for low and high frequencies a relatively large error in the measured impedance, especially observed above for the real part, is expected.

4.7.2 Impedance with grazing mean flow

Figure 4.20 shows the measured impedance Z_{h-}, cf. equation (4.7), for the L=1 cm orifice with double sharp $27°$ edges as function of frequency f in case no mean flow is present, and in case of grazing mean flow with turbulent boundary layer V. The difference in impedance due to the flow is depicted in figure 4.21. With grazing flow the value of the impedance (both real and imaginary part) oscillates around the no flow value. At low frequency the flow increases the resistance, here absorption of sound occurs. For increasing frequency this effect diminishes, and at around f=320 Hz a region starts where the resistance is decreased by the grazing flow. In this region the resistance with flow becomes negative, this means sound production takes place. At about f=590 Hz there is a minimum in the resistance, after which a sharp transition to a second region of sound absorption is seen. The increase in resistance due to the
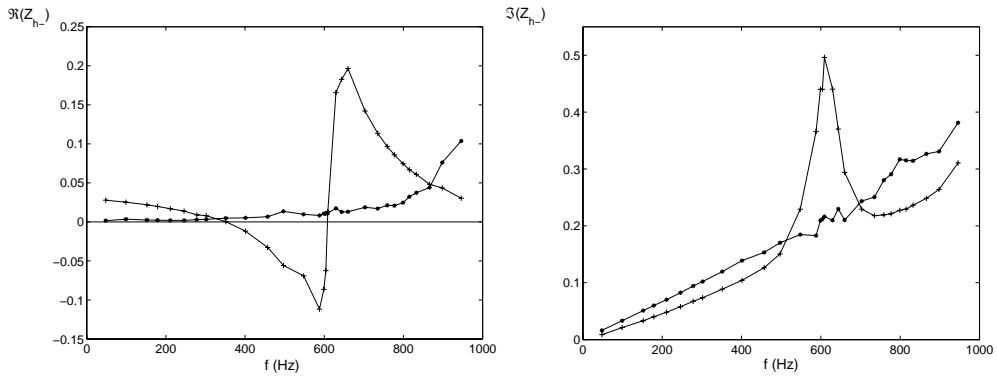
Figure 4.20: Real and imaginary part of the aperture impedance Z_{h-} for the L=1 cm slit with double sharp 27° edges without flow (∗ markers) and with grazing flow (+ markers) as function of frequency f in case of turbulent boundary layer V.
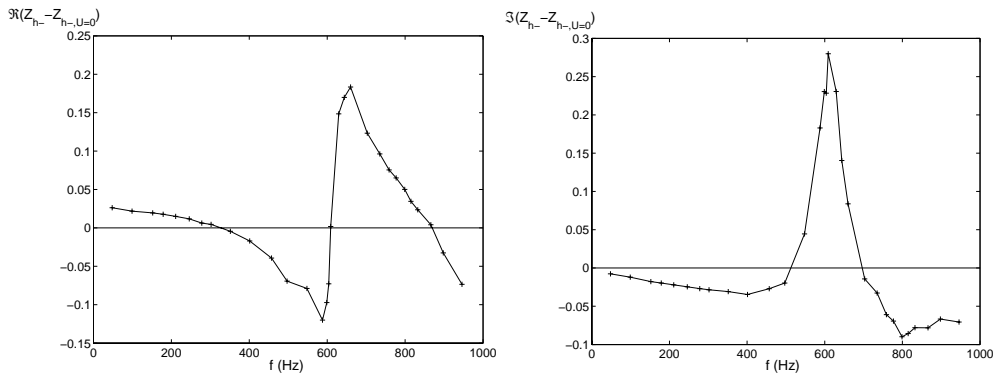
Figure 4.21: Change of the real and imaginary part of the aperture impedance Z_{h-} due to grazing flow as function of frequency f for the 1 cm orifice with double sharp 27° edges with turbulent boundary layer V.

flow in this region is much larger than at low frequencies. The sharp transition in the resistance coincides with a peak in the imaginary part of the impedance. In a region of about $f = 500$ Hz to $f = 700$ Hz around this peak the effect of the flow is to increase the imaginary part of the impedance, and therefore the reactance, whereas outside this region the reactance is decreased by the flow. Globally, for this particular boundary layer case the effect of the grazing flow on the impedance is quite large compared to the value of the impedance without flow.

4.7.3 Linearity

The linearity of the orifice impedance with grazing flow is investigated by measuring at different sound pressure levels. Results for the $L=1$ cm slot with double sharp $27°$ edges with turbulent boundary layer V at several frequencies are plotted in figure 4.22. The graphs show the relative change of the real and imaginary part of the orifice impedance Z_{h-} with respect to a reference value $Z_{h-,ref}$ as function of the amplitude of the acoustic velocity through the orifice $|u_h|$ over the mean flow velocity U_0. The value of the impedance at the lowest acoustic velocity amplitude is taken as reference $Z_{h-,ref}$. Note that the scale $|u_h|/U_0 = 10^{-4}$ to $|u_h|/U_0 = 1$ in figure 4.22 corresponds to sound pressure levels from about 70 dB up to 150 dB just beneath the orifice.
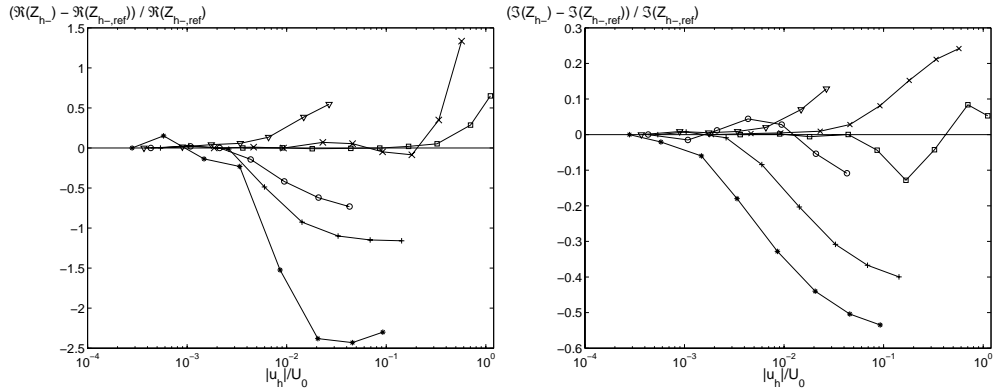
Figure 4.22: Relative change of the orifice impedance Z_{h-} with respect to a reference value $Z_{h-,ref}$ for the 1 cm orifice with double sharp $27°$ edges in case of turbulent boundary layer V as function of the amplitude of the acoustic velocity through the orifice $|u_h|$ over the mean flow velocity U_0. For $Z_{h-,ref}$ the value at the lowest acoustic velocity amplitude is taken. $\square$ markers: $f = 48$ Hz, $\times$ markers: $f = 302$ Hz, $+$ markers: $f = 588$ Hz, $*$ markers: $f = 609$ Hz, $\circ$ markers: $f = 660$ Hz, ∇ markers: $f = 898$ Hz.

For the lowest frequency, f=48 Hz, linear behaviour is observed up to a relative amplitude $|u_h|/U_0 = 0.2$ for the real part and up to $|u_h|/U_0 = 5 \cdot 10^{-2}$ for the imaginary part of the impedance. At f=302 Hz, just before the resistance becomes negative, see figure 4.20, impedance is linear up to a relative amplitude $|u_h|/U_0$ of 10^{-2}. Strong nonlinear behaviour is only seen for $|u_h|/U_0$ larger than 0.1. For the frequencies f=588 Hz and f=660 Hz, at which the resistance has a minimum respectively maximum, cf. figure 4.20, the onset of nonlinear behaviour is at approximately $|u_h|/U_0 = 2 \cdot 10^{-3}$. For f=609 Hz, corresponding to the sharp transition from negative to positive resistance and the peak in the imaginary part of the impedance, cf. figure 4.20, the onset of nonlinearity seems to be at even lower amplitude: at about $|u_h|/U_0 = 3 \cdot 10^{-4}$. At a frequency of f=898Hz, beyond the strong oscillations in impedance, linearity is observed up to $|u_h|/U_0$ several times 10^{-3}.

Considering the deviations in the impedance from the (linear) reference value at a given amplitude, the effect of nonlinearity increases from f=48 Hz to subsequently f=302, f=898 Hz, f=660 Hz, f=588 Hz and f=609 Hz. Nonlinearity thus seems to be strongest in the region where the oscillations in impedance are observed, here the onset of nonlinear behaviour is at lower amplitudes and the deviation from the linear impedance is largest.

In following measurements on the linear behaviour of the orifice impedance under grazing flow the acoustic amplitudes are mostly close to the onset of nonlinearity, in order to have maximum signal amplitude.

4.7.4 Non-dimensional scaled resistance and reactance

Figures 4.23 and 4.24 show the non-dimensional scaled resistance and reactance, as defined in equation (4.7), for the L=1 cm orifice with double 27° edges for the different boundary layer flows. Non-dimensional scaled resistance and reactance for the L=5 cm aperture are depicted in figure 4.25. The results are plotted versus the Strouhal number $\omega L/U_0$ based on the orifice width in stream wise direction and the main flow velocity outside the boundary layer. For the L=1 cm orifice similar features are seen for all boundary layers. For increasing Strouhal number about 4 regions are observed. For low Strouhal number resistance is positive, implying sound absorption. For higher Strouhal number a region is found where resistance is negative, implying sound production due to the grazing flow. Subsequently, two more regions of alternately positive and negative resistance follow. A similar oscillating behaviour is seen for the reactance. For both resistance and reactance the oscillations damp out for high Strouhal number. The Strouhal numbers of the oscillations in the reactance more or less coincide with those of the oscillations in the resistance. These specific features in resistance and reactance generally shift to a higher Strouhal number for decreasing boundary layer thickness. Furthermore, the amplitudes of the oscillations increase with decreasing laminar/transitional boundary layer thickness (BL I to IV). For the turbulent boundary layer V larger oscillations in the resistance and reactance

Figure 4.23: Non-dimensional scaled resistance and reactance due to grazing mean flow for the $L=1$ cm orifice with double $27°$ edges for boundary layers I, II and III. The boundary layer momentum thickness θ_0 scaled to the slit width L is indicated for each case.

Figure 4.24: Non-dimensional scaled resistance and reactance due to grazing mean flow for the L=1 cm orifice with double 27° edges for boundary layers IV, V, VI and VII. The boundary layer momentum thickness θ_0 scaled to the slit width L is indicated for each case.
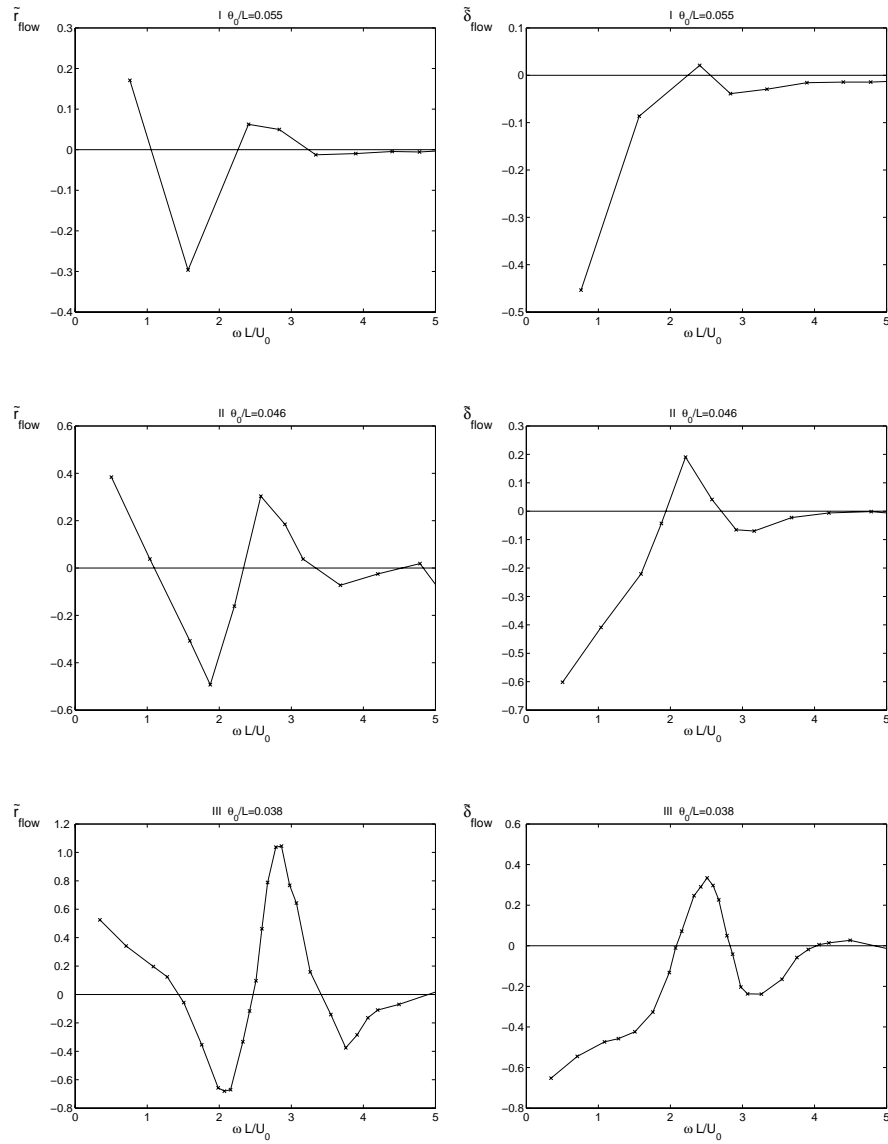
Figure 4.25: Non-dimensional scaled resistance and reactance due to grazing mean flow for the L=5 cm orifice for boundary layers VIII, IX and X. The boundary layer momentum thickness θ_0 scaled to the slit width L is indicated for each case.
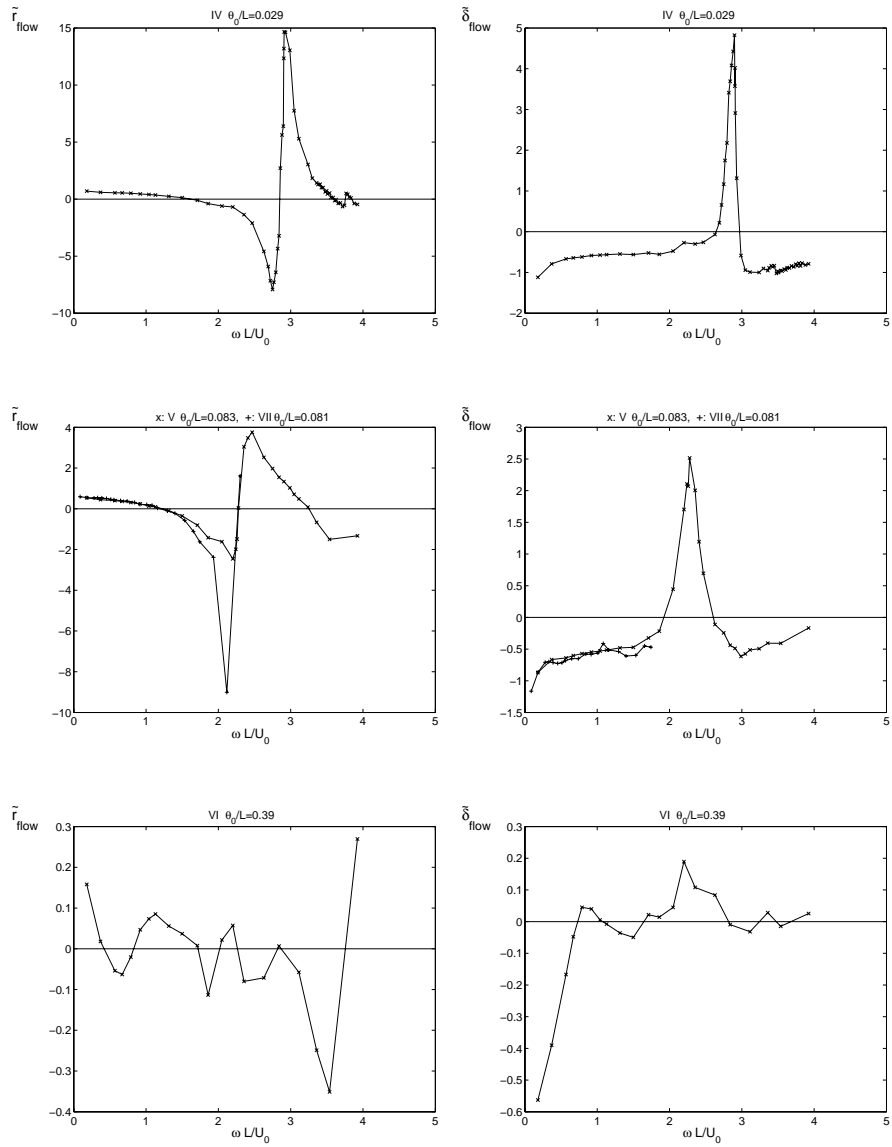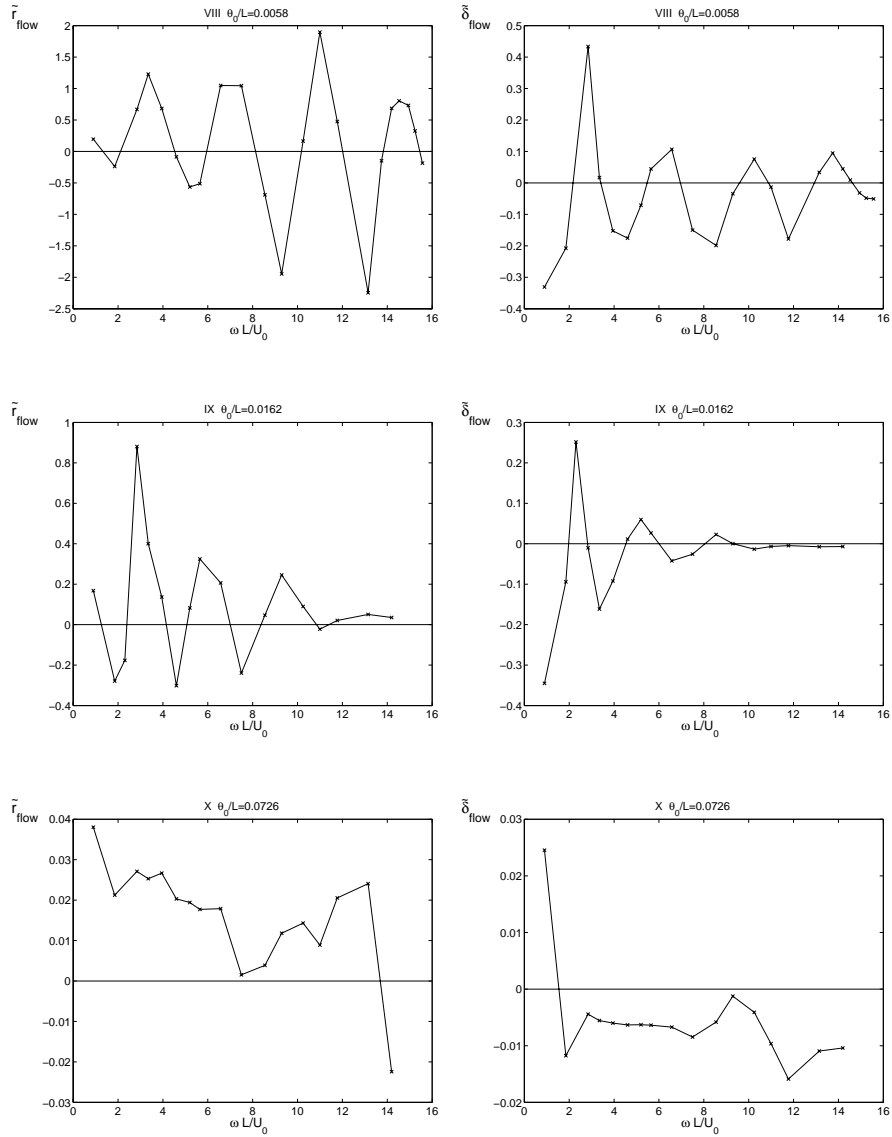
are observed than for the laminar boundary layers I to III, although the boundary layer thickness of V is generally larger than those of I to III. For the spoiler tripped turbulent wake VI qualitatively the same features for the resistance and reactance as discussed are observed up to a Strouhal number of 1.7. However, for larger Strouhal number especially the resistance is not found to damp out to 0 (at least up to the largest Strouhal number measured). The results for turbulent boundary layer flows V and VII, which have nearly the same characteristics but different Mach number, are very close, although the first peak of negative resistance at $\omega L/U_0 \simeq 2$ is stronger for BL VII.

For the L=5 cm orifice more oscillations in resistance and reactance are found. Furthermore, for the turbulent wake boundary layer X less clearly defined behaviour is found. In this case the error in the measurements is of the same order as the measured effect itself. For the transitional boundary layer VIII, the thinnest one, most oscillations are seen. Also the oscillations are at a higher Strouhal number and have a larger amplitude compared to the turbulent boundary layer IX case. This is the same as seen in mutually comparing the correspondent boundary layers IV respectively V for the L=1 cm orifice. Furthermore, in the results for transitional and turbulent boundary layers VIII respectively IX the first resonance in resistance and reactance has a smaller amplitude and seems to be at a slightly higher Strouhal number, compared to their corresponding cases for the L=1 cm slot.

4.7.5   Effective Strouhal number

As pointed out by others, e.g. Golliard [36], the impedance of the orifice is closely connected to the hydrodynamic instability of the shear layer developing in the orifice. A better way to compare orifice impedance results for different boundary layers would therefore be to consider them as a function of the Strouhal number based on the phase velocity U_c of the hydrodynamic instability wave, i.e. the convection velocity of vorticity in the aperture, rather than as function of the Strouhal number based on the main flow velocity U_0. Golliard [36] used the convection velocity as a fit parameter to get a better agreement with the theoretical prediction of Howe [47], see section 4.3 above. Goldman and Panton [34] for instance also discussed the use of an effective convection velocity, although they gave it a more general interpretation.

Here we attempt to use calculations of the convective velocity of hydrodynamic instability in a shear layer with generalized hyperbolic-tangent form as presented by Michalke [67, 68], see appendix B.2. As shown there, for given profile, set by the profile parameter m, the phase velocity U_c of the hydrodynamic instability non-dimensionalized by the mean flow velocity U_0 is a function of the Strouhal number based on the momentum thickness θ of the shear layer and U_0, cf. figure B.3:

$$\frac{U_c}{U_0} = f(\frac{\omega\theta}{U_0}, m) \tag{4.19}$$

Since the form of the shear layer changes and the momentum thickness increases with distance from the upstream edge, no unambiguous convection velocity can be found. An indication of the margin encountered in the scaling can be given by considering the boundary layer profile at the upstream edge, and the shear layer profile at the downstream edge. The values of the momentum thickness for these profiles can be extracted from section 4.6 for the different experimental configurations. Concerning the form of the shear layers, it is found that generally a reasonably good fit can be obtained between experiments, cf. figures 4.11, 4.12 and 4.13, and the generalized hyperbolic-tangent profile, equation B.8. This is illustrated in figure 4.26, where the measured shear layer profiles for the 1 cm orifice with double 27° edges and transitional boundary layer flow IV are fitted with equation B.8. The values of the shear layer momentum thickness used in the fits is close to those calculated from the measured profiles, cf. figure 4.15. As shown, the profile parameter m varies between ∞ for the boundary layer to $m = 1.5$ for the shear layer 8 mm from the upstream edge. The hyperbolic-tangent profiles are shifted in the y-direction as to give the best fit with experimental data. For the boundary layer this actually gives a slight offset in the wall position. Note that shifting the fit profiles does not affect the calculated phase velocity. For the turbulent boundary layer flows, no. V for the 1 cm slots and no. IX for the 5 cm slot, and for the 5 cm slot with transitional boundary layer flow VIII
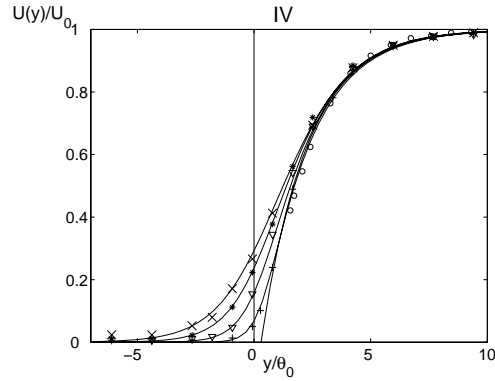
Figure 4.26: Measured shear layer profiles (markers) for the 1 cm wide orifice with double 27° edges with transitional boundary layer flow IV, cf. figure 4.11, fitted with the hyperbolic-tangent profile (corresponding solid lines), equation (B.8), for different distances from upstream edge x_s. $\circ$ markers: $x_s = 0$ mm (boundary layer profile), $\theta = \theta_0 = 0.29$ mm, profile parameter $m = \infty$. $+$ markers: $x_s = 2$ mm, $\theta = 0.32$ mm, $m = 5$. ∇ markers: $x_s = 4$ mm, $\theta = 0.35$ mm, $m = 3$. $*$ markers: $x_s = 6$ mm, $\theta = 0.39$ mm, $m = 2$. $\times$ markers: $x_s = 8$ mm, $\theta = 0.44$ mm, $m = 1.5$.

shear layer profiles could be fitted less well with the generalized hyperbolic-tangent profile than shown in the figure above.

The measured resistance and reactance for the 1 cm orifice with double 27° edges and transitional boundary layer flow IV, cf. figure 4.24, can now be plotted versus the Strouhal number based on the convection velocity, calculated for either the boundary layer profile or the shear layer profile at the downstream edge. For the boundary layer profile $\theta = \theta_0 = 0.29$ mm and $m = \infty$. The shear layer profile at the downstream edge is not measured, however the momentum thickness can be estimated at $\theta = 1.6\theta_0 = 0.46$ mm using figure 4.15. The profile parameter is chosen $m = 1$ on basis of figure 4.26. Results are shown in figure 4.27. A significant range in the Strouhal number is observed. The oscillation in the resistance and corresponding peak in reactance is at $\omega L/U_c \approx 4$ or at $\omega L/U_c \approx 6$ respectively, when U_c is calculated for the boundary layer profile at the upstream edge or for the shear layer profile at the downstream edge.

A scaling of the Strouhal number is done for the experiments with the 1 cm slit with double 27° edges for boundary layer flows I to V, depicted in figures 4.23 and 4.24. The convective velocity is calculated from Michalke's results for a shear layer profile halfway the slot, at $x_s = 5$ mm. The profile parameter is taken $m = 2$, providing a reasonably good fit with measured shear layer profiles. The momentum thickness at $x_s = 5$ mm is determined from figure 4.15. Results are shown in figure 4.28 and 4.29. In the graphs also a vertical dotted line is drawn. This line indicates

Figure 4.27: Non-dimensional scaled resistance and reactance for the 1 cm orifice with double 27° edges and transitional boundary layer flow IV versus Strouhal number based on the convection velocity U_c of the hydrodynamic instability. $\times$ markers: U_c calculated for the boundary layer: $\theta = \theta_0 = 0.29$ mm, $m = \infty$. $*$ markers: U_c calculated for the shear layer at downstream edge: $\theta = 1.6\theta_0 = 0.46$ mm, $m = 1$.

Figure 4.28: Non-dimensional scaled resistance and reactance for the L=1 cm orifice with double 27° edges for laminar boundary layers I, II and III versus Strouhal number based on the convective velocity U_c. The convective velocity is calculated from Michalke's results, appendix B.2, for the generalized hyperbolic-tangent shear layer profile with $m = 2$. The momentum thickness is that halfway the slit, at $x_s = 5$ mm, cf. figure 4.15. The boundary layer momentum thickness θ_0 scaled to the slit width L is indicated for each case.

Figure 4.29: Non-dimensional scaled resistance and reactance for the L=1 cm orifice with double 27° edges for transitional boundary layer IV and turbulent boundary layer V against Strouhal number based on the convective velocity U_c. The convective velocity is calculated from Michalke's results, appendix B.2, for the generalized hyperbolic-tangent shear layer profile with $m = 2$. The momentum thickness is that halfway the slit, at $x_s = 5$ mm, cf. figure 4.15. The boundary layer momentum thickness θ_0 scaled to the slit width L is indicated for each case.

the Strouhal number $\omega L/U_c$ at which $\omega\theta/U_0 = 0.07$. For values $\omega\theta/U_0 \leq 0.07$, and thus Strouhal numbers $\omega L/U_c$ less than the value indicated by the line, the convection velocity is independent of profile parameter m, cf. figure B.3. Furthermore, note that only the range $\omega\theta/U_0 < 0.25$, for which U_c is given, is considered. For comparison the resistance and reactance for the 1 cm slot versus Strouhal number $\omega L/U_0$ for boundary layer flows I to V, cf. figures 4.23 and 4.24, are plotted together in figure 4.30. The same results plotted versus Strouhal number on the convective velocity, cf. figures 4.28 and 4.29 above, are displayed together in figure 4.31. Here, the resistance and reactance are scaled to the average of their absolute value for each case. In the same way, scaling of the results for the L=5 cm aperture with transitional boundary layer flow VIII and sandpaper tripped turbulent boundary layer flow IX, depicted in figure 4.25, is performed. Also here the hyperbolic-tangent profile parameter is taken $m = 2$, the momentum thickness is that halfway the slit, at $x_s = 25$ mm, cf. figure 4.16. Results are shown in figure 4.32. Again the vertical dotted lines indicate the Strouhal number at which $\omega\theta/U_0 = 0.07$. The results for the 5 cm slot for boundary layer flows VIII and IX versus Strouhal number based on the mean flow velocity U_0, cf. figure 4.25, are plotted together in figure 4.33. The same results versus Strouhal number based on the convective velocity, cf. figure 4.32 above, are plotted together in figure 4.34. The resistance and reactance are scaled to the average of the absolute value for both cases.

Looking at figures 4.30 and 4.31 for the L=1 cm slot, the characteristic features in the non-dimensional scaled resistance and reactance are closer at the same Strouhal number for the different boundary layers when using U_c instead of U_0. Especially the results for laminar boundary layers I, II and III coincide very well. Also, the results for transitional boundary layer IV are much closer to those of the other boundary layers, when using the effective Strouhal number. Especially the transition of negative to positive resistance and corresponding peak in reactance, around $\omega L/U_c = 5$, coincides better. In the region where resistance is negative results for transitional boundary layer IV and turbulent boundary layer V become very similar, when using the convective velocity. For the L=5 cm slot, figures 4.33 and 4.34 show that using the convective velocity is mainly beneficial for the reactance, at least up to $\omega L/U_c = 13$. Comparing the results for the 1 cm slot and the 5 cm slot versus Strouhal number on the convective velocity, the characteristic features seem to be at a slightly lower Strouhal number for the 5 cm slot. Furthermore, it was already observed that for the 5 cm slot still oscillations in resistance and reactance are seen for higher Strouhal numbers, where resistance and reactance tend to zero for the 1 cm slot. This could be explained by the fact that the ratio of boundary layer or shear layer momentum thickness θ to slot width L is much smaller for the 5 cm slot compared to the 1 cm slot. When assuming that oscillations in the non-dimensional scaled resistance and reactance (that is deviation from a zero value) can only occur when hydrodynamic instability occurs, an estimate of the maximum Strouhal number where oscillations are still
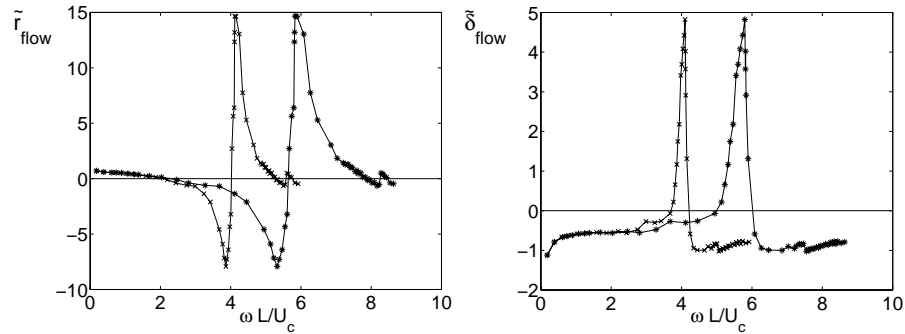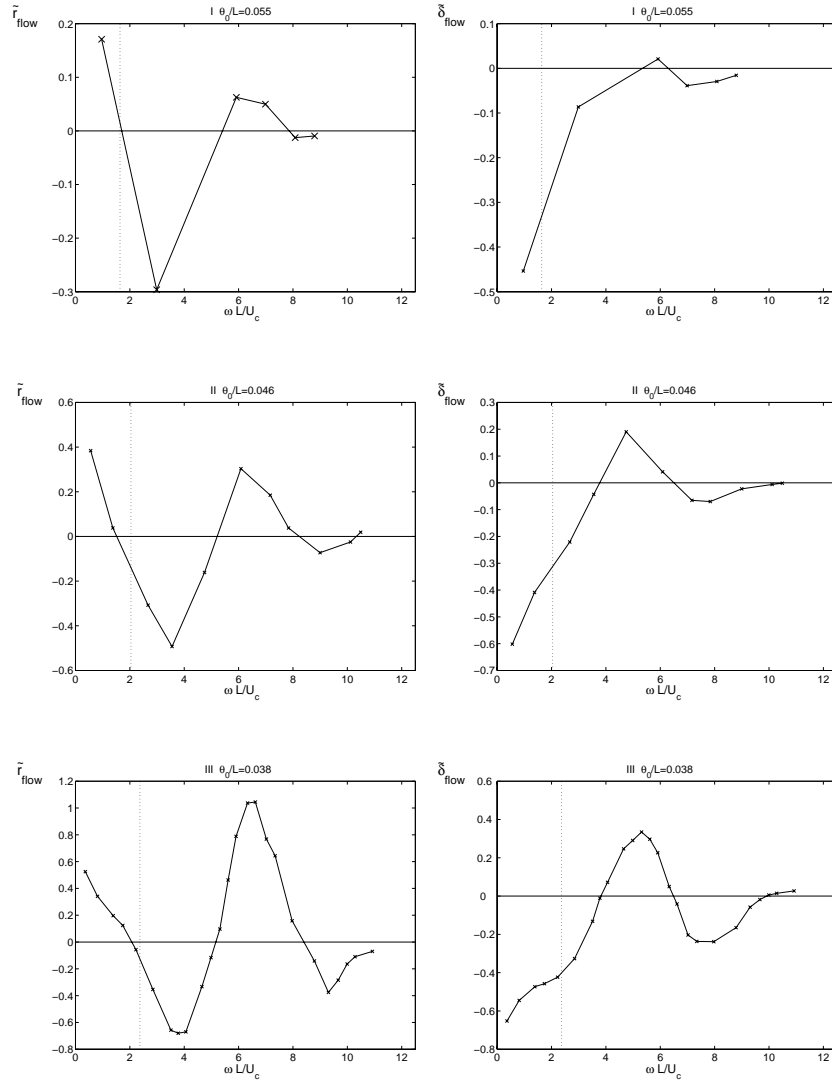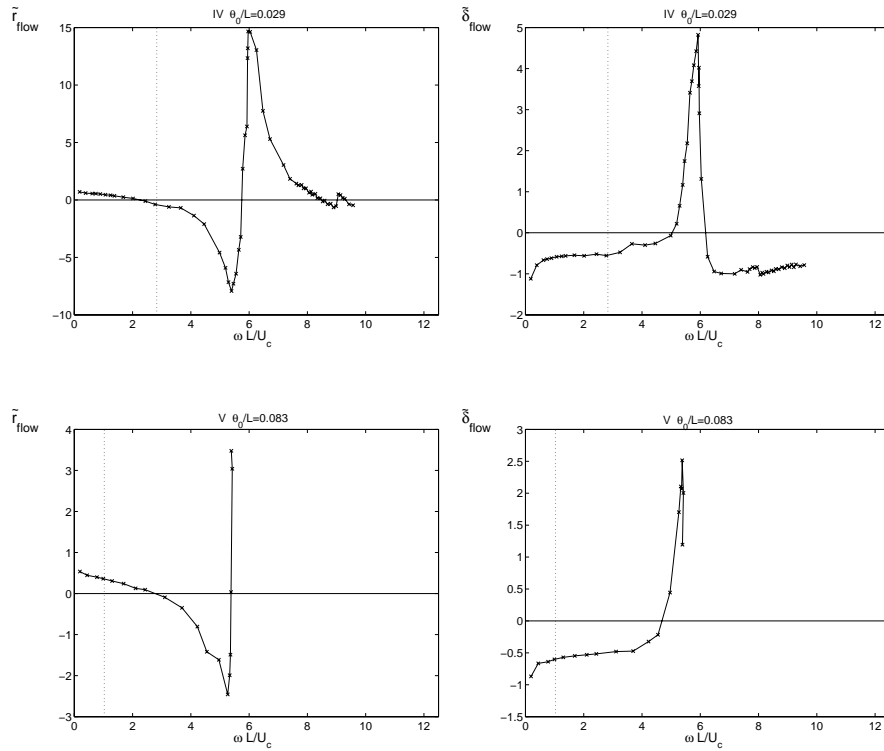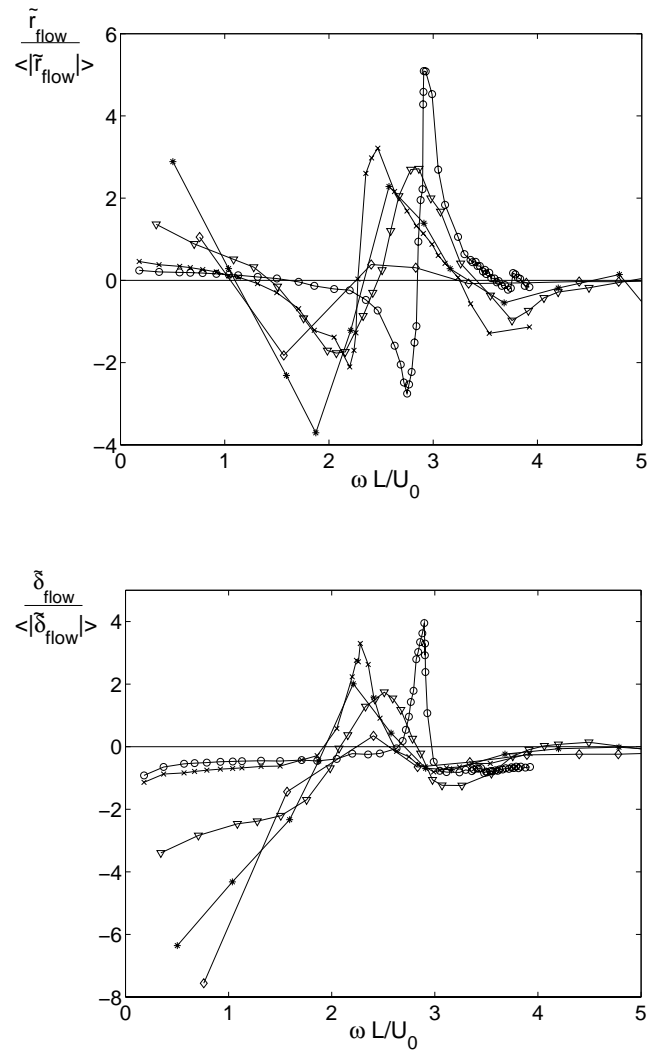
Figure 4.30: Non-dimensional scaled resistance and reactance for the $L{=}1$ cm orifice with double $27°$ edges for boundary layers I to V against Strouhal number on the mean flow velocity U_0: data of figures 4.23 and 4.24. The resistance and reactance are scaled to the average of their absolute value. $\diamond$ markers: BL I, $*$ markers: BL II, ∇ markers: BL III, $\circ$ markers bL IV, $\times$ markers: BL V.
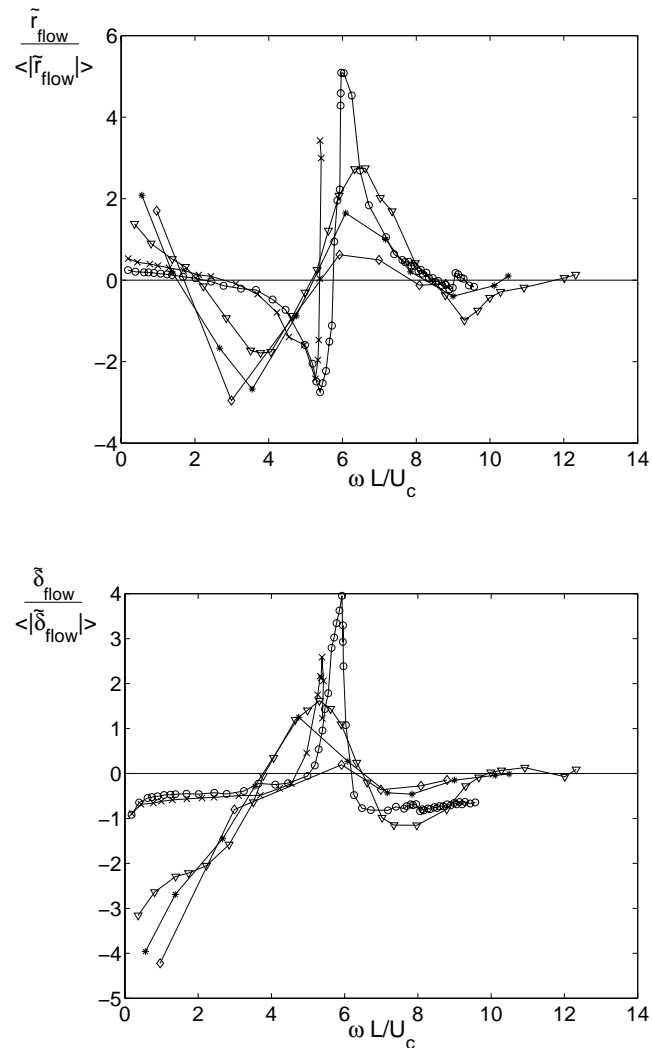
Figure 4.31: Non-dimensional scaled resistance and reactance for the L=1 cm orifice with double 27° edges for boundary layers I to V against Strouhal number based on the convective velocity U_c: data of figures 4.28 and 4.29. The resistance and reactance are scaled to the average of their absolute value. ⋄ markers: BL I, ∗ markers: BL II, ∇ markers: BL III, ∘ markers bL IV, × markers: BL V.

Figure 4.32: Non-dimensional scaled resistance and reactance for the $L{=}5$ orifice for transitional boundary layer VIII and turbulent boundary layer IX versus Strouhal number based on the convective velocity U_c. The convective velocity is calculated from Michalke's results, appendix B.2, for the generalized hyperbolic-tangent shear layer profile with $m = 2$. The momentum thickness is that halfway the slit, at $x_s = 25$ mm, cf. figure 4.15. The boundary layer momentum thickness θ_0 scaled to the slit width L is indicated for each case.

Figure 4.33: Non-dimensional scaled resistance and reactance for the $L{=}5$ orifice for transitional boundary layer VIII ($+$ markers) and turbulent boundary layer IX ($*$ markers) versus Strouhal number based on the mean flow velocity U_0: data of figure 4.25. The resistance and reactance are scaled to the average of their absolute value.
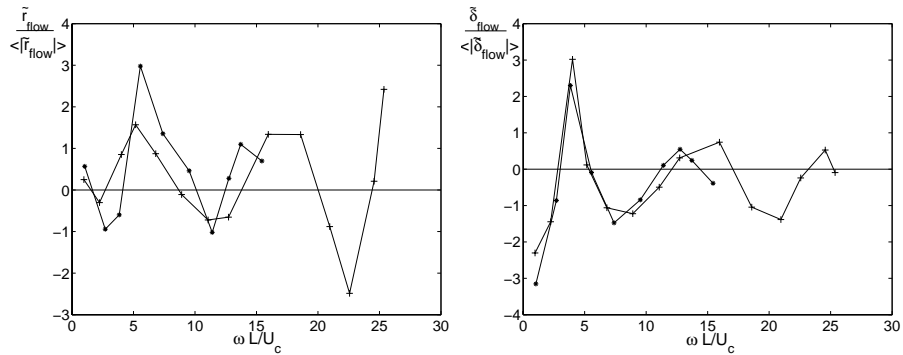
Figure 4.34: Non-dimensional scaled resistance and reactance for the $L{=}5$ orifice for transitional boundary layer VIII ($+$ markers) and turbulent boundary layer IX ($*$ markers) versus Strouhal number based on the convective velocity U_c: data of figure 4.32. The resistance and reactance are scaled to the average of their absolute value.

observed can be made. From appendix B.2, in particular figure B.2, it follows that for a shear layer with generalized hyperbolic-tangent profile hydrodynamic instability occurs up to a Strouhal number on the momentum thickness, $\omega\theta/U_0$, less than about 0.25. This value differs only slightly with profile parameter m. Using this, and the concerning ratios of boundary layer momentum thickness θ_0 (which is the minimum momentum thickness) to slit width L, the concerning maximum Strouhal number $\omega L/U_0$ is about 4.5, 5.4, 6.6, 8.6 and 3 for the 1 cm slot with boundary layer flows I to V respectively. For the 5 cm slot the values are indeed much higher, namely 43 and 15 for the boundary layer flows VIII respectively IX. The above mentioned numbers are fairly in agreement with what is observed in figures 4.30 and 4.33. It has to be noted that sandpaper tripped turbulent boundary layer flow V with the 1 cm slit seems to be a slight exception here, and for the 5 cm slot with transitional boundary layer VIII measurements could not be performed at sufficient high Strouhal number in order to assess where resistance and reactance due to the mean flow attenuate to zero.

4.7.6   Influence of edge geometry

The influence of the edge geometry of the orifice on the resistance and reactance due to grazing flow is investigated for the $L = 1$ cm slot with turbulent boundary layer flow V. The different edge geometries are as shown in figure 4.7. The slots with asymmetrical edge geometries, fig.4.7b and c, are used both with the sharp edge upstream and downstream. Results are given in figure 4.35. The edge geometry clearly affects the amplitudes of the oscillations in resistance and reactance. Compared to the double 90° edge geometry, the geometry with the single sharp 0° edge upstream gives nearly the same results. Results for the single sharp 27° edge upstream are also very similar regarding the reactance. For the resistance a more significant difference is seen, mostly in the region around a Strouhal number of 3, where it is positive, the resistance is larger. Placing the sharp edges downstream has a larger effect, especially for the 27° edge. The amplitudes of the oscillations in resistance are larger compared to both the double 90° edge geometry and the corresponding geometries with the sharp edge upstream. For the single sharp 0° edge downstream the reactance increases in the region where it is positive. For the 27° edge also a significant effect on the reactance is seen in the regions where it is negative. For the geometry with sharp 27° edges both upstream and downstream a slightly further increase is seen in the amplitude of the oscillations. In conclusion, mainly the downstream edge geometry affects the orifice impedance with grazing flow. The oscillations in non-dimensional scaled resistance and reactance are found to increase when sharp edges are used compared to the normal 90° edge geometry. The strongest effect is seen for the sharp 27° edges.
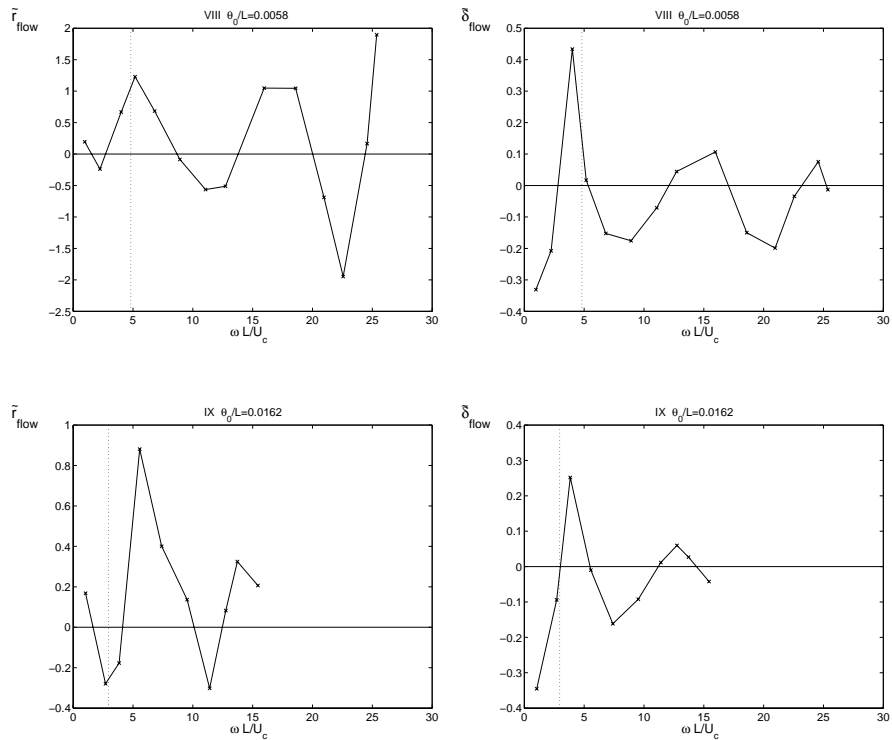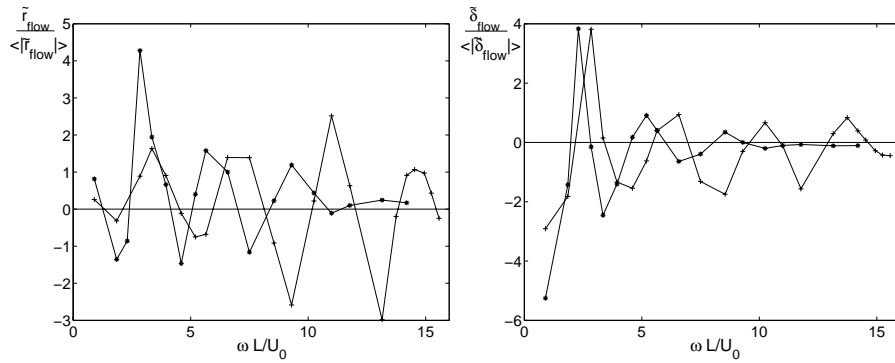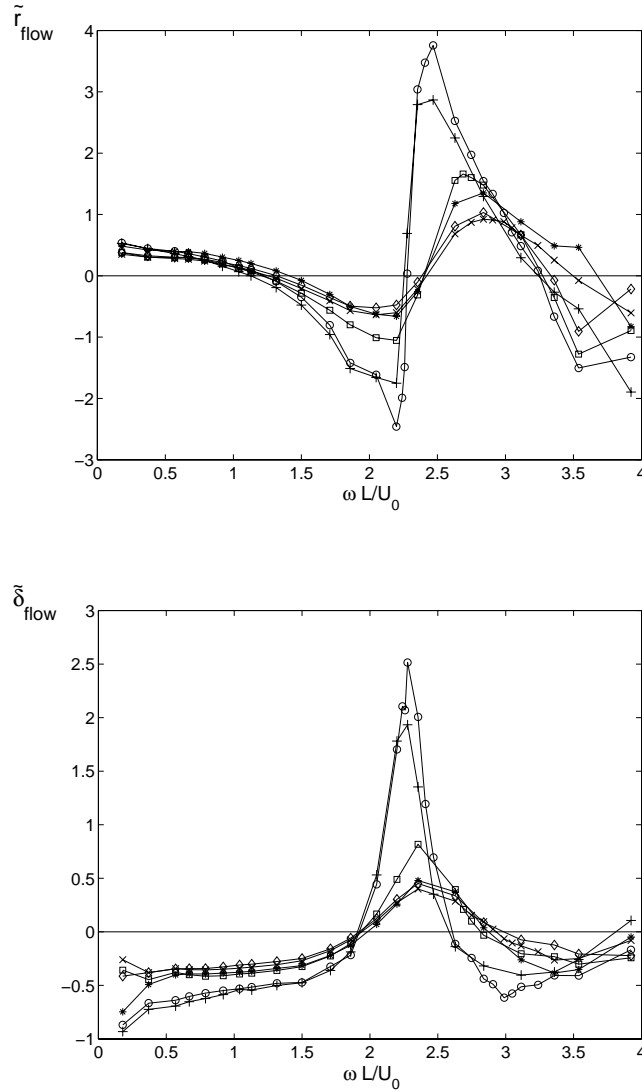
Figure 4.35: Non-dimensional scaled resistance and reactance for the $L{=}1$ orifice with different edge geometries, cf. figure 4.7, in case of boundary layer flow V. $\times$ markers: $90°$ edges both sides, $*$ markers: single sharp $27°$ edge upstream, $+$ markers: single sharp $27°$ edge downstream, $\circ$ markers: sharp $27°$ edges both sides, $\diamond$ markers: single sharp $0°$ edge upstream, $\square$ markers: single sharp $0°$ edge downstream.

4.8   Conclusion

The effect of grazing mean flow on the acoustical impedance of a rectangular orifice is investigated experimentally. For this purpose an impedance tube set-up with an accurate multi-microphone technique is used.

Measurements are done for slots with different width L in the flow direction, viz. 1 cm and 5 cm. Furthermore, different boundary layer flows, both laminar and turbulent, are considered. In this context boundary layer characterization as well as shear layer profile measurements are carried out.

Both resistance and reactance due to the grazing flow display an oscillating behaviour as function of Strouhal number on the orifice width. By using the phase velocity U_c of the hydrodynamic instability, these oscillations are more or less found at the same Strouhal numbers $\omega L/U_c$ for all configurations. On basis of the shear layer profile measurements, this convective velocity is (roughly) calculated using data for the generalized hyperbolic-tangent profile given in literature.

The presence of hydrodynamic instability, which is for given profile dependent on the Strouhal number $\omega\theta/U_0$ based on the shear layer momentum thickness θ and main flow velocity outside the boundary layer/shear layer U_0, seems to govern the presence of the oscillations in resistance and reactance. Above a certain Strouhal number the hydrodynamic instability as well as the oscillations vanish. Consequently, the ratio of slot width to momentum thickness determines the number of oscillations seen.

For boundary layers with similar shape the amplitudes of the oscillations increase with decreasing boundary layer thickness (for fixed aperture width). Furthermore, the onset of non-linearity seems to be at lower amplitudes within the regions of strong oscillations in impedance.

The influence of the edge geometry has been investigated for the 1 cm wide slot. The amplitudes of the oscillations in resistance and reactance due to the grazing flow were observed to be larger for sharp edge geometries. Especially, the form of the downstream edge is important.

Chapter 5

Grazing flow over an orifice: modal analysis

5.1 Introduction

In this chapter the effect of grazing flow on the acoustical properties of an orifice in a wall will be modelled using modal analysis. First, the considered geometry and the accompanying matching procedure to obtain a scattering matrix for this specific problem will be given. Also the calculation of an orifice impedance from the scattering matrix will be treated.

First, as a test, calculations are done for the orifice geometry without any mean flow. Convergence of the model is treated and comparison with potential theory is made for the scattering at the orifice and the singular behaviour of the acoustic field at the orifice's edges.

Next, model calculations for a uniform grazing flow are presented. Also here, convergence of the model is investigated, and the behaviour of the acoustic field near the edges is addressed. Furthermore, results are compared with the theoretical prediction by Howe' source model [47], appendix A. In particular attention is given here to the influence of the geometrical ratios in the orifice configuration.

Finally, the effect of non-uniform grazing flow on orifice impedance is modelled. Convergence is treated and influence of grazing flow boundary layer thickness is investigated. Model results are compared to experimental data from chapter 4.

Also, for the configurations with mean grazing flow, the effect of calculating orifice impedance from either a pressure difference or a one-sided pressure on the results for non-dimensional scaled resistance and reactance is discussed.

5.2   Mode matching

The considered geometry is given in figure 5.1. Basically, it consists of two parallel two-dimensional rectangular ducts infinite in the x-direction with height h_1 and h_2 respectively. The lower one carries mean flow $U(y)$, while in the upper duct the fluid is quiescent. The orifice is represented by an interconnection with length L between the two ducts. The complete geometry is divided into five ducts indicated by the boxed numbers. The mean flow profile in duct 1 continues unaltered in the orifice region duct 3, and subsequently in duct 4. The acoustic pressure and velocity in each duct is determined as an expansion of eigenmodes, calculated according to chapter 2. Matching, i.e applying continuity of the relevant variables, at the interfaces between ducts 1 and 2 and duct 3 as well as between ducts 4 and 5 and duct 3 gives the acoustical behaviour of the orifice geometry in the form of a scattering matrix.

The mode matching procedure is similar in most aspects to that for the area expansion in a duct. For the basics one is referred to section 3.2, where this has been discussed extensively for different mean flow configurations, viz. non-uniform flow, uniform flow and non-uniform flow with slip. Here, only the mode matching procedure for non-uniform flow with slip will be dealt with explicitly, as it is the most extensive one. For this flow configuration it namely contains all aspects of the non-uniform flow configuration as well as the application of the Kutta condition, which is also relevant for uniform flow. An extension to uniform flow and non-uniform flow is easily made.

Ducts 1 and 4 in figure 5.1 have height h_1 and number of points in y-direction N_1, ducts 2 and 5 have height h_2 and number of points N_2. Consequently, duct 3 has height $h_3 = h_1 + h_2$ with $N_3 = N_1 + N_2$ points. In duct 1 eigenmodes and
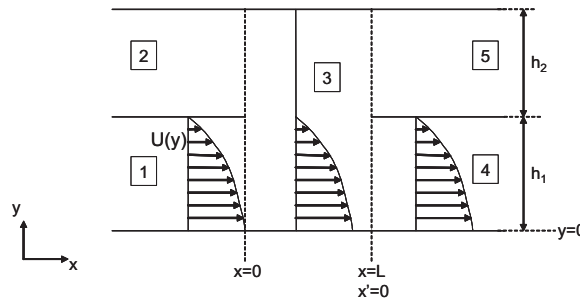

Figure 5.1: Considered geometry for modelling the effect of grazing flow on the acoustical behaviour of an orifice by modal analysis. The orifice is represented by an interconnection between two parallel two-dimensional rectangular ducts infinite in x-direction. The lower duct carries mean grazing flow $U(y)$.

wavenumbers are calculated according to section 2.2. N_1 acoustic and N_1 neutral hydrodynamic modes propagating (or decaying) in the $+x$-direction and N_1 acoustic modes propagating or decaying in the $-x$-direction are found. In duct 2 mean flow is absent, the modes are solved according to section 2.4, equation (2.20) with Mach number $M_0 = 0$. Here, N_2 acoustic modes propagating or decaying in either direction are found. Clearly, duct 4 is identical to duct 1, and duct 5 is identical to duct 2, concerning their eigenmodes and wavenumbers. In duct 3 the modes are determined according to section 2.5. This gives N_3 acoustic modes and $N_1 + 2$ hydrodynamic modes propagating in $+x$-direction and N_3 acoustic modes propagating/decaying in $-x$-direction. Continuity of the non-dimensional pressure and velocity disturbance p_* resp. v_*, and continuity of $q_* = \mathrm{i}\frac{\partial p_*}{\partial x_*}$, cf. appendix D, at the interfaces at $x = 0$ and $x = L$ as well as the Kutta condition at the upstream edge gives the following set of equations:

$$
\begin{aligned}
\mathbf{Q_1^+ C_1^+} + \mathbf{Q_1^- C_1^-} &= \mathbf{Q_3^+ C_3^+} + \mathbf{Q_3^- C_3^-} \quad \left.\right\} N_1 \\
\mathbf{Q_2^+ C_2^+} + \mathbf{Q_2^- C_2^-} &= \phantom{\mathbf{Q_3^+ C_3^+} + \mathbf{Q_3^- C_3^-}} \quad \left.\right\} N_2
\end{aligned}
$$

$$
\mathbf{V_1^+ C_1^+} + \mathbf{V_1^- C_1^-} = \mathbf{V_3^+ C_3^+} + \mathbf{V_3^- C_3^-} \quad \left.\right\} N_1
$$

$$
\begin{aligned}
\mathbf{P_1^+ C_1^+} + \mathbf{P_1^- C_1^-} &= \mathbf{P_3^+ C_3^+} + \mathbf{P_3^- C_3^-} \quad \left.\right\} N_1 \\
\mathbf{P_2^+ C_2^+} + \mathbf{P_2^- C_2^-} &= \phantom{\mathbf{P_3^+ C_3^+} + \mathbf{P_3^- C_3^-}} \quad \left.\right\} N_2
\end{aligned}
$$

$$
\begin{aligned}
\mathbf{Q_1^+ C_4^+} + \mathbf{Q_1^- C_4^-} &= \mathbf{Q_3^+ C_3^{+\prime}} + \mathbf{Q_3^- C_3^{-\prime}} \quad \left.\right\} N_1 \\
\mathbf{Q_2^+ C_5^+} + \mathbf{Q_2^- C_5^-} &= \phantom{\mathbf{Q_3^+ C_3^{+\prime}} + \mathbf{Q_3^- C_3^{-\prime}}} \quad \left.\right\} N_2
\end{aligned} \qquad (5.1)
$$

$$
\mathbf{V_1^+ C_4^+} + \mathbf{V_1^- C_4^-} = \mathbf{V_3^+ C_3^{+\prime}} + \mathbf{V_3^- C_3^{-\prime}} \quad \left.\right\} N_1
$$

$$
\begin{aligned}
\mathbf{P_1^+ C_4^+} + \mathbf{P_1^- C_4^-} &= \mathbf{P_3^+ C_3^{+\prime}} + \mathbf{P_3^- C_3^{-\prime}} \quad \left.\right\} N_1 \\
\mathbf{P_2^+ C_5^+} + \mathbf{P_2^- C_5^-} &= \phantom{\mathbf{P_3^+ C_3^{+\prime}} + \mathbf{P_3^- C_3^{-\prime}}} \quad \left.\right\} N_2
\end{aligned}
$$

$$
\mathbf{V_{nf}^+ C_3^+} + \mathbf{V_{nf}^- C_3^-} = 0
$$

$$
\mathbf{V_{nf}^+ k_3^+ C_3^+} + \mathbf{V_{nf}^- k_3^- C_3^-} = 0
$$

Here the columns of $\mathbf{Q}$, $\mathbf{V}$ and $\mathbf{P}$ contain the modes for $\mathbf{q}_*$, $\mathbf{v}_*$ and $\mathbf{p}_*$. A distinction in $+x$ (right) running and $-x$ (left) running modes is made by the additional superscripts $+$ and $-$ respectively. The subscripts indicate the duct number, cf. figure 5.1. Since the matrices containing the modes for duct 4 and 5 are identical to those for duct 1 respectively duct 2, they have subscripts 1 and 2. $\mathbf{V_{nf}}$ contains the modes for the

velocity disturbance at the no flow side of the interface between mean flow and still fluid in duct 3. Matrix $\mathbf{k_3}$ contains the wavenumbers in duct 3 on the diagonal. The vectors $\mathbf{C}$ contain the coefficients of the modes. The modes in duct 1, 2 and 3 are taken with respect to x, such that the x-dependence of the acoustic disturbances is $\exp(-\mathrm{i}kx)$. The modes in duct 4 and 5 are taken with respect to $x' = x - L$, thus acoustic disturbances have $\exp(-\mathrm{i}kx')$ as x-dependence. Consequently, in the matching between ducts 3 and ducts 4 and 5 the modes in duct 3 are shifted. This is accounted for in the coefficients for the modes in duct 3, and is reflected by the additional accent in vectors $\mathbf{C}$, cf. equation (5.1). In this context the following relations hold:

$$\mathbf{C}_3^{+'} = \mathbf{E}^+ \mathbf{C}_3^+, \tag{5.2}$$
$$\mathbf{C}_3^- = \mathbf{E}^- \mathbf{C}_3^{-'}.$$

Here, matrices $\mathbf{E}^+$ and $\mathbf{E}^-$ contain the corresponding values of $\exp(-\mathrm{i}k_3^+ L)$ respectively $\exp(\mathrm{i}k_3^- L)$ on the diagonal. Equations (5.1) are written in a single matrix equation:

$$\underbrace{\begin{pmatrix}
-\mathbf{Q}_1^- & 0 & 0 & 0 & \mathbf{Q}_3^+ & \mathbf{Q}_3^- \mathbf{E}^- \\
0 & -\mathbf{Q}_2^- & 0 & 0 & & \\
-\mathbf{V}_1^- & 0 & 0 & 0 & \mathbf{V}_3^+ & \mathbf{V}_3^- \mathbf{E}^- \\
-\mathbf{P}_1^- & 0 & 0 & 0 & \mathbf{P}_3^+ & \mathbf{P}_3^- \mathbf{E}^- \\
0 & -\mathbf{P}_2^- & 0 & 0 & & \\
0 & 0 & -\mathbf{Q}_1^+ & 0 & \mathbf{Q}_3^+ \mathbf{E}^+ & \mathbf{Q}_3^- \\
0 & 0 & 0 & -\mathbf{Q}_2^+ & & \\
0 & 0 & -\mathbf{V}_1^+ & 0 & \mathbf{V}_3^+ \mathbf{E}^+ & \mathbf{V}_3^- \\
0 & 0 & -\mathbf{P}_1^+ & 0 & \mathbf{P}_3^+ \mathbf{E}^+ & \mathbf{P}_3^- \\
0 & 0 & 0 & -\mathbf{P}_2^+ & & \\
0 & 0 & 0 & 0 & \mathbf{V}_{nf}^+ & -\mathbf{V}_{nf}^- \mathbf{E}^- \\
0 & 0 & 0 & 0 & \mathbf{V}_{nf}^+ \mathbf{k}_3^+ & -\mathbf{V}_{nf}^- \mathbf{k}_3^- \mathbf{E}^-
\end{pmatrix}}_{\mathbf{S_1}}
\begin{pmatrix}
\mathbf{C}_1^- \\ \mathbf{C}_2^- \\ \mathbf{C}_4^+ \\ \mathbf{C}_5^+ \\ \mathbf{C}_3^+ \\ \mathbf{C}_3^{-'}
\end{pmatrix} =$$

$$\underbrace{\begin{pmatrix}
\mathbf{Q}_1^+ & 0 & 0 & 0 \\
0 & \mathbf{Q}_2^+ & 0 & 0 \\
\mathbf{V}_1^+ & 0 & 0 & 0 \\
\mathbf{P}_1^+ & 0 & 0 & 0 \\
0 & \mathbf{P}_2^+ & 0 & 0 \\
0 & 0 & \mathbf{Q}_1^- & 0 \\
0 & 0 & 0 & \mathbf{Q}_2^- \\
0 & 0 & \mathbf{V}_1^- & 0 \\
0 & 0 & \mathbf{P}_1^- & 0 \\
0 & 0 & 0 & \mathbf{P}_2^- \\
0 & 0 & 0 & 0 \\
0 & 0 & 0 & 0
\end{pmatrix}}_{\mathbf{S_2}}
\begin{pmatrix}
\mathbf{C}_1^+ \\ \mathbf{C}_2^+ \\ \mathbf{C}_4^- \\ \mathbf{C}_5^-
\end{pmatrix}. \tag{5.3}$$

Here, matrix $\mathbf{S_1}$ is square with $6N_1 + 4N_2 + 2$ rows and columns. matrix $\mathbf{S_2}$ is $6N_1 + 4N_2 + 2$ rows by $3N_1 + 2N_2$ columns. The scattering matrix $\mathbf{S}$ is given by: $\mathbf{S} = \mathbf{S_1}^{-1}\mathbf{S_2}$. It relates the coefficients of the modes propagating/decaying away from the orifice region duct 3 as well as the coefficients of the modes in duct 3 to the coefficients of the modes propagating/decaying towards the orifice region:

$$\begin{pmatrix} \mathbf{C_1^-} \\ \mathbf{C_2^-} \\ \mathbf{C_4^+} \\ \mathbf{C_5^+} \\ \mathbf{C_3^+} \\ \mathbf{C_3^-}{}' \end{pmatrix} = \mathbf{S} \begin{pmatrix} \mathbf{C_1^+} \\ \mathbf{C_2^+} \\ \mathbf{C_4^-} \\ \mathbf{C_5^-} \end{pmatrix}. \tag{5.4}$$

Note that in equation (5.3) the $+x$ propagating / decaying acoustic modes in duct 3 are counted from the left side, whereas the $-x$ propagating / decaying acoustic modes are counted from the right side. This is reflected by the use of coefficient vectors $\mathbf{C_3^+}$ and $\mathbf{C_3^-}{}'$, and results in the use of the above defined matrices $\mathbf{E}^+$ and $\mathbf{E}^-$, which account for the propagation/decaying of the corresponding modes in duct 3. Here, for the evanescent acoustic modes, both $\mathbf{E}^+$ and $\mathbf{E}^-$ contain exponentially small numbers. By doing so, the occurrence of both very large and very small numbers in rows and columns of matrix $\mathbf{S_1}$, possibly leading to difficulties in the inversion, is reduced. If namely both the $+x$ and $-x$ propagating / decaying acoustic modes in duct 3 were counted from, say, the left side, matrices would have to be used, analogous to $\mathbf{E}^+$ and $\mathbf{E}^-$, which contain exponentially small numbers for the $+x$ decaying acoustic modes and exponentially large numbers for the $-x$ decaying acoustic modes.

5.3 Calculation of the impedance

As in the previous chapter, the acoustical behaviour of the orifice with grazing flow will be expressed in terms of an impedance. The impedance Z_h of an orifice was given by equation (4.3) for the low frequency limit. For the orifice geometry considered here, figure 5.1, the impedance can be calculated from the propagation of the plane waves. Figure 5.2 shows the geometry again, here also the Fourier transformed (that is with the factor $\exp(\mathrm{i}\omega t)$ dropped) plane wave acoustic pressures and velocities (in x-direction) in ducts 1 to 4 at the interface with the orifice region duct 3 are indicated. The plane wave pressure at these interfaces is just the sum of the pressure amplitude of the plane wave propagating to the right and the pressure amplitude of the plane wave propagating to the left: $p_1 = p_1^+ + p_1^-$ etcetera. As an approximation the pressure p_- at the no flow side, in this case above the orifice, is given by the average of pressures p_2 and p_5. Similarly, the pressure p_+ at the mean flow side, beneath the orifice, is given by the average of p_1 and p_4. The area averaged acoustic velocity u_h through

the orifice is calculated by taking the volume in duct 3 above the orifice as a control volume to which continuity of mass is applied. In linearized form:

$$\frac{\partial}{\partial t}\iiint_V \rho' dV + \iint_S \rho_0(\overrightarrow{n} \cdot \overrightarrow{v}')\mathrm{d}S = 0, \tag{5.5}$$

with ρ_0 the mean mass density and ρ' the acoustic density disturbance and v' the acoustic velocity. With the harmonic time dependence $\exp(\mathrm{i}\omega t)$ of the acoustic variables, and with $p' = c_0^2\rho'$, we have:

$$u_h = \frac{h_2}{L}(u_2 - u_5) - \mathrm{i}\frac{\omega h_2}{\rho_0 c_0^2}p_-. \tag{5.6}$$

With $u_2 = (p_2^+ - p_2^-)/\rho_0 c_0$ and $u_5 = (p_5^+ - p_5^-)/\rho_0 c_0$, see for example equation (4.9), and the non-dimensionalization employed with modal analysis, cf. equation (2.8), this becomes:

$$u_{h*} = \frac{h_{2*}}{L_*}\big((p_{2*}^+ - p_{2*}^-) - (p_{5*}^+ - p_{5*}^-)\big) - \mathrm{i}\omega_* h_{2*}p_{-*}. \tag{5.7}$$

Duct height h_1 is used here as characteristic length scale. All the quantities of interest are now expressed in the dimensionless pressures. In the modal analysis the amplitudes of the plane wave modes are normalized to unity. So for p_{1*}^+ and p_{1*}^- the coefficient $\mathbf{C_1^+}(1)$ respectively $\mathbf{C_1^-}(1)$ can be used, etcetera. Furthermore, the impedance, given
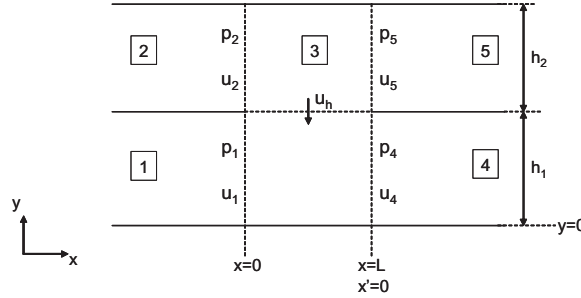
Figure 5.2: Orifice geometry in the modal analysis method, also shown in figure 5.1. Here the relevant quantities for calculating the orifice impedance are indicated: $p_{1,2,4,5}$ are the pressure disturbances due to the plane waves in ducts 1,2,4 and 5 respectively at the interface with orifice region duct 3, u_h is the (area averaged) acoustic velocity through the orifice. u_h is calculated from the acoustic velocities due to the plane waves in duct 2 and 5 (no mean flow side of the orifice) at the interface with duct 3, where also the compressibility of the volume above the orifice is accounted for.

in equation (4.3), is expressed in non-dimensional variables:

$$Z_h = \frac{p_{-*} - p_{+*}}{u_{h*}}. \tag{5.8}$$

Note that in the calculations of impedance a symmetric plane wave excitation above the orifice will be used. This means that plane waves propagating towards the orifice region are imposed in ducts 2 and 5. In ducts 1 and 4 beneath the orifice, where mean flow is present, an anechoic condition is applied. This means that no modes propagate there towards the orifice region.

5.4 No mean flow

First, as a test the results of the modal analysis method for the current orifice geometry will be studied in case no mean flow is present. Convergence in the calculation of the impedance without mean flow (a quantity which is used later on to calculate the non-dimensional scaled resistance and reactance due to mean flow) as well as convergence of the modal expansions will first be treated. Subsequently, results of the current model for the scattering at the orifice as well as the singular behaviour of the acoustic disturbances at the edges of the orifice will be compared to what is predicted by potential theory.

5.4.1 Convergence

Calculation of the orifice impedance without grazing mean flow Z_{h0}, according to section 5.3, has been done in case dimensionless frequency is $\omega h_1/c_0 = 0.01$ and ratio of duct heights and slit width is $h_1 = h_2 = L$ for different numbers of points N_1 in duct 1. The relative error ΔZ_{h0} as function of the number of points N_1 is shown in figure 5.3. Here, the relative error is defined as the relative difference between the value calculated with N_1 points and with $N_1 = N_{ref}$ points:

$$\Delta Z_{h0,N_1} = \left| \frac{Z_{h0,N_1} - Z_{h0,N_{ref}}}{Z_{h0,N_{ref}}} \right|.$$

In this case for the reference value: $N_{ref} = 200$. The absolute value of the relative error in the orifice impedance approximately decreases as $N_1^{-1.13}$ up to $N_1 = 60$.

Besides the convergence of the calculated orifice impedance, also the convergence of the modal expansion in the orifice region duct 3, cf. figure 5.1, is of interest. For the same configuration as above: $\omega h_1/c_0 = 0.01$, $h_1 = h_2 = L$, with number of points $N_1 = N_2 = 100$, $N_3 = 200$, figure 5.4 shows the absolute value of the coefficients $\mathbf{C}_3^+(n)$ of the acoustic modes propagating/decaying in the $+x$-direction (which are counted from the upstream edge of the orifice), and the absolute value of the coefficients $\mathbf{C}_3^{-\prime}(n)$

of the acoustic modes propagating/decaying in the $-x$-direction (which are counted from the downstream edge of the orifice) as function of the index n of the modes on a log-log scale. Note that in order to obtain a useful comparison of the value of the coefficients, each corresponding mode (with index n) for the pressure disturbance $\mathbf{P}_{e,n}$ is normalized such that:

$$\frac{1}{N_3} \sum_{i=1}^{i=N_3} |\mathbf{P}_{e,n}(i)|^2 = 1.$$

For both $+x$ and $-x$ propagating/decaying modes the coefficients approximately decrease as $n^{-1.7}$ above $n = 1$.
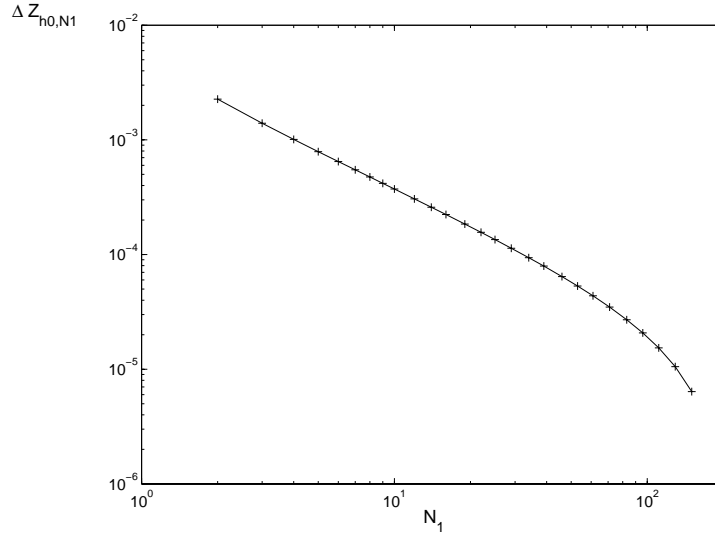
Figure 5.3: Convergence of calculated orifice impedance Z_{h0} without grazing mean flow. The relative error $\Delta Z_{h0,N_1}$ in Z_{h0} with respect to a reference value is plotted versus number of points N_1 in duct 1 on a log-log scale. Number of points used for calculation of reference value $N_1 = N_{ref} = 200$. Up to $N_1 = 60$ the relative error decreases approximately as $N_1^{-1.13}$. Dimensionless frequency $\omega h_1/c_0 = 0.01$, $h_1 = h_2 = L$.
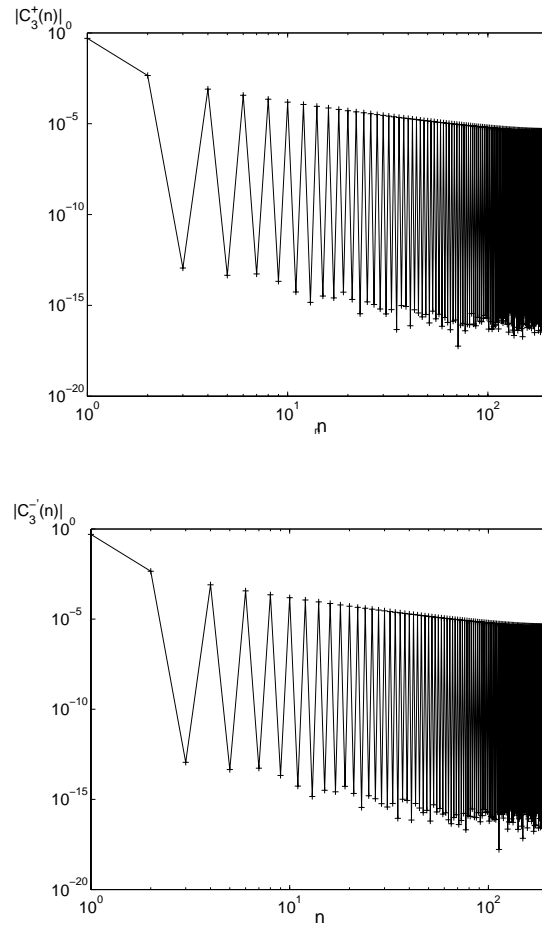
Figure 5.4: Absolute value of the coefficients $\mathbf{C}_3^+(n)$ of the acoustic modes propagating/decaying in the $+x$-direction (which are counted from the upstream edge of the orifice), and the absolute value of the coefficients $\mathbf{C}_3^{-'}(n)$ of the acoustic modes propagating/decaying in the $+x$-direction (which are counted from the downstream edge of the orifice) as function of the index n of the modes on a log-log scale in absence of mean flow. Absolute value of the coefficients decreases as $n^{-1.7}$. Dimensionless frequency $\omega h_1/c_0 = 0.01$, $h_1 = h_2 = L$, number of discrete points $N_1 = N_2 = 100$, $N_3 = 200$.

5.4.2   Comparison with potential theory

In case grazing mean flow is absent, the acoustic behaviour of the present orifice geometry can also be modelled with potential theory. For this purpose a conformal mapping of the geometry is employed, see for instance Morse and Feshbach [73] and Morse and Ingard [74]. First, the results for the scattering of plane waves at the orifice geometry obtained by the modal analysis method will be compared to what is predicted by potential theory. Subsequently, the behaviour of the acoustic field close to the edges of the orifice as obtained by modal analysis is compared to the singular behaviour found in potential theory.

Scattering

The present orifice geometry is considered with duct heights $h_1 = h_2$ and ratio of slit width to duct height $L/h_1 = 0.1271$. In the modal analysis calculations number of points is $N_1 = N_2 = 100$. In duct 2 and duct 5 plane waves are sent towards the orifice region duct 3, yielding a symmetric excitation. The ducts 1 and 4 beneath the orifice are anechoic, i.e. no acoustic waves here propagate towards the orifice region. Due to the symmetry of the configuration (there is no mean flow) the reflection coefficient of the plane waves is $R = \mathbf{C_2^-}(1)/\mathbf{C_2^+}(1) = \mathbf{C_5^+}(1)/\mathbf{C_5^-}(1)$, and the transmission coefficient can be defined as $T = \mathbf{C_1^-}(1)/\mathbf{C_2^+}(1) = \mathbf{C_4^+}(1)/\mathbf{C_5^-}(1)$. Results for the reflection and transmission coefficient obtained by modal analysis are compared with the results of potential theory in figure 5.5. Good correspondence is observed. For higher frequency the deviation between modal analysis results and potential theory increases, especially for the phases. This is expected as the potential theory is only valid in the low frequency limit. Note that for the case without mean flow the scattering results obtained by the present discretized modal analysis are also compared to results obtained by an analytical modal analysis model. Excellent agreement was observed.

Edge singularity

For non-viscous flow the acoustic velocity at the edges of the orifice goes to infinity. In potential theory the acoustic velocity v' in the vicinity of an edge is proportional to one over the square root of the distance r from the edge: $v' \propto r^{-\frac{1}{2}}$, yielding $1/v'^2 \propto r$. For the present orifice configuration a modal analysis calculation is performed for dimensionless frequency $\omega h_1/c_0 = 0.01$, $h_1 = h_2 = L$, and number of points $N_1 = 100$ in case a symmetric excitation with plane waves is imposed (as above). The acoustic velocity in the y-direction, $\mathbf{v_*}$ in dimensionless and discretized form, is obtained from the summation of the velocity modes $\mathbf{V}$. These velocity modes are obtained from the solved pressure modes P according to equation (2.15), where a Mach number equal to zero is substituted. The acoustic velocity at the left interface of orifice region duct 3, i.e. at the x position of the left edge of the orifice, is plotted against position y_*, as
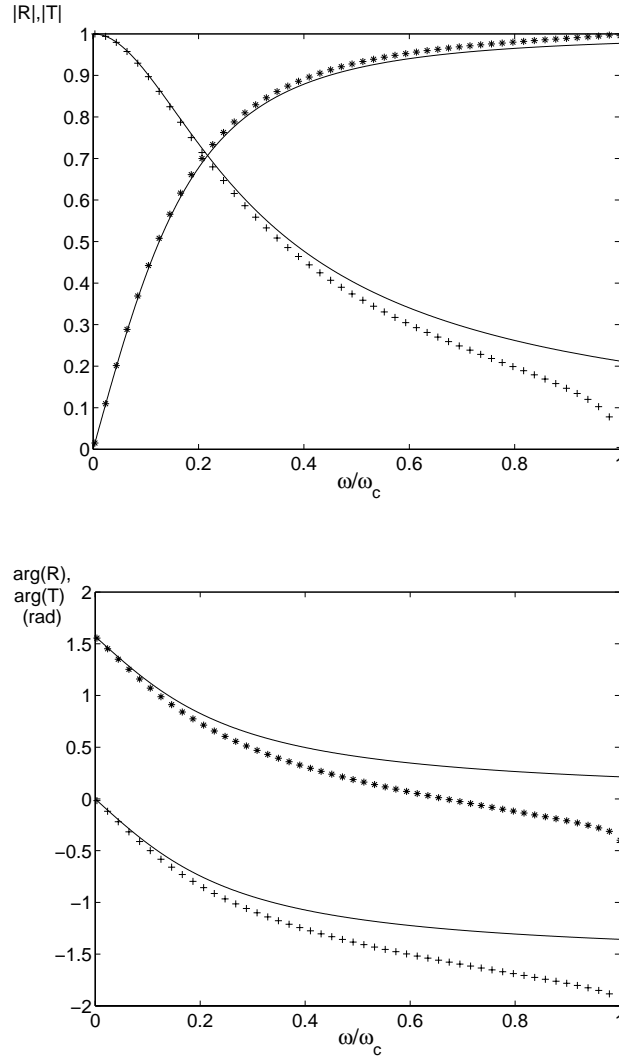
Figure 5.5: Absolute value and phase of the reflection coefficient R ($*$ markers), and transmission coefficient T ($+$ markers) calculated with modal analysis method compared to potential theory (corresponding solid lines). On the horizontal axis is the angular frequency divided by the cut-off angular frequency ω_c of the first higher order mode in duct 1 ($\omega_c h_1/c_0 = \pi$). Configuration: $h_1 = h_2$, $L/h_1 = 0.1271$, $N_1 = N_2 = 100$.
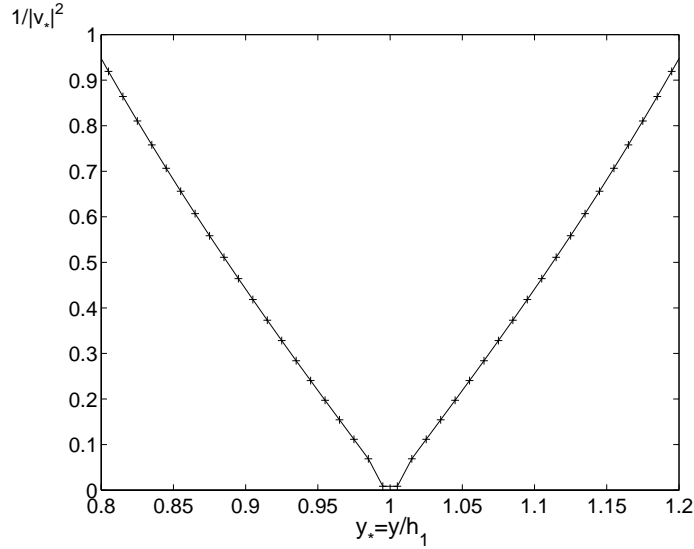
Figure 5.6: Singular behaviour of (non-dimensional) acoustic velocity v_* near the edge of the orifice at $y_* = y/h_1 = 1$. In modal analysis calculations proportionality between $1/|v_*|^2$ and the distance from the edge is found, consistent with potential theory. Configuration: dimensionless frequency $\omega h_1/c_0 = 0.01$, $h_1 = h_2 = L$, $N_1 = 100$.

$1/|v_*|^2$ versus y_* in figure 5.6. Note that the edge is at $y_* = y/h_1 = 1$. For the right orifice edge the same result is obtained due to the symmetry of the configuration. Indeed, near the edge proportionality between $1/|v_*|^2$ and the distance from the edge is found.

5.5   Uniform flow

For uniform grazing flow results of the modal analysis method can be compared to those of the model of Howe, appendix A. The difference in geometry surrounding the orifice, i.e. ducts versus free space respectively, is overcome by using the non-dimensional scaled resistance and reactance due to the mean flow, defined in equation (4.6). As shown these quantities are in fact derived as parameters independent on surrounding geometry on basis of Howe's results for a rectangular slot. Besides comparing the results of the two models, first the convergence of the modal analysis method, the behaviour of the solution near the orifice's edges and the formalism of calculating the impedance (using pressure difference or one-sided pressure) will be addressed. Fur-

thermore, attention will be given to the influence of the ratio of the duct heights and slit width in the currently used orifice geometry.

5.5.1 Convergence

The non-dimensional scaled resistance $\tilde{r}_{flow}$ and reactance $\tilde{\delta}_{flow}$ due to grazing mean flow is calculated as function of the number of discrete points in case the dimensionless frequency is $\omega_* = \omega h_1/c_0 = 0.01$, and the duct heights h_1 and h_2 and slit width L are equal: $h_1 = h_2 = L$. Figure 5.7 shows a log-log plot of the relative error $\Delta \tilde{r}_{flow}$ and $\Delta \tilde{\delta}_{flow}$ as function of the number of points N_1 in duct 1. Here, the relative error in the non-dimensional scaled resistance is defined as:

$$\Delta \tilde{r}_{flow,N_1} = \left| \frac{\tilde{r}_{flow,N_1} - \tilde{r}_{flow,N_{ref}}}{\tilde{r}_{flow,N_{ref}}} \right|.$$

with $\tilde{r}_{flow,N_1}$ the calculated value of $\tilde{r}_{flow}$ with N_1 points, and $\tilde{r}_{flow,N_{ref}}$ the value with a reference number of points N_{ref}. Here $N_{ref} = 200$. For the error in the non-dimensional scaled reactance an analogous equation holds. For different Strouhal numbers about the same convergence rate is seen in $\tilde{r}_{flow}$ and $\tilde{\delta}_{flow}$. The relative error $\Delta \tilde{r}_{flow,N_1}$ and $\Delta \tilde{\delta}_{flow,N_1}$ decrease approximately as $N_1^{-1.35}$. Note that for some Strouhal numbers the relative error in $\tilde{r}_{flow}$ is quite large. This is caused by the fact that at these Strouhal numbers the value for $\tilde{r}_{flow}$ is close to zero.

Besides the convergence of the result for the non-dimensional scaled resistance and reactance also the convergence of the modal expansion in the orifice region duct 3, cf. figure 5.1, is investigated. For the same configuration as above, with $\omega h_1/c_0 = 0.01$, $h_1 = h_2 = L$, $N_1 = N_2 = 100$, $N_3 = 200$ and Strouhal number $\omega L/U_0 = 3$, figure 5.8 shows the absolute value of the coefficients $\mathbf{C_3^{ac+}}(n)$ of the acoustic modes propagating/decaying in the $+x$-direction (which are counted from the upstream edge of the orifice), and the absolute value of the coefficients $\mathbf{C_3^{-'}}(n)$ of the acoustic modes propagating/decaying in the $-x$-direction (which are counted from the downstream edge of the orifice) as function of the index n of the modes on a log-log scale. Note the additional superscript ac here denoting the $+x$ acoustic modes, since $\mathbf{C_3^+}$ also contains the coefficients for the $+x$ propagating hydrodynamic modes. In both cases good convergence is observed, above $n = 1$ the coefficients approximately decrease as n^{-3}. Note that for the $+x$ propagating/decaying acoustic modes the contribution of the modes with an uneven pressure distribution -these modes have even index n- is relatively large compared to the contribution of the modes with even pressure distribution. For the $-x$ propagating/decaying acoustic modes the opposite is observed.

5.5.2 Behaviour at the edges of the orifice

Also for partly uniform flow the acoustic velocity in y-direction at the edges of the orifice can be studied. Especially the behaviour at the downstream edge is interesting
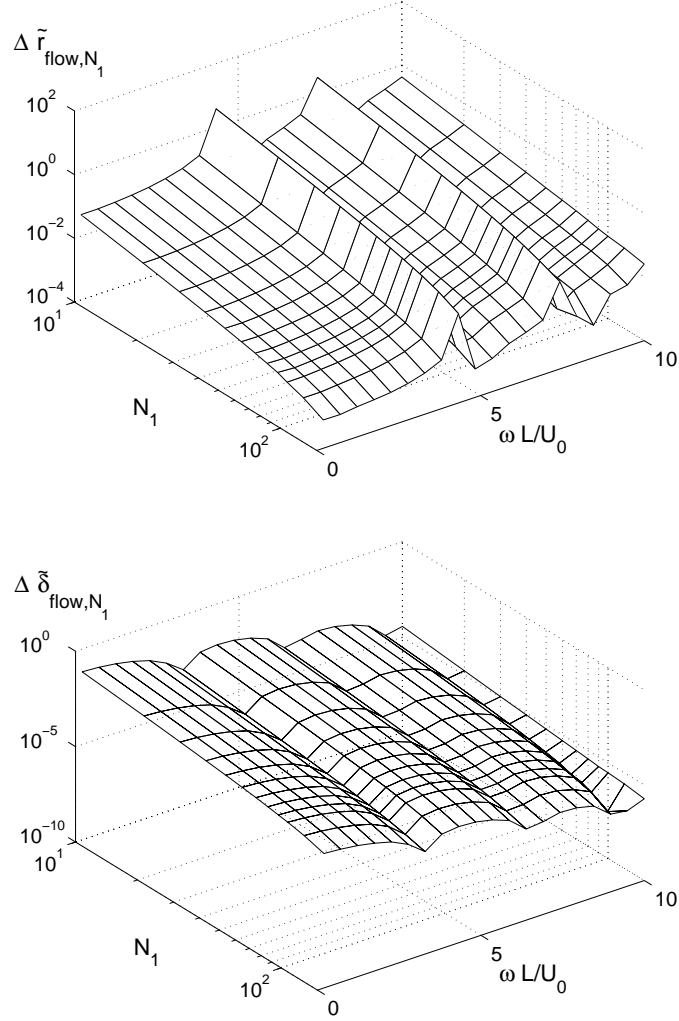
Figure 5.7: Convergence of calculated non-dimensional scaled resistance and reactance, $\tilde{r}_{flow}$ resp. $\tilde{\delta}_{flow}$, due to grazing uniform flow as function of Strouhal number $\omega L/U_0$. The relative error in $\tilde{r}_{flow}$ and $\tilde{\delta}_{flow}$ with respect to a reference value, i.e. $\Delta\tilde{r}_{flow,N_1}$ resp. $\Delta\tilde{\delta}_{flow,N_1}$, is plotted against number of points in duct 1, N_1, on a log-log scale. Number of points used for calculation of reference value $N_1 = N_{ref} = 200$. Error decreases approximately as $N_1^{-1.35}$. Dimensionless frequency $\omega h_1/c_0 = 0.01$, $h_1 = h_2 = L$.
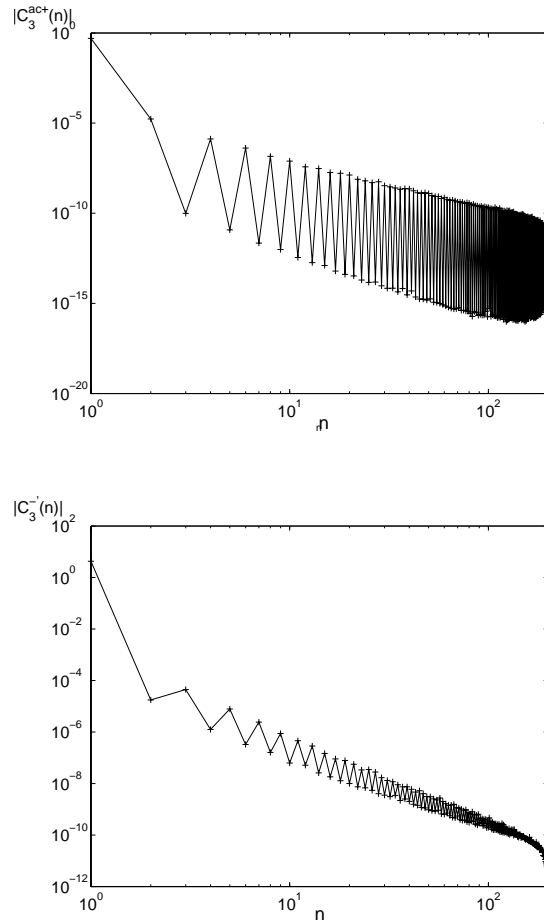
Figure 5.8: Absolute value of the coefficients $\mathbf{C_3^{ac+}}(n)$ of the acoustic modes propagating/decaying in the $+x$-direction (which are counted from the upstream edge of the orifice), and the absolute value of the coefficients $\mathbf{C_3^{-'}}(n)$ of the acoustic modes propagating/decaying in the $-x$-direction (which are counted from the downstream edge of the orifice) as function of the index n of the modes on a log-log scale for uniform grazing flow. The absolute value of the coefficients decreases as n^{-3} Dimensionless frequency $\omega h_1/c_0 = 0.01$, $h_1 = h_2 = L$, number of discrete points $N_1 = N_2 = 100$, $N_3 = 200$, Strouhal number $\omega L/U_0 = 3$.

as no condition is applied here, opposed to the upstream edge, where a Kutta condition is explicitly applied. The acoustic velocity in the y-direction, $\mathbf{v}_*$ in dimensionless and discretized form, is obtained from the summation of the velocity modes $\mathbf{V}$. These velocity modes are obtained from the solved pressure modes $\mathbf{P}$ according to equation (2.15), where for the no mean flow part a Mach number equal to zero is substituted. However, due to the discontinuity of the velocity over the infinitely thin shear layer, the values of the mode at the last point with flow, $N_f = N_1$, and the first point without mean flow, $N_f + 1 = N_1 + 1$ are given by:

$$\mathrm{i}(\omega_* - M_0 k_*)\mathbf{V}(N_f) = -\frac{\mathrm{d}P}{\mathrm{d}y_*}\mid_{N_f},$$

$$\mathrm{i}\omega_*\mathbf{V}(N_f + 1) = -\frac{\mathrm{d}P}{\mathrm{d}y_*}\mid_{N_f+1}, \tag{5.9}$$

with (see also e.g. eq.(2.29)):

$$\frac{\mathrm{d}P}{\mathrm{d}y_*}\mid_{N_f} = \frac{\mathbf{P}(N_f) - \mathbf{P}(N_f - 1)}{2\Delta h_*} - \frac{\mathrm{i}(\omega_* - M_0 k_*)V_{flow}}{2},$$

$$\frac{\mathrm{d}P}{\mathrm{d}y_*}\mid_{N_f+1} = \frac{\mathbf{P}(N_f + 2) - \mathbf{P}(N_f + 1)}{2\Delta h_*} - \frac{\mathrm{i}\omega_*V_{noflow}}{2}. \tag{5.10}$$

Where V_{flow} and V_{noflow} are the explicitly solved modes for the velocity disturbance at the flow side respectively the no flow side of the interface between mean flow and no mean flow. For the configuration $\omega h_1/c_0 = 0.01$, $h_1 = h_2 = L$ and Strouhal number $\omega L/U_0 = 3$, the absolute value of the non-dimensional acoustic velocity disturbance v_* at the x-position of the upstream edge as well as the x-position of the downstream edge is plotted against position $y_* = y/h_1$ in figure 5.9. At the upstream edge, $x_* = 0$, $y_* = 1$, the acoustic velocity is indeed zero, both at the flow side and the no flow side, due to the imposed Kutta condition. Furthermore, no singular behaviour near the edge is seen. At the x-position of the downstream edge the acoustic velocity increases rapidly when moving to the edge itself at $x_* = L_*$, $y_* = 1$, especially in the region without flow. Note that here, at the interface between mean flow and no mean flow, an allowed discontinuity in velocity is seen. The results of the calculations with different numbers of discrete points N_3 in duct 3 do not readily suggest a singularity at the downstream edge (i.e. that the velocity tends to infinity). In that case namely a more significant difference between the results of the calculations with different numbers of points would be expected close to the edge. In any case the behaviour of the acoustic velocity near the downstream edge differs from the $v_* \propto r^{-\frac{1}{2}}$ behaviour without mean flow.

5.5.3   Influence of impedance definition

Here, the calculated orifice impedance, to be presented as the non-dimensional resistance and reactance due to the grazing mean flow, will be treated for uniform grazing
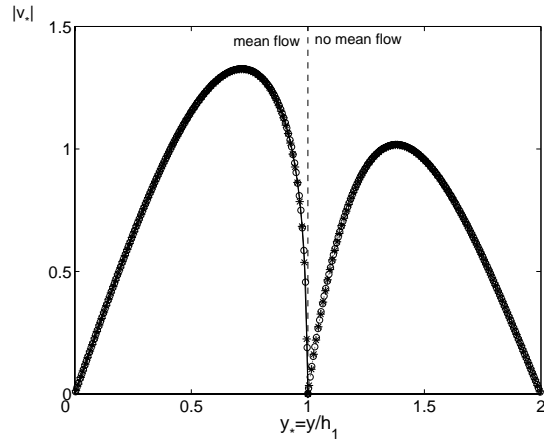
(a) $x_* = 0$, upstream edge
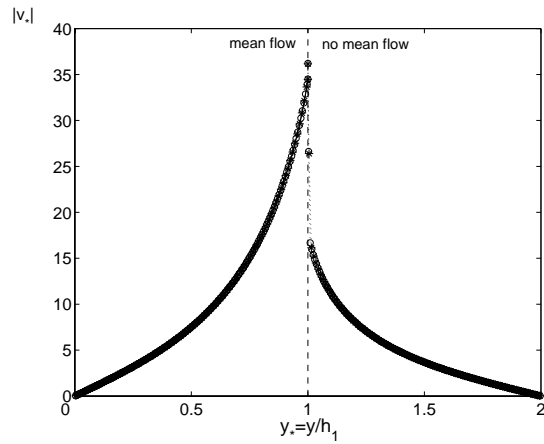
(b) $x_* = L_*$, downstream edge

Figure 5.9: Absolute value of the non-dimensional acoustic velocity v_* at the x-position of the upstream edge respectively the downstream edge of the orifice. $*$ markers: calculation with $N_3 = 200$ points, $\circ$ markers: calculation with $N_3 = 300$ points. The dashed vertical lines indicate the y_* position of the edge, or the interface between mean flow and no mean flow. Configuration: dimensionless frequency $\omega h_1/c_0 = 0.01$, $h_1 = h_2 = L$, Strouhal number $\omega L/U_0 = 3$.

flow (infinitely thin shear layer). The calculation of the orifice impedance is given in section 5.3. The most obvious way is to calculate the impedance from the pressure difference over the orifice. In Howe's model for the orifice impedance under uniform grazing flow, appendix A, also the pressure difference is considered. Comparison between modal analysis results and Howe's results can thus readily be made.

However, in the experiments, cf. chapter 4, only the pressure at the no flow side of the orifice can be measured. Consequently, the impedance is calculated from only the pressure at the no flow side. A justification is given there by arguing that the radiation pressure at the grazing flow side of the orifice is nearly independent of the flow. By subtracting the impedance without flow, as is done in calculating the non-dimensional scaled resistance and reactance, the pressure at the flow side of the orifice can therefore be eliminated.

In order to investigate any difference, calculation of the orifice impedance for uniform grazing flow with the modal analysis method is compared in case the pressure difference is used and in case the pressure at the no flow side of the orifice is used. Results are presented in figure 5.10. Clearly, a significant difference between the two formalisms is seen. Especially for large Strouhal number the resistance seems to tend to minus infinity. The inconsistency here may be connected to the fact that the infinitely thin shear layer is always unstable. The growth rate of the instability in the orifice increases proportionally to the Strouhal number. It is observed that this leads to an ever increasing amplitude of the acoustic pressure and velocity field with increasing Strouhal number (when the amplitude of the pressure waves used as excitation remains constant). For large Strouhal number, the large amplitudes of the fields may lead to the difference between the two formalisms of calculating the impedance, and especially the diverting behaviour of the resistance. Later on, it is actually seen that for non-uniform grazing flow, in which case the instability of the shear layer vanishes above a certain Strouhal number, no significant difference is present between the two ways of calculating impedance. In the following modal analysis calculations for uniform grazing flow, which wil be compared to Howe's model, impedance is calculated from the pressure difference over the orifice.

5.5.4   Incompressible limit

In order to compare with results from Howe's model, which is an incompressible (low Helmholtz number, low Mach number) approach, also the approach of an incompressible limit in the modal analysis method has to be ensured. For this purpose calculations are done for different values of the dimensionless frequency, i.e. Helmholtz number, $\omega_* = \omega h_1/c_0$. The ratio of the duct heights h_1 and h_2 and the slit width L is kept constant at $h_1 = h_2 = L$. Furthermore, the number of points in the discretization of y in duct 1 respectively duct 2 is $N_1 = 100$ and, consequently, $N_2 = 100$. For each dimensionless frequency calculations are done without mean flow and with uniform mean flow in order to obtain the non-dimensional scaled resistance $\tilde{r}_{flow}$
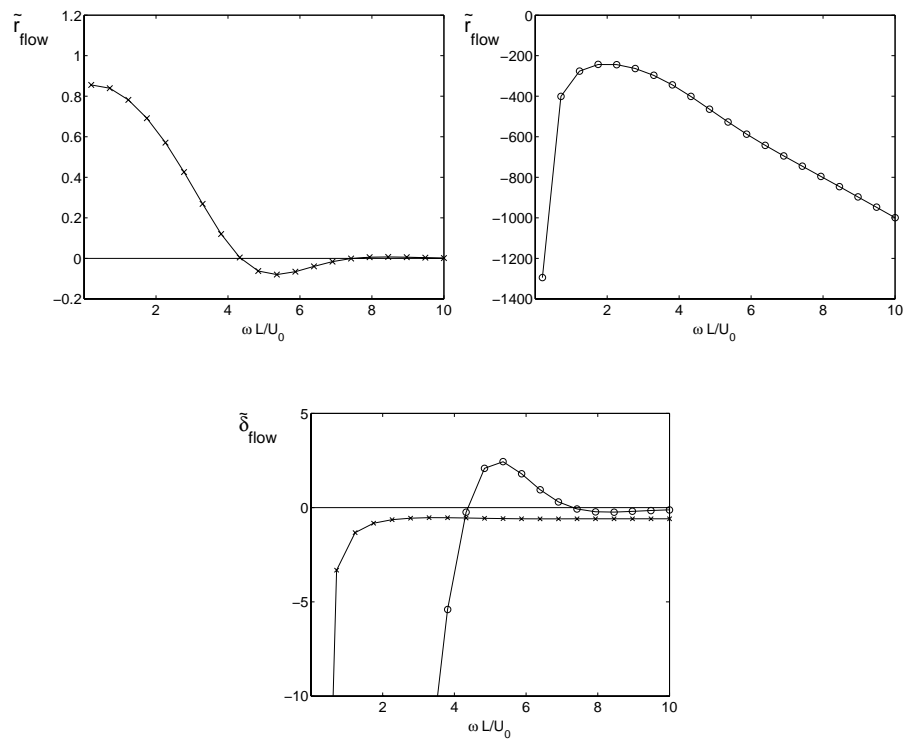
Figure 5.10: Modal analysis calculation of the non-dimensional scaled resistance and reactance of an orifice due to uniform grazing flow. $\times$ markers: impedance calculated from pressure difference over orifice, $\circ$ markers: impedance calculated from pressure at no flow side of orifice. Parameters are: $\omega h_1/c_0 = 0.01$, $h_1 = h_2 = L$, number of points in duct 1 $N_1 = 100$.

and reactance $\tilde{\delta}_{flow}$ due to the flow. Calculations with mean flow at fixed dimensionless frequency are done at various Mach numbers. Results for $\tilde{r}_{flow}$ and $\tilde{\delta}_{flow}$ versus Strouhal number are shown in figure 5.11. At the lowest dimensionless frequency, $\omega_* = 0.001$, results seem to be converged fairly well to a low frequency limit. The results for resistance and reactance at dimensionless frequencies $\omega_* = 0.1$, $\omega_* = 0.01$ and $\omega_* = 0.001$ are very close. Only for Strouhal number less than about 3 a difference is seen between $\omega_* = 0.1$ and $\omega_* = 0.001$, which is at maximum about 5 percent. Between $\omega_* = 0.01$ and $\omega_* = 0.001$ only a slight difference of 1 percent at maximum is seen below Strouhal 1. Furthermore, the good correspondence of the resistance and reactance against Strouhal number for different frequencies, shows that these parameters are indeed only a function of the Strouhal number as predicted by Howe's model (when frequency is low enough and duct height to slit width ratio is fixed).

5.5.5   Influence of ratio of duct height and orifice width

Comparison of the modal analysis results with Howe's model, appendix A, is made for different ratios of duct heights h_1, h_2 to aperture width L in figure 5.12. Here, the dimensionless frequency is fixed. At given Strouhal number a lower dimensionless frequency yields a lower Mach number. At very low Mach numbers, which especially occur for large h_1/L ratios, problems in the calculations were encountered. Therefore, the dimensionless frequency is set at $\omega_* = \omega h_1/c = 0.01$. As discussed above the low-frequency limit is well approached for this value. For the largest duct height to slit width ratio used, i.e. $h_1/L = 25$, this yields a (still problem free) minimum Mach number of $M = 4 \cdot 10^{-5}$ for Strouhal number $\omega L/U_0 = 10$. Furthermore, the ratio of the duct heights is fixed at unity: $h_1 = h_2$. Number of points in duct 1 is $N_1 = 100$. Although the results of modal analysis calculations are qualitatively very similar to those of Howe's model, quantitatively they do not agree. Also a clear dependence on the ratio of duct height to slit width is seen. This means that for the modal analysis calculations the non-dimensional scaled resistance and reactance due to the flow are actually not independent on the geometry surrounding the orifice.
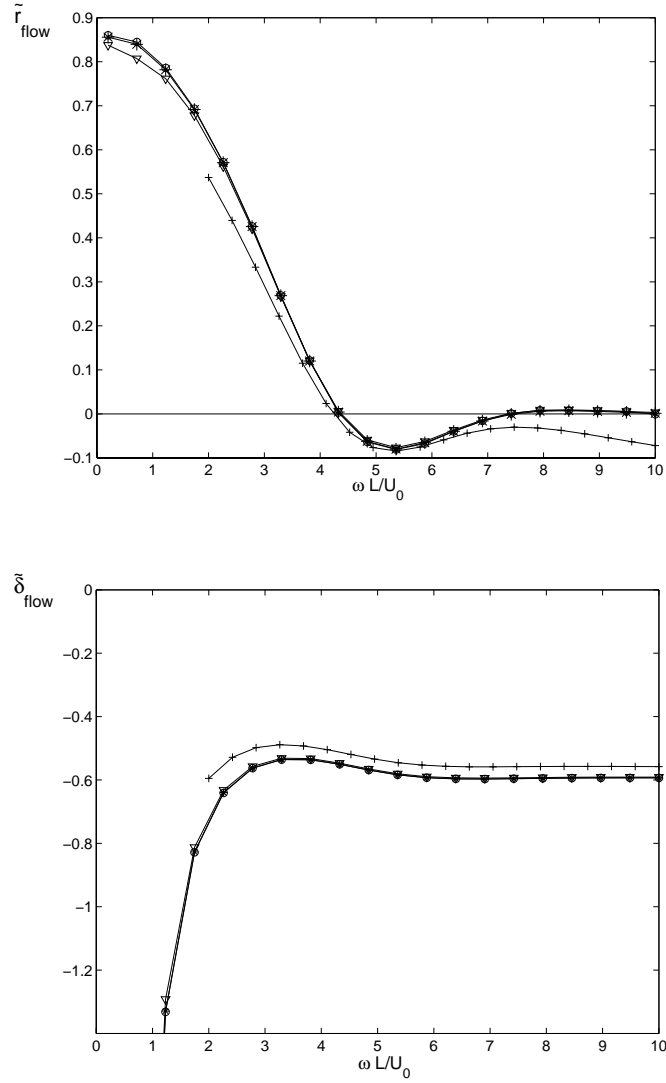
Figure 5.11: Non-dimensional scaled resistance $\tilde{r}_{flow}$ and reactance $\tilde{\delta}_{flow}$ due to the flow versus Strouhal number $\omega L/U_0$ calculated with modal analysis for different dimensionless frequencies $\omega_* = \omega h_1/c_0$. ∘ markers: $\omega_* = 0.001$, ∗ markers: $\omega_* = 0.01$, ∇ markers: $\omega_* = 0.1$, + markers: $\omega_* = 1$. Ratio of duct heights and slit width is $h_1 = h_2 = L$. Number of points in duct 1 is $N_1 = 100$.
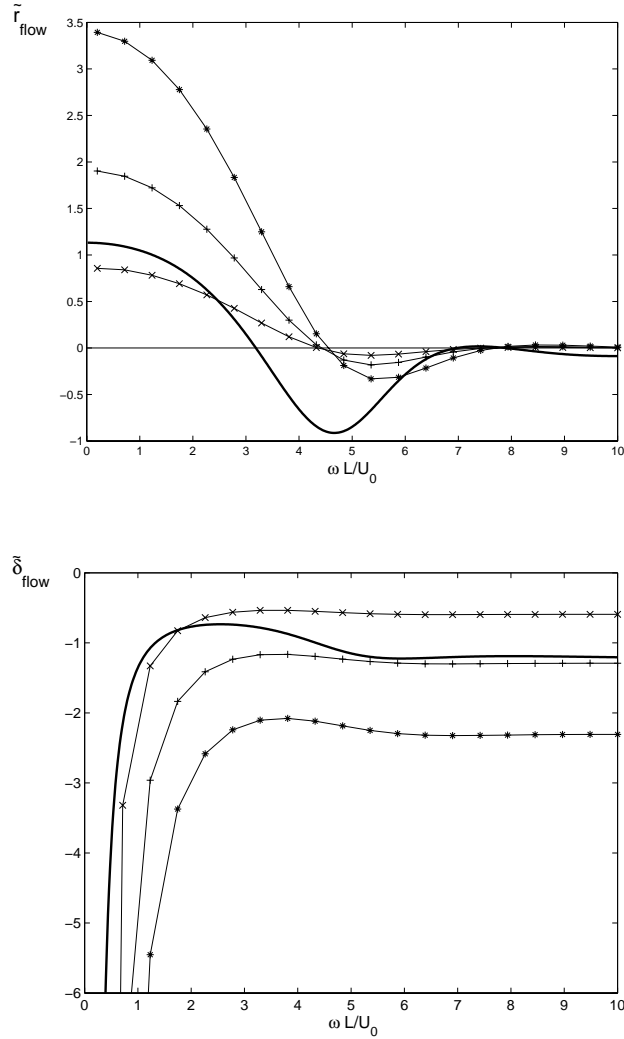
Figure 5.12: Non-dimensional scaled resistance $\tilde{r}_{flow}$ and reactance $\tilde{\delta}_{flow}$ due to the flow versus Strouhal number. Modal analysis calculation for different ratios of duct heights to slit width. $\times$ markers: $h_1/L = 1$, $+$ markers: $h_1/L = 5$, $*$ markers: $h_1/L = 25$. Ratio of duct heights is unity: $h_1 = h_2$, dimensionless frequency $\omega_* = \omega h_1/c_0 = 0.01$. Number of points in duct 1 is $N_1 = 100$. Thick solid lines without markers: results of Howe's model, cf. appendix A.

5.6   Non-uniform flow

In this section modal analysis results for the current orifice geometry with non-uniform grazing flow are presented. First, the influence of impedance definition (i.e. calculating it from a pressure difference or a one-sided pressure) and convergence of the method are addressed. Subsequently, the influence of the boundary layer thickness of the grazing flow on the acoustical behaviour of the orifice will be investigated. Some comparison with experimental results from chapter 4 is made.

5.6.1   Influence of impedance definition

As already mentioned in section 5.5 about uniform grazing flow above, the orifice impedance is most straightforwardly calculated from the pressure difference over the orifice. In experiments, cf. chapter 4, however only the pressure at the no flow side of the orifice can be measured. Consequently, the impedance is calculated from only the pressure at the no flow side. A justification is given there by arguing that the radiation pressure at the grazing flow side of the orifice is nearly independent on the flow. By subtracting the impedance without flow, as is done in calculating the non-dimensional scaled resistance and reactance, the pressure at the flow side of the orifice can therefore be eliminated. Here, calculation of the orifice impedance with the modal analysis method for non-uniform grazing flow is compared in case the pressure difference is used and in case the pressure at the no flow side of the orifice is used. The non-uniform flow profile function employed is given by:

$$f(y) = \begin{cases} 1 - (\frac{y}{h_1})^m & 0 \leq y \leq h_1, \\ \\ 0 & h_1 < y \leq h_2, \end{cases} \tag{5.11}$$

where the main flow velocity is given by $U(y) = U_0 f(y)$. In this case U_0 equals the maximum velocity, it is considered as the velocity outside the boundary layer. The momentum thickness θ, relative to the orifice width L, for this profile is given by:

$$\frac{\theta}{L} = \left(\frac{1}{m+1} - \frac{1}{2m+1}\right)\frac{h_1}{L}. \tag{5.12}$$

Figure 5.13 shows the non-dimensional scaled resistance $\tilde{r}_{flow}$ and reactance $\tilde{\delta}_{flow}$ due to the grazing flow, cf. equation (4.6), as function of the Strouhal number $\omega L/U_0$, when using the pressure difference and when using the pressure at the no flow side only. The parameters in the calculation are: dimensionless frequency (Helmholtz number on duct height h_1) $\omega h_1/c_0 = 0.05$, duct heights $h_1 = h_2$, orifice width $L = 0.2h_1$, number of points in duct 1 $N_1 = 100$, flow profile parameter $m = 64$ ($\theta/L = 0.038$). Nearly the same results are obtained when using pressure difference and pressure at the no flow side only. Note that this was also observed for all other calculations to be presented

Figure 5.13: Modal analysis calculation of the non-dimensional scaled resistance and reactance of an orifice due to grazing flow. $\times$ markers: impedance calculated from pressure difference over orifice, $\circ$ markers: impedance calculated from pressure at no flow side of orifice. Parameters are: $\omega h_1/c_0 = 0.05$, duct heights $h_1 = h_2$, orifice width $L = 0.2h_1$, number of points in duct 1 $N_1 = 100$. Flow profile function is that given by equation (5.11), with profile parameter $m = 64$.

below. This result is very different from that obtained for uniform grazing flow. In that case namely a significant difference between the two ways of calculating the impedance is seen. As discussed there, this may partly be connected to the fact that for uniform flow the growth rate of the shear layer instability increases proportionally with the Strouhal number, giving ever increasing amplitudes of the acoustic fields for an increasing Strouhal number. For non-uniform flow the shear layer instability vanishes above a certain Strouhal number, such that the amplitudes of the obtained acoustical fields are limited.

Furthermore, the resistance and reactance calculated here show good resemblance with experimental data, see chapter 4. In both cases similar oscillating behaviour is seen. In the graphs of figure 5.13 above, the Strouhal number, at which the shear layer becomes stable, is indicated by the vertical dotted lines. Roughly the oscillations in resistance and reactance vanish at this point.

5.6.2   Convergence

The impedance for the configuration above has also been calculated for a number of $N_1 = 50$ and $N_1 = 150$ points in duct 1. Corresponding results for the non-dimensional scaled resistance and reactance due to the flow, here derived from the impedance calculated from the pressure difference over the orifice, are shown in figure 5.14. Qualitatively the (oscillating) behaviour is similar for different numbers of points. An exception is the non-dimensional scaled reactance $\tilde{\delta}_{flow}$ for $N_1 = 150$. Compared to the calculations with $N_1 = 50$ and $N_1 = 100$ the positive peaks in $\tilde{\delta}_{flow}$ radically change to an opposite negative value. The oscillations do not have the same amplitude and are not at exactly the same Strouhal number for the different numbers of points. Thus the resistance and reactance do not converge for an increasing number of points. For the resistance, however, convergence seems to be reasonably good below a Strouhal number of about 1.5. Also at high Strouhal numbers, where the effect of flow on impedance vanishes, convergence seems to be less problematic, this is especially observed for the reactance. The above observed problems with convergence of the method is also reported by Leroux [62], who applied a similar modal analysis model in studying the propagation of acoustic waves in ducts with wall impedance and non-uniform mean flow.

The data displayed in the graphs above is plotted again in figure 5.15, but as function of the Strouhal number based on the phase velocity U_c of the hydrodynamic instability, instead of the velocity U_0 outside the boundary layer. This phase velocity of the hydrodynamic instability mode in the orifice region is calculated from its wavenumber according to equation (2.32). As a result the oscillations in resistance and reactance are now found at virtually the same Strouhal number. Note that calculation of the Strouhal number based on the phase velocity of the hydrodynamic instability mode can only be done when instability is present. At a certain Strouhal

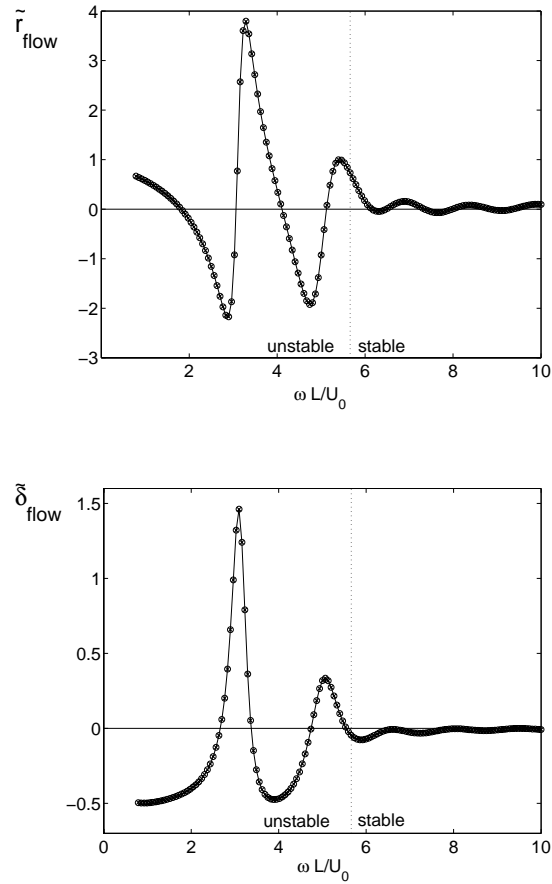Figure 5.14: Modal analysis calculation of the non-dimensional scaled resistance and reactance of an orifice due to grazing flow versus Strouhal number $\omega L/U_0$ for different numbers of points. Impedance is calculated using the pressure difference over the orifice. $+$ markers: $N_1 = 50$, $\times$ markers: $N_1 = 100$, $*$ markers: $N_1 = 150$. Parameters are: $\omega h_1/c_0 = 0.05$, duct heights $h_1 = h_2$, orifice width $L = 0.2h_1$. Flow profile function is that given by equation (5.11), with profile parameter $m = 64$.

Figure 5.15: Modal analysis calculation of the non-dimensional scaled resistance and reactance of an orifice due to grazing flow versus Strouhal number $\omega L/U_c$ based on the phase velocity of the hydrodynamic instability for different numbers of points. Impedance is calculated using the pressure difference over the orifice. + markers: $N_1 = 50$, × markers: $N_1 = 100$, * markers: $N_1 = 150$. Parameters are: $\omega h_1/c_0 = 0.05$, duct heights $h_1 = h_2$, orifice width $L = 0.2h_1$. Flow profile function is that given by equation (5.11), with profile parameter $m = 64$.

number in the plot of resistance and reactance, as displayed in figure 5.14, the hydro-
dynamic instability vanishes. Therefore, only a part of the data in figure 5.14 reappears
in figure 5.15. Furthermore, comparing with experimental data for $\tilde{r}_{flow}$ and $\tilde{\delta}_{flow}$
versus Strouhal number $\omega L/U_c$ for the 1 cm wide orifice, as displayed in figure 4.31,
yields good agreement. The characteristic oscillations are observed at nearly the same
Strouhal numbers. Note here that the momentum thickness to slit width ratio for the
modal analysis calculations is, using equation (5.12), $\theta/L = 0.038$. This corresponds
to the boundary layer flow III case in the experiments.

5.6.3   Influence of boundary layer thickness

Besides calculations for the above given configuration with flow profile parameter
$m = 64$, yielding $\theta/L = 0.038$, also calculations with profile parameter $m = 53$ are
performed. This gives a thicker boundary layer with $\theta/L = 0.046$ (comparable to
the 1 cm slot with boundary layer flow II in experiments). Since no convergence in
the calculation of the impedance is obtained, the number of points taken in the two
cases is such that the ratio of the momentum thickness θ and the spacing between
the points Δh is equal. For $m = 64$ number of points is $N_1 = 100$ as above, for
$m = 53$ number of points is $N_1 = 83$. This gives $\theta/\Delta h = 0.76$ for both cases. Results
for the non-dimensional scaled resistance and reactance versus Strouhal number on
the phase velocity of the hydrodynamic instability are plotted in figure 5.16. The
oscillations in resistance and reactance are virtually at the same Strouhal number
$\omega L/U_c$ for the two cases with different boundary layer thickness. Note that this is not
the case when the Strouhal number $\omega L/U_0$ based on the mean flow velocity outside the
boundary layer would be used. Furthermore, the amplitudes of the oscillations increase
with decreasing boundary layer thickness corresponding with what is observed in
experiments. Also, the amplitudes are of the same order as in experiments for these
calculations. Note that for profile parameter $m = 53$ and $m = 64$ the ratio of shear
layer momentum thickness to duct height h_3 is $\theta/h_3 = 0.0046$ and $\theta/h_3 = 0.0038$
respectively. In chapter 2, section 2.7.2, it was shown for the hyperbolic-tangent shear
layer profile that for $\theta/h_3 < 0.025$ the hydrodynamic instability of the shear layer
calculated with modal analysis in a duct geometry approached the result obtained
for a shear layer which is unbounded in transverse direction. Therefore, for the above
calculations the influence of the duct walls on the calculated hydrodynamic instability
is supposed to be absent. Comparison with experiments, in which the shear layer is
unbounded in the direction perpendicular to the mean flow, is thus justified in that
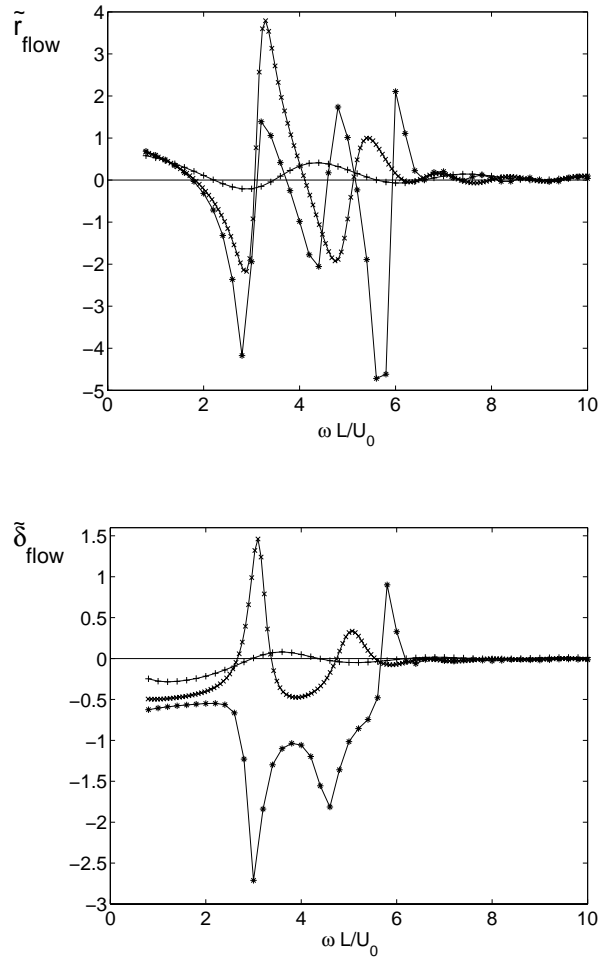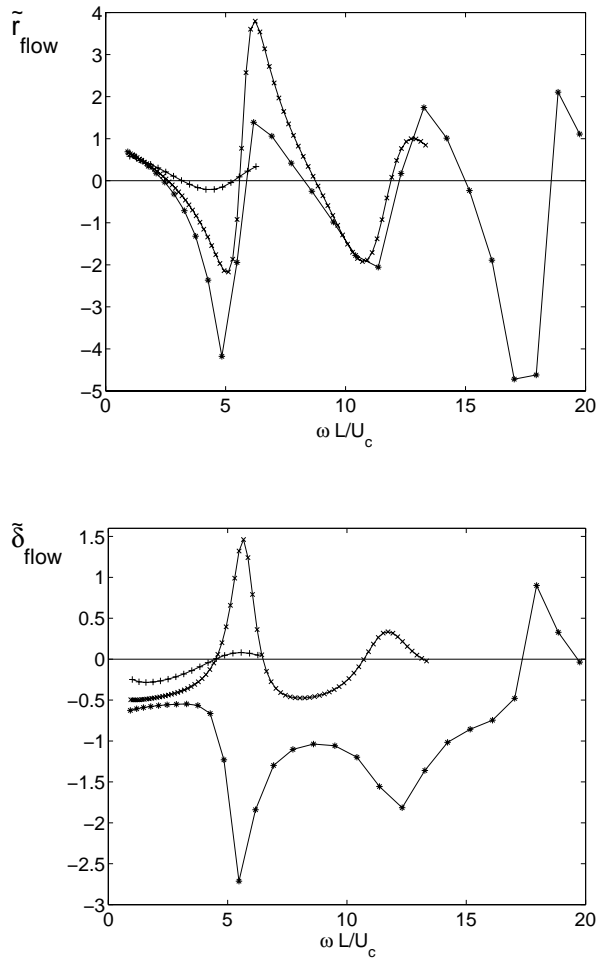respect.
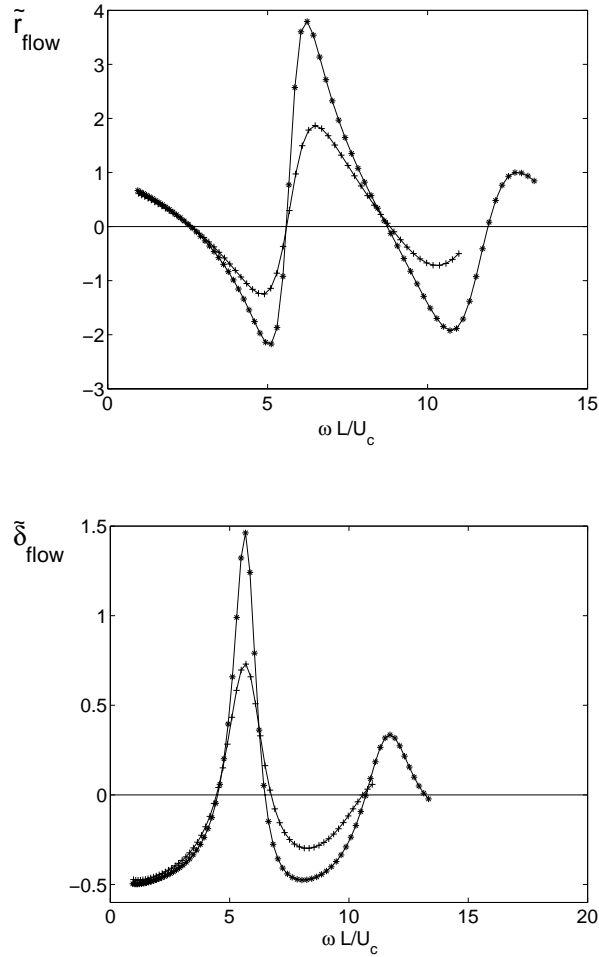
Figure 5.16: Modal analysis calculation of the non-dimensional scaled resistance and reactance of an orifice due to non-uniform grazing flow versus Strouhal number $\omega L/U_c$ based on the phase velocity of the hydrodynamic instability for different boundary layer thicknesses. Flow profile function is that given by equation 5.11. + markers: $m = 53$, $\theta/L = 0.046$, $N_1 = 83$. $*$ markers: $m = 64$, $\theta/L = 0.038$, $N_1 = 100$. Ratio of momentum thickness to spacing between points equals $\theta/\Delta h = 0.76$ in both cases. Other parameters are: $\omega h_1/c_0 = 0.05$, duct heights $h_1 = h_2$, orifice width $L = 0.2h_1$. Impedance is calculated using the pressure difference over the orifice.

5.7   Conclusion

In this chapter the modal analysis method has been applied to an orifice over which grazing mean flow is present. Here, the orifice is modelled as an interconnection between two parallel ducts. The calculation of the orifice impedance for this geometry has been treated.

Model calculations for the configuration in case mean grazing flow is absent show good convergence. Furthermore, favourable comparison of results with the low frequency limit prediction by potential theory is shown for the scattering at the orifice and the singular behaviour of the acoustic field near the edges of the orifice.

For a uniform grazing mean flow also good numerical convergence of the method is found. As expected, the behaviour of the acoustic field near the upstream edge is found to be non-singular due to the application of the Kutta condition. At the downstream edge the field seems to be non-singular, in any case different (singular) behaviour is found than for the case in which mean flow is absent. A comparison is made between the modal analysis results and the results of Howe's incompressible source model, treated in appendix A. In the modal analysis method an incompressible limit is found for the non-dimensional scaled resistance and reactance due to the grazing flow, $\tilde{r}_{flow}$ respectively $\tilde{\delta}_{flow}$. As in Howe's model, in this limit $\tilde{r}_{flow}$ and $\tilde{\delta}_{flow}$ only depend on the Strouhal number. Qualitative, but not exact quantitative, agreement is observed between $\tilde{r}_{flow}$ and $\tilde{\delta}_{flow}$ as obtained by modal analysis (in the incompressible limit) and as predicted by Howe's model. Moreover, the non-dimensional scaled resistance and reactance due to the grazing flow calculated by modal analysis unexpectedly depend on the ratio of duct height to slit width. Furthermore, they differ when calculating the impedance either from the pressure difference over the orifice or from the pressure at the no flow side of the orifice only.

For non-uniform grazing flow numerical convergence of the modal analysis method is not achieved at all Strouhal numbers. Results of calculations are therefore tentatively compared to experimental data of chapter 4, for fixed duct height to slit width ratio. It is found that the model's results for the non-dimensional scaled resistance and reactance due to the grazing flow are very similar to experimental results. In the calculations the typical oscillations in resistance and reactance are virtually at the same Strouhal number, based on the phase velocity of the hydrodynamic instability of the shear layer, for different numbers of discrete points. In this respect convergence of the method is established. However, generally no convergence is observed for the amplitudes of these oscillations. An exception to this is the observed convergence in non-dimensional scaled resistance below a Strouhal number of about 1.5. Furthermore, in the high Strouhal number limit, where the oscillations vanish, convergence is established. The Strouhal numbers at which the oscillations are found in the model calculations correspond very well to experimentally found values. For different boundary layer thickness oscillations in the resistance and reactance are again

at the same Strouhal number, when it is based on the phase velocity of the hydrodynamic instability of the shear layer. When keeping the ratio of momentum thickness to spacing between discrete points constant, the amplitude of the oscillations increase with decreasing boundary layer thickness, which is consistent with experimental data. As opposed to the uniform flow case, for non-uniform grazing flow no significant difference is observed for the non-dimensional scaled resistance and reactance due to the flow when calculating the impedance either from the pressure difference over the orifice or from the pressure at the no flow side of the orifice.

Appendix A

Source model for orifice impedance under uniform grazing flow

Howe[45, 47] considered a two-sided grazing main flow $U_\pm$ in the x_1-direction with infinitesimally small boundary layer thickness (large Reynolds number) over an aperture in an infinitesimally thin wall, cf. figure A.1. The $+$ and $-$ subscripts refer to the $x_2 > 0$, respectively $x_2 < 0$ region. In the aperture a shear layer develops, which separates the flows above and beneath the wall. Potential flow is assumed, except for the infinitesimally thin region of the shear layer (vortex sheet), where all vorticity is considered to be concentrated. $\varphi_\pm(\omega)$ and $p_\pm(\omega)$ are the Fourier transformed velocity potential respectively pressure for uniform linear perturbations taken at sufficiently large distance from the wall. Following Howe an $e^{-\mathrm{i}\omega t}$-convention is taken for the harmonic disturbances here, with ω the angular frequency. The pressure difference $(p_+ - p_-)(\omega)$ induces a flow through the aperture, corresponding to an additional velocity potential $\phi(\mathbf{x}, \omega)$, so that the total velocity potential of the perturbation is:

$$\varphi(\mathbf{x}, \omega) = \varphi_\pm(\omega) + \phi(\mathbf{x}, \omega). \tag{A.1}$$

Regarding the flow as locally incompressible: $M^2 = (\frac{U_\pm}{c_0})^2 \ll 1$ and $He^2 = (kL)^2 \ll 1$, with c_0 the (mean) sound velocity, $k = \frac{\omega}{c_0}$ the wavenumber and L the characteristic size of the aperture, the velocity potential satisfies the Laplace equation:

$$\nabla^2 \phi(\mathbf{x}, \omega) = 0. \tag{A.2}$$

With the boundary condition for the flow velocity in the x_2-direction, i.e. normal to the wall: $v_2(\mathbf{x}, \omega) = 0$ at $x_2 = 0$ outside the aperture, the velocity potential is solved
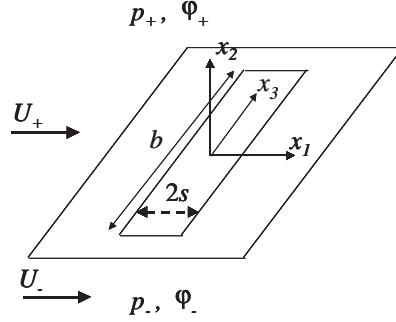
Figure A.1: Two-sided grazing flow over an aperture.

with use of the Green's function:

$$G(\mathbf{x}, \mathbf{y}, \omega) = \frac{-1}{4\pi|\mathbf{x} - \mathbf{y}|} + \frac{-1}{4\pi|\mathbf{x} - \mathbf{y}'|}, \qquad \mathbf{y}' = (y_1, -y_2, y_3), \qquad (A.3)$$

to obtain :

$$\varphi(\mathbf{x}, \omega) = \varphi_\pm(\omega) - \frac{\text{sign}(x_2)}{2\pi} \cdot \int_{-\infty}^{\infty} \frac{v_2(y_1, \pm 0, y_3, \omega)}{|\mathbf{x} - \mathbf{y}|} \mathrm{d}y_1 \mathrm{d}y_3, \qquad y_2 = 0, \qquad (A.4)$$

where the flow velocity in normal direction in the aperture $v_2(x_1, \pm 0, x_3, \omega)$ is unknown. By using the relations:

$$p(\mathbf{x}, \omega) = -\rho_0(-\mathrm{i}\omega + U_\pm \frac{\partial}{\partial x_1})\varphi(\mathbf{x}, \omega), \qquad (A.5)$$

$$v_2(x_1, 0, x_3, \omega) = (-\mathrm{i}\omega + U_\pm \frac{\partial}{\partial x_1})\zeta(x_1, x_3, \omega), \qquad (A.6)$$

with ρ_0 the mean fluid density, this equation can be rewritten into a relation between the pressure $p(\mathbf{x}, \omega)$ and the normal displacement of the shear layer in the aperture $\zeta(x_1, x_3, \omega)$:

$$p(\mathbf{x}, \omega) = p_\pm(\omega) - \frac{\rho_0\text{sign}(x_2)}{2\pi}(\omega + \mathrm{i}U_\pm \frac{\partial}{\partial x_1})^2 \cdot \int_S \frac{\zeta(x_1, x_3, \omega)}{|\mathbf{x} - \mathbf{y}|} \mathrm{d}y_1 \mathrm{d}y_3, \qquad y_2 = 0,$$
$$(A.7)$$

where the integration is now restricted to the area S of the aperture. This equation implies that $\zeta(x_1, x_3, \omega)$ is continuous over the vortex sheet (same value at $x_2 = \pm 0$), which is reasonable in the infinitesimally thin wall case. However, recently Jing *et al.* [48] and Peat *et al.* [86] argued continuity of particle velocity rather than displacement

over the vortex sheet, whereas Aurégan *et al.* [6, 8] concluded that an intermediate boundary condition between displacement and velocity continuity, depending on the boundary layer conditions, was most realistic to obtain a fit of the experimental results.

Finally, by demanding continuity of pressure over the aperture (at $x_2 = \pm 0$), an equation for the shear layer displacement is found:

$$[(\omega + \mathrm{i}U_+ \frac{\partial}{\partial x_1})^2 + (\omega + \mathrm{i}U_- \frac{\partial}{\partial x_1})^2] \cdot \frac{1}{2\pi} \int_S \frac{\zeta(x_1, x_3, \omega)\mathrm{d}y_1\mathrm{d}y_3}{\sqrt{(x_1' - y_1')^2 + (x_3' - y_3')^2}} = \frac{p_+ - p_-}{\rho_0}. \quad \text{(A.8)}$$

After integration with respect to the differential operator on the left hand side we find:

$$\int_S \frac{\zeta'(y_1', y_3', \omega)\mathrm{d}y_1'\mathrm{d}y_3'}{\sqrt{(x_1' - y_1')^2 + (x_3' - y_3')^2}} + \lambda_1(x_3')e^{\mathrm{i}\sigma_1 x_1'} + \lambda_2(x_3')e^{\mathrm{i}\sigma_2 x_1'} = 1, \quad \text{(A.9)}$$

where the scaling:

$$\zeta' = \frac{\rho_0 \omega^2 L \zeta}{\pi(p_+ - p_-)}, \qquad x' = \frac{x}{L}, \qquad y' = \frac{y}{L},$$

is used to obtain a dimensionless form. Here L is the characteristic size of the aperture in streamwise direction. Furthermore:

$$\sigma_1 = \frac{\omega L(1 + \mathrm{i})}{U_+ + \mathrm{i}U_-} = \sigma_+ \frac{1 + \mathrm{i}}{1 + \mathrm{i}\mu}, \qquad \sigma_2 = \frac{\omega L(1 - \mathrm{i})}{U_+ - \mathrm{i}U_-} = \sigma_+ \frac{1 - \mathrm{i}}{1 - \mathrm{i}\mu}, \quad \text{(A.10)}$$

are the dimensionless Kelvin-Helmholtz wave numbers of the instability waves of the shear layer, with $\sigma_+ = \frac{\omega L}{U_+}$ the Strouhal number based on velocity U_+ and L, and μ the ratio of flow velocities: $\mu = \frac{U_-}{U_+}$. The terms on the left hand side of equation (A.9) with coefficients λ_1 and λ_2 represent the instability waves of the vortex sheet. For ω real: $\sigma_1 = \sigma_2^*$, so that one of the waves will grow exponentially in the x_1-direction, which yields the instability. Note that equally strong grazing flow at both sides: $U_- = U_+$ or $\mu = 1$, gives $\sigma_1 = \sigma_2 = \sigma_+$. The two terms in Eq. (A.9) are then replaced by: $(\lambda_1(x_3') + \lambda_2(x_3')x_1')e^{\mathrm{i}\sigma_+ x_1'}$. Since in this case σ_+ is real, the motion of the vortex sheet is stable.

Equation (A.9) is (in general numerically) solved for the vortex sheet displacement by applying the Kutta condition, $\zeta = \frac{\partial \zeta}{\partial x_1} = 0$, at the upstream edge. The shear layer thus leaves the upstream edge tangentially. Note that no condition is applied at the downstream edge. With ζ found, the volume flux Q through the aperture can be calculated directly by:

$$Q(\omega) = \int_{-\infty}^{\infty} v_2(x_1, 0, x_3, \omega)\mathrm{d}x_1\mathrm{d}x_3 \quad = \int_S -\mathrm{i}\omega\zeta(x_1, x_3, \omega)\mathrm{d}x_1\mathrm{d}x_3, \quad \text{(A.11)}$$

with use of equation (A.6). The acoustic behaviour of the aperture is then expressed in the Rayleigh conductivity K_R defined as:

$$K_R \equiv \frac{Q}{\varphi_+ - \varphi_-} = \mathrm{i}\omega\rho_0 \frac{Q}{p_+ - p_-}. \tag{A.12}$$

For a rectangular aperture with large aspect ratio, $b \gg 2s$, cf. figure A.1, an exact analytical expression for the Rayleigh conductivity was found:

$$K_R = \frac{\pi b}{2(F(\sigma_1, \sigma_2) + \Psi)}, \tag{A.13}$$

where $\sigma_{1,2}$ are as defined in equation (A.10), and in this case are based on the half-width s of the slot (so L is replaced by s). The function F is given by:

$$F(\sigma_1, \sigma_2) = \frac{-\sigma_1 J_0(\sigma_2)G(\sigma_1) + \sigma_2 J_0(\sigma_1)G(\sigma_2)}{\sigma_1 W(\sigma_2)G(\sigma_1) - \sigma_2 W(\sigma_1)G(\sigma_2)},$$

$$G(x) = J_0(x) - 2W(x), \qquad W(x) = \mathrm{i}x(J_0(x) - \mathrm{i}J_1(x)), \tag{A.14}$$

with J_0 and J_1 Bessel functions of the first kind of zeroth and first order respectively. Ψ is related to the local approximations of the Green's functions on either side of the aperture. For instance, for a three-dimensional free space on both sides:

$$\Psi_{\pm 3D} = \ln(\frac{4b}{s}) - 1. \tag{A.15}$$

Figure A.2 shows a plot of the Rayleigh conductivity of a slot with aspect ratio $\frac{b}{2s} = 10$ for one-sided grazing flow, $\mu = 0$, according to equation (A.13). Here the conductivity:

$$K_R = 2R_e(\Gamma_R - \mathrm{i}\Delta_R), \tag{A.16}$$

is scaled to the hydraulic radius of the aperture: $R_e = \sqrt{\frac{2sb}{\pi}}$. Γ_R and Δ_R correspond to a reactance respectively resistance of the orifice, which according to the present theory thus only depend on the Strouhal number, for given aspect ratio and flow velocity ratio μ. For $\Delta_R > 0$, Q is proportional to $-(p_+ - p_-)$, cf. eqs. (A.12) and (A.16). The power P performed by the pressure load on the aperture flow equals $P = -(p_+ - p_-) \cdot Q$. So for $\Delta_R > 0$ the power is positive: $P \propto (p_+ - p_-)^2 > 0$. Energy is thus transferred from the pressure field to the aperture flow, which implies sound absorption. It can be seen in figure A.2 that sound absorption takes place for low Strouhal numbers, $\frac{\omega s}{U_+} < 1.6$. For higher Strouhal numbers, $1.6 < \frac{\omega s}{U_+} < 3.5$, Δ_R is negative, here sound production occurs.

Grace *et al.* [37] computed the Rayleigh conductivity, according to the present theory of Howe [47, 45], for 8 different shapes of wall apertures, such as a square and
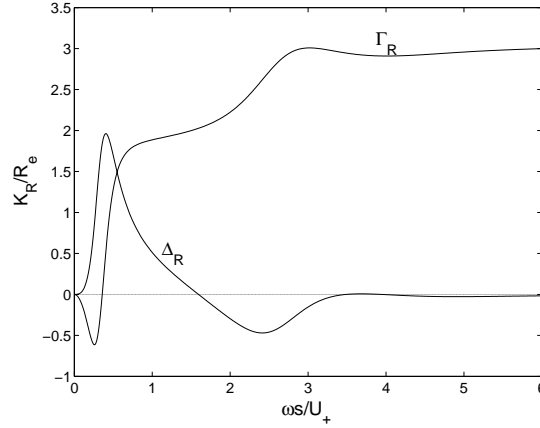
Figure A.2: Scaled Rayleigh conductivity of a slot with aspect ratio $\frac{b}{2s} = 10$ in a infinitesimally thin wall for one-sided grazing flow, $U_- = 0$, according to the theory of Howe [47, 45].

a circle. It was found that, especially for one-sided grazing flow, K_R is very similar to that displayed in figure A.2 for all geometries.

Furthermore Howe investigated the influence of wall thickness d on the Rayleigh conductivity [47, 46]. For a thin wall approximation, $\frac{d}{L} \ll 1$, and for the wavelengths of disturbances on the vortex sheet large compared to d ($\sigma_+ \ll \frac{L}{d}$), the vertical displacement of fluid in the aperture was regarded independent on x_2, and thus the same as the vortex sheet displacement $\zeta(x_1, x_3, \omega)$ at the upper and lower end of the aperture at $x_2 = \pm\frac{1}{2}d$. Instead of demanding continuity of pressure over the vortex sheet, as in the infinitesimally thin wall case, now the pressure difference between the upper and lower end of the aperture can be set equal to the inertia $-\rho_0 d\frac{\partial^2 \zeta}{\partial t^2} = \rho_0 d\omega^2 \zeta$. From equation (A.7) the equivalent of equation (A.8) is then deduced for a wall of finite thickness:

$$d\omega^2 \zeta(x_1, x_3, \omega) + [(\omega + \mathrm{i}U_+ \frac{\partial}{\partial x_1})^2 + (\omega + \mathrm{i}U_- \frac{\partial}{\partial x_1})^2]$$
$$\cdot \frac{1}{2\pi} \int_S \frac{\zeta(x_1, x_3, \omega)\mathrm{d}y_1 \mathrm{d}y_3}{\sqrt{(x_1' - y_1')^2 + (x_3' - y_3')^2}} = \frac{p_+ - p_-}{\rho_0}. \tag{A.17}$$

The Rayleigh conductivity of rectangular orifices was calculated for several thicknesses and for one-sided as well as even two-sided grazing flow [46]. It was argued that the introduction of a finite wall thickness in all cases modifies the stability of the shear layer motion (in the two-sided grazing flow case the motion also becomes unstable).

For one-sided grazing flow the Rayleigh conductivity was found to be very similar to the infinitely thin wall case. Especially the low Strouhal number region of sound absorption remains nearly unaffected. For walls with $\frac{d}{L} > 0.05$ the region of sound production vanishes. It was however questioned, whether the thin wall approximation still holds in this case.

Appendix B

Hydrodynamic (in)stability of a free shear layer

B.1 Rayleigh's equation

In case viscosity can be neglected the motion of a perfect and isentropic fluid is described by the Euler equations for conservation of momentum and mass:

$$\rho \frac{\mathrm{D}\overrightarrow{v}}{\mathrm{D}t} = -\overrightarrow{\nabla}p \tag{B.1}$$

,

$$\frac{1}{\rho}\frac{\mathrm{D}\rho}{\mathrm{D}t} = -\overrightarrow{\nabla}\cdot\overrightarrow{v}, \tag{B.2}$$

$$\frac{\mathrm{D}}{\mathrm{D}t} = \frac{\partial}{\partial t} + \overrightarrow{v}\cdot\overrightarrow{\nabla}.$$

With ρ the density, p the pressure and $\overrightarrow{v}$ the velocity vector. Considering small perturbations in a two-dimensional flow, where the mean flow velocity $U(y)$ is only a function of y, linearization of the Euler equations can be employed. With $\rho = \rho_0 + \rho'$, $p = p_0 + p'$, where $\rho' << \rho_0$, and $\overrightarrow{v} = U(y)\overrightarrow{e}_x + u'\overrightarrow{e}_x + v'\overrightarrow{e}_y$, with $\overrightarrow{e}_x, \overrightarrow{e}_y$ unit vectors in the x- and y-direction, gives, from equation (B.1), the linearized Euler equations for momentum:

$$\rho_0\left(\frac{\partial u'}{\partial t} + U\frac{\partial u'}{\partial x} + \frac{\mathrm{d}U}{\mathrm{d}y}v'\right) = -\frac{\partial p'}{\partial x}, \tag{B.3}$$

and:

$$\rho_0\left(\frac{\partial v'}{\partial t} + U\frac{\partial v'}{\partial x}\right) = -\frac{\partial p'}{\partial y}. \tag{B.4}$$

Regarding the flow as incompressible the velocity disturbance can be written as function of a disturbance stream function ψ:

$$u'(x,y,t) = \frac{\partial \psi(x,y,t)}{\partial y}, \qquad v'(x,y,t) = -\frac{\partial \psi(x,y,t)}{\partial x}. \tag{B.5}$$

If we take the following complex form for this stream function:

$$\psi(x,y,t) = \phi(y)e^{\mathrm{i}(\omega t - kx)}, \tag{B.6}$$

and subtract $\frac{\partial}{\partial y}$eq.(B.3) from $\frac{\partial}{\partial x}$eq.(B.4), Rayleigh's stability equation is obtained [93],[29]:

$$\left(U(y) - \frac{\omega}{k}\right)\left(\frac{\mathrm{d}^2\phi(y)}{\mathrm{d}y^2} - k^2\phi(y)\right) - \frac{\mathrm{d}^2 U(y)}{\mathrm{d}y^2}\phi(y) = 0. \tag{B.7}$$

B.2 Instability for the generalized hyperbolic-tangent shear layer profile

Michalke [67, 68, 69] investigated the spatial instability of a free shear layer. He considered a generalized hyperbolic-tangent velocity profile for the shear layer [68]:

$$\begin{aligned}
\frac{U(y)}{U_0} &= 1 - (1 + me^{mf(m)\frac{y}{\theta}})^{-1/m}, \\
f(m) &= \int_0^1 \frac{1-z}{1-z^m}\mathrm{d}z,
\end{aligned} \tag{B.8}$$

which has an inflexion point at $y = 0$. Here θ is the momentum thickness of the shear layer:

$$\theta = \int_{-\infty}^{\infty} \frac{U(y)}{U_0}\left(1 - \frac{U(y)}{U_0}\right)\mathrm{d}y. \tag{B.9}$$

The quantity m is a profile parameter setting the steepness of the no flow ($y \leq 0$) to flow ($y \geq 0$) transition. This is illustrated by figure B.1, showing the shear layer profile for different values of m. For $m = \infty$ the profile becomes:

$$\frac{U(y)}{U_0} = \begin{cases} 0 & y \leq 0 \\ 1 - e^{-0.5\frac{y}{\theta}} & y \geq 0 \end{cases} \qquad m = \infty.$$

For $m = 1$ the tanh profile is obtained as extensively studied in [67]:

$$\frac{U(y)}{U_0} = 0.5\left(1 + \tanh(0.5\frac{y}{\theta})\right), \qquad m = 1. \tag{B.10}$$

By solving Rayleigh's equation (B.7), where the angular frequency ω is taken real, $\phi(y)$ as well as the corresponding complex wavenumbers k of the hydrodynamic wave
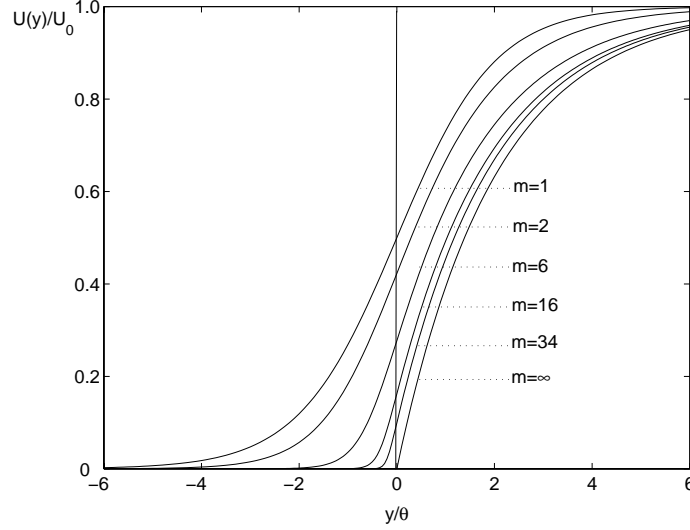
Figure B.1: Generalized hyperbolic-tangent shear layer flow profiles as given by equation (B.8) for different values of m.

is obtained. Note that if some $\phi(y)$ with wavenumber k is a solution, also its complex conjugate $\phi^*(y)$ with corresponding complex conjugate k^* is a solution. Figure B.2 shows the results for the real and imaginary part of k for different values of the profile parameter as obtained by Michalke. For the $m = 1$ case the results were experimentally confirmed by Freymuth [32] for low frequencies. The real part of k governs the phase velocity U_c of the wave according to: $U_c = \omega/\Re(k)$. The phase velocity calculated from the data of k is given in figure B.3. The imaginary part of k gives the growth rate of the instability. In case the imaginary part of the wavenumber is nonzero an exponentially growing and an 'opposite' exponentially decaying hydrodynamic is found. It can be seen that for about $\frac{\omega\theta}{U_0} < 0.07$ the value of the wave number k (both real and imaginary part) is independent of the shear layer profile parameter m.
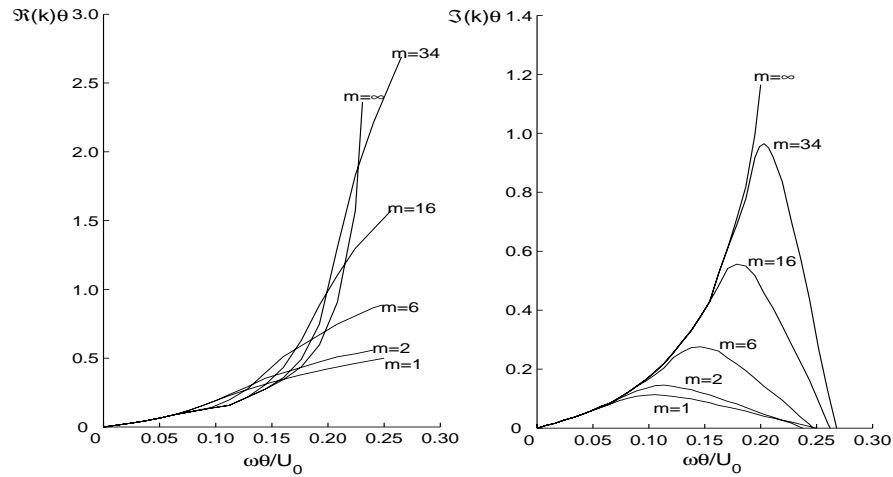
Figure B.2: Real and imaginary part of wavenumber k times shear layer momentum thickness θ versus Strouhal number based on θ and mean flow velocity outside the shear layer U_0. Results for different values of the generalized hyperbolic-tangent shear layer profile parameter m as calculated by Michalke [67, 68, 69].
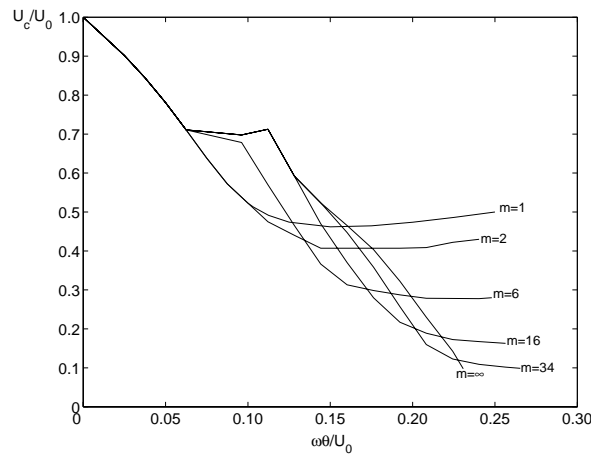
Figure B.3: Phase velocity U_c of the hydrodynamic wave scaled to mean flow velocity outside the shear layer U_0 versus Strouhal number based on shear layer momentum thickness θ and U_0. Results for different values of the generalized hyperbolic-tangent shear layer profile parameter m as calculated from the data of Michalke [67, 68, 69].

Appendix C

Differential matrices

Discrete derivatives

Consider a Taylor series expansion of a function $f(y)$ around $y = y_0$:

$$f(y_0 + \Delta y) = \sum_{n=0}^{\infty} \frac{1}{n!} \frac{\mathrm{d}^n f(y)}{\mathrm{d}y^n}|_{y=y_0} (\Delta y)^n. \tag{C.1}$$

Discretization of y in points with spacing Δh gives the discrete form:

$$f_{n+\Delta n} = f_n + f_n' \Delta n \Delta h + \frac{1}{2} f_n'' (\Delta n \Delta h)^2 + \frac{1}{6} f_n''' (\Delta n \Delta h)^3 + ... , \tag{C.2}$$

where the subscripts indicate the index of the discrete point. A prime denotes the first derivative, double prime the second derivative, and so on. With the equation above the first and second derivative of f at discrete point n can be derived for different orders of accuracy:

$$f_n' = \frac{-f_{n-1} + f_{n+1}}{2\Delta h} \qquad\qquad + O((\Delta h)^2),$$
$$f_n'' = \frac{f_{n-1} - 2f_n + f_{n+1}}{(\Delta h)^2} \qquad\qquad + O((\Delta h)^2), \tag{C.3}$$

$$f_n' = \frac{f_{n-2} - 8f_{n-1} + 8f_{n+1} - f_{n+2}}{12\Delta h} \qquad\qquad + O((\Delta h)^4),$$
$$f_n'' = \frac{-f_{n-2} + 16f_{n-1} - 30f_n + 16f_{n+1} - f_{n+2}}{12(\Delta h)^2} \qquad\qquad + O((\Delta h)^4), \tag{C.4}$$

$$f'_n = \frac{-f_{n-3} + 9f_{n-2} - 45f_{n-1} + 45f_{n+1} - 9f_{n+2} + f_{n+3}}{60\Delta h} \qquad + O((\Delta h)^6),$$

$$f''_n = \frac{2f_{n-3} - 27f_{n-2} + 270f_{n-1} - 490f_n + 270f_{n+1} - 27f_{n+2} + 2f_{n+3}}{180(\Delta h)^2} \quad + O((\Delta h)^6).$$

$$(C.5)$$

Boundary condition

In the modal analysis the domain of y is restricted to a duct with walls at $y = 0$ and $y = h$. Variables are discretized at N points in the y-direction. The points have spacing $\Delta h = N/h$, while the first and last point are a distance $\Delta h/2$ from the wall, cf. section 2.2. At the walls the first derivative of pressure w.r.t. y equals 0. This boundary condition can be incorporated by adding ghost points outside the duct, see figure C.1. Equations for the first derivative of $f(y)$ at the walls, $y = 0$ and $y = h$, as a function of the value of f at the surrounding (ghost) points can be derived, similar to equations (C.3, C.4, C.5). From those equations it is clear that the values of f at the discrete points around the position, where the first derivative is considered, appear asymmetrically. This means that by taking $f_{-1} = f_1$, $f_{-2} = f_2$ etcetera, and $f_{N+1} = f_N$, $f_{N+2} = f_{N-1}$ etcetera, the first derivative of f at the walls will be zero.

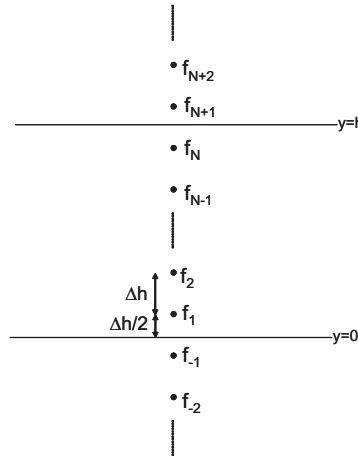Figure C.1: Introduction of ghost points at the duct walls when employing discretization of the y-coordinate in order to incorporate the boundary conditions in the differential matrices.

Differential matrices

Combining equations (C.3, C.4, C.5) with the boundary conditions at the walls gives the $N \times N$ matrices $\mathbf{D_1}$ and $\mathbf{D_2}$ for the first respectively second order derivative w.r.t. y. For order of accuracy $(\Delta h)^2$:

$$\mathbf{D_1} = \frac{1}{2\Delta h} \begin{pmatrix} -1 & 1 & & & \\ -1 & 0 & 1 & & \\ & \ddots & \ddots & \ddots & \\ & & -1 & 0 & 1 \\ & & & -1 & 1 \end{pmatrix},$$

$$\mathbf{D_2} = \frac{1}{(\Delta h)^2} \begin{pmatrix} -1 & 1 & & & \\ 1 & -2 & 1 & & \\ & \ddots & \ddots & \ddots & \\ & & 1 & -2 & 1 \\ & & & 1 & -1 \end{pmatrix}.$$

(C.6)

For order of accuracy $(\Delta h)^4$:

$$\mathbf{D_1} = \frac{1}{12\Delta h} \begin{pmatrix} -8 & 9 & -1 & & & \\ -7 & 0 & 8 & -1 & & \\ 1 & -8 & 0 & 8 & -1 & \\ & \ddots & \ddots & \ddots & \ddots & \ddots \\ & 1 & -8 & 0 & 8 & -1 \\ & & 1 & -8 & 0 & 7 \\ & & & 1 & -9 & 8 \end{pmatrix},$$

$$\mathbf{D_2} = \frac{1}{12(\Delta h)^2} \begin{pmatrix} -14 & 15 & -1 & & & \\ 15 & -30 & 16 & -1 & & \\ -1 & 16 & -30 & 16 & -1 & \\ & \ddots & \ddots & \ddots & \ddots & \ddots \\ & -1 & 16 & -30 & 16 & -1 \\ & & -1 & 16 & -30 & 15 \\ & & & -1 & 15 & -14 \end{pmatrix}.$$

(C.7)

For order of accuracy $(\Delta h)^6$:

$$
\mathbf{D_1} = \frac{1}{60\Delta h}
\begin{pmatrix}
-45 & 54 & -10 & 1 & & & & \\
-36 & -1 & 45 & -9 & 1 & & & \\
8 & -45 & 0 & 45 & -9 & 1 & & \\
-1 & 9 & -45 & 0 & 45 & -9 & 1 & \\
& \ddots & \ddots & \ddots & \ddots & \ddots & \ddots & \ddots \\
& -1 & 9 & -45 & 0 & 45 & -9 & 1 \\
& & -1 & 9 & -45 & 0 & 45 & -8 \\
& & & -1 & 9 & -45 & 1 & 36 \\
& & & & -1 & 10 & -54 & 45
\end{pmatrix},
$$

$$
\text{(C.8)}
$$

$$
\mathbf{D_2} = \frac{1}{180(\Delta h)^2}
\begin{pmatrix}
-220 & 243 & -25 & 2 & & & & \\
243 & -488 & 270 & -27 & 2 & & & \\
-25 & 270 & -490 & 270 & -27 & 2 & & \\
2 & -27 & 270 & -490 & 270 & -27 & 2 & \\
& \ddots & \ddots & \ddots & \ddots & \ddots & \ddots & \ddots \\
& 2 & -27 & 270 & -490 & 270 & -27 & 2 \\
& & 2 & -27 & 270 & -490 & 270 & -25 \\
& & & 2 & -27 & 270 & -488 & 243 \\
& & & & 2 & -25 & 243 & -220
\end{pmatrix}.
$$

Appendix D

Continuity conditions mode matching

Consider a control volume around the interface between two ducts indicated 1 and 2. The integral equations for conservation of mass and momentum are:

$$\iint_S \rho(\overrightarrow{n} \cdot \overrightarrow{v}) \mathrm{d}S = 0, \tag{D.1}$$

and:

$$\iint_S \rho \overrightarrow{v}(\overrightarrow{n} \cdot \overrightarrow{v}) \mathrm{d}S + \iint_S p \overrightarrow{n} \mathrm{d}S = 0. \tag{D.2}$$

Linearization:

$$
\begin{aligned}
p_1 &= p_0 + p_1', \\
\rho_1 &= \rho_0 + \rho_1', \\
\overrightarrow{v}_1 &= (u_0 + u_1')\overrightarrow{e}_x + v_1'\overrightarrow{e}_y, \\
p_2 &= p_0 + p_2', \\
\rho_2 &= \rho_0 + \rho_2', \\
\overrightarrow{v}_2 &= (u_0 + u_2')\overrightarrow{e}_x + v_2'\overrightarrow{e}_y
\end{aligned}
\tag{D.3}
$$

gives:

$$\rho_0 u_1' + u_0 \rho_1' = \rho_0 u_2' + u_0 \rho_2' \tag{D.4}$$

for mass conservation, and:

$$u_0^2 \rho_1' + 2\rho_0 u_0 u_1' + p_1' = u_0^2 \rho_2' + 2\rho_0 u_0 u_2' + p_2', \tag{D.5}$$

respectively:

$$v_1' = v_2' \tag{D.6}$$

for momentum conservation in the x- and y-direction. Equation (D.5) can be rewritten as:

$$(\rho_0 u_1' + u_0 \rho_1')u_0 + \rho_0 u_0 u_1' + p_1' = (\rho_0 u_2' + u_0 \rho_2')u_0 + \rho_0 u_0 u_2' + p_2'. \tag{D.7}$$

Subsequently, subtracting u_0 times equation (D.4) and substituting $p' = c_0^2 \rho'$ gives:

$$\rho_0 u_0 u_1' + c_0^2 \rho_1' = \rho_0 u_0 u_2' + c_0^2 \rho_2'. \tag{D.8}$$

Dividing equation (D.4) by ρ_0 and subtraction $u_0/(\rho_0 c_0^2)$ times equation (D.8) yields:

$$u_1'(1 - M_0^2) = u_2'(1 - M_0^2), \tag{D.9}$$

with $M_0 = u_0/c_0$. Consequently we have:

$$u_1' = u_2'. \tag{D.10}$$

Substituting this in the linearized conservation equations (D.4,D.5) returns:

$$\rho_1' = \rho_2', \tag{D.11}$$

and:

$$p_1' = p_2'. \tag{D.12}$$

The continuity of velocity disturbances u' and v' also implies the continuity of the derivative w.r.t. x of the pressure disturbance $\partial p'/\partial x$, using equation (2.4) and the fact that the derivative of the mean flow, $\mathrm{d}U/\mathrm{d}y$, is continuous. The above yields continuity of dimensionless parameters p_*, v_* and u_*, cf. equation (2.8), and from the definition given in equation (2.12) continuity of q_*. In the mode matching procedure the continuity of q_*, v_* and p_* is utilized.

Appendix E

Modal analysis in 2D cylindrical geometry

In Chapter 2 the method of finding eigenmodes and accompanying wavenumbers for the linear pressure and velocity disturbance in a two-dimensional rectangular duct is presented. Here, the method is extended to a two-dimensional cylindrical duct. We start from the same equations for a perfect and isentropic fluid, given by eqs. (2.1) through (2.3). Quantities are generally now a function of spatial coordinates x and radius r and time t. Any dependence on the angular coordinate is left out of consideration. Linearization then gives analogous to equations (2.4) through (2.6):

$$\rho_0 \Big(\frac{\partial}{\partial t} + U \frac{\partial}{\partial x} \Big) u' + \rho_0 \frac{\mathrm{d}U}{\mathrm{d}r} v' = -\frac{\partial p'}{\partial x}, \qquad (E.1)$$

$$\rho_0 \Big(\frac{\partial}{\partial t} + U \frac{\partial}{\partial x} \Big) v' = -\frac{\partial p'}{\partial r}, \qquad (E.2)$$

$$\frac{1}{\rho_0 c_0^2} \Big(\frac{\partial}{\partial t} + U \frac{\partial}{\partial x} \Big) p' = -\Big(\frac{\partial u'}{\partial x} + \frac{\partial v'}{\partial r} + \frac{v'}{r} \Big). \qquad (E.3)$$

Here u' and v' are the velocity disturbance in x- and r-direction respectively. The mean flow U is a function of r only. Note here that in cylindrical coordinates (r, θ, x) the divergence of a vector $\overrightarrow{a}$ is given by:

$$\overrightarrow{\nabla} \cdot \overrightarrow{a} = \frac{1}{r} \frac{\partial r a_r}{\partial r} + \frac{1}{r} \frac{\partial a_\theta}{\partial \theta} + \frac{\partial a_x}{\partial x}.$$

Similar to equation (2.7) we can derive from these equations:

$$\frac{1}{c_0^2} \Big(\frac{\partial}{\partial t} + U \frac{\partial}{\partial x} \Big)^2 p' - \Big(\frac{\partial^2 p'}{\partial x^2} + \frac{\partial^2 p'}{\partial r^2} + \frac{1}{r} \frac{\partial p'}{\partial r} \Big) = 2\rho_0 \frac{\mathrm{d}U}{\mathrm{d}r} \frac{\partial v'}{\partial x}. \qquad (E.4)$$

Non-dimensionalization according to:

$$p_* = \frac{1}{\rho_0 c_0^2} p', \qquad\qquad (x_*, r_*) = (\frac{x}{R}, \frac{r}{R}),$$

$$(u_*, v_*) = \frac{1}{c_0}(u', v'), \qquad\qquad \omega_* = \frac{\omega R}{c_0}, \qquad\qquad \text{(E.5)}$$

$$M(r) = M_0 f(r) = \frac{1}{c_0} U(r), \qquad t_* = \frac{c_0 t}{R},$$

with R the duct radius, gives the non-dimensional form of equations (E.2,E.3):

$$\Big(\frac{\partial}{\partial t_*} + M_0 f \frac{\partial}{\partial x_*}\Big) v_* = -\frac{\partial p_*}{\partial r_*}, \qquad\qquad \text{(E.6)}$$

$$\Big(\frac{\partial}{\partial t_*} + M_0 f \frac{\partial}{\partial x_*}\Big)^2 p_* - \Big(\frac{\partial^2}{\partial x_*^2} + \frac{\partial^2}{\partial r_*^2} + \frac{1}{r_*}\frac{\partial}{\partial r_*}\Big) p_* = 2M_0 \frac{\mathrm{d}f}{\mathrm{d}r_*}\frac{\partial v_*}{\partial x_*}, \qquad \text{(E.7)}$$

analogous to equations (2.9) and (2.10). Writing the complex form:

$$p_* = P(r_*)\exp(-ik_* x_*)\exp(i\omega_* t_*),$$

$$v_* = V(r_*)\exp(-ik_* x_*)\exp(i\omega_* t_*), \qquad\qquad \text{(E.8)}$$

$$q_* = Q(r_*)\exp(-ik_* x_*)\exp(i\omega_* t_*),$$

where $q_* = i\partial p_*/\partial x_*$, leads to:

$$i(\omega_* - M_0 f k_*)V = -\frac{\mathrm{d}P}{\mathrm{d}r_*}, \qquad\qquad \text{(E.9)}$$

$$(1 - M_0^2 f^2)k_*^2 P + 2\omega_* M_0 f k_* P - \omega_*^2 P - \frac{\mathrm{d}^2 P}{\mathrm{d}r_*^2} - \frac{1}{r_*}\frac{\mathrm{d}P}{\mathrm{d}r_*} = -2iM_0 \frac{\mathrm{d}f}{\mathrm{d}r_*}k_* V. \quad \text{(E.10)}$$

Subsequently, by discretization of r_* the generalized eigenvalue problem analogous to equation (2.17) is found:

$$k_* \begin{pmatrix} \mathbf{I} - M_0^2\mathbf{f^2} & 2iM_0\mathbf{f_a} & \mathbf{0} \\ \mathbf{0} & iM_0\mathbf{f} & \mathbf{0} \\ \mathbf{0} & \mathbf{0} & \mathbf{I} \end{pmatrix} \begin{pmatrix} \mathbf{Q} \\ \mathbf{V} \\ \mathbf{P} \end{pmatrix} =$$

$$\begin{pmatrix} -2\omega_* M_0\mathbf{f} & \mathbf{0} & \omega_*^2\mathbf{I} + \mathbf{D_2} + \mathbf{r_*^{-1}D_1} \\ \mathbf{0} & i\omega_*\mathbf{I} & \mathbf{D_1} \\ \mathbf{I} & \mathbf{0} & \mathbf{0} \end{pmatrix} \begin{pmatrix} \mathbf{Q} \\ \mathbf{V} \\ \mathbf{P} \end{pmatrix}. \qquad \text{(E.11)}$$

Here, matrix $\mathbf{r_*^{-1}D_1}$ represents the discretization of $\frac{1}{r_*}\frac{dP}{dr_*}$. The matrices $\mathbf{D_1}$ and $\mathbf{D_2}$ give the first respectively second derivative with respect to r_*. They are identical to the matrices for the first and second derivative with respect to y_* used with cartesian coordinates (Appendix C), since also here the boundary condition at $r_* = 0$ and $r_* = R$ is $dP/dr_* = 0$. For more specific flow configurations, the generalized eigenvalue problem has to be adapted analogous to what is explained in sections 2.3, 2.4 or 2.5.

Bibliography

[1] M. Åbom, H. Bodén; Error analysis of two-microphone measurements in ducts with flow; J. Acoust. Soc. Am, vol. 83, pp. 2429-2438, 1988.

[2] N.K. Agarwal, M.K. Bull; Acoustic wave propagation in a pipe with fully developed turbulent flow; J. Sound & Vibr., vol. 132(2), pp. 275-298, 1989.

[3] R.J. Alfredson, P.O.A.L. Davies; Performance of exhaust silencer components; J. Sound & Vibr., vol. 15(2), pp. 175-196, 1971.

[4] S. Allam, M. Åbom; Investigation of damping and radiation using full plane wave decomposition in ducts; J. Sound & Vibr., vol. 292, pp. 519-534, 2006.

[5] Y. Aurégan; Comportement aero-acoustique basse-frequence d'une expansion; 14ème Congrès Français de Mécanique, no. 451, Toulouse 1999.

[6] Y. Aurégan, R. Starobinski, V. Pagneux; Influence of grazing flow and dissipation effects on the acoustic boundary conditions at a lined wall; J. Acoust. Soc. Am, vol. 109(1), pp. 59-64, 2001.

[7] Y. Aurégan, A. Debray, R. Starobinski; Low frequency sound propagation in a coaxial cylindrical duct: application to sudden area expansions and to dissipative silencers; J. Sound & Vibr., vol. 243(3), pp. 461-473, 2001.

[8] Y. Aurégan, M. Leroux; Failures in the discrete models for flow duct with perforations: an experimental investigation; J. Sound & Vibr., vol. 265(1), pp. 109-121, 2003.

[9] Y. Aurégan, M. Leroux, V. Pagneux; Measurement of liner impedance with flow by an inverse method; 10th AIAA/CEAS Aeroacoustics conference, AIAA 2004-2838, 2004.

[10] P. Banks-Lee, H. Peng; Length error analysis for impedance tube measurements; J. Acoust. Soc. Am, vol. 85(4), pp. 1769-1772, 1989.

[11] G.K. Batchelor; An introduction to fluid dynamics; Cambridge University Press, 1970; ISBN 0-521-09817-3.

[12] A. Bers; Space-time evolution of plasma instabilities - absolute and convective. in: Handbook of plasma physics: volume 1 basic plasma physics, edited by A.A. Galeev and R.N. Sudan; North-Holland Publishing Company., 1983; ISBN 0-444-86645-0.

[13] A. Bihhadi, Y. Gervais; Propagation in duct with mean flow and temperature gradients; Acta Acoustica, vol. 2 pp. 343-357, 1994.

[14] C.P.A. Blom; Discontinuous Galerkin method on tetrahedral elements for aeroacoustics; PhD thesis, Universiteit Twente, NL, 2003.

[15] H. Bodén, M. Åbom; Influence of errors on the two-microphone method for measuring acoustic properties in ducts; J. Acoust. Soc. Am, vol. 79(2), pp. 541-549, 1986.

[16] S. Boij, B. Nilsson; Reflection of sound at area expansions in a flow duct; J. Sound & Vibr., vol. 260(3), pp. 477-498, 2003.

[17] S. Boij, B. Nilsson; Scattering and absorption of sound at flow duct expansions; J. Sound & Vibr., vol. 289(3), pp. 577-594, 2006.

[18] R.J. Briggs; Electron-stream interaction with plasmas; MIT Press, 1964.

[19] A.M. Cargill; Low frequency acoustic radiation from a jet pipe - a second order theory; J. Sound & Vibr., vol. 83(3), pp. 339-354, 1982.

[20] W. T. Chu; Further experimental studies on the transfer-function technique for impedance tube measurements; J. Acoust. Soc. Am, vol. 83, pp. 2255-2260, 1988.

[21] D.G. Crighton, F.G. Leppington; Radiation properties of the semi-infinite vortex sheet: the initial-value problem; J. Fluid. Mech., vol. 64(2), pp. 393-414, 1974.

[22] D.G. Crighton; Basic principles of aerodynamic noise generation; Progress in Aerospace Sciences, vol. 16, pp. 31-96, 1975.

[23] A. Cummings; Sound transmission at sudden area expansions in circular ducts, with superimposed mean flow; J. Sound & Vibr., vol. 38, pp. 149-155, 1975.

[24] A. Cummings, H. Haddad; Sudden area changes in flow ducts: Further thoughts; J. Sound & Vibr., vol. 54(4), pp. 611-612, 1977.

[25] A. Cummings; The effect of grazing turbulent pipe-flow on the impedance of an orifice; Acustica, vol. 61, pp. 233-242, 1986.

[26] P.O.A.L. Davies; Practical flow duct acoustics; J. Sound & Vibr., vol. 124(1),pp. 91-115, 1988.

[27] N.S. Dickey, A. Selamet; An experimental study of the impedance of perforated plates with grazing flow; J. Acoust. Soc. Am, vol. 110(5), pp. 2360-2370, 2001.

[28] J.H.M. Disselhorst; Acoustic resonance in open tubes; PhD thesis, Universiteit Twente, NL, 1978.

[29] P. Drazin and W. Reid; Hydrodynamic stability; Cambridge University Press, 1981; ISBN 0-521-22798-4.

[30] I.D.J. Dupère, A.P. Dowling; The absorption of sound near abrupt axisymmetric area expansions; J. Sound & Vibr., vol. 239(4), pp. 709-730, 2001.

[31] W. Eversman; The effect of boundary layer on the transmission and attenuation of sound in an acoustically treated circular duct; J. Acoust. Soc. Am, vol. 49(5), pp. 1372-1380, 1971.

[32] P. Freymuth; On transition in a separated laminar boundary layer; J. Fluid. Mech., vol. 25(4), pp. 683-704, 1966.

[33] G.R. Gogate, M.L. Munjal; Analytical solution of sound propagation in lined or unlined circular ducts with laminar mean flow; J. Sound & Vibr., vol. 160(3), pp. 465-484, 1993.

[34] A.L. Goldman, R.L. Panton; Measurement of the acoustic impedance of an orifice under a turbulent boundary layer; J. Acoust. Soc. Am, vol. 60(6), pp. 1397-1404, 1976.

[35] A. Goldman, C.H. Chung; Impedance of an orifice under a turbulent boundary layer with pressure gradient; J. Acoust. Soc. Am, vol. 71(3), pp. 573-579, 1982.

[36] J. Golliard; Noise of Helmholtz-resonator like cavities excited by a low Mach-number turbulent flow; PhD thesis, l'Université de Poitiers, Fr, 2002; ISBN 90-6743-964-9.

[37] S.M. Grace, K.P. Horan, M.S. Howe; The influence of shape on the Rayleigh conductivity of a wall aperture in the presence of grazing flow; Journal of Fluids and Structures, vol. 12, pp. 335-351, 1998.

[38] H. von Helmholtz; On discontinuous movement of fluids; Phil. Mag. (4), 36, 337-346, 1868.

[39] A.S. Hersh, I. Catton; Effects of shear flow on sound propagation in rectangular ducts; J. Acoust. Soc. Am, vol. 50(2), pp. 992-1003, 1971.

[40] A.S. Hersh, B. Walker, M. Bucka; Effect of grazing flow on the acoustic impedance of Helmholtz resonators consisting of single and clustered orifices; AIAA paper 78-1124, 1978.

[41] J.O. Hinze; Turbulence, 2nd edition; McGraw-Hill, 1975; ISBN 0-07-029037-7.

[42] G.C.J. Hofmans; Vortex sound in confined flows; PhD thesis, Technische Universiteit Eindhoven, NL, 1998. ISBN 90-386-0697-4.

[43] M.S. Howe; Contribution to the theory of aerodynamic sound, with application to excess jet noise and the theory of the flute; J. Fluid. Mech., vol. 71(4), pp. 625-673, 1975.

[44] M.S. Howe; Attenuation of sound in a low Mach number nozzle flow; J. Fluid. Mech., vol. 91, pp. 209-229, 1979.

[45] M.S. Howe; The influence of mean shear on unsteady aperture flow, with application to acoustical diffraction and self-sustained cavity oscillations; J. Fluid. Mech., vol. 109, pp. 125-146, 1981.

[46] M.S. Howe; Influence of wall thickness on Rayleigh conductivity and flow-induced aperture tones; Journal of Fluids and Structures, vol. 11, pp. 351-366, 1997.

[47] M.S. Howe; Acoustics of fluid-structure interactions; Cambridge University Press, 1998; ISBN 0-521-63320-6.

[48] X. Jing, X. Sun, J. Wu, K. Meng; Effect of grazing flow on the acoustic impedance of an orifice; AIAA Journal, vol. 39(8), pp. 1478-1484, 2001.

[49] D.S. Jones, J.D. Morgan; The instability of a vortex sheet on a subsonic stream under acoustic radiation; Proc. Camb. Phil. Soc. 72, 465-488, 1972.

[50] F.C. Karal; The analogous acoustical impedance for discontinuities and constrictions of circular cross section; J. Acoust. Soc. Am; vol. 25(2), pp. 327-334, 1953.

[51] Lord Kelvin; Hydrokinetic solutions and observations; Phil. Mag. (4), 42, 362-377, 1871.

[52] R. Kirby, A. Cummings; The impedance of perforated plates subjected to grazing gas flow and backed by porous media; J. Sound & Vibr., vol. 217(4), pp. 619-636, 1998.

[53] G. Kirchhoff; Über den Einfluß der Warmteleitung in einem Gase auf die Schallbewegung; Pogg. Ann. 134(6), pp. 177-193.

[54] S.H. Ko; Sound attenuation in acoustically lined circular ducts in the presence of uniform flow and shear flow; J. Sound & Vibr., vol. 22, pp. 193-210, 1972.

[55] S. H. Ko; Theoretical prediction of sound attenuation in acoustically lined annular ducts in the presence of uniform and shear flow; J. Acoust. Soc. Am, vol. 54(6), pp. 1592-1606, 1973.

[56] S.H. Ko; New approach to the solution of eigenvalue problems in circular flow ducts (a Taylor series method); J. Acoust. Soc. Am; vol. 70(1), pp. 205-212, 1981.

[57] J.W. Kooi, S.L. Sarin; An experimental study of the acoustic impedance of helmholtz resonator arrays under a turbulent boundary layer; AIAA paper 81-1998, 1981.

[58] G. Kooijman, J. Golliard, A. Hirschberg; Orifice impedance under grazing flow measured with a single microphone method; 10th AIAA/CEAS Aeroacoustics conference, AIAA 2004-2846, 2004.

[59] R.F. Lambert, E.A. Steinbrueck; Acoustic synthesis of a flowduct area discontinuity; J. Acoust. Soc. Am; vol. 67(1), pp. 59-65, 1980.

[60] Seong-Hyun Lee, Jeong-Guon Ih; Emperical model of the acoustic impedance of a circular orifice in grazing flow; J. Acoust. Soc. Am, vol. 114(1), pp. 98-113, 2003.

[61] L. Lees, C.C. Lin; Investigation of the stability of the laminair boundary layer in a compressible fluid; NACA Tech. Note, No. 1115, 1946.

[62] M. Leroux; Propagation acoustique en conduit traité: influence de l'ecoulement sur la propagation avec impédance de paroi; PhD thesis, l'Université du Maine, Le Mans, Fr, 2005.

[63] M.J. Lighthill; On sound generated aerodynamically I: General theory; Proceedings of the Royal Society of London, Series A, vol. 211, no. 1107 , pp. 564-587, 1952.

[64] M.J. Lighthill; On sound generated aerodynamically II: Turbulence as a source of sound; Proceedings of the Royal Society of London, Series A, vol. 222, no. 1148, pp. 1-32, 1954.

[65] C. Malmary, S. Carbonne; Acoustic impedance measurement with grazing flow; AIAA paper 2001-2193, 2001.

[66] R. Mani; Sound propagation in parallel sheared flow in ducts: the mode estimation problem; Proceedings of the Royal Society of London, vol. 371, no. 1746, pp. 393-412, 1980.

[67] A. Michalke; On spatially growing disturbances in an inviscid shear layer; J. Fluid. Mech., vol. 23(3), pp. 521-544, 1965.

[68] A. Michalke; The influence of the vorticity distribution on the inviscid instability of a free shear layer; Fluid Dynamics Transactions, vol. 4, pp. 751-760, 1969.

[69] A. Michalke; The instability of free shear layers, a survey on the state of art; Deutsche Luft- und Raumfart, Mitteilung 70-04, 1970.

[70] M.N. Mikhail, A.N. Abdelhamid; Transmission and far-field radiation of sound waves in and from lines duct containing shear flow; AIAA paper 73-1013, 1973.

[71] W. Möhring, E.A. Muller, F. Obermeier; Problems in flow acoustics; Reviews of modern physics 55, pp. 707-724, 1983.

[72] R.E. Motsinger, R.E. Kraft; Design and performance of duct acoustic treatment. in: H.H. Hubbard; Aeroacoustics of flight vehicles, theory and practice, vol. 2: noise control; Acoustical Society of America, 1995; ISBN 1-56396-406-6.

[73] P.M. Morse, H. Feshbach; Methods of theoretical physics; McGraw-Hill, 1953; ISBN 0976202123.

[74] P.M. Morse, K.U. Ingard; Theoretical acoustics, Princeton University Press, 1968; ISBN 0-691-08425-4.

[75] P. Mungur, G.M.L Gladwell; Acoustic wave propagation in a sheared fluid contained in a duct; J. Sound & Vibr., vol. 9(1) pp. 28-48, 1969.

[76] P. Mungur, H. E. Plumblee; Propagation and attenuation of sound in a soft walled annular duct containing a sheared flow; NASA SP-207, pp.305-327, 1969.

[77] R.M. Munt; The interaction of sound with a subsonic jet issuing from a semi-infinite cylindrical pipe; J. Fluid. Mech., vol. 83(4), pp. 609-640, 1977.

[78] R.M. Munt; Acoustic transmission properties of a jet pipe with subsonic flow: 1. The cold jet reflection coefficient; J. Sound & Vibr., vol. 142(3), pp. 413-436, 1990.

[79] R.T. Nagel, R.S. Brand; Boundary layer effects on sound in a circular duct; J. Sound & Vibr., vol. 85(1), pp. 19-29, 1982.

[80] A.H. Nayfeh, J.E. Kaiser, B.S. Shaker; Effect of mean-velocity profile shapes on sound transmission through two-dimensional ducts; J. Sound & Vibr., vol. 34, pp. 413-423, 1974.

[81] A.H. Nayfeh, J.E. Kaiser, D.P. Telionis; Acoustics of aircraft engine-duct systems; AIAA Journal, vol. 13, pp. 130-153, 1975.

[82] B.E. Nilsson, O. Brander; The propagation of sound in cylindrical ducts with mean flow and bulk-reacting lining; Journal of the Institute of Mathematics and its Applications, vol. 26, pp. 269-298, 1980.

[83] H. Özdemir; High-order discontinuous Galerkin method on hexahedral elements for aeroacoustics; PhD thesis, Universiteit Twente, NL, 2006; ISBN 90-365-2391-5.

[84] V. Pagneux, B. Froelich; Influence of low Mach number shear flow on acoustic propagation in ducts; J. Sound & Vibr., vol. 246(1), pp. 137-155, 2001.

[85] K.S. Peat; The acoustical impedance at discontinuities of ducts in the presence of a mean flow; J. Sound & Vibr., vol. 127(1), pp. 123-132, 1988.

[86] K.S. Peat, Jeong-Guon Ih and Seong-Hyun Lee; The acoustic impedance of a circular orifice in grazing mean flow: Comparison with theory; J. Acoust. Soc. Am, 114(6), pp. 3076-3086, 2003.

[87] M.C.A.M. Peters; Aeroacoustical sources in internal flows; PhD thesis, Technische Universiteit Eindhoven, NL, 1993; ISBN 90-386-0282-0.

[88] M.C.A.M. Peters, A. Hirschberg, A.J. Reijnen, A.P.J. Wijnands; Damping and reflection coefficient measurements for an open pipe at low Mach and low Helmholtz numbers; J. Fluid. Mech., vol. 256, pp. 499-534, 1993.

[89] A.D. Pierce; Acoustics, an introduction to its physical principles and applications; McGraw-Hill, 1989; ISBN 0-88318-612-8.

[90] A. Powell; Theory of vortex sound; J. Acoust. Soc. Am, vol. 36(1), pp. 177-195, 1964.

[91] D.C. Pridmore-Brown; Sound propagation in a fluid flowing through an attenuating duct; J. Fluid. Mech., vol. 4, pp. 393-406, 1958.

[92] Rayleigh; On the stability, or instability, of certain fluid motions; Proc. London Math. Soc. 11, 57-70, 1880.

[93] Rayleigh; The theory of sound, 2nd edition; MacMillan, London, 1929.

[94] S.W. Rienstra; Edge influence on the response of shear layers to acoustic forcing; PhD thesis, Technische Universiteit Eindhoven, NL, 1979.

[95] S.W. Rienstra; A small Strouhal number analysis for acoustic wave-jet flow-pipe interaction; J. Sound & Vibr., vol. 86(4), pp. 539-556, 1983.

[96] S.W. Rienstra, N. Peake; Modal scattering at an impedance transition in a lined duct flow; AIAA paper 2005-2852, 2005.

[97] D. Ronneberger; Experimentelle Untersuchungen zum akustischen Reflexionsfaktor von unstetigen Querschnittsänderungen in einem luftdurchströmten Rohr; Acustica, vol. 19, pp. 222-235, 1967/68.

[98] D. Ronneberger; The acoustical impedance of holes in the wall of flow ducts; J. Sound & Vibr., vol. 24(1), pp. 133-150, 1972.

[99] D. Ronneberger; The dynamics of shearing flow over a cavity - a visual study related to th acoustic impedance of small orifices; J. Sound & Vibr., vol. 71(4), pp. 565-581, 1980.

[100] D. Ronneberger; Theoretische und experimentelle Untersuchung der Schallausbreitung durch Querschnittssprünge und Lochplatten in Strömungskanälen, Abschlußbericht Ro 369/11, 12, 14; Drittes Physikalisches Institut der Universität Göttingen, 1987.

[101] S.D. Savkar; Propagation of sound in ducts with shear flow; J. Sound & Vibr., vol. 19(3), pp. 355-372, 1971.

[102] H. Schlichting; Boundary layer theory, 7th edition; Springer, 1979; ISBN 0-07-055334-3.

[103] P.N. Shankar; On acoustic refraction by duct shear layers; J. Fluid. Mech., vol. 47(1), pp. 81-91, 1971.

[104] P.N. Shankar; Sound propagation in duct shear layers; J. Sound & Vibr., vol. 22(2), pp. 221-232, 1972.

[105] P.N. Shankar; Acoustic refraction and attenuation in cylindrical and annular ducts; J. Sound & Vibr., vol. 22(2), pp. 233-246, 1972.

[106] R.N. Starobinski, E.I. Ioudine; On the low frequency sound propagation in a lined duct; Journal of Acoustic, Science Academy of CCCP, XVIII, pp. 115-118, 1972.

[107] M.A. Swinbanks; The sound field generated by a source distribution in a long duct carrying sheared flow; J. Sound & Vibr., vol. 40, pp. 51-76, 1975.

[108] D.H. Tack, R.F. Lambert; Influence of shear flow on sound attenuation in a lined duct; J. Acoust. Soc. Am, vol. 38, pp. 655-666, 1965.

[109] P. Testud; Aéro-acoustique des diaphragmes en conduit: sifflement et cavitation; PhD thesis, l'Université du Maine, Le Mans, Fr, 2006.

[110] H. Tijdeman; On the propagation of sound in cylindrical tubes; J. Sound & Vibr., vol. 39(1), pp. 1-33, 1975.

[111] G.G. Vilenski, S.W. Rienstra; Acoustic modes in ducted shear flow; submitted to J. Fluid Mech., 2006.

[112] G.G. Vilenski, S.W. Rienstra; Numerical study of acoustic modes in ducted shear flow; submitted to J. Sound & Vibr., 2006.

[113] B.E. Walker, A.F. Charwat; Correlation of the effects of grazing flow on the impedance of Helmholtz resonators; J. Acoust. Soc. Am, vol. 72(2), pp. 550-555, 1982.

Summary

Acoustical Response of Shear Layers

In the present work the linear acoustical response of shear layers is investigated for two different geometrical configurations. Both theoretical modelling and experiments are carried out.

The first studied configuration is a sudden area expansion in a duct with mean flow. Here, a shear layer, separating a region with mean flow from a region where the fluid is quiescent, is formed downstream of the area discontinuity. Theoretical modelling for this configuration is done by means of a modal analysis method. The geometry is split into a duct upstream and a duct downstream of the area expansion. The acoustical field in both ducts is found as an expansion of eigenmodes by solving a generalized eigenvalue problem, derived from the linearized Euler equations for conservation of mass and momentum. Here, a discretization in the transverse direction of the duct is employed. By mode matching, a procedure in which continuity of mass- and momentum flux at the interface between the two ducts is applied, the aeroacoustical behaviour is found in the form of a scattering matrix. This scattering matrix relates the modes propagating away from the area discontinuity to the modes propagating towards the area discontinuity. The influence of the mean flow profile, and in particular the application of an acoustical Kutta condition at the edge, on the scattering at the area expansion is investigated. A relatively small influence is observed, and a smooth transition from the case where a Kutta condition is not imposed to the case where it is imposed is seen. Scattering results for plane waves have also been compared to results of an alternative model proposed by Boij and Nilsson, as well as to experimental data of Ronneberger. The alternative model considers an area expansion in a rectangular duct and an infinitely thin shear layer. The experimental data of Ronneberger are obtained for an expansion in a cylindrical tube. In this context, the scaling rule, proposed by Boij and Nilsson, for the comparison of results obtained in a rectangular and a cylindrical geometry, is examined. For this purpose both modal analysis calculations are carried out for rectangular and cylindrical geometry. The scaling rule appears to be reasonably valid in a wide Strouhal number range. How-

ever, it is found that a deviation can occur around a certain critical Strouhal number. Here, a specific behaviour of the scattering is found, which depends on the ratio of the upstream and downstream duct heights or duct radii. Furthermore, comparison of results of the modal analysis method with those of the alternative model and the experimental data provided by Ronneberger shows fairly good correspondence. Also, an improved prediction of the experimental results by the modal analysis method is obtained in some cases when accounting for the non-uniform mean flow profile.

The second configuration studied is that of a shear layer formed in a rectangular orifice in a wall due to the presence of mean grazing flow. Experimentally, the acoustical response of such a shear layer in an orifice is investigated by means of a multi-microphone impedance tube set-up. Care was taken to remain in the regime of linear perturbations. The acoustical behaviour is expressed as a change of orifice impedance due to the grazing flow. Here, the real and imaginary part of the difference of the non-dimensional impedance with flow and the non-dimensional impedance without flow are scaled to the Mach number and the Helmholtz number respectively. The obtained quantities are denoted as the non-dimensional scaled resistance due to the mean flow, respectively the non-dimensional scaled reactance due to the mean flow. This procedure was originally proposed by Golliard on basis of the theory of Howe. The influence of the boundary layer characteristics is investigated. For this purpose boundary layer characterization is performed by means of hot-wire measurements. The Strouhal number dependency of the non-dimensional scaled resistance and reactance due to the flow shows an oscillatory shape. When the Strouhal number is based on the phase velocity of the hydrodynamic instability in the shear layer, rather than the mean flow velocity, these oscillations coincide for different boundary layer flows. The phase velocity is deduced from the shear layer profiles, measured with a hot-wire, using the spatial instability analysis for parallel flows by Michalke. For laminar boundary layer flows the amplitudes of the oscillations increase with decreasing boundary layer thickness. Furthermore, the oscillating behaviour appears to vanish around a Strouhal number, at which the shear layer becomes stable. Since the instability of a shear layer depends on the Strouhal number based on its momentum thickness, the ratio of shear layer momentum thickness and orifice width determines the number of observed oscillations in impedance. The influence of the edge geometry of the orifice on the impedance with grazing flow is examined. It was found that the amplitudes of oscillations in the impedance increase when using sharp edges. Especially the downstream edge of the orifice is important.

Similar to the configuration of an area expansion in a duct, theoretical modelling for the aeroacoustical response of a shear layer in an orifice is done by means of the modal analysis method. In this case the considered geometry is that of two parallel rectangular ducts, of which one carries mean flow. The orifice is represented by an interconnection between the two ducts. This geometry is split into five ducts, in each of which the acoustic field is solved as an expansion of eigenmodes. Mode matching at

the relevant interfaces gives the acoustical behaviour in terms of a scattering matrix, which relates the modes propagating away from the orifice to the modes propagating towards the orifice. From the scattering matrix an orifice impedance is calculated. Modal analysis results are compared with those from an analytical model, proposed by Howe, which considers the low Helmholtz number, low Mach number acoustical response of an infinitely thin shear layer in an orifice in a thin wall separating unbounded uniform grazing flows. Qualitatively, good correspondence is seen between the two models. However, an unexpected influence of the geometrical ratios in the duct configuration on the non-dimensional scaled resistance and reactance is present in case of the modal analysis method. Also, the results both obtained by Howe's theory and by the modal analysis method seem to display non-physical behaviour, especially in the high Strouhal number limit. For non-uniform grazing flow over an orifice convergence of the modal analysis method is a problematic issue. However, a tentative comparison with experimental results shows that the model at least qualitatively predicts the behaviour of the impedance with grazing flow fairly well. In particular, the oscillations in Strouhal number dependency of the non-dimensional scaled resistance and reactance due to the flow, and the related influence of the boundary layer thickness of the flow, are accurately predicted.

Samenvatting

Akoestische Responsie van Schuiflagen

De lineaire akoestische responsie van schuiflagen is onderzocht voor twee verschillende geometrieën. Er is zowel een theoretische modellering als een experimentele studie verricht.

De eerste geometrie betreft een plotselinge doorsnedeverandering in een kanaal met hoofdstroming. In dit geval wordt een schuiflaag gevormd stroomafwaarts van de doorsnedeverandering. Deze schuiflaag scheidt een gebied met hoofdstroming van een gebied waar het medium stilstaat. De theoretische modellering voor deze configuratie betreft een mode analyse methode. De geometrie wordt hierbij opgedeeld in een kanaal stroomopwaarts en een kanaal stroomafwaarts van de doorsnedeverandering. Na oplossing van een gegeneraliseerd eigenwaardeprobleem, afgeleid van de gelineariseerde Euler vergelijkingen voor massa- en impulsbehoud, wordt het akoestisch veld in ieder kanaal gevonden als een reeksontwikkeling van eigenmodes. Hierbij is een discretisatie toegepast in de dwarsrichting van het kanaal. Door *mode matching*, waarbij continuïteit van massa- en impulsstroom wordt geëist op het grensvlak van de twee kanalen, wordt het aeroakoestisch gedrag gevonden in de vorm van een verstrooiingsmatrix. Deze verstrooiingsmatrix relateert de modes die zich van de doorsnedeverandering vandaan voortplanten aan de modes die zich ernaartoe voortplanten. De invloed van het hoofdstroomprofiel, en meer in het bijzonder de toepassing van een akoestische Kutta voorwaarde aan de rand, op de akoestische verstrooiing aan de doorsnedeverandering is onderzocht. Het effect is relatief klein, en een geleidelijke overgang van het geval waarbij de Kutta voorwaarde wordt toegepast naar het geval waarin deze niet wordt toegepast is gevonden. Resultaten voor de verstrooiing van vlakke golven zijn ook vergeleken met de resultaten van een alternatief model gepresenteerd door Boij en Nilsson, alsmede met experimentele data van Ronneberger. Het alternatieve model beschouwt een doorsnedeverandering in een rechthoekig kanaal en een oneindig dunne schuiflaag. De experimentele data van Ronneberger zijn voor een doorsnedeverandering in een cilindrische pijp. Hiermee samenhangend is de schaalregel, voorgesteld door Boij en Nilsson, om resultaten voor een rechthoekige geome-

trie te vergelijken met die voor een cilindrische geometrie onderzocht. Hiertoe zijn berekeningen uitgevoerd met het mode analyse model voor zowel rechthoekige als cilindrische geometrie. De schaalregel blijkt redelijk goed toepasbaar in een breed gebied van Strouhalgetallen. Een afwijking kan zich echter voordoen rond een bepaald kritisch Strouhalgetal. Hier wordt dan een specifiek gedrag van de akoestische verstrooiing gevonden, die afhangt van de verhouding van de hoogtes danwel stralen van het stroomopwaartse en het stroomafwaartse kanaal. Verder laat een vergelijking van de resultaten van de mode analyse methode met die van het alternatieve model en met de experimentele data redelijke goede overeenstemming zien. In een aantal gevallen wordt een betere voorspelling van de experimentele resultaten door het mode analyse model verkregen als de niet-uniformiteit van het hoofdstroomprofiel in beschouwing wordt genomen.

De tweede bestudeerde geometrie is die van een schuiflaag in een rechthoekig opening in een wand, veroorzaakt door een scherende hoofdstroming. De akoestische responsie van deze schuiflaagconfiguratie is experimenteel onderzocht met behulp van een multi-microfoon methode in een impedantiebuis opstelling. Hierbij is zorgvuldigheid betracht om in het gebied van lineaire verstoringen te blijven. Het akoestische gedrag is uitgedrukt als een verandering in de akoestische impedantie van de opening ten gevolge van de scherende hoofdstroming. Het reële en imaginaire deel van het verschil van de dimensieloze impedantie met stroming en de dimensieloze impedantie zonder stroming worden geschaald met het Machgetal respectievelijk het Helmholtzgetal. De hiermee verkregen grootheden worden aangeduid als de dimensieloze geschaalde weerstand ten gevolge van de stroming respectievelijk de dimensieloze geschaalde reactantie ten gevolge van de stroming. Deze procedure is oorspronkelijk voorgesteld door Golliard op basis van de theorie van Howe. De invloed van grenslaagkarakteristieken van de scherende hoofdstroming is onderzocht. Hiervoor is een grenslaagkarakterisatie uitgevoerd door middel van hittedraadmetingen. De Strouhal afhankelijkheid van de dimensieloze geschaalde weerstand en -reactantie ten gevolge van de stroming vertoont een oscillerende vorm. Als het Strouhalgetal wordt gebaseerd op de fasesnelheid van de hydrodynamische instabiliteit in de schuiflaag, in plaats van de hoofdstroomsnelheid, vallen deze oscillaties samen voor verschillende grenslaagstromingen. De fasesnelheid is hierbij afgeleid uit de schuiflaagprofielen, gemeten met een hittedraad, gebruikmakend van de ruimtelijke instabiliteitsanalyse voor parallelle stromingen door Michalke. Voor laminaire grenslaagstromingen nemen de amplitudes van de oscillaties toe met afnemende grenslaagdikte. Het oscillerende gedrag blijkt verder te verdwijnen bij een bepaald Strouhalgetal, waar de schuiflaag stabiel wordt. Aangezien de instabiliteit van een schuiflaag afhangt van het Strouhalgetal gebaseerd op de impulsverliesdikte, bepaalt de verhouding van impulsverliesdikte van de schuiflaag en de breedte van de opening het totaal aantal oscillaties in de impedantie. Verder is de invloed van de randgeometrie van de opening op de impedantie onderzocht. De amplitudes van de oscillaties in impedantie blijken toe te

nemen indien de randen scherp zijn. Met name de stroomafwaartse rand speelt een rol.

Theoretische modellering van de aeroakoestische responsie is, analoog aan de configuratie van een doorsnedeverandering in een kanaal, gedaan met behulp van de mode analyse methode. In dit geval bestaat de beschouwde geometrie uit twee parallelle rechthoekige kanalen, waarvan in één hoofdstroming aanwezig is. De opening wordt voorgesteld door een verbinding tussen de twee kanalen. Deze geometrie wordt opgedeeld in vijf kanalen, in elk waarvan het akoestisch veld wordt bepaald als een reeksontwikkeling van eigenmodes. *Mode matching* op de grensvlakken geeft het akoestische gedrag als een verstrooiingsmatrix, die de modes die van de opening vandaan propageren koppelt aan de modes die ernaar toe propageren. Op basis van de verstrooiingsmatrix kan een impedantie van de opening worden berekend. Resultaten van het mode analyse model zijn vergeleken met die van een theoretisch model van Howe. Dit model beschouwt de akoestische responsie van een oneindige dunne schuiflaag in een opening in een oneindig dunne wand, die twee ongebonden uniforme scherende stromingen scheidt, in de limiet van lage Helmholtzgetallen en lage Machgetallen. Kwalitatief wordt goede overeenstemming gevonden tussen de twee modellen. In het mode analyse model is echter een onverwachte invloed vastgesteld van de geometrische verhoudingen in de configuratie op de dimensieloze geschaalde weerstand en -reactantie . Tevens lijkt zowel de theorie van Howe als het mode analyse model onfysische resultaten te geven, met name in de limiet van hoge Strouhalgetallen. In het geval van niet-uniforme scherende stroming over een opening is de convergentie van de mode analyse methode problematisch. Desalniettemin laat vergelijking met experimentele resultaten zien dat het model in ieder geval kwalitatief de impedantie met scherende stroming redelijk goed voorspelt. In het bijzonder worden de oscillaties in de Strouhalgetal afhankelijkheid van de dimensieloze geschaalde weerstand en -reactantie tengevolge van de stroming, en de samenhangende invloed van de grenslaagdikte van de stroming, nauwkeurig voorspeld.

Dankwoord

Aan het einde van mijn promotiewerk en het einde van dit boekje wil ik graag de gelegenheid aangrijpen om een aantal mensen te bedanken. Immers, mijn naam mag dan wel als enige op de kaft prijken, de totstandkoming van dit proefschrift zou niet mogelijk zijn geweest zonder deze mensen, die ieder op hun eigen wijze een bijdrage hebben geleverd.

Allereerst ben ik veel dank verschuldigd aan mijn eigenlijk eerste promotor Mico. Zijn enthousiasme en betrokkenheid zijn onmisbaar geweest in deze afgelopen vier jaren ('gisteravond zat ik nog eens te denken ..., en ik werd ongerust ... '). Mico's constante stroom ideeën en suggesties waren erg waardevol, tegelijkertijd wist hij me voldoende vrijheid te geven om het onderzoek zelf in te vullen. Niet in de laatste plaats ben ik hem ook zeer dankbaar voor het stimuleren van bezoeken aan congressen, zomercursussen, en onze 'French connection' in le Mans ('ik zou gewoon gaan, we hebben budget').

Rini, mijn officieel eerste promotor, wil ik bedanken voor zijn oprechte interesse, en voor de zorgvuldige manier waarop hij het proefschrift in wording gelezen heeft. Zijn constructieve suggesties waren voor mij van grote waarde.

Une partie importante de cette thèse est dédiée à l'analyse multi-modale. Je suis reconnaissant à mon co-promotor Yves Aurégan d'avoir mis cette méthode à ma disposition. Etant donné le niveau déplorable de mon français et du néerlandais d'Yves, notre communication s'est faite en anglais. Malgré cela je profite de cette occasion pour exprimer, en français, ma gratitude pour notre agréable collaboration. J'ai gardé un sentiment de grande satisfaction de mes visites au Mans, qui ont été très efficaces et produit beaucoup de résultats. L'approche pragmatique d'Yves a été une grande source d'inspiration. Je ne veux pas non plus passer sous silence son rôle comme 'Matlab-gourou'. Concernant mes visites au Mans je tiens aussi à remercier Vincent Pagneux pour ses contributions aux discussions modales et orthogonales. D'autre part je remercie Maud Leroux pour son hospitalité et son aide.

De inzet van technici ten behoeve van het werk beschreven in dit proefschrift is zeer waardevol geweest. Dankzij de betrokkenheid en het inzicht van Jan Willems, vooral bij het ontwerp van de impedantiebuisopstelling, is het mogelijk geweest om op z'n

Curriculum vitae

7 november 1978
　　Geboren te 's-Hertogenbosch

1991-1997
　　Gymnasium, Jeroen Bosch College te 's-Hertogenbosch

1997-2002
　　Technische Natuurkunde, Technische Universiteit Eindhoven

- Interne stage bij de capaciteitsgroep Fysica en Toepassingen van Versnellers
- Externe stage bij ASML, groep Contamination and Temperature Control, te Veldhoven
- Afstudeeronderzoek bij FOM Instituut voor Plasmafysica Rijnhuizen, groep Laserplasma and XUV optics, te Nieuwegein

2002-2007
　　Promotieonderzoek bij de capaciteitsgroep Gasdynamica en Aeroakoestiek, Technische Universiteit Eindhoven

Stellingen behorende bij het proefschrift

Acoustical Response of Shear Layers

door

Gerben Kooijman

31 januari 2007

1. Modellen voor de akoestische responsie van een schuiflaag in een wandperforatie, waarin de schuiflaag oneindig dun wordt verondersteld, beschrijven niet het experimenteel vastgestelde limietgedrag van schuiflagen met afnemende dikte.
Dit Proefschrift

2. In tegenstelling tot het geval van een wandperforatie is voor een doorsnedeverandering in een kanaal met stroming de (in)stabiliteit van de schuiflaag niet van invloed op de akoestische responsie bij hoge Strouhalgetallen.
Dit Proefschrift

3. Numeriek niet convergerende modelresultaten kunnen toch opmerkelijke gelijkenis vertonen met experimentele resultaten.
Dit Proefschrift

4. De effectiviteit van een (semi-)anechoïsche kamer hangt af van de details van de inrichting. In het uitvoeren van aeroakoestische experimenten in een (semi-)anechoïsche kamer is het daarom van belang referentiemetingen uit te voeren.

5. In een college inleiding plasmafysica verdient het de voorkeur om a priori uit te gaan van de mogelijkheid van meervoudig geïoniseerde plasma's.

6. Een verhoging van de gasdichtheid in een laser gegenereerd xenon plasma leidt niet noodzakelijkerwijs tot een verhoogde opbrengst van EUV straling.
R. de Bruijn, K. Koshelev, G. Kooijman, E.S. Toma, F. Bijkerk; Journal of Quantitative Spectroscopy & Radiative Transfer, vol. 81, pp. 97-105, 2003

7. Subsidie bij de aanschaf van nieuwe auto's, die in gebruik minder milieubelastend zijn dan oudere auto's, kan toch leiden tot een grotere milieubelasting.

   J.L. Sullivan, M.M. Costic, W. Han; SAE Transactions: Journal of Materials & Manufacturing, vol. 107, pp. 335-350, 1998

8. Grootschalige toepassing van Concentrated Solar Power (CSA) als duurzame energiebron is voor het westen, waaronder Europa, gezien de wens om in hun energievoorziening onafhankelijk(er) te worden van politiek instabiele- of autoritair geregeerde regio's, geen voor de hand liggende optie.

   I. Bouwmans; L.J. Carton; G.P.J. Dijkema; R.M. Stikkelman; L.J. de Vries; Concentrated Solar Power als onderdeel van de Europese energievoorziening; TU Delft, Faculty of Technology, Policy and Management, Energy and Industry Group, 2006

9. Ten behoeve van concurrentie dienen meerdere partijen (ongeveer) hetzelfde product aan te bieden. Dat dit tot vervlakking kan leiden blijkt bijvoorbeeld uit het Nederlandse televisieprogramma-aanbod.

10. Het hanteren van betaalde servicenummers leidt tot de paradoxale situatie dat consumenten meer moeten betalen in geval van een slechtere dienstverlening.